27
6-18-82

(2)

CONF-811203--Vol 2

I-3861

HOT ELECTRON RING PHYSICS

of the 2nd workshop

MASTER

CONF-811203-- Vol. 2

DE82 016599

proceedings

VOLUME 2

DECEMBER 1-3, 1981

SAN DIEGO, CALIFORNIA

SPONSORED BY

FUSION ENERGY DIVISION
OAK RIDGE NATIONAL LABORATORY
Oak Ridge, Tennessee

Operated by Union Carbide Corporation under contract W-7405-eng-26
with the Office of Fusion Energy, U.S. Department of Energy

and

JAYCOR
San Diego, California

proceedings of the 2nd workshop

CONF-811203

HOT-ELECTRON-RING PHYSICS

DISCLAIMER

This book was prepared as an account of work sponsored by an agency of the United States Government. Neither the United States Government nor any agency thereof, nor any of their employees, makes any warranty, express or implied, or assumes any legal liability or responsibility for the accuracy, completeness, or usefulness of any information, apparatus, product, or process disclosed, or represents that its use would not infringe privately owned rights. Reference herein to any specific commercial product, process, or service by trade name, trademark, manufacturer, or otherwise, does not necessarily constitute or imply its endorsement, recommendation, or favoring by the United States Government or any agency thereof. The views and opinions of authors expressed herein do not necessarily state or reflect those of the United States Government or any agency thereof.

VOLUME 2

DECEMBER 1-3, 1981
SAN DIEGO, CALIFORNIA

Date Published - June 1982

N. A. UCKAN
Editor

SPONSORED BY
FUSION ENERGY DIVISION
OAK RIDGE NATIONAL LABORATORY
Oak Ridge, Tennessee
Operated by Union Carbide Corporation
for the Department of Energy
and
JAYCOR
San Diego, California

DISTRIBUTION OF THIS DOCUMENT IS UNLIMITED

PREFACE

The Second Workshop on Hot Electron Ring Physics was held at San Diego, California, on December 1-3, 1981, under the sponsorship of the Oak Ridge National Laboratory (ORNL) and JAYCOR. About 70 participants representing both the United States and Japan attended the workshop. The first workshop in this series was held at Oak Ridge, Tennessee, December 3-5, 1979 (see *EBT Ring Physics: Proceedings of the Workshop*, CONF-791228, Oak Ridge, Tennessee).

The workshop organizing committee members were:

N. A. Uckan, Chairman, ORNL

N. A. Krall, Chairman, JAYCOR

Diane Miller, Arrangements/Finance, JAYCOR

DeLena Akers, Proceedings, ORNL

The purposes of the workshop were (1) to evaluate and review the progress made in the experimental and theoretical understanding of the hot electron ring properties since the first workshop; (2) to assess various techniques used in the analyses of ring equilibrium, stability, heating, scaling, etc.; and (3) to identify the processes that influence the operating regimes of present and future experiments.

Technical coverage in the workshop was very broad and included the presentation of 43 papers (11 experimental and 32 theoretical), followed by open forum discussions of topics selected by the workshop participants.

These proceedings include (1) workshop summaries prepared by the session chairmen and (2) full-length manuscripts that were submitted to the workshop and presented at the following workshop sessions: Overview (2 invited papers); Stability (12 papers); Ring Properties and Scaling (10 papers); Ring Heating (9 papers); Synchrotron Emission (5 papers); and Ions, Tandems, Equilibria, and Power Balance (5 papers). Open-forum discussions are partially reported at the end of the proceedings. An Author Index, the Attendance List, and the Agenda conclude the proceedings. (Because of the need for the camera-ready publication, variations in style and format were inevitable.)

The local host for the workshop was JAYCOR, and a special acknowledgment is due to Nick Krall and Diane Miller for the excellent arrangements and warm hospitality at San Diego. The efforts of session chairmen provided an enthusiastic forum for discussion of the papers that contributed largely to the sucess of the workshop. The assistance of DeLena Akers in the preparation and coordination of these proceedings is gratefully acknowledged. Thanks are also due to Caila Cox and to the staff of the ORNL FED Reports Office for handling many details of the publication.

The organizing committee wishes to express its appreciation to McDonnell Douglas Astronautics Company; Science Applications, Inc.; and TRW, Inc.; for co-hosting the workshop reception.

N. A. Uckan
Oak Ridge, Tennessee
January 1982

CONTENTS — VOLUME I

1. SUMMARY OF THE WORKSHOP 1

2. OVERVIEW..... 21

HOT ELECTRON RINGS: DIAGNOSTIC REVIEW AND SUMMARY OF MEASUREMENTS — G. R. Haste 23

A PERSPECTIVE ON EBT ELECTRON RING THEORY — N. A. Krall 45

3. STABILITY 81

CURVATURE DRIVEN INSTABILITIES IN A HOT ELECTRON PLASMA: RADIAL ANALYSIS — H. L. Berk, J. W. Van Dam, M. N. Rosenbluth, D. A. Spong 83

RADIAL STRUCTURE OF INSTABILITY MODES IN THE EBT HOT ELECTRON ANNULUS — D. A. Spong, H. L. Berk, J. W. Van Dam, and M. N. Rosenbluth 93

STABILITY OF LOW FREQUENCY MODES IN A HOT ELECTRON BUMPY TORUS — K. T. Tsang and P. J. Catto 117

KINETIC THEORY OF EBT STABILITY — C. Z. Cheng 143

STABILIZATION OF THE HIGH-BETA PLASMA INSTABILITY WITH ECH HOT ELECTRON ANNULUS IN THE SYMMETRIC MIRROR — S. Hiroe, T. Kunibe, H. Akiyama, and M. Inutake 145

EXPERIMENTAL HOT-TO-WARM ELECTRON DENSITY RATIO FOR INSTABILITY THERSHOLD IN THE ELMO BUMPY TORUS — S. Hiroe, L. A. Berry, R. J. Colchin, J. C. Glowienda, G. R. Haste, D. L. Hillis, and T. Uckan 167

STABILIZATION OF THE FLUTE INSTABILITY BY A D.C. ELECTRIC FIELD IN TOROIDAL PLASMAS — I. Alexeff 181

NECESSARY AND SUFFICIENT CRITERIA FOR THE STABILITY OF A HOT PARTICLE RING - PLASMA SYSTEM — T. M. Antonsen, Jr. and Y. C. Lee 191

SIMULATION STUDIES ON STABILITY AND β LIMITS OF EBT — Y. Ohsawa and J. M. Dawson 213

PARAMETRIC DECAY INSTABILITIES IN ECR HEATED PLASMAS — M. Porkolab 237

THE WHISTLER INSTABILITY AT RELATIVISTIC ENERGIES — N. T. Gladd 247

HIGH-FREQUENCY MICROINSTABILITIES IN HOT-ELECTRON PLASMAS — Y-J. Chen, W. M. Nevins, and G. R. Smith 279

STABILITY OF ANISOTROPIC RELATIVISTIC HOT ELECTRON PLASMA IN THE ELMO BUMPY TORUS — K. T. Nguyen, T. Kammash, and R. J. Kashuba 289

4. RING PROPERTIES AND SCALING 315

HARD X-RAY MEASUREMENTS OF THE HOT ELECTRON RINGS IN EBT-S — D. L. Hillis 317

INTERACTION OF MICROWAVE WITH HOT ELECTRON RING IN NAGOYA BUMPY TORUS — M. Tanaka, M. Hosokawa, M. Fujiwara, and H. Ikegami 339

RING TEMPERATURE SCALING — N. A. Uckan 361

PARAMETRIC STUDY OF THE RELATIVISTIC ELECTRON RING — S. Hamasaki, N. A. Krall, and J. L. Sperling 373

PROSPECTS FOR CONTROL OF ELMO RINGS — G. E. Guest and R. A. Dandl 393

NONADIABATICITY AND HIGH ENERGY PARTICLE ORBITS IN EBT — L. W. Owen, L. E. Deleanu, and C. L. Hedrick 409

THE NONADIABATIC MOTION OF HOT ANNULUS ELECTRONS IN EBT-I AND EBT-P — R. E. Juhala, M. A. Prelas, and C. B. Wallace 425

HEATING OF ENERGETIC ELECTRONS AND ELMO RING FORMATION IN SYMMETRIC MIRROR FACILITY — B. H. Quon, R. A. Dandl, N. H. Lazar, and R. F. Wuerker 441

SPATIAL STRUCTURE OF THE SM-1 SYMMETRIC MIRROR HOT ELECTRON RING USING DIAMAGNETIC MEASUREMENTS — L. L. Lao, B. H. Quon, R. A. Dandl, and N. H. Lazar 463

BUMPY TORUS ANNULUS STARTUP — J. L. Sperling, S. Hamasaki, and N. A. Krall 471

CONTENTS — VOLUME II

5. RING HEATING 485

RAY TRACING STUDIES OF MICROWAVE HEATING OF THE ANNULUS IN EBT DEVICES — D. B. Batchelor, R. C. Goldfinger, and H. Weitzner 487

FOKKER-PLANCK CALCULATIONS OF ELECTRON CYCLOTRON RESONANT HEATING (ECRH) IN MIRROR GEOMETRY — B. W. Stallard, Y. Matsuda, and W. M. Nevins 505

MULTIPLE FREQUENCY ECH (MFECH) IN SM-1 AND STM-1 — N. Lazar, J. Barter, R. Dandl, W. DiVergilio, B. Quon, and R. Wuerker 519

SIMULATION OF ELECTRON CYCLOTRON RESONANCE HEATING WITH MULTIPLE FREQUENCIES IN MIRROR GEOMETRY — T. K. Samec, B. I. Hauss, and G. Guest 531

SIMULATION OF MULTI-FREQUENCY ECRH — T. D. Rognlien 545

THEORY OF MULTIFREQUENCY ECRH — J. E. Howard, M. A. Lieberman, A. J. Lichtenberg, and R. H. Cohen 561

DOPPLER-SHIFTED RESONANCE ABSORPTION BY HOT ELECTRONS — J. W. Shearer 583

ENHANCEMENT OF EBT RING PARAMETERS DURING ION CYCLOTRON HEATING — F. W. Baity, J. C. Glowienka, D. L. Hillis, and T. L. Owens 597

NONSTANDARD HEATING EXPERIMENTS IN EBT — J. C. Glowienka, W. A. Davis, D. L. Hillis, T. Uckan, F. M. Bieniosek, and L. Solensten 609

6. SYNCHROTRON EMISSION 633

SYNCHROTRON EMISSION MEASUREMENTS FROM THE HOT ELECTRON RINGS IN EBT — J. Wilgen and T. Uckan 635

SYNCHROTRON EMISSION FROM THE RING ELECTRONS IN EBT — T. Uckan and N. A. Uckan 657

ELECTROMAGNETIC INTERACTIONS OF NON-MAXWELLIAN PLASMAS — S. Tamor 689

ANALYTIC EXPRESSIONS FOR SYNCHROTRON RADIATION FROM EBT — D. Winske, D. A. Boyd, and G. D. Tsakiris 701

ELECTRON SYNCHROTRON EMISSION FROM THE EBT RING PLASMA — C. M. Celata 717

7. IONS, TANDEMS, EQUILIBRIA, AND POWER BALANCE 719

ION RING SCALING STUDIES FOR AN EBT REACTOR — M. R. Gordinier and R. J. Kashuba 721

RING POWER BALANCE OBSERVING PLASMA STABILITY CONSTRAINTS — R. B. Campbell and B. G. Logan 739

NUMERICAL STUDY OF VLASOV EQUILIBRIUM FOR BUMPY CYLINDER PLASMA WITH HOT ELECTRON RINGS — T. Watanabe, K. Hamamatsu, J. W. Van Dam, and K. Nishikawa 761

SENSITIVITY OF HEAVY ION BEAM PROBE TO HOT ELECTRONS IN EBT — F. M. Bieniosek and K. A. Conner 793

THE "NEGATIVE" TANDEM MIRROR — P. Poulsen, S. L. Allen, T. A. Casper, D. P. Grubb, R. A. Jong, W. E. Nexsen, G. D. Porter, and T. C. Simonen 815

8. OPEN FORUM 827

MHD STABILITY OF TANDEM MIRRORS — P. Poulsen, A. Molvig, J. Shearer 829

AUTHOR INDEX 833

ATTENDANCE LIST 835

AGENDA 839

5. RING HEATING

RAY TRACING STUDIES OF MICROWAVE HEATING OF THE ANNULUS IN EBT DEVICES*

D. B. Batchelor and R. C. Goldfinger
Oak Ridge National Laboratory
Oak Ridge, Tennessee 37830

H. Weitzner
New York University
New York, NY 10012

Electron cyclotron absorption of ordinary and extraordinary waves by the combined core-plasma and relativistic annuli have been studied numerically. A fully relativistic damping package has been developed for the RAYS geometrical optics code, which allows the contribution from an arbitrary number of cyclotron harmonics to be included. The rays are traced in finite beta bumpy cylinder plasma equilibria which is obtained from the ORNL two-dimensional (2-D) equilibrium code. These results for direct, single-pass absorption are combined with results from a statistical model for the deposition of multiply reflected and mode converted waves to obtain estimates of the power deposited in the core, surface, and annulus plasma components. Self-consistent estimates of the annulus power losses for EBT-I, EBT-S, and EBT-P are obtained using the same ring equilibrium model.

1. INTRODUCTION

In this paper we present detailed numerical calculations of the microwave power deposition in the various plasma components of EBT devices. Previous studies using the RAYS geometrical optics code[1,2,3] have concentrated on power deposition in the core and surface plasma components. The picture which emerged was one of weakly damped rays making many transits across the device, with wall reflections and

*Research sponsored by the Office of Fusion Energy, U.S. Department of Energy, under contract W-7405-eng-26 with the Union Carbide Corporation.

repeated ordinary-extraordinary mode conversions playing an important role in the ultimate energy deposition. In order to deal with the complicated essentially random nature of the wave propagation after a few wall reflections, a simple zero dimensional power balance model was developed which treated the source, sinks, and conversion properties of the ordinary and extraordinary modes in a globally averaged way.[4] Wave absorption by the annulus was included in the power balance model empirically by measured estimates of the fraction of power going to the rings. Recently, we have developed a fully relativistic damping package for the RAYS code that involves no expansion in T_e/mc^2 and allows an arbitrary number of cyclotron harmonics to be included.[5] Combining ray tracing studies with the power balance model, we are now able to theoretically treat the complete power deposition problem. A great many simplifying approximations are, of course, still necessary to make progress.

Our calculations are carried out using a bumpy cylinder equilibrium with parameters chosen to model as closely as possible the plasma configurations of EBT-I and EBT-P. Initially, we trace an ensemble of rays through the plasma which are launched at varying angles from a point at the midplane near the vacuum vessel wall. The power carried by each ray is weighted by a suitable antenna radiation pattern and the power deposited in each plasma component for a single pass through the device is determined by integrating over a solid angle. Typically, we find that only a small fraction of the total injected power is absorbed in a single pass. Hence, the power remaining after a single pass is spread across the wall surface and greatly randomized with respect to direction of propagation; the deposition of this power can be calculated using the power balance model. In the end, we obtain estimates for the total power deposited in the core, annulus, and surface plasma components.

2. EQUILIBRIUM MODEL

The finite beta magnetic fields and annulus density profile are calculated using a two-dimensional (2-D) tensor pressure MHD equilibrium code[6]

$$B(r,z) = \underset{\sim}{\psi} \times \underset{\sim}{\nabla}\theta \quad ,$$

where ψ satisfies

$$\Delta^*\psi + \underset{\sim}{\nabla} \ln \sigma \cdot \underset{\sim}{\nabla}\psi = -\frac{r^2}{\sigma}\frac{\partial P_{\parallel}}{\partial \psi}$$

and

$$\sigma = 1 + \frac{P_{\perp} - P_{\parallel}}{B^2}$$

$$P_{\parallel}(B,\psi) = \hat{P}_{\parallel}(B)g(\psi) + P(\psi)$$

$$P_{\perp}(B,\psi) = \hat{P}_{\perp}(B)g(\psi) + P(\psi)$$

$$\hat{P}_{\parallel}(B) = \frac{S}{2}(B_c - B)^2 \text{ for } B < B_c$$

$$\hat{P}_{\perp}(B) = \frac{S}{2}(B_c^2 - B^2) \text{ for } B < B_c$$

$$\hat{P}_{\parallel} = \hat{P}_{\perp} = 0 \quad \text{for } B > B_c$$

S = annulus strength factor related to beta

B_c = cutoff field related to annulus length

$g(\psi)$ = cubic polynomial which vanishes outside $\psi_1 < \psi < \psi_2$.
determines radial extent of annulus

To model EBT-I, $g(\psi)$ is adjusted to give an annulus extending from r_{min} = 8 cm to r_{max} = 12 cm with the annulus pressure peak at $r_{peak} \approx$ 10 cm. This places the annulus pressure peak near the radial location of the vacuum second harmonic resonance for the nominal EBT-I operating current of 5000 A in the toroidal field coils. In our calculations the magnetic field is scaled so as to place the vacuum second harmonic resonance at r_{peak}. B_c is adjusted to give a half pressure annulus length of about 11 cm. The parameter s is fixed so as to give β = 0.085 where

$$\beta \equiv \frac{(8\pi n_A T_A)\max}{B(o)^2} \quad .$$

This corresponds to local $\beta = (8\pi n_A T_A)_{max}/B^2_{\text{second harmonic}} = 0.13$. The externally imposed vacuum bumpy cylinder field is due to filamentary current loops spaced 20 cm from the midplane with a radius necessary to produce a 2:1 mirror ratio on axis.

The wave absorption depends independently on the annulus density n_A and temperature T_A, although the equilibrium code provides information only about the pressure. We have, therefore, adopted a simple model in which T_A is constant and $n_A \propto P = P_\perp + P_\parallel$

$$n_A(\underset{\sim}{x}) = n_A(B,\psi) = \frac{\beta B^2(o)}{8\pi T_A} \frac{P(B,\psi)}{P}$$

The core density is chosen to be a function of $\psi(\underset{\sim}{x})$ alone, which is

flat inside the annulus and decreases through the annulus to a constant level n_∞ in the surface plasma.

$$n_c(\underset{\sim}{x}) = n_c[\psi(x)] = \begin{cases} n_o, & \psi < \psi(r_{min},0) \\ \dfrac{1 + c - \mathrm{TANH}\left(\dfrac{\psi(\underset{\sim}{x}) - \psi_o}{\delta^2}\right)}{1 + c + \mathrm{TANH}\left(\dfrac{\psi_o}{\delta^2}\right)}, & \psi(r_{min},0) < \psi(\underset{\sim}{x}) < \psi(r_{max},0) \\ n_\infty, & \psi > \psi(r_{max},o) \end{cases}$$

where

$$\psi_o = \psi(r_o,0)$$

$$c = \mathrm{TANH}\left(\frac{\psi_o}{\delta^2}\right) \frac{n_\infty}{1 - n_\infty}$$

The core temperature is taken to be proportional to the core density

$$T_c(\underset{\sim}{x}) = T_e \frac{n_c(\underset{\sim}{x})}{n_o} \quad .$$

Current plans call for the individual sectors of EBT-P to be geometrically similar to EBT-I although larger by nearly a factor of 2. The mirror ratio again ~2:1. To perform ray tracing calculations for EBT-P, we have simply scaled the EBT-I 2-D equilibrium geometry by a factor of 1.9. Again the vacuum second harmonic resonance is placed at

$r_{peak} \simeq 18$ cm. The assumed plasma parameters used in these calculations are shown in Table I.

3. RELATIVISTIC DAMPING MODEL

In our calculations the absorption is calculated using Poynting's theorem

$$\frac{d}{ds}|\underset{\sim}{S}| = \frac{4\pi}{c}\underset{\sim}{E}^* \cdot \underset{\sim}{\sigma}^H \cdot \underset{\sim}{E} ,$$

where s is the arc length along a ray, $\underset{\sim}{S} = \mathrm{Re}[\underset{\sim}{E}^* \times (\underset{\sim}{n} \times \underset{\sim}{E})]$ = Poynting's vector, $\underset{\sim}{n} = c\underset{\sim}{k}/\omega$ = real refractive index, and σ^H = Hermitian part of the relativistic conductivity tensor. The real refractive index is determined from the ray tracing code, which uses the cold plasma dispersion relation

$$D(\underset{\sim}{n}) = \det[\underset{\sim}{D}] = \det[(1 - n^2)\underset{\sim}{I} + \underset{\sim}{n}\underset{\sim}{n} + \frac{4\pi i}{\omega}\underset{\sim}{\sigma}^A] = 0,$$

where σ^A = anti-Hermitian part of the plasma conductivity. Two plasma components are included in $\underset{\sim}{\sigma}^A$: a cold core plasma component and an annulus component for which σ^A is also assumed to be of the cold form. The electric field eigenvectors, $\underset{\sim}{E}$, used in the equation are determined from the cold plasma dispersion tensor with both components included, $\underset{\sim}{D} \cdot \underset{\sim}{E} = 0$. It should be mentioned that this procedure gives accurate values for the damping rate near the second harmonic resonance but is not valid near the fundamental resonance because of finite T_e modification to the eigenvectors. Details for the calculations for σ^H may be found in Ref. 5.

Figure 1 shows the local value of $k_i \equiv \mathrm{Im}\{\underset{\sim}{k}\}$ as a function of Ω_e/ω for various values of T_e. The calculation is for a frequency of f_μ = 60 GHz, density $n_e = 4.4 \times 10^{12}/\mathrm{cm}^3$, and perpendicular propagation $n_\parallel$ = 0. Twenty cyclotron harmonics are included in $\underset{\sim}{\varepsilon}^H$. It can be seen that for fixed Ω_e/ω, k_i is a decreasing function of T_e at large T_e. Just below the second harmonic resonance ($\Omega_e/\omega \leq 0.5$), as would be expected at the annulus pressure peak, the maximum of k_i occurs at $T_e \sim 90$ keV.

4. RAY TRACING RESULTS FOR SINGLE-PASS ABSORPTION

The microwaves in EBT are injected from waveguides located at the midplane of each mirror sector. In order to calculate the direct power deposition in a single pass through the plasma, an ensemble of rays with various angles of propagation are traced from a point near the cavity wall representing the waveguide opening. The rays are followed until they emerge from the plasma at the cavity wall. For extraordinary mode rays, one or more reflections may occur in the plasma at the right-hand cutoff. The absorption is calculated on the basis of two plasma components, annulus and core, as described above. Three absorption processes are involved (1) absorption by the annulus in the vicinity of the second harmonic resonance, (2) absorption by the core at the second harmonic, and (3) absorption by the core at the fundamental resonance. Since the fundamental resonance is inaccessible to the midplane-launched extraordinary mode, direct absorption at the fundamental occurs only for the ordinary mode.

Figures 2a and 2b show typical ray paths for the extraordinary mode in the equatorial plane and midplane, respectively. In Fig. 2a the location of the annulus, the fundamental and finite β second harmonic resonance, and the right-hand cutoff are shown, and in Fig. 2b the intersection of the midplane with the annulus and the cavity wall are shown. Since the equilibrium for EBT-P was obtained from the EBT-I case by simple scaling and $\omega_{pe}(o)/\omega$ and $\Omega_e(o)/\omega$ were the same in both cases, the shapes of the ray paths are virtually identical for the two devices (slight differences exist because of the higher β used in

the EBT-P calculations). We have given the results for both devices on Fig. 2. Associated with each ray are two pairs of numbers [$(f_x^{ann}, f_x^{second})_I$ and $(f_x^{ann}, f_x^{second})_P$], which indicate the fraction of power initially carried by the ray deposited in the annulus and in the core component at the second harmonic resonance for EBT-I and EBT-P, respectively. We see that of order 10-20% of a typical ray's energy is absorbed by the annulus in EBT-I, whereas only a few percent is absorbed by the annulus in EBT-P. On the other hand the core component in EBT-I absorbs only a small amount of power at the second harmonic resonance, and in EBT-P most of the power is lost to the core. The ordinary mode is much more weakly damped by both the annulus and core at the second harmonic resonance. The ordinary mode can, however, propagate directly to the fundamental resonance. Because of the low density and temperature of the core component in EBT-I, a maximum of a few percent of the energy carried by an ordinary mode ray is absorbed at the fundamental. The high density and temperature of the core component in EBT-P and the larger plasma size result in ordinary mode absorption of up to 50%.

In EBT-I and EBT-S the microwaves are launched from a waveguide without any directive antenna structure. The radiation pattern is not known, so we make the plausible assumption that power is distributed in the solid angle $d\Omega$ according to the law

$$P d\Omega = \frac{3P_{inj}}{2\pi} \cos^2\theta d\Omega \quad ,$$

where θ is the angle with respect to the axis of the waveguide. This pattern is symmetric about the axis and gives total injected power P_{inj} when integrated over the foward hemisphere. The fraction $\langle f \rangle$ of the injected power, which is deposited in a given plasma component, is determined by integrating over solid angle

$$\langle f\rangle = \frac{1}{P_{inj}} \int d\phi \, d\theta \, \sin\theta \, f(\theta,\phi)P(\theta) \quad ,$$

where $f(\theta,\phi)$ is the fraction of power lost to that component by the ray launched in direction θ,ϕ.

Numerically carrying out the integral above with $f(\theta,\phi)$ obtained from ray tracing, we find the fraction of extraordinary mode power deposited in the annulus and in the core component at the second harmonic resonance to be

$$\langle f\rangle^{x}_{ann} = 0.063 \qquad \langle f\rangle^{x}_{second} \sim 0.01 \ , \qquad \text{(extraordinary mode)}$$

and for the ordinary mode at the annulus, core at the second harmonic and core at the fundamental,

$$\langle f\rangle^{o}_{ann} = 0.007 \qquad \langle f\rangle^{o}_{second} \sim 0.0 \qquad \langle f\rangle^{o}_{fund} \sim 0.001 \ .$$

(ordinary mode)

The dominant mode waveguide used to launch the microwaves in EBT-I is oriented so as to excite predominantly ordinary mode. We assume that the injected power P_{inj} is partitioned between excited ordinary mode P_{inj} and extraordinary mode P^{x}_{inj}, $P_{inj} = P^{x}_{inj} + P^{o}_{inj}$, and that the radiation pattern for both modes is $P(\theta)$. Taking an 80-20 ordinary-extraordinary mode mix, $P^{o}_{inj} = 0.8 \ P_{inj}$, $P^{x}_{inj} = 0.2 \ P_{inj}$, gives for the single-pass power deposited in the annulus

$$P_{ann} = \langle f\rangle^{x}_{ann} P^{x}_{inj} + \langle f\rangle^{o}_{ann} P^{o}_{inj} = 0.018 \ P_{inj} \quad ,$$

in the core at the second harmonic

$$P_{second} = \langle f\rangle^{x}_{second}\, P^{x}_{inj} + \langle f\rangle^{o}_{second} P^{o}_{inj} = 0.002\ P_{inj} \quad .$$

Only about 2% of the total injected power is absorbed in one pass of the microwave through the device. The remaining 0.187 P_{inj} in the extraordinary mode and 0.79 P_{inj} in the ordinary mode is spread widely around the surface of the cavity wall; absorption is discussed in the next section in terms of the power balance model. Similar calculations for EBT-P, assuming again the $\cos^2\theta$ radiation pattern, gives

$$\langle f\rangle^{x}_{ann} = 0.017 \qquad \langle f\rangle^{x}_{second} = 0.264$$

$$\langle f\rangle^{o}_{ann} = 0.005 \qquad \langle f\rangle^{o}_{second} \leq 0.001 \qquad \langle f\rangle^{o}_{fund} = 0.0429 \quad .$$

For EBT-P an unpolarized wave launching system is planned for which one expects a roughly 50-50 ordinary-extraordinary mode mix to be excited. With the average fractional absorptions above, the single-pass power deposition is

$$P_{ann} = 0.011\ P_{inj} \qquad P_{second} = 0.132\ P_{inj} \qquad P_{fund} = 0.022 \quad .$$

5. POWER BALANCE MODEL

In order to account for deposition of the power remaining after a single pass through the cavity, the 0-D power balance model is modified with an improved model for annulus power deposition and by including a loss channel for absorption by the core component at the second harmonic resonance. The power balance equations take the form (see Ref. 4 for details),

$$P_x - (\alpha_x^{ann} + \alpha_x^{second})\, W_x^I - \tau^I W_x^I + \tau^I W_o - (\gamma_a + \gamma_T) W_x^I = 0$$

$$P_o - (\alpha_o^{fund} + \alpha_o^{second} + \alpha_o^{ann}) W_o - (\tau^I + \tau^{II})\, W_o + \tau_x^I W_x^I + \tau^{II} W_x^{II} = 0$$

$$\gamma_T W_x^{II} - \alpha_x^{II} W_x^{II} - \tau^{II} W_x^{II} + \tau^{II} W_o = 0 \quad ,$$

where P_x and P_o are the powers remaining in each mode after a single pass, W_x^I and W_x^{II} are the extraordinary mode energy densities in regions I and II, and W_o is the ordinary mode energy density, assumed uniform throughout the device.

The annulus absorption rate coefficients α_x^{ann} and α_o^{ann} are obtained from the following simple model. A cylindrical surface is constructed having a radius equal to that peak of the annulus pressure profile r_p and length equal to the half pressure annulus length ℓ_A. Assuming an isotropic flux of waves in the jth mode with group velocity c, we have total power passing through this surface,

$$\text{flux} = 2\pi r_p \ell_A c W^j = c S_{ann} W^j \quad ,$$

where S_{ann} is the surface area of the idealized annulus surface. We now trace a collection of rays for each mode from a point just outside the annulus covering all solid angles. The fraction of power absorbed in one passage through the annulus is calculated and this fraction is averaged over the solid angle. The power absorbed by the annulus from this isotropic flux is then assumed to be

$$P_j^{ann} = c\langle f\rangle_{ann}^j\, S_{ann}\, W^j \quad .$$

A similar model is used to treat the heating of the core plasma at the second harmonic, except that the relevant surface area S_{second} is taken

as that of the second harmonic resonance surface which lies in the core plasma.

For the assumed annulus parameters quoted above we find $\langle f\rangle^{x}_{ann}$ = 0.093, $\langle f\rangle^{o}_{ann}$ = 0.013 for EBT-I and $\langle f\rangle^{x}_{ann}$ = 0.041, $\langle f\rangle^{o}_{ann}$ = 0.011 for EBT-P. Absorption by the core at the second harmonic is $\langle f\rangle^{second}_{x} \simeq$ 0.02, $\langle f\rangle^{second}_{o} \simeq 0$ for EBT-I and $\langle f\rangle^{second}_{x}$ = 0.83, $\langle f\rangle^{second}_{o}$ = 0.03 for EBT-P.

Although the results of the power balance model for EBT-I depend weakly on what is assumed for the mix of ordinary-extraordinary modes excited by the waveguide, the average mode conversion coefficient, the Budden tunneling parameters, and the like, we find that typically the total (one pass + randomized) power deposition is $P_{ann} \sim 0.25\ P_{Tot}$, $P_{core} \sim 0.25\ P_{tot}$, $P_{second} \sim 0$, and $P_{surface} \sim 0.5\ P_{tot}$. For EBT-P the results, assuming a 50-50 mode mix, are $P_{ann} \sim 0.045\ P_{Tot}$, $P_{core} \sim 0.27\ P_{tot}$, $P_{second} \simeq 0.65\ P_{tot}$, and $P_{surface} \simeq 0.033\ P_{tot}$.

6. CONCLUSIONS

Experimental estimates of the power losses from the annuli can be obtained using the ring stored energy and the decay time after power turnoff. Experiments performed on EBT-I using a total 40 kW of 18 GHz power indicated a power loss per ring ~50 W.[7] This is considerably less than the ~400 W which has previously been reported.[8] Assuming the microwave distribution system to have an efficiency of 66%, the microwave power injected into each cavity is P_{inj} = 0.66 × 40 kW/24 ~ 1.1 kW. The estimated 50 W, therefore, represents ~4.5% of the total injected power. The theoretical estimate of 25% (~280 W/cavity) power deposition is significantly higher. For comparison, when the classical losses (drag, scattering, and synchrotron radiation) are integrated over the assumed ring and core plasma profiles, one obtains $P_{classical}$ ~ 13 W/cavity.

At best with a zero-dimensional model such as this, one would expect only rough agreement with experiment. Some uncertainty exists in the global averages used to obtain the rate coefficients for mode conversion tunnelling and absorption. However, experiment with the power balance model has shown that the power ultimately deposited in the annulus is only weakly dependent on the various rate coefficients throughout their credible range with the exception of the annulus fractional absorption $\langle f \rangle^{j}_{ann}$. Part of the discrepancy may lie in the measurements themselves. For example, any particle and energy losses due to scattering by microwave would not contribute to ring decay in a microwave turnoff experiment. The existing discrepancy certainly indicates a need to examine the ring absorption process to discover any physical effects not included in the model which would reduce ring power absorption. Several possibly important effects have been identified and are now being investigated: anisotropy of the annulus distribution function, nonlinear superdiabatic limits to heating, and finite ρ/L effects on the linear heating operator.

The lower fraction of injected power absorbed by the ring in EBT-P (~4.5%) is due to the decrease in local damping rate at high temperatures (Fig. 1) and the strong absorption by the core component at the second harmonic. Assuming 1 MW of gyrotron power and 0.66 distribution efficiency, this amounts to ~850 W/ring. For comparison, the classical losses for the same ring and plasma profiles used in the absorption calculations are ~4 kW/ring. The conclusion is that an EBT-P annulus having the assumed parameters is inconsistent with the heating model presented here. It should be pointed out that these calculations do not include the 400 kW of 28-GHz profile heating power. Waves at this frequency have no second harmonic in the core plasma and should be much more efficiently absorbed by the annuli. Both the linear heating and classical losses scale linearly with density, whereas heating decreases with temperature and classical losses increase with temperature (syncrotron radiation dominates at 1 MeV). Therefore, if one assumes that these are the correct heating and loss

models, a steady-state ring temperature lower than 1 meV would be expected with 1 MW of microwave power (this neglects the higher efficiency of 28 GHz).

The projections for EBT-P must be regarded as speculative, based as they are on postulated ring geometry and distribution function. Furthermore, the process of integrating the results of three complex theoretical models is so cumbersome (2-D equilibrium, ray tracing, and power balance) and the computations of relativistic damping at temperatures >0.5 MeV are so time consuming that no proper sensitivity studies have been performed. Undoubtedly, some aspects to the power deposition are sensitive to details of the assumed equilibrium and ring distribution. For example, the absorption by the core at the second harmonic is essentially proportional to core density, temperature, and χB at the resonance. Although the calculations are far from definitive, they indicate the importance of investigating methods to increase ring heating efficiency and of a continued study of the ring heating and ring loss processes.

REFERENCES

1. D. B. Batchelor and R. C. Goldfinger, Nucl. Fusion 20, 403 (1980).

2. D. B. Batchelor, R. C. Goldfinger, and H. Weitzner, IEEE Trans. Plasma Sci. PS-8, 78 (1980).

3. D. B. Batchelor and R. C. Goldfinger, "RAYS: A Geometrical Optics Code for EBT," ORNL/TM-6844, 1982.

4. D. B. Batchelor, Nucl. Fusion 21, 1651 (1981).

5. D. B. Batchelor and H. Weitzner, "Electron Cyclotron Damping in Fully Relativistic Plasmas" (to be published).

6. D. B. Nelson and C. L. Hedrick, Nucl. Fusion 19, 235 (1979).

7. G. R. Haste, "Hot Electron Rings: Diagnostics Review and Summary of Measurement," this meeting.

8. F. W. Baity, Jr., et al., "Summary of EBT-I Experimental Results," ORNL/TM-6457, Sect. 5.1 (1978).

FIGURE CAPTIONS

Fig. 1. Fully relativistic k_i vs Ω_e/ω for various values of T_e. Twenty cyclotron harmonics are included.

Fig. 2. Extraordinary mode ray paths and fractional power deposition (f_x^{ann}, f_x^{second}) for EBT-I and EBT-P. For EBT-I the x-axis scale is -18 cm to +18 cm and the z-axis scale is 0 cm to 20 cm.

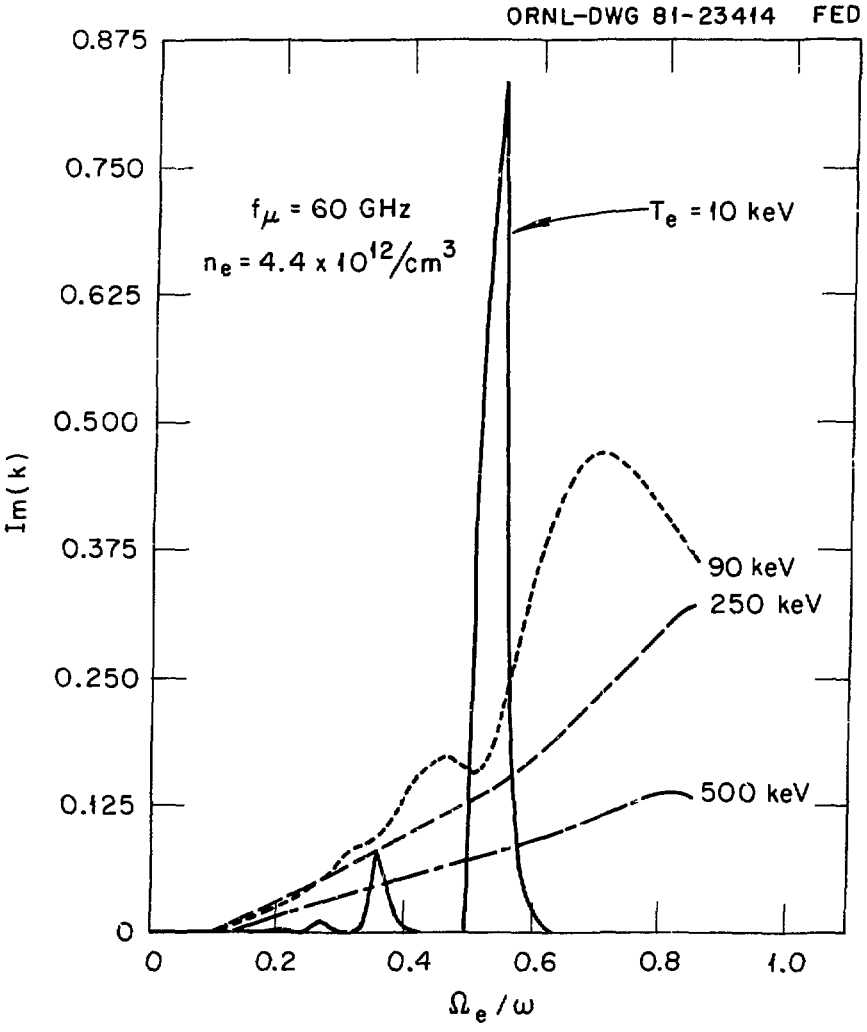
ORNL-DWG 81-23414 FED
0.875
0.750
0.625
0.500
0.375
0.250
0.125
0
Im(k)
f_μ = 60 GHz
$n_e = 4.4 \times 10^{12}/cm^3$
T_e = 10 keV
90 keV
250 keV
500 keV
0
0.2
0.4
0.6
0.8
1.0
Ω_e/ω

Fig. 1

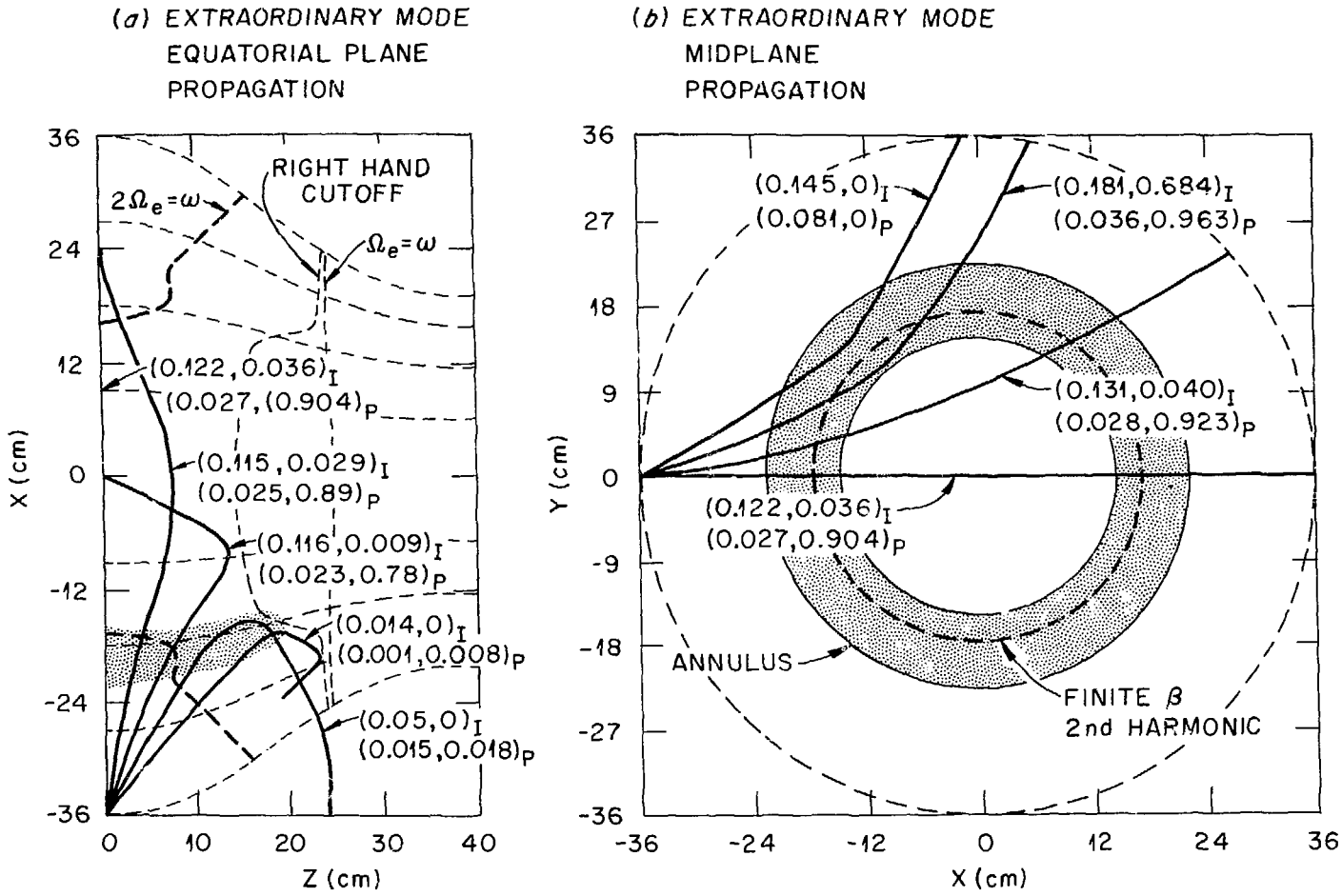
(a) EXTRAORDINARY MODE
EQUATORIAL PLANE
PROPAGATION
RIGHT HAND
CUTOFF
$2\Omega_e=\omega$
$\Omega_e=\omega$
(0.122,0.036)$_I$
(0.027,(0.904)$_P$
(0.115,0.029)$_I$
(0.025,0.89)$_P$
(0.116,0.009)$_I$
(0.023,0.78)$_P$
(0.014,0)$_I$
(0.001,0.008)$_P$
(0.05,0)$_I$
(0.015,0.018)$_P$
X (cm)
Z (cm)
(b) EXTRAORDINARY MODE
MIDPLANE
PROPAGATION
(0.145,0)$_I$
(0.081,0)$_P$
(0.181,0.684)$_I$
(0.036,0.963)$_P$
(0.131,0.040)$_I$
(0.028,0.923)$_P$
(0.122,0.036)$_I$
(0.027,0.904)$_P$
ANNULUS
FINITE β
2nd HARMONIC
Y (cm)
X (cm)

Fig. 2

Dup

FOKKER-PLANCK CALCULATIONS OF ELECTRON CYCLOTRON RESONANT HEATING (ECRH) IN MIRROR GEOMETRY*

B. W. Stallard, Y. Matsuda, W. M. Nevins
Lawrence Livermore National Laboratory, University of California
Livermore, CA 94550

ABSTRACT

A time dependent, bounce-averaged Fokker-Planck code, with quasi-linear diffusion at fundamental and second harmonic frequencies, has been used to study cold plasma trapping and heating of hot electrons in mirror geometry. Both electron-electron and electron-ion Coulomb collisions are included. The code can model either cavity heating (electric field throughout cavity as in EBT) or beam controlled heating (electric field spatially restricted as in the TMX-Upgrade tandem mirror). The heating method has implications for the equilibrium energy and anisotropy of the hot electrons. In TMX-Upgrade, off-midplane heating at the second harmonic in the thermal barrier is planned as a means to control anisotropy ($T_{\parallel}/T_{\perp}$). By spatially limiting (limit in B) the microwave beam and with strong single-pass absorption, the mean hot electron energy may also be controlled since the heating rate decreases at high energy due to the relativistic mass shift of the resonance to higher magnetic field.

For a given magnetic field geometry and cold plasma density (temperature) $n_s(T_s)$, parameters of the hot electrons scale with the quantity $\chi \equiv \mathscr{E}^2/n_s\omega$, where $\mathscr{E}$ is the electric field and ω is the rf frequency. The important processes for particle feed of the hot electrons are trapping of cold electrons at the fundamental followed by heating at both fundamental and second harmonics.

*Work performed under the auspices of the U.S. Department of Energy by the Lawrence Livermore National Laboratory under contract number W-7405-ENG-48.

As χ increases, the efficiency of trapping increases. The variation of hot electron parameters as χ and T_s are varied is presented.

INTRODUCTION

The tandem mirror experiment TMX-Upgrade at LLNL employs ECRH to form thermal barriers and potential plugs in each end cell. Axial profiles of magnetic field, plasma potential and density are shown in Fig. 1. The thermal barrier requires hot, mirror-trapped electrons

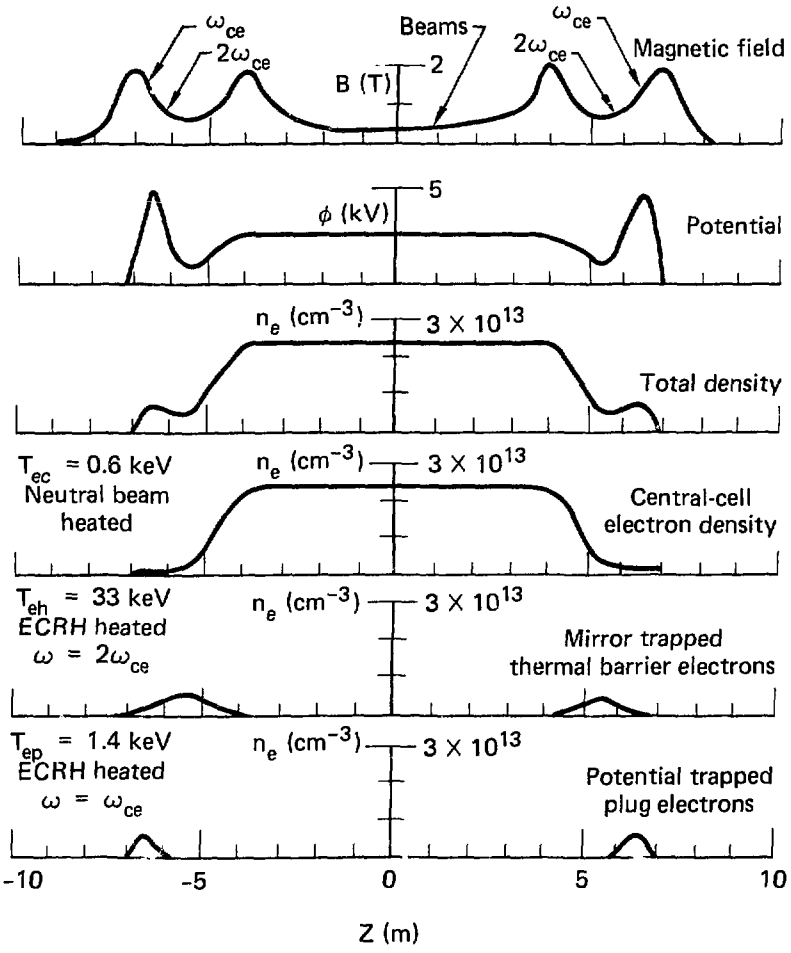

FIG. 1. TMX-Upgrade axial profiles of magnetic field, plasma potential and electron density. Microwave power is applied in the end cells to heat two distinct electron populations.

of mean energy and density, $\bar{E}_h \sim 50$ keV and $n_h \lesssim 5 \times 10^{12}$ cm^{-3}, respectively. To establish the barrier a hot to cold density ratio $n_h/n_c >> 1$ is necessary at the bottom of the magnetic well. In the potential plug the mean electron parameters are $T_w \sim 1.4$ keV and $n_w \sim 7 \times 10^{12}$ cm^{-3}. For electron heating four 200 kW, 28 GHz pulsed gyrotrons are used, one at each heating location. Heating occurs at the fundamental resonance in the potential plug and at the second harmonic in the barrier.

In TMX the desired hot electron energy is much less than the ring energy in EBT-like devices. For the large magnetic scale length in TMX, the energy predicted by adiabatic energy scaling ($\rho/L \approx$ const) observed in several experiments[1] is too large for creation of the thermal barrier, since plasma beta would limit n_h to a small value. For fixed total electron density set by charge neutrality with the ions, a small value of n_h implies n_h/n_c no longer large enough to establish the barrier. To limit the electron energy we plan to employ beam controlled heating as opposed to cavity heating. The idea is shown in Fig. 2. By spatially limiting the microwave field, the hot electrons become "de-tuned" from resonance as their energy becomes mildly relativistic. The heating rate is considerably reduced as the resonance shifts to higher magnetic fields where the rf power is weaker. The usefulness of this scheme is sensitive to the $k_{||}$ spectrum of the waves and is presently under investigation. A control of hot electron anisotropy, important for microinstability,[2] is also possible by varying the mirror ratio for off-midplane heating. This is achieved by adjustment of the magnetic field and the aiming of the microwave beam in the thermal barrier.

FOKKER-PLANCK CODE

To study equilibria and the time dependent evolution of the hot electron population a bounce-averaged Fokker-Planck code has been written. The features of the code are the following:

- v,θ coordinates; non-relativistic
- symmetric axial profiles

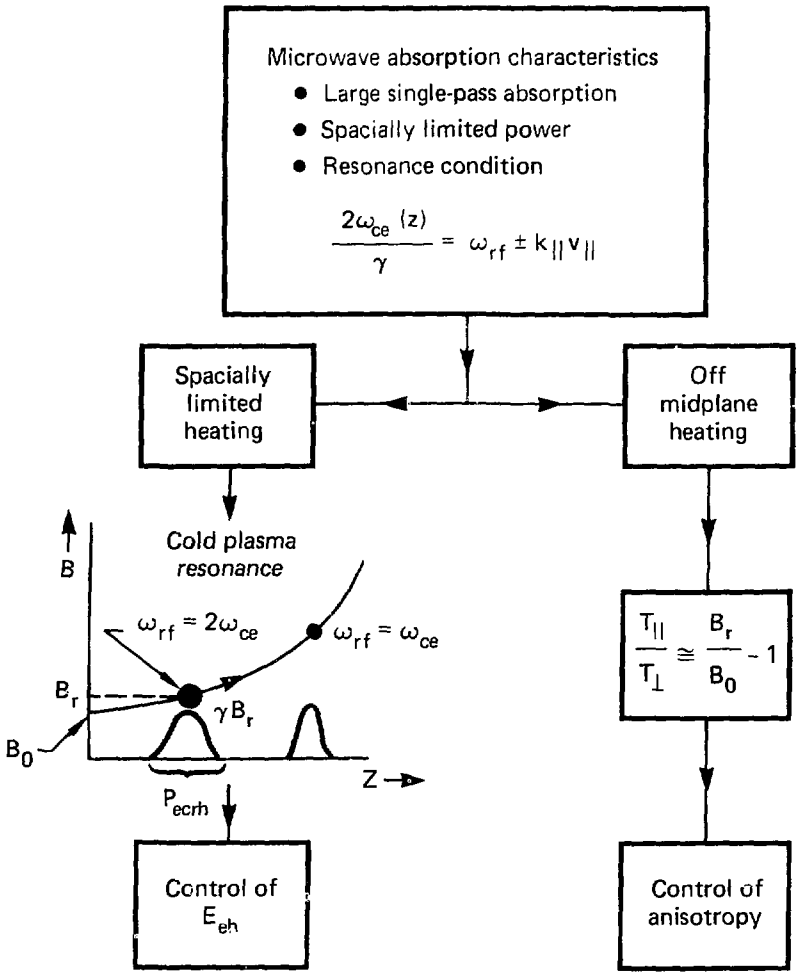

FIG. 2. Illustration of a scheme to control hot electron energy and anisotropy in TMX-Upgrade by using spatially confined ECRH.

- Coulomb collisions: electron-electron and electron-ion (fixed ions)
- electron heating at $\omega = \omega_{ce}$, $2\,\omega_{ce}$: quasi-linear rf diffusion with right hand polarized electric field $\mathscr{E}$ and $k_{\parallel} = 0$
- pseudo-relativistic: magnetic field dependent rf profile with mass dependent shift of the resonant magnetic field.

The midplane (field minimum) velocity space is depicted in Fig. 3. The particle source for mirror-trapped electrons is a low

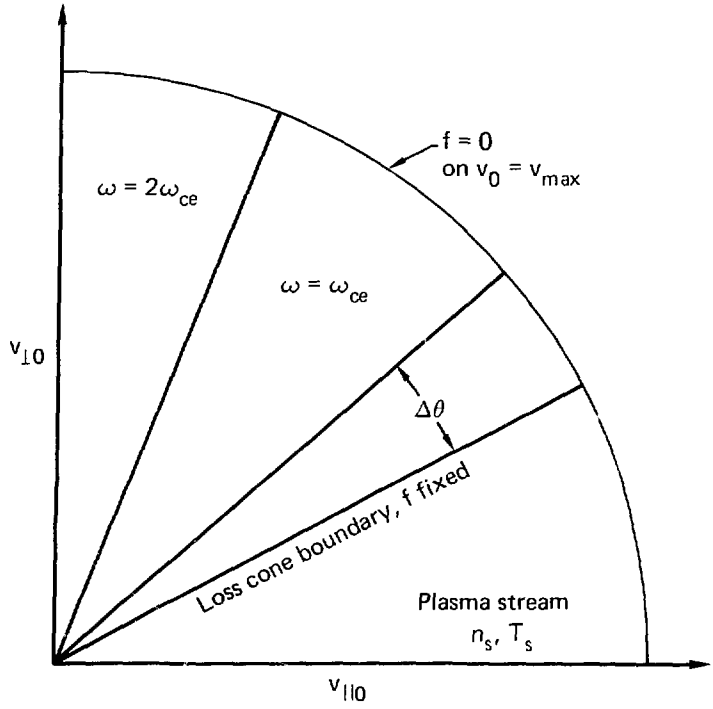

FIG. 3. Midplane (magnetic minimum) velocity space for the Fokker Planck code showing resonant lines and imposed boundary conditions.

temperature Maxwellian plasma stream of density n_s and temperature T_s which fills the loss cone. Electrons are trapped at low energy by both collisions and rf diffusion across the loss cone boundary. Both processes determine losses into the loss cone over the entire energy range and across a $v_0 = v_{max}$ boundary.

The Fokker-Planck equation to be solved and the appropriate boundary conditions are:

$$\frac{\partial f}{\partial t} = \sum_{\ell} \left[\frac{1}{v_\perp} \frac{\partial}{\partial v_\perp} \left(\frac{1}{v_\perp} D_\ell \frac{\partial f}{\partial v_\perp} \right) \right] - \left(\frac{\partial f}{\partial t} \right)_c \tag{1}$$

$f(v, \theta_{lc}, t) = n_s \, g_s(v)$ Boundary condition at loss cone with plasma source g_s

$f(v_{max}, \theta, t) = 0$ Boundary condition at $v_0 = v_{max}$

Locally, the rf diffusion coefficient is

$$D_\ell = \pi \left(\frac{e}{2m}\right)^2 \mathscr{E}_\ell^2 \, \delta(\omega - \ell\omega_c) \, J_{\ell-1}^2 \left(N_\perp \frac{v_\perp}{c} \frac{\omega}{\omega_c}\right) ,$$

where $\mathscr{E}_\ell(B_r)$ is the rf electric field at resonance. The resonant magnetic field $B_r = \gamma B_{r0}$ is increased from the cold plasma resonant field B_{r0} by the relativistic mass factor γ. Defining $f(v,\theta) \equiv n_s f'(v,\theta,t)$, we note that $(\partial f/\partial t)_c = n_s^2 \, (\partial f'/\partial t)_c$ for binary collisions. Performing the bounce average $\langle f \rangle \equiv \tau_b^{-1} \, \S \, f \, ds/v_\parallel$, the steady state solution is

$$0 = \pi \left(\frac{e}{2m}\right)^2 \sum_\ell \frac{\mathscr{E}_\ell^2}{n_s} \left\langle \frac{1}{v_\perp} \frac{\partial}{\partial v_\perp} \left(\frac{1}{v_\perp} \, \delta(\omega - \ell\omega_c) \, J_{\ell-1}^2\right) \frac{\partial f'}{\partial v_\perp} \right\rangle - \left\langle \frac{\partial f'}{\partial t} \right\rangle_c \tag{2}$$

From Eq. 2 we see that for fixed magnetic geometry and stream source boundary condition g_s, the steady state form of f' is determined as a function of the parameters $\chi_\ell = \mathscr{E}_\ell^2/n_s\omega$. The χ_ℓ are convenient scaling parameters since solutions for other values of $\mathscr{E}_\ell$, n_s and ω, for the same values of χ_ℓ, are then immediately known.

For a low temperature plasma stream electron trapping by second harmonic heating is much weaker than the fundamental. Strong trapping and heating should occur when rf diffusion at the fundamental is competitive with Coulomb losses into the loss cone, i.e., ν_{RF} $(\omega = \omega_c) > \nu_c/(\Delta\theta)^2$. An electron with small enough pitch angle to reach the fundamental resonance can be lost if it scatters through an angle $\Delta\theta$ to reach the loss cone as shown in Fig. 3. Numerically the strong trapping condition is

$$\frac{3}{2} T_s \text{ (keV)} \gtrsim \left[\frac{n_s \times 10^{-11} \text{ (cm}^{-3}) \; f \text{ (GHz)}}{\Delta\theta^2 \, \mathscr{E}_1^2 \text{ (V/cm)}}\right]^2 . \tag{3}$$

The particle and power flow for the calculation is shown schematically in Fig. 4, where the trapped electrons are arbitrarily separated into warm and hot populations. In the code the energy spectrum is continuous. Electrons are both trapped and lost by collisions and rf diffusion. For cases of interest $E_h >> T_s$, the current J_{net} feeding the hot population is small compared to the trapped currents. A cold electron just trapped has a small probability of reaching high energy compared to the probability of loss dur-

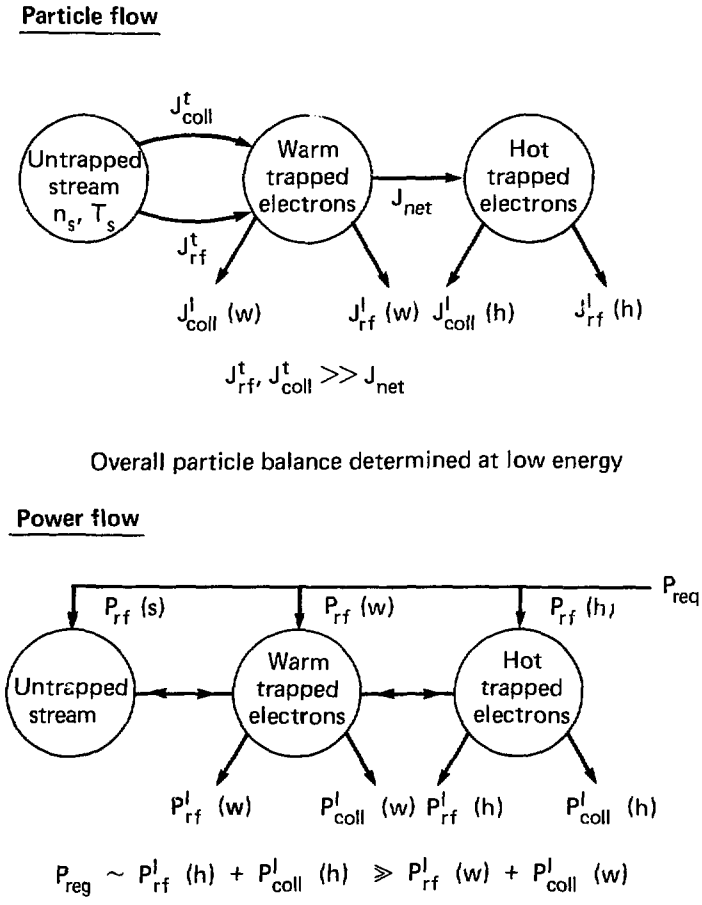

FIG. 4. Schematic of electron particle and power flow with ECRH. A low energy plasma stream is the particle source.

ing heating. Consequently, the overall particle balance is determined at low energy $E \sim T_s$.

To calculate power flow, the current flux at energy E is weighted by the same energy. For parameters such that $n_h/n_c >> 1$ most of the energy loss is at high energy. Consequently, the required rf power can be roughly estimated from the collisional and diffusion losses of the hot electrons.

PARAMETER CALCULATIONS FOR TMX-UPGRADE

Studies of hot electron equilibria as a function of χ have been carried out for several values of plasma stream temperature under the assumption of zero ambipolar potential. The TMX-Upgrade magnetic geometry was used. The rf electric field was 100 v/cm and the index $N_\perp = 1$ at both fundamental and second harmonic resonances. Heating at the fundamental (second harmonic) resonance was at a mirror ratio of 2.3 (1.15). The spatial variation of the rf field for the calculation was chosen to fit the beam profile in the experiment. Due to relativistic de-tuning, this results in a factor 10 decrease from the peak rf power at resonance for an energy E_{10} = 63 keV. The variation with χ of density, mean energy, required rf power and the fraction of hot electrons is shown in Fig. 5a-d. The hot electron fraction is defined as the number of electrons with energies exceeding 2 keV, the approximate depth of the thermal barrier. Electrons with lower energy are expelled by the potential.

The plasma energy and density are seen to be increasing functions of χ and plasma stream temperature, as expected, since rf diffusion becomes relatively stronger compared to collisional losses. The saturation in mean electron energy shown in Fig. 5b results from the relativistic de-tuning of the rf diffusion. The dashed curves are a plot of the strong trapping condition given by Eq. (3). Based on these calculations, EBT-like devices ($n_{eh} << n_{ec}$) have values of χ relatively small compared to that required for TMX-Upgrade.

Example calculations for TMX-Upgrade for plasma stream parameters $n_s = 5 \times 10^{11}$ cm^{-3} and T_s = 400 eV are shown in Fig. 6-8. In

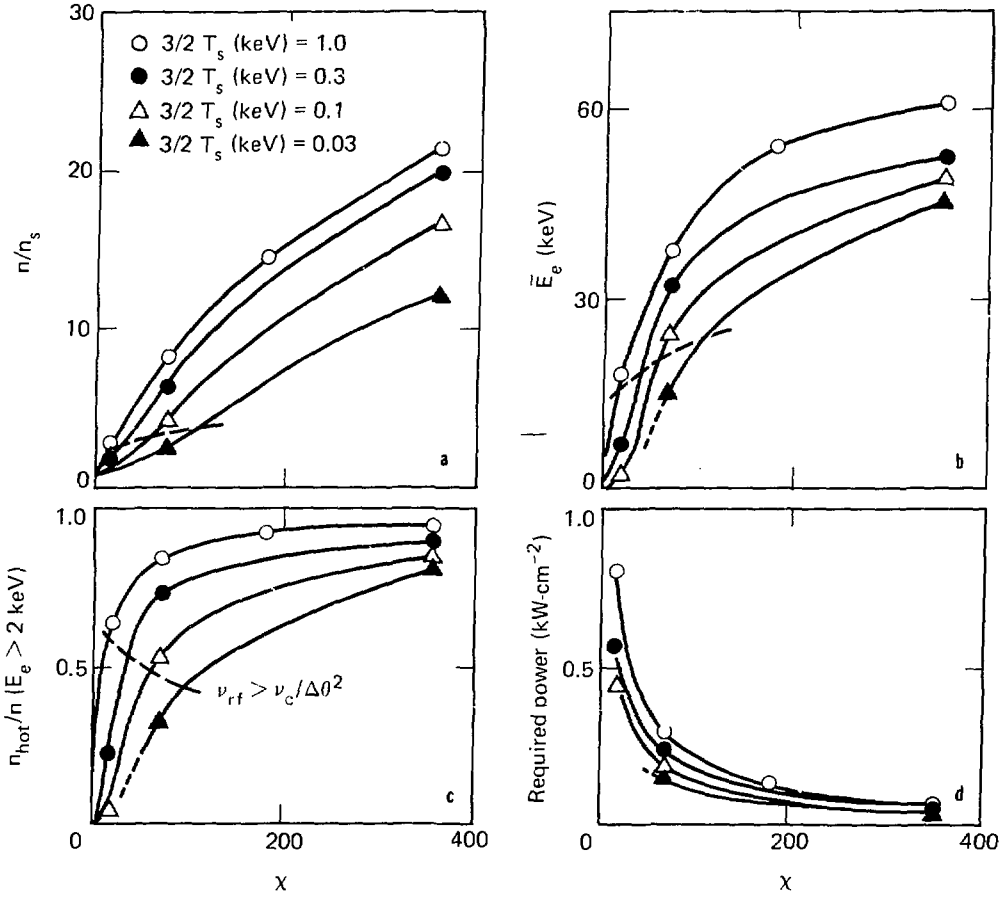

$$\chi = \frac{\mathcal{E}^2 \text{ (v - cm}^{-1}}{n_s \text{ (10}^{11} \text{ cm}^{-3})} \quad f \text{ (GHz)}$$

FIG. 5. Plots of a) plasma density, b) mean electron energy, c) fraction of hot electrons, and d) required ECRH power as a function of χ with relativistic de-tuning. The parameter for the curves is stream energy 3/2 T_S. Plasma potential is assumed zero.

Fig. 6 we show the axial profiles of density, mean electron energy, and parallel and perpendicular plasma pressure. Contour plots of the distribution function $f(v,\theta)$ at the midplane are shown in Fig. 7. At moderate energies f is distorted along the resonant heating lines. At high energy where the rf diffusion is reduced due to the

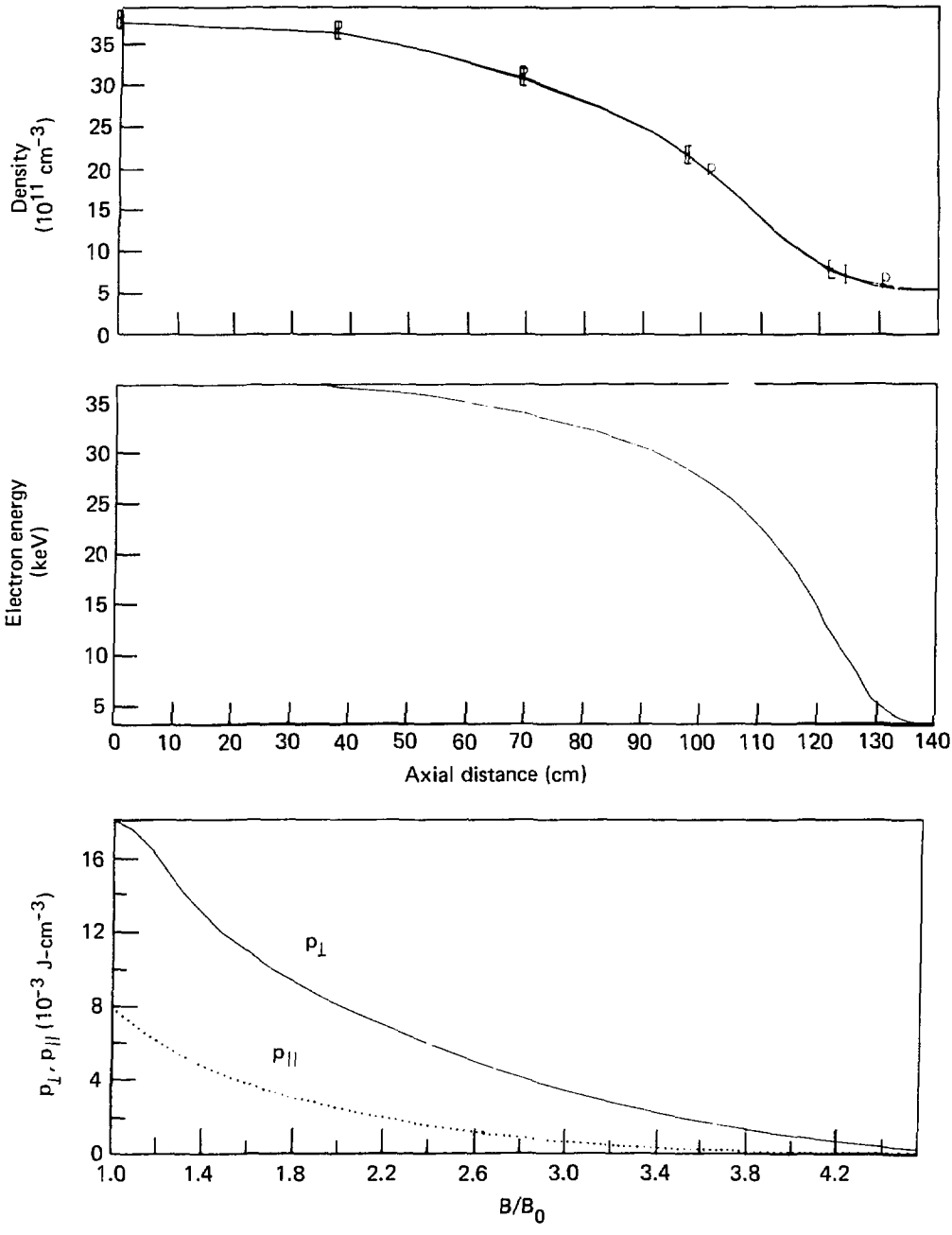

FIG. 6. Calculated axial profiles of density, mean electron energy and plasma pressure for TMX-Upgrade. Stream conditions are $n_s = 5 \times 10^{11}$ cm^{-3} and $3/2\ T_s = 0.6$ keV.

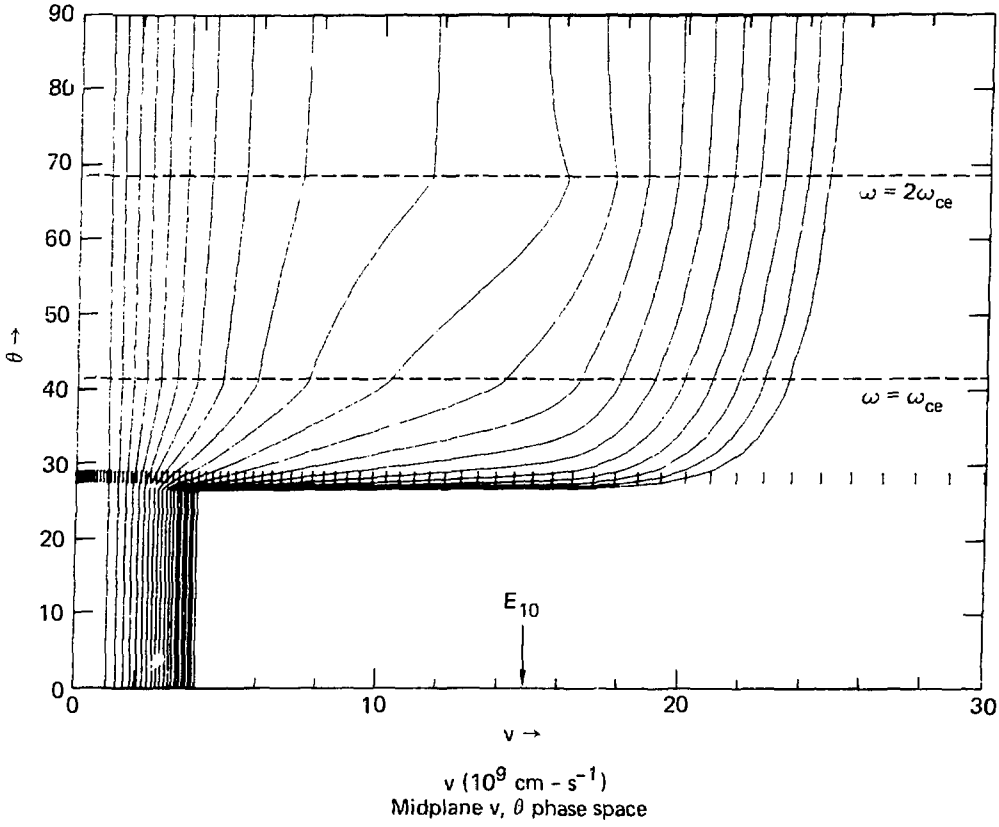

FIG. 7. Contour plot of the distribution function in midplane phase space. Distance between contours is 0.58.

de-tuning, the contours are weak functions of θ since Coulomb collisions are the dominant processes. The same distribution function, integrated over the angle θ, is plotted as a function of energy in Fig. 8. The distribution is clearly non-Maxwellian. At low energy the stream component is visible. At moderate energy the distribution flattens due to rf diffusion. A break in the curve at an energy near E_{10} = 63 keV shows the effect of the relativistic de-tuning. At higher energy the distribution is Maxwellian-like due to collisions.

The control of anisotropy by varying the mirror ratio for resonance is illustrated in Fig. 9. In Fig. 9a the variation of $E_{\perp}/E_{\parallel}$ as

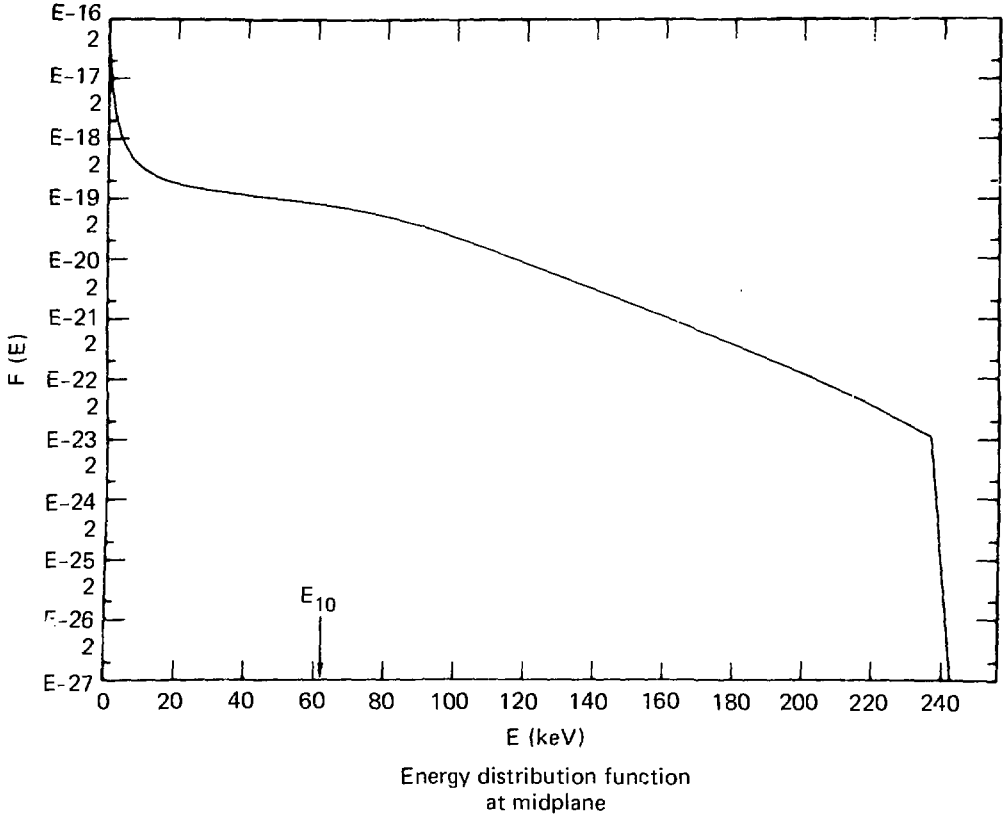

FIG. 8. Energy distribution function F(E) at the midplane.

a function of mirror ratio in the magnetic well is shown for the same case as Fig. 6-8 (solid curve). In Fig. 9b the results for second harmonic heating very near the bottom of the magnetic well are plotted. For beam controlled heating, $E_{\perp}/E_{\parallel}$ increases from 2.3 to 3.3 at the field minimum. This variation may allow us to explore the stability boundary for the anisotropy driven whistler instability which is shown in the figure.[2]

Cavity heating is compared with beam controlled heating in Fig. 9. For these calculations the relativistic de-tuning is turned off. By allowing resonance at any energy, the code models cavity heating where electrons remain resonant near the bottom of the magnetic well. Since no energy dependent limit is placed on rf diffusion, an energetic electron has a high probability of diffusing

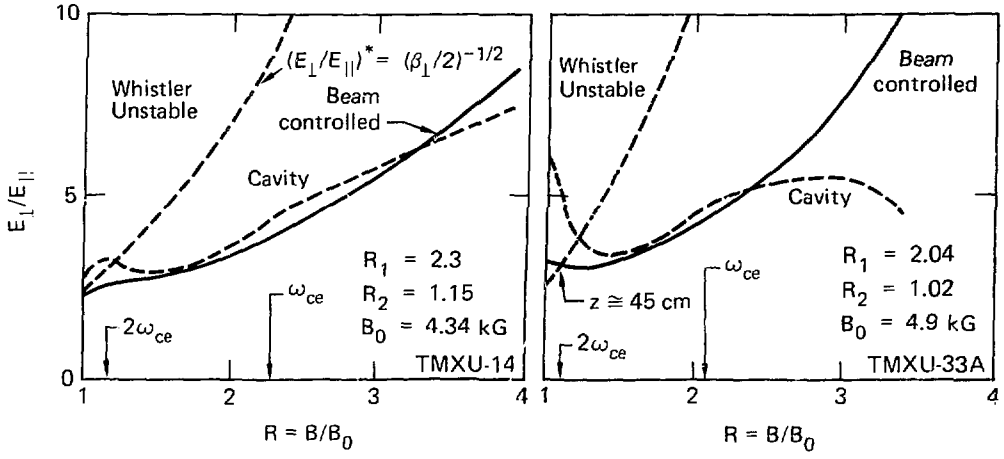

FIG. 9. Plots of energy anisotropy as a function of B/B_0 in the magnetic well, comparing beam controlled and cavity heating. Anisotropy increases as the mirror ratio for second harmonic heating decreases from 1.15 to 1.02. The region for whistler instability is shown for plasma parameters $n_0 = 4 \times 10^{12}$ cm^{-3} and E_h = 50 keV.

higher in energy to the v_{max} boundary (v_{max} = c for the calculation) where it is assumed lost. Thus, losses due to angle scattering into the loss cone become smaller than losses across the v_{max} boundary. The result is a greater peaking of hot electrons near the bottom of the magnetic well. The losses at the v_{max} boundary model rapid losses due to a non-adiabatic energy limit as suggested by the observed ρ/L = constant scaling.[1]

Comparing beam controlled (solid curves) with cavity (dashed curves) a major difference is the increased hot electron anisotropy with cavity heating. The anisotropy is also a more sensitive function of the mirror ratio for second harmonic heating.

SUMMARY

The Fokker-Planck model has demonstrated the sensitivity of the hot electron parameters to the parameter χ. As χ increases the plasma parameter n_h/n_c scales from the EBT regime ($n_h/n_c < 1$) to the

TMX-Upgrade regime ($n_h/n_c >> 1$). The efficiency of fueling the hot electron population from the cold stream population, which increases with χ, is the dominant process.

In addition, the model has predicted long hot electron populations with significant density extending to large mirror ratio and moderate energy anisotropy. This result is a consequence of slow angle scattering into the loss cone as the particle loss process. On the other hand, the cavity heating model, which allows loss at a velocity boundary, in some measure simulates a non-adiabatic energy loss process. For this case electrons, which contribute little to density, would be lost by fast angle scattering. The calculations predict higher anisotropy and a shorter hot electron population.

REFERENCES

1. N. A. Uckman, Bull. Am. Phys Soc. 26, 994 (1981).
2. G. E. Guest and D. J. Sigmar, Nuc. Fus. 11, 151 (1971).
3. Y. Matsuda, W. M. Nevins, R. M. Cohen, Proc. Workshop on EBT Stability Theory, Oak Ridge (1981); also UCRL-85826.

MULTIPLE FREQUENCY ECH (MFECH) IN SM-1 AND STM-1

N. Lazar, J. Barter, R. Dandl*, W. DiVergilio, B. Quon, R. Wuerker
TRW, Inc.
One Space Park, Redondo Beach, California 90278

Plasma properties were studied in a simple mirror (SM-1) and a five-cell axisymmetric tandem mirror (STM-1) using multiple frequency ECH. The cold plasma properties depend predominantly on total power but the efficency for producing the diamagnetic ring plasma depends critically on heating with multiple frequencies. The effects of frequency separation of the heating sources will be demonstrated. Noise fluctuations in the axial current are suppressed with increasing ring-β, but the observed frequency spectrum are not well understood. Annulus β in the multiple mirror is also dependent on MFECH. Plans for and experiments in the new facility will be described.

MULTIPLE FREQUENCY ELECTRON CYCLOTRON HEATING (MFECH) IN SM-1 AND STM-1

We have reported[1] that when multiple frequency electron cyclotron heating (MFECH) is used to produce and heat energetic electron plasmas in a simple mirror, significant improvement in the power efficiency is observed. In this paper, we present evidence that medium energy particles are involved in the heating/confinement improvement, i.e., particles in the energy range 1-50 keV. We also argue that because the fraction of the total current of electrons produced and streaming through the mirrors is small, that subtle heating and confinement effects may be critical in the observed improvements. We present data describing our basis for this thesis and some plans for future experiments in STM-1.

In Figure 1 we show the upper half of an elevation view of our single mirror cell SM-1. The flux lines and surfaces of $|B|$ where $\omega_\mu = \omega_{ce}$ and $\omega_\mu = 2\omega_{ce}$ (ω_μ = applied heating frequency, ω_{ce} the cyclotron frequency for non-relativistic electrons) are shown. In Figure 2, we list the device parameters, size and plasma characteristics. With MFECH we observed significant improvements in the efficiency in producing the energetic electron population as measured by the energy stored in the plasma ($W_\perp = \overline{nE_\perp V}$) determined from the total diamagnetic flux. In Figure 3, we show how, at a given power, $W_\perp$ may be increased by as much as a factor of ten with MFECH. We also noted that the operating window was much wider when using MFECH. Under conditions suitable for producing the highest values of $W_\perp$ for each frequency (or combination of frequency), disruptions in the plasma are seen and we note these disruptions occur at much higher power and $W_\perp$ when using MFECH.

During our experiments, a number of additional relevant observations were made which led us to the conclusion that the higher values of $W_\perp$ observed were due to increases in the density of energetic electrons. For example, the temperature of the energetic electrons (Ee $\approx$ 375 keV) is found to be independent of operating conditions whenever appreciable values of $W_\perp$ are seen. Further, the increases in density did not arise from density increases of the cold electron source population nor in the confinement time

of electrons after they are heated to relativistic energies. A summary of these observations are presented in Figure 4.

From these observations, we have drawn the conclusions that the efficiency improvements result from heating/confinement improvements in the source of particles which feed the energetic population. We note that the experiments are carried out in steady state, so

$$\frac{n_H V_H}{\tau_H} = \eta n_c \, v_c A = \eta \frac{n_c}{\tau_c} \, \ell A$$

For our conditions, $\tau_c \approx 10^{-4}$ sec $n_c \sim a n_H$ (where a = 1-3) and $\tau_H \sim 0.2$-0.5 sec. Hence $\eta \cong 10^{-4}$, clearly a small fraction of the streaming electron population ("streaming" defined as the total flux of electrons produced and lost). Thus a change in a heating or confinement process involving only a small fraction of the streaming population may result in a large change in the resident hot population.

An illustration of how a subtle change in heating can affect the stored energy is shown in Figure 5. Here we depict the measured stored energy $W_\perp$ when heating with two frequencies at a constant power as a function of the frequency difference between the two frequencies. The large increase (a factor of two) occurs with only Δf_μ = 40 MHz (compared to the heating frequencies f_μ = 9.5 GHz). We interpret this observation to suggest the heating confinement improvement involves non-relativistic electrons at the fundamental cyclotron resonance. In Figure 5, the energies at the top of the scale refer to particles whose bounce frequency equals the corresponding frequency separation.

Another illustration of the sensitivity of the two frequency heating is shown in Figure 6. Here, we show oscilloscope traces of the current to a probe placed on axis for cases in which two frequencies spaced by 300 MHz are used. In these experiments one of the sources is pulsed on for $\sim$ 380 μsec as shown on the bottom trace of each picture (labeled P). Two current traces are taken; I_w is the current for electrons with energies above 1 keV; I_c the total current of electrons. Above a critical power threshold for the second source (P_2 = 200w) we note that a burst of electrons are emitted

∿ 20 μsec following turnoff of the microwave power. These electrons have energy above 1 keV in contrast to the upper trace where the burst is absent. These bursts are not present when only one frequency is used. The electrons appear to be somehow confined in a group when the power level is high enough and escape in a relatively short burst if both frequencies are absent. Again, we have evidence for relatively low energy particles having their heating/confinement affected by relatively minor changes in the gross heating power.

We are planning to exploit our five cell symmetric mirror facility, STM-1, to investigate further these heating processes (Figure 7). Ultimately, we wish to determine the precise mechanisms which result in the formation of rings (as contrasted to discs or spherical distributions) in all the earlier symmetric mirror and EBT observations. This determination should permit the appropriate device modification to allow us to produce arbitrarily thick ELMO rings or disc configurations. In STM-1, with independent stream production ECH sources in the end cells, and ring (and/or disc) heating sources in separate cells, we should have the opportunity of defining heating processes with great precision.

REFERENCES

1. N. H. Lazar, R. A. Dandl, W. F. DiVergilio, B. H. Quon and R. F. Wuerker, Bull. Amer. Phys. Soc. 25, 993 (1980).

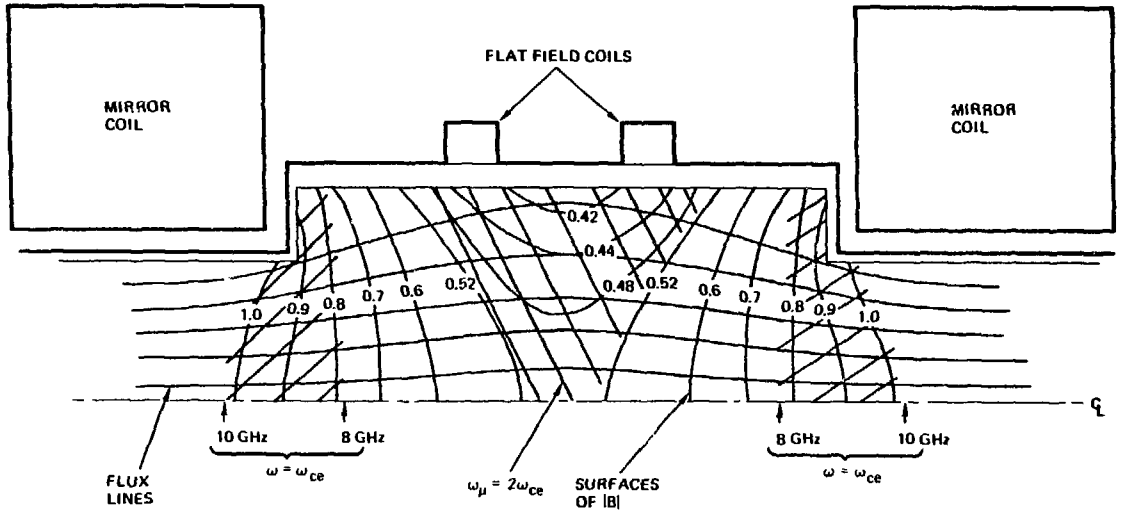

Half of Vertical Section Through Proposed STMX Showing Flux Lines and Surfaces of $|B|$. The Regions Where $\omega_\mu \approx \omega_{ce}$ and $\omega_\mu = 2\omega_{ce}$ For the Frequencies Available Are Shown Cross Hatched

Fig. 1

SM-1 FACILITY

MAGNETIC FIELD	Mirror Ratio	$R_m = 2.2$
	Mirror Length	$L = 71$ cm
	Field Line Curvature	$rR_c = 650$ cm^2
	Maximum Field	$B_{MAX} = 3.5 - 4.5$ kg
MICROWAVE SOURCE	$f_1 = 8.3$ GHz	$P = 2$ kW
	$f_2 = 9.2$ GHz	$P = 1$ kW
	$f_3 = 9.5$ GHz	$P = 1$ kW
	$f_4 = 10.1$ GHz	$P = 2$ kW
PLASMA PARAMETERS	$n_c - 1\text{-}10 \times 10^{11}$ cm^{-3}	$T_e = 10 - 50$ eV
	$n_h - 1 \times 10^{11}$ cm^{-3}	$T_h = 350\text{-}400$ keV

Fig. 2

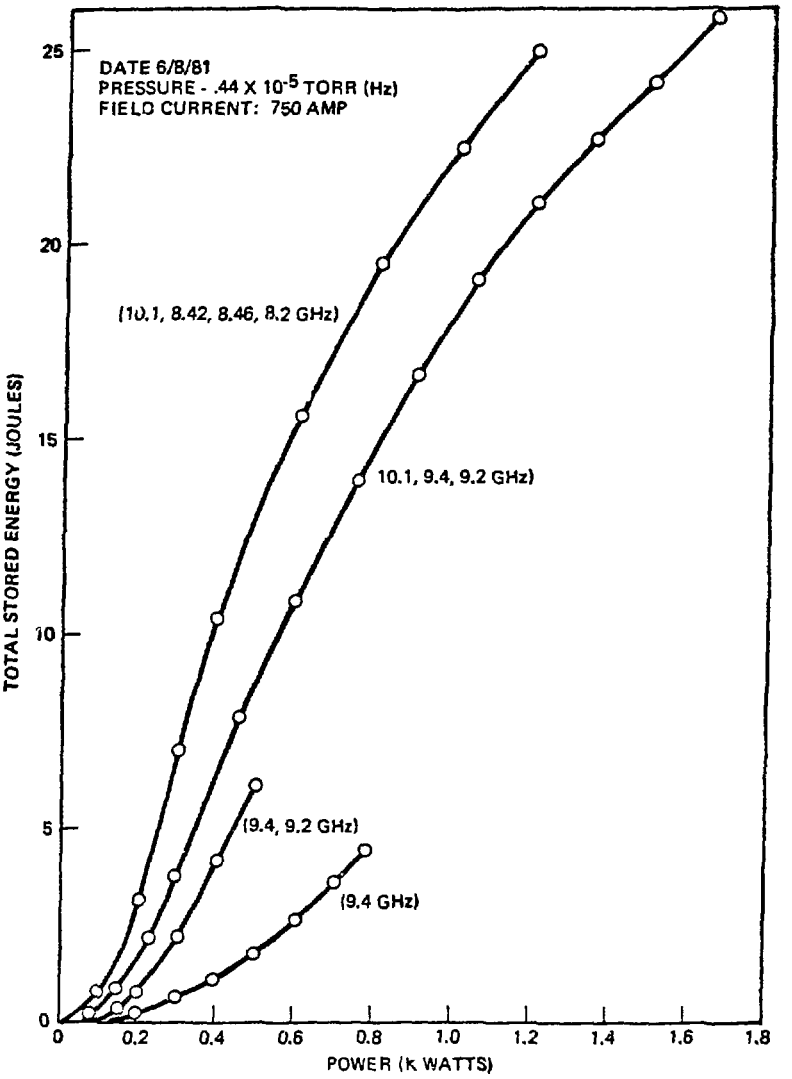
DATE 6/8/81
PRESSURE - .44 X 10-5 TORR (Hz)
FIELD CURRENT: 750 AMP
(10.1, 8.42, 8.46, 8.2 GHz)
10.1, 9.4, 9.2 GHz)
(9.4, 9.2 GHz)
(9.4 GHz)
TOTAL STORED ENERGY (JOULES)
POWER (K WATTS)
0
5
10
15
20
25
0
0.2
0.4
0.6
0.8
1.0
1.2
1.4
1.6
1.8

Fig. 3

Additional Observations

- Density of Cold Plasma Independent of MFECH
- Temperature of Hot Electrons Independent of MFECH
- Delay Time Independent of MFECH
- Total X-Ray Flux Prop To $W_\perp$

<u>CONCLUSION</u>:

Increase in $W_\perp$ Due To Increase in Hot Electrons

Fig. 4

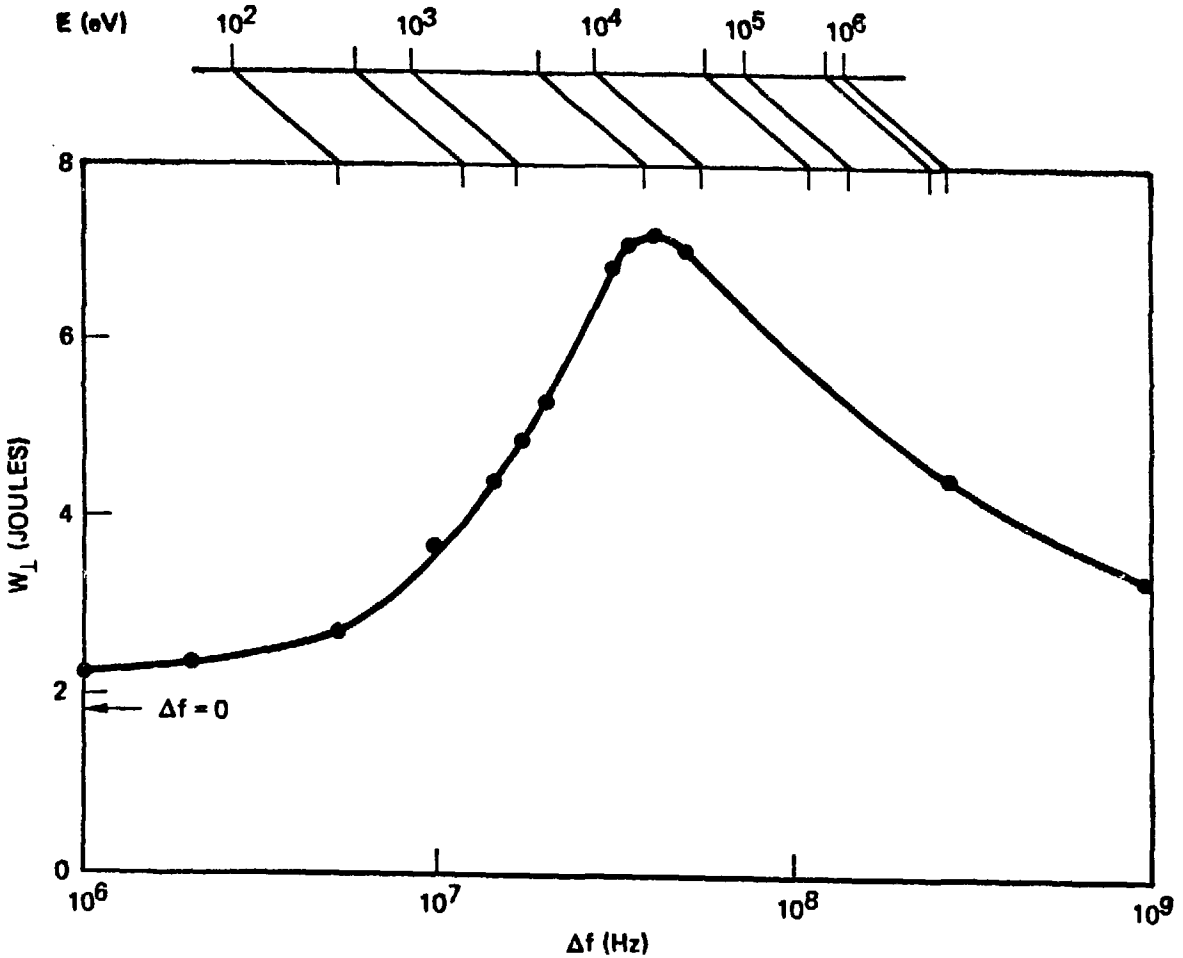
E (eV)
10^2
10^3
10^4
10^5
10^6
8
6
4
2
0
W_L (JOULES)
Δf = 0
10^6
10^7
10^8
10^9
Δf (Hz)

Fig. 5

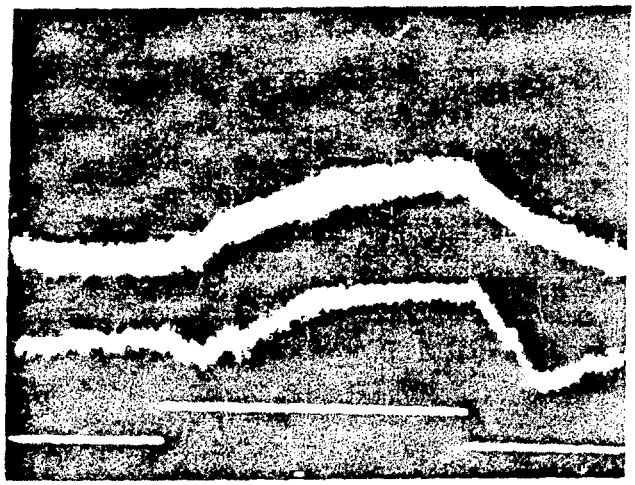

I_W

I_C

P

P_1 = 200 Watts

P_2 = 180 Watts

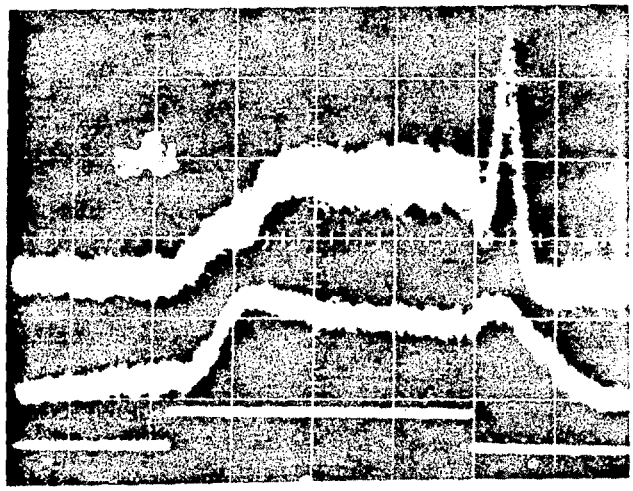

I_W

I_C

P

P_1 = 200 Watts

P_2 = 200 Watts

τ(100 μs/Div)

Fig. 6

TRW

SYMMETRIC TANDEM MIRROR FACILITY

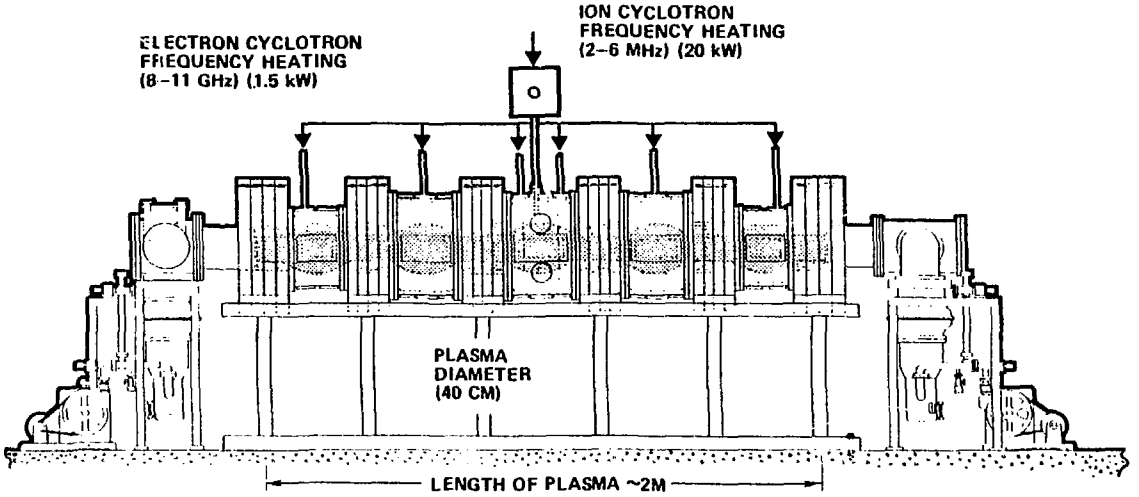

Fig. 7

SIMULATION OF ELECTRON CYCLOTRON RESONANCE HEATING WITH MULTIPLE FREQUENCIES IN MIRROR GEOMETRY

T. K. Samec and B. I. Hauss
TRW, Inc.
One Space Park, Redondo Beach, California 90278

and

G. E. Guest
AMPC, Inc.
2210 Encinitas Blvd., Encinitas, California 92024

ABSTRACT

Monte Carlo simulations of multiple frequency electron cyclotron resonance heating have been performed. The observed differences with single frequency heating may provide explanations for the experimentally observed improvements in plasma parameters which result from multiple frequency heating.

1. INTRODUCTION

Experiments on ECH produced plasmas in TRW's single cell axisymmetric mirror machine (SM-1) have shown[1,2,3] that the stored diamagnetic energy can be significantly increased by replacing the single frequency microwave power input by multiple inputs at closely spaced frequencies: the stored energy is found to increase monotonically with the number of input frequencies at a fixed power, and the range of microwave power over which stable discharges can be obtained is also extended[1,2,3]. Since none of the parameters of the energetic electron annulus seem to change except for its density, the dominant influence of multiple frequency heating then seems to be an improvement of the fraction of cold electrons which are successfully heated into the energetic population. The numerical work presented here exposes features of the microwave heating process which are sensitive to the details of the heating spectrum. More specifically, the use of a Monte Carlo test particle simulation code has allowed direct measurements of heating rates ($d\langle W\rangle/dt$) and diffusivity ($d\langle \delta W^2\rangle/dt$) which are found to be both drastically different from the appropriate quasi-linear values and sensitive to the input microwave spectrum even for small frequency separations. It is thought that the detailed results of such Monte Carlo calculations will soon lend themselves to quantitative comparisons with experimental measurements in the STM-1 facility.

2. THE NUMERICAL MODEL

The test particle code is constructed around the numerical solution of the following reduced set of equations of motion:

$$\dot{u} = -\frac{\varepsilon}{m\sqrt{\Omega}}\left[E_1 + E_2 \cos(\omega_2 - \omega_1)\, t + E_3 \ldots\right] - (\Omega - \omega_1)\, v \qquad (1a)$$

$$\dot{v} = -\frac{e}{m\sqrt{\Omega}}\left[E_2 \sin(\omega_2 - \omega_1)\, t + E_3 \ldots\right] + (\Omega - \omega_1)\, u \qquad (1b)$$

$$\dot{v}_z = -\frac{1}{2}(u^2 + v^2)\, d\Omega/dz \qquad (1c)$$

$$\dot{z} = v_z \tag{1d}$$

where $\Omega(z) = e\,B(z)/m$ is the local electron gyrofrequency and

$$u = \vec{v} \cdot \vec{E}_1/(E_1 \sqrt{\Omega})$$

$$v = \vec{v} \cdot (\vec{E}_1 \times \vec{B})/(E_1\, B \sqrt{\Omega})$$

are the components of velocity $\vec{v}$ as measured with respect to the applied infinite wavelength uniform transverse field E_1 and normalized so that the half-sum of their squares reproduces the magnetic moment which remains invariant in the absence of microwave fields. These equations are thus written in a rotating frame so that only the slow time variations ($\Omega - \omega_1$, $\omega_2 - \omega_1$, etc.) are followed explicitly.

Coulomb collisions are presently included as a pitch-angle scattering operator[4] for each particle, this is appropriate for the energy range of interest here (1 to 10 keV) but would be inappropriate for the lower energy non-Maxwellian population in which case a more careful treatment is needed and available[5].

3. TYPICAL SM-1 PARAMETERS

For the purpose of modeling the SM-1 configuration the following choices were made:

$$\Omega(z) = \frac{\Omega(o)}{2}\left[R + 1 - (R - 1)\cos\left(\frac{nz}{L}\right)\right]$$

$$R = 2.2,\ L = 0.35\ \text{m}$$

$$\omega = \Omega_\mu = R_\mu\, \Omega(o) = 2\pi \times 10^{10}\ \text{rad/s}$$

$$R_\mu = 2$$

and finally estimating the cavity to have $Q \approx 10$ leads to a field amplitude of approximately 500 V/m = E_1 for an input power of 1 kW. The background plasmas are usually low density and low temperature

$$n_{e\ cold} \gtrsim 10^{11}\ cm^{-3}$$

$$T_{e\ cold} \lesssim 60\ eV$$

while the relativistic population which forms the ring has

$$n_{e\ hot} \lesssim 10^{11}\ cm^{-3}$$

$$T_{e\ hot} \sim 375\ keV$$

4. SOME PRELIMINARY REMARKS

The fundamental resonance is very close to the mirror throat, a mirror confined particle should then experience two interactions with the resonance; one just before reaching its turning point and another one just after. The interference between these two closely spaced interactions plays an important role in determining the long time behavior which is influenced by interference between successive interactions which are separated by midplane crossings. The short-time interference response is obtained by expanding the equations of motion in the vicinity of the turning point z_T and assuming that the orbit is not altered by the microwave fields, the first order modification of the magnetic moment is then:

$$\Delta(\sqrt{\mu}) = \cos(\phi_T) \cdot \frac{eE}{m} \frac{2\pi}{\omega^{3/2}} \left(\frac{2L_B}{\rho_\perp}\right)^{2/3} Ai\left(-\frac{\Delta z}{L_B}\left(\frac{2L_B}{\rho_\perp}\right)^{2/3}\right) \qquad (3)$$

where Ai is the standard Airy function, $\rho_\perp$ is the gyroradius at resonance, L_B the magnetic field gradient length, $\Delta z = z_T - z_\mu$ is the distance between the turning point z_T and the resonance z_μ, and ϕ_T is the phase difference

between the applied field and the particle velocity at the turning point. This rather simple result points out immediately the existence of phase-independent surfaces on which the change in magnetic moment, energy and thus particle orbit vanish. To the order of the calculation which led to equation 3 these surfaces are given by

$$-\frac{\Delta z}{L_B}\left(\frac{2L_B}{\rho_\perp}\right)^{2/3} = x_j$$

where Ai $(x_j) = 0$; the locii of these "null-heating" surfaces are shown in Figure 1 for the parameters given in Section 3. Should the energy of an electron be altered by the resonant interation then its turning point will change and the two changes are simply related:

$$W\,(1 - R_\mu/R_T) = \text{constant}$$

where R_T is the mirror ratio at the turning point. These "heating lines" are also shown in Figure 1 and are seen to intersect the null heating lines on which particles would accumulate and heating would be inhibited except for those particles with turning points near the resonance. Interspersed between the null-heating lines additional stationary structures may be found, these "superadiabatic" structures obtain from accounting for the phase change associated with the transit from one turning point to the next and using equation 3 to update the magnetic moment between midplane crossings. Should the phase change be completely random then a quasi-linear heating rate and diffusivity can be calculated:

$$\frac{d}{dt}\langle W\rangle = \frac{1}{m}\left(\frac{2\pi eE}{\omega}\right)^2\left(\frac{2L_B}{\rho_\perp}\right)^{4/3} A_i^2\left(-\frac{\Delta z}{L_B}\left(\frac{2L_B}{\rho_\perp}\right)^{2/3}\right)\frac{1}{\tau_b} \tag{4}$$

$$\frac{d}{dt}\langle \delta W^2\rangle = 2W_{\perp R}\frac{d}{dt}\langle W\rangle \tag{5}$$

where τ_b is the bounce period.

Finally, the size of an interaction with the resonance can be estimated using equation 3, for the parameters given in Section 3, this works out to approximately 100 eV with a mild variation with energy.

5. RESULTS

Monte Carlo measurements of the heating rate are relatively simple to perform. An ensemble of particles is started at a given energy, spread over a given range of turning points with randomly distributed phases, as the particles are advanced in time the average energy $\langle W \rangle$ of the ensemble can be used to determine the heating rate; the diffusivity is more easily measured at high energy where the relative changes in energy are small, the ensemble averaged value of $\langle (W - \langle W \rangle)^2 \rangle$ is then used.

At low energy ($W(t = o) = 100$ eV) a heating rate of 6 MeV/s is measured, it is independent of the applied spectrum and is consistent with an average of equation 4 over the distribution of turning points used in the simulation. In this case the energy changes are larger than the spacing between null heating surfaces (Figure 1) and completely stochastic heating should occur.

At a higher energy of 1 keV the situation is somewhat more complicated. Even with a sample containing as many as 640 particles, single frequency heating is difficult to measure: three different histories are shown in Figure 2 (cases 1, 2, and 3), this illustrates the sensitivity of the results to initial conditions and the impracticality of a heating rate measurement. In contrast, a two-frequency heating rate measurement (case 4) with a frequency spread of only 40 MHz provides reproducible results with a heating rate of 6 MeV/s, a value close to the quasi-linear value. This result is however of relatively little interest because at the plasma densities of interest Coulomb scattering is strong enough to provide randomization of turning points by an amount comparable to the spacing between null heating surface (Figure 1) in one-half bounce and thus restore stochastic heating.

Of more interest is a higher energy case (10 keV) in which the single pass interaction is sufficiently small that fine-grained structure can be identified. A typical measurement of diffusivity is shown in Figure 3 where the squared average spread in energy $<(W - <W>)^2>$ is plotted as a function of time for an ensemble of particles started in the midplane with random initial phases and a common turning point. The random phase initialization allows a measurement of the heating rate in the random phase approximation by measuring the spread due to the first interaction with the resonance.

The agreement between these measurements and equation 5 is displayed in Figure 4. The long-time behavior of the spread in energy is seen in Figure 3 to be diffusive in nature ($\propto t$) but the diffusion rate is much smaller than the quasi-linear rate, as is shown in Figure 4 the ratio between the quasi-linear rate and the measured rate can exceed an order of magnitude. The difference between the long-time result and the random phase result resides in the fact that the equations of motions (equations 1a through 1d) preserve the phase information and thus do not preclude periodic (superadiabatic) behavior. The quasi-linear rate can be restored by increasing the microwave power: this requires only $E = 2$ kV/m at $R_T = 2.0$. Another alternative is to apply multiple frequencies[6]. By applying two frequencies with equal power, the diffusivity can be strongly altered as is shown in Figure 5 where it is seen that for a turning point mirror ratio $R_T = 2.02$ (which corresponds to the peak diffusivity found in Figure 4) a frequency mismatch equal to an odd harmonic of the bounce frequency[7] will restore the quasi-linear value of the diffusivity. The value of $R_T = 2.02$ did however nor constitute a <u>barrier</u> to heating since the microwave induced diffusivity is finite. Of more interest is the neighborhood of the null of the quasi-linear diffusivity, $R_T = 2.042$. As is seen in Figure 5 this region is remarkably insensitive to break up by two-frequency heating. A large frequency mismatch is needed to destroy this heating barrier. This does not however help in destroying the heating barriers associated with the <u>lowest</u> of all applied frequencies. Particles with turning points located in the vicinity of the resonance of the lowest applied frequency do not experience the higher frequencies at all. In such a case, it is more beneficial to apply many closely spaced frequencies than a few widely spaced ones.

The importance of pitch angle scattering by Coulomb collisions is not restricted to the randomization of turning points which was discussed earlier. Very weak pitch angle scattering results in orbit modifications which cause non-diffusive phase randomization[8] which proceeds at a rate[9]

$$<\delta\psi^2> \propto \left(\frac{L}{\rho}\right)^2 \frac{\nu}{\omega_b} (\omega_b t)^3$$

which is much faster than pitch angle scattering ($<\delta\theta^2> \propto \nu t$). Complete phase randomization in one half bounce occurs for 5 keV electrons, for these particles the random phase rates given in equations 4 and 5 apply. Phase randomization in the weak gradient near the resonance is very weak and the Airy function interference response is preserved.

6. CONCLUDING REMARKS

Large differences between single and multiple frequency heating have been observed in test particle simulations, generally multiple frequencies increase the microwave heating and energy diffusion rates. A detailed comparison with experimental results is however not possible until the macroscopic consequences of the fine-grained effects discussed here are quantified. Such a comparison requires calculations spanning the electron energy range from the low energy population ($w \sim T_e$) on through to the energy range in which harmonic heating is dominant.

This work was supported by the Department of Energy (DEAC 03-80 ET 51017) and the TRW IR&D program.

REFERENCES

1) N.H. Lazar, R.A. Dandl, W.F. DiVergilio, B.H. Quon and R.F. Wuerker, Bull. Am. Phys. Soc. 25, 993, paper 8D4, 1980.

2) Symmetric Tandem Mirror Program, Annual Progress Report, TRW S/N 35638, October 1980.

3) B.H. Quon, R.A. Dandl, N.H. Lazar and R.F. Wuerker, Bull. Am. Phys. Soc. 26, 893, paper 2W5, 1981.

4) K.T. Tsang, Y. Matsuda and H. Okuda, Phys. Fluids 18, 1282, 1975.

5) T.K. Samec, R. Margulies and Y.C. Lee, Bull. Am. Phys. Soc. 22, 1136, paper 5D6, 1977.

6) C.R. Menyuk and Y.C. Lee, Phys. Fluids 23, 2225, 1980.

7) T.D. Rognlien, Bull. Am. Phys. Soc. 26, 1035, paper 8R8, 1981.

8) H. Momota and T. Takizuka, Phys. Fluids 17, 2290, 1974.

9) T. K. Samec, B. I. Hauss and G. Guest, Bull. Am. Phys. Soc. 26 928, paper 4P23, 1981.

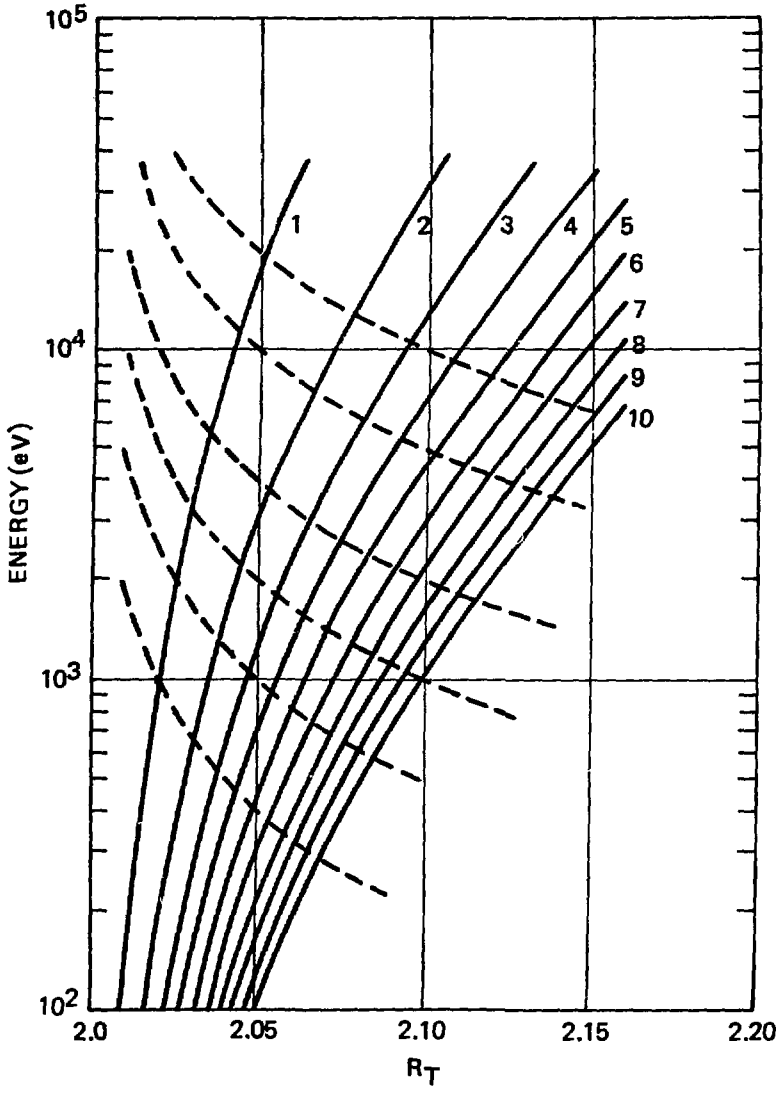

FIGURE 1. Null heating surfaces (—) and heating trajectories(---) in energy versus turning point mirror ratio R_T, for $R_\mu = 2$.

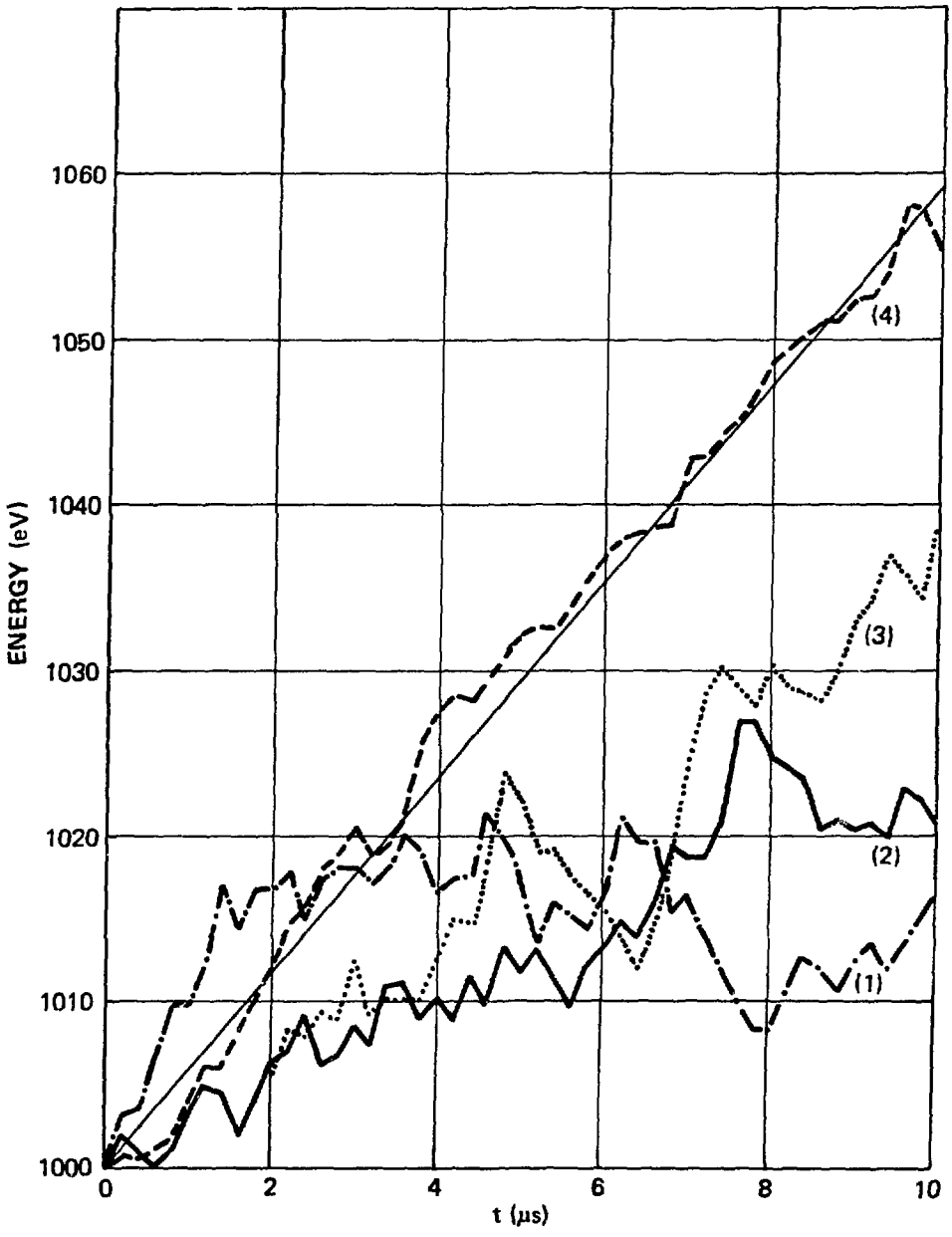

FIGURE 2. Time evolution of the ensemble averaged energy of 640 particles started at 1 keV. Cases 1, 2, and 3 correspond different initial samples with single frequency heating, Case 4 is for 2 frequency heating.

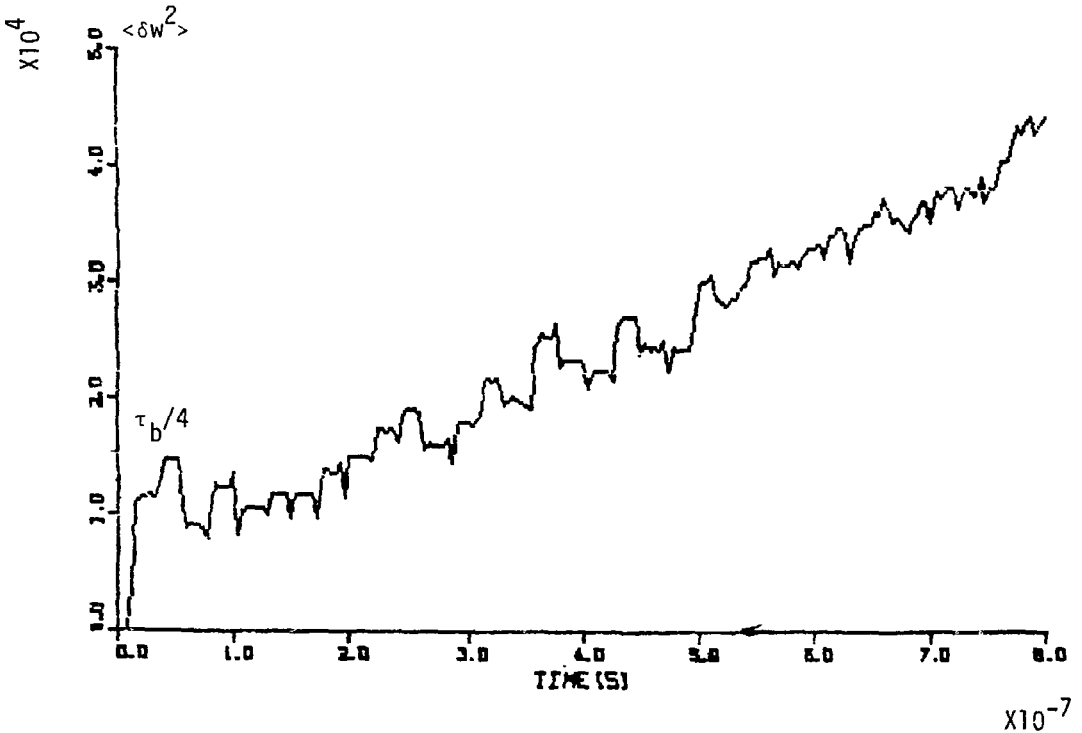

FIGURE 3. The evolution of the ensemble averaged energy spread for w_0 = 10 keV and R_T = 2.01.

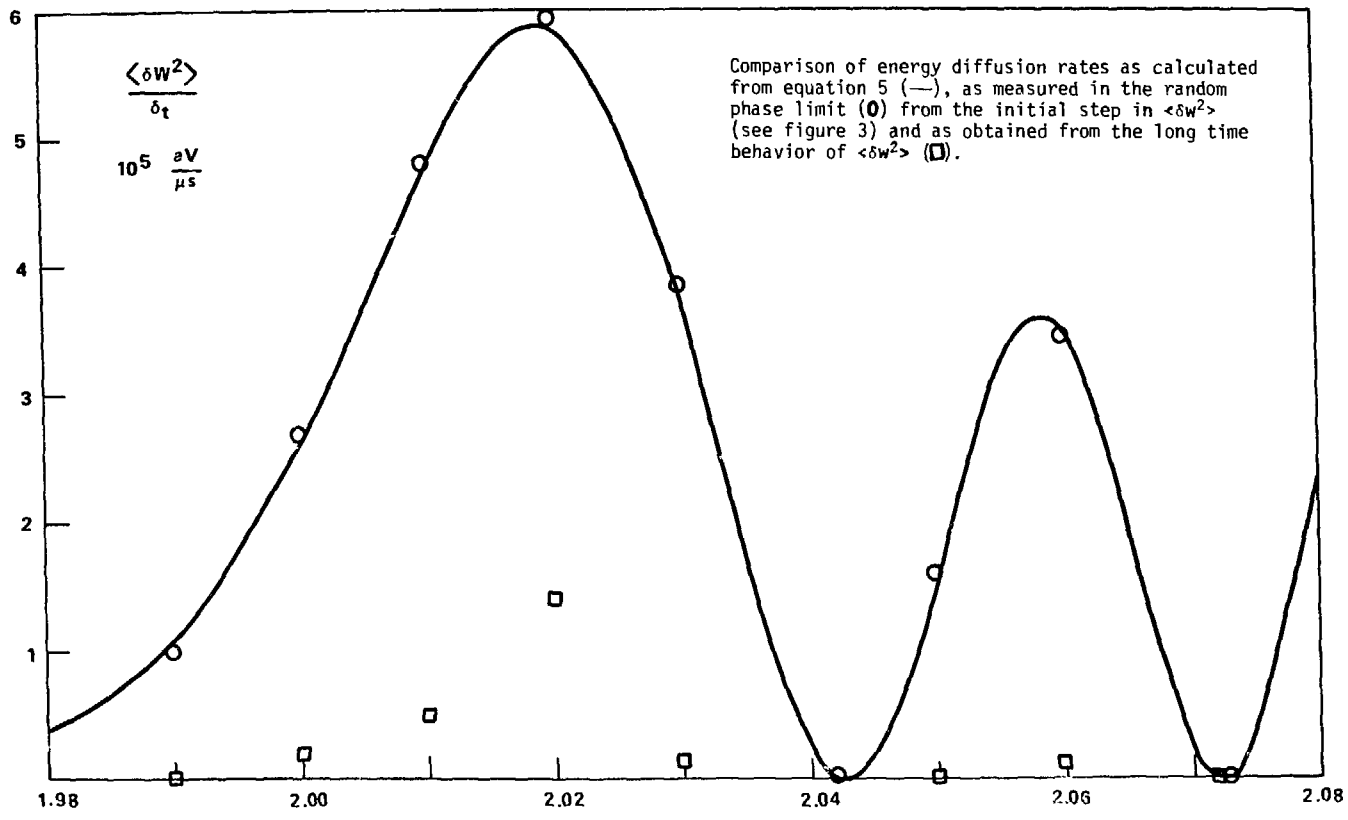
$\frac{\langle \delta W^2 \rangle}{\delta_t}$
$10^5 \frac{aV}{\mu s}$
Comparison of energy diffusion rates as calculated from equation 5 (—), as measured in the random phase limit (O) from the initial step in $\langle \delta W^2 \rangle$ (see figure 3) and as obtained from the long time behavior of $\langle \delta W^2 \rangle$ (□).
6
5
4
3
2
1
1.98
2.00
2.02
2.04
2.06
2.08

FIGURE 4

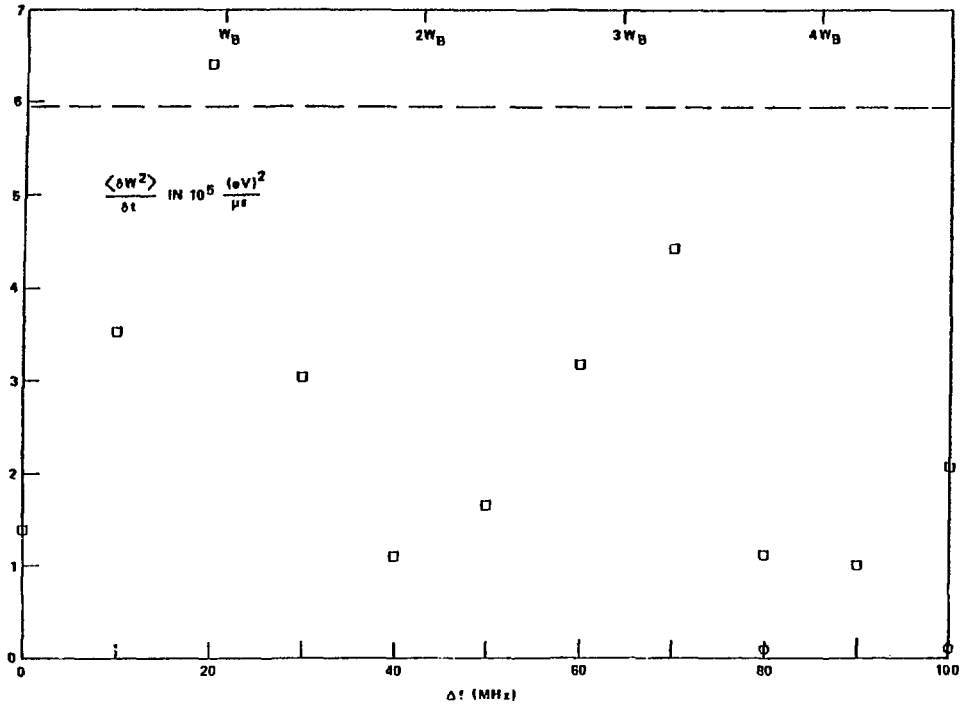

Figure 5. Energy diffusion at 10 keV for R_T = 2.02 (□) and R_T = 2.042 (0) as a function of mismatch frequency $\Delta f = f_z - f$, in two frequency heating. The reference level (---) is for simple frequency heating at R_T = 2.02 in the random phase limit.

Dup

SIMULATION OF MULTI-FREQUENCY ECRH*

T. D. Rognlien
Lawrence Livermore National Laboratory, University of California
Livermore, California 94550

ABSTRACT

We use a test particle simulation code to investigate electron cyclotron heating in a magnetic mirror well. A comparison is made between heating with one frequency and heating with two closely spaced frequencies. The calculations are motivated by experimental evidence from the SM-1 experiment[1] at TRW, Inc., which shows that multi-frequency heating substantially increases the hot electron beta for a constant ECRH power. The code follows electron orbits in the presence of one or two monochromatic ECRH waves using guiding center equations and an equation for the electron gyrophase. Coulomb collisions with electrons and ions are simulated as a Monte Carlo scattering process. We find for the parameters of SM-1 that at the fundamental resonance the heating rate, or velocity rf diffusion coefficient, begins to decrease significantly from the quasilinear value for $\varepsilon_e \gtrsim 10$ keV due to superadiabatic effects. As suggested by Howard et al.[2], using multiple frequencies pushes the superadiabatic boundary to higher energies. For a given energy, the optimum frequency separations for two frequencies are those which cause the axial bounce resonances to interlace; i.e., odd multiples of the bounce frequency, ω_b. This interlacing increases the chance of resonance overlap and thus stochasticity. If the frequency difference is equal to an even multiple of ω_b, the diffusion coefficient returns to near its one frequency value. More generally, for more than two frequencies one should choose the frequency separation such that the bounce resonances interlace evenly. Detailed calculations are presented for SM-1 parameters.

*Work performed under the auspices of the U.S. DOE by the Lawrence Livermore National Laboratory under contract number W-7405-ENG-48.

1. INTRODUCTION

Recent experimental measurements[1] on the SM-1 mirror device at TRW, Inc. have shown more than a doubling of the hot electron beta when two or more closely spaced ECRH heating frequencies are used compared to the single frequency case. The mean energy of the hot electrons does not change as the beta ($= nT/(B^2/2\mu_0)$ measured by a diamagnetic loop increases, indicating that the effect of multiple frequencies is to increase the hot electron density. With a mirror ratio R = 2-3, there are two non-relativistic cyclotron resonance heating zones in the device; the fundamental resonance occurs near the mirror throat, and the second harmonic resonance occurs near the midplane. The picture which has evolved is that the multiple frequencies are increasing the feeding rate of warm electrons heated at the fundamental which are subsequently heated to several hundred keV energies by the second harmonic resonance.[1]

In this paper, we wish to investigate a mechansim by which the heating rate of warm electrons can be enhanced by multiple frequencies. In a mapping calculation which models two frequency heating, Howard et al.[2] have shown that the second frequency can increase the energy at which electron heating stops owing to superadiabaticity. We have found a similar result by following the detailed orbits of test electrons, including collisions, in monochromatic ECRH fields. In addition, we have found the condition for optimum heating occurs when the frequency separation, $\Delta\omega$, is an odd multiple of the axial bounce frequency ω_b; i.e., $\Delta\omega = (2n+1)\omega_b$. Since ω_b varies as the square root of energy, this condition cannot be met simultaneously at all energies; the condition should be applied at the energy corresponding to the boundary of superadiabatic motion.[3,4]

The plan of the paper is as follows: In Sec. 2 we present the model used to describe the electron heating which includes guiding center equations and Monte Carlo collision terms. The two limits of the electron heating, stochastic or quasilinear diffusion and superadiabatic motion, are discussed in Sec. 3. We present numerical code results in Sec. 4 for the effectiveness of two-frequency heating in the SM-1 experiment. Section 5 contains a discussion of the results.

2. GEOMETRY AND EQUATIONS

We consider the motion of an electron trapped in the magnetic well shown in Fig. 1. Any radial or azimuthal drifts are neglected. Two right-hand-polarized electromagnetic waves are assumed present with frequencies $\omega_{1,2}$ and electric field strengths $E_{1,2}$. The wavenumber perpendicular to the magnetic field $\underset{\sim}{B}$, is $k_\perp = 2\ \mathrm{cm}^{-1}$ and the parallel wavenumber is zero.

The non-relativistic guiding-center equations in MKS units for the electron motion are

$$\frac{d\mu}{dt} = \frac{e}{Bm_e} v_\perp J_0(k_\perp \rho_\perp) \sum_{i=1}^{2} E_i \cos(\omega_i t - \phi) \tag{1}$$

$$\frac{dv_\parallel}{dt} = \frac{e}{m_e}\frac{d\Phi}{dz} - \mu\frac{dB}{dz} \tag{2}$$

$$\frac{d\varphi}{dt} = \omega_c \left\{ 1 + \frac{J_0(k_\perp \rho_\perp)}{Bv_\perp} \sum_{i=1}^{2} E_i \sin(\omega_i t - \phi) \right\} \tag{3}$$

where only the first harmonic heating term has been included. Here $\mu = v_\perp^2/2B$ is the magnetic moment, $v_{\perp,\parallel}$ is the velocity perpendicular (parallel) to $\underset{\sim}{B}$, e is the electronic charge, J_0 is the Bessel function of the first kind, ω_c is the cyclotron frequency, $\rho_\perp = v_\perp/\omega_c$, ϕ is the gyrophase, and Φ is the static ambipolar potential.

Coulomb collisions with electrons and ions are included using Monte Carlo terms in the equations of motion as described elsewhere.[5] The assumed density of cold electrons and ions is shown in Fig. 1. Since we consider electrons in the 10 keV range of energy, it is only the pitch angle scattering which is important for particles being heated by ECRH. In the code, we include interactions with cold electrons and ions but omit collisions with hot electrons. This is valid for $n_h v/n_c v_h << 1$, where $n_{h,c}$ is the hot (cold) electron density, and v and v_h are the velocities of the test electron and hot electron, respectively. A simple way of including pitch angle collisions is to change the pitch angle, θ, at each time-step, Δt, according to

$$\Delta\theta = \left(\frac{3\ \Delta t}{t_D/2}\right)^{1/2} \xi \tag{4}$$

where ξ is a random variable chosen from a uniform distribution between -1 to 1, and t_D is Spitzer's 90^0 deflection time for stationary scatterers.[6] The factor of 2 in Eq. (4) accounts for scattering off electrons and ions.

3. TYPES OF ELECTRON HEATING

3.1 STOCHASTIC OR QUASILINEAR DIFFUSION

Because the magnetic field varies along the electron orbit, the heating from cyclotron resonance with the wave ($\omega = \omega_c$) is localized spatially. If, during the time between two such resonances, the wave phase and gyrophase are decorrelated, the localized kicks the electron receives can be considered statistically independent and a diffuson coefficient can be readily constructed. Such decorrelations can be caused by collisions, finite wave bandwidth, or intrinsic stochasticity from wave resonance overlap.[3,4]

A number of authors have considered the size of the velocity kick, $\Delta v_\perp$, received by a particle passing through a spatially varying cyclotron resonance. We use the reference of Rognlien and Matsuda[7] in order to emphasis the less generally known correct relation between $\Delta v_\perp$ and the heating rate. To translate the analysis of an electrostatic flute mode in Ref. [7] to the right-hand-polarized mode used here, make the replacements $E_{flute} \to 2E$ and $2J_1(k_\perp \rho_\perp) \to (k_\perp \rho_\perp)\, J_0(k_\perp \rho_\perp)$. This yields the velocity kick

$$\Delta v_\perp = 2\pi \frac{E}{B} J_0(k_\perp \rho_\perp) \left(\frac{2L_B}{\rho_\perp}\right)^{2/3} Ai(-x) \sin\psi_0 \tag{5}$$

where $x = (2L_B/\rho_\perp)^{2/3} (v_\parallel/v_\perp)^2$, $L_B = B(dB/dz)^{-1}$, Ai is the Airy function, and ψ_0 is the initial relative phase between the wave phase and gyrophase. All variables are evaluated at the resonance point, $\omega = \omega_c(z)$.

Before one can calculate change in energy, $\Delta\varepsilon$, or the heating rate, it is necessary to calculate $\Delta v_\perp$ to second order in E, as in Ref. [7]. Then

$$\Delta\varepsilon = \frac{m_e}{2} [2v_\perp \langle\Delta v_\perp\rangle + \langle\Delta v_\perp \Delta v_\perp\rangle] \tag{6}$$

where the bracket denote averaging over many electrons with random phase ψ_0. In the limit $k_\perp \rho_\perp \ll 1$, both terms in Eq. (5) contribute equally,[7] yielding

$$\Delta\varepsilon = m_e \langle\Delta v_\perp \Delta v_\perp\rangle \quad . \tag{7}$$

The velocity diffusion coefficient and the heating rate only require knowledge of the time between kicks, Δt_k. Roughly, $\Delta t_k \approx L_R/v_{\parallel}$, where L_R is the distance between resonances on each side of the midplane. The local quasilinear diffusion coefficient is thus

$$D_q = \frac{\langle \Delta v_\perp \Delta v_\perp \rangle}{2\Delta t_k} \quad . \tag{8}$$

The heating rate is $\Delta\epsilon/\Delta t_k = 2m_e D_q$.

The usefulness of the quasilinear diffusion coefficient is that it can be incorporated in finite-difference Folker-Planck codes[8] which allow a time-dependent modeling of the evolution of the electron distribution function. On the other hand, there are situations when successive kicks are, in fact, correlated. This can lead to the reduction and elimination of any heating as discussed in the next section.

3.2 SUPERADIABATIC MOTION

The motion of a charged particle subjected to a monochromatic wave near the cyclotron frequency in a mirror well has been studied by a number of authors.[3,4] The motion is characterized by a series of bounce resonances which, for a quadratic well, satisfy the equation[3]

$$\omega_1 = \ell\omega_{c0}(1 + v_{\parallel 0}^2/2v_{\perp 0}^2) - 2p\omega_b \tag{9}$$

where ℓ is the harmonic number, p is an integer, the zero subscript denotes midplane values, and ω_b is the bounce frequency. Particles located on a resonace have their kicks reinforced on successive bounces because the wave phase and gyrophase have the same relative phase at each heating point. If the electric field is large enough, the excursion of particles about these resonances is sufficient to bring them close to neighboring resonances. This resonance overlap results in stochastic motion.[3,4]

For first harmonic heating without collisions, a detailed analysis[3] predicts superadiabatic motion for energies greater than ϵ_b, where

$$\epsilon_b = [m_e z_B(1 + z_r^2/z_B^2)]^{1/4} z_r \omega^{1/2} (eE)^{3/4} \tag{10}$$

in MKS units. Here the magnetic field assumed is $B = B_0(1 + z^2/z_B^2)$, ω is the wave frequency, and z_r is the position of the resonance. Below ε_b the motion becomes more stochastic owing to resonance overlap until $\varepsilon \lesssim \varepsilon_b/5$ where all of the phase space is stochastic[3] and quasilinear theory can be used. Collisions and other "external" forms of decorrelation will have the effect of increasing ε_b and there will then always be some small diffusion at higher energies.

4. SIMULATION RESULTS

4.1 SM-1 SYMMETRIC MIRROR

The bulk of our calculations have been performed to model the SM-1 experiment.[1] The profiles of magnetic field and density used are shown in Fig. 1. We are interested in the heating of electrons in the 10 keV range by the fundamental resonance. The subsequent heating by the second harmonic to higher energies is not considered. We take $\omega_1 = 2\omega_{c0}$ so that the wedge region of velocity space in Fig. 2 corresponds to the heating region. The loss cone corresponds to a mirror ratio of $R = 2.2$. The ambipolar field is neglected so $\Phi = 0$ in Eq. (2).

Our procedure is to inject an ensemble of electrons at a given energy with a uniform distribution from $R = 2$ to $R = 2.2$, which corresponds to pitch angles, θ, from 45^0 to 42.4^0. Each time an electron crosses the midplane, its total velocity is recorded. The ensemble average $\langle(\langle v\rangle - v)^2\rangle$ is calculated and plotted versus time as shown in Fig. 3 for 15 keV electrons. The three sets of data points correspond to three cases for one wave with $E_1 = 5$ V/cm; Δ, the quasilinear model where the gyrophase is artifically decorrelated each bounce period; O, Coulomb collisions are present which cause a partial decorrelation; and $\square$, collisions are absent and superadabatic motion results. A diffusion coefficient is calculated by fitting an equally-weighted least-squares linear fit to the straight portion of the data giving a curve $\langle(\langle v\rangle - v)^2\rangle = \alpha t + \beta$. The average diffusion coefficient in the wedge region of Fig. 2 is then

$$D = \frac{1}{2}\frac{d}{dt}(\alpha t + \beta) = \frac{\alpha}{2} \quad . \tag{11}$$

Although we calculate D using the total velocity, the direction of the diffusion at the midplane is not strictly in velocity, but also causes some change in

pitch angle.[7] For the range of pitch angles near the resonance R = 2 line in Fig. 2, this effect is small. Alternately, D can be thought of as the local diffusion coefficient for the perpendicular velocity at the heating point. We also mention that the mean velocity <v> does not appear to vary from the injection velocity, v_0, indicating that there is no measurable velocity drag. Second order contributions to <v> are obscured by statistical fluctuations.

The ratio of the measured diffusion coefficient, D, to the quasilinear value, D_q, is shown in Fig. 4 at various electron energies. Coulomb collisions are present. Two cases are shown: the one frequency case has E_1 = 5 V/cm and $\omega_1 = 6 \times 10^{10}\ s^{-1}$; and the two frequency case has $E_1 = E_2 = 5/\sqrt{2}$ V/cm and $\omega = \omega_1 - \Delta\omega$ with $\Delta\omega = 1.5 \times 10^8 s^{-1}$. The quasilinear coefficient, D_q is independent of energy for $k_\perp \rho_\perp \ll 1$ and can be calculated from Eq. (8) by averaging over pitch angles from 45^0 to 42.2^0. It has also been verified with the code by randomizing the gyrophase on each pass through the midplane (see Δ data points in Fig. 2).

For the one frequency case, D begins to decrease significantly for $\varepsilon_e \gtrsim$ 5 keV as a result of some of the particles becoming superadiabatic. Because D decreases, the heating rate does also and the feeding of particles to higher energy is hampered. If collisions are omitted, the same trend is followed except D follows a curve about 50% below the O's for ε_e > 5 keV and motion becomes completely superadiabatic between 10 and 15 keV. This is in agreement with Eq. (10) which for $z_r = z_B$ = 30 cm and E = 5 V/cm yields ε_b = 11 keV. Even though the collisional pitch angle scattering is very weak with $\Delta\theta \sim 10^{-3}$ radians per bounce at 10 keV, the gyrophase diffusion is greatly enhanced by the non-uniform magnetic field.[9] This enhancement accounts for the fact that collisions do significantly effect the wave-particle correlation.

For the two frequency case in Fig. 4, the difference frequency corresponds to the bounce frequency of 13 keV electrons. Electrons below this value have their value of D restored to almost the quasilinear value. Consequently, heating is improved and the superadiabatic limit is pushed to higher energy.

The influence of chosing different values of $\Delta\omega$ is shown in Fig. 5 for ε_e = 10 keV. The value of D peaks for $\Delta\omega$ equal to odd multiples of ω_b and D returns to near its one frequency value for $\Delta\omega = 2n\omega_b$. The reason for this oscillatory behavior is the manner which the two sets of bounce resonances of Eq. (9) for each of the waves interlace as discussed in Sec. 5.

4.2 TMX-UPGRADE TANDEM MIRROR

Finally, we note that we have done calculations of first harmonic electron heating for the TMX-U experiment scheduled for operation next year at Lawrence Livermore National Laboratory. Our conclusion is that the one frequency diffusion coefficient is equal to the quasilinear value for energies at least up to 50 keV, the planned operating energy. Consequently, no improvement in heating efficiency would be expected for multiple-frequencies based on the mechanism we believe is important for SM-1. The different behavior of TMX-U electrons may be attributed to the larger electric field, high density (collisionality), and smaller ω_b (longer system).

5. DISCUSSION

The two-frequency results for SM-1 in Figs. 4 and 5 can be explained as follows. The resonances described by Eq. (9) are plotted on Fig. 6 near ε_e = 10 keV. The indice p scans from p = -53 on the left to p = -45 on the right. Electrons near these resonances experience cumulative kicks which lead to large excursions away from the line. As mentioned in Sec. 3.2, when the width of the oscillation about the resonance touches the adjacent broadened resonance, stochasticity results.[4] When a second frequency is present, another set of resonances occurs. If $\omega_2 - \omega_1 = \Delta\omega = (2n+1)\omega_b$, the two sets of resonances interlace. This halves the distance between resonances and thus makes it easier for them to overlap. To maintain constant power, the electric field is reduced by $\sqrt{2}$ which only reduces the oscillation width by $2^{1/4}$ [Ref. 4]. This reduction in width is more than compensated by the halving of the distance between resonances. If $\Delta\omega = 2n\omega_b$, the two sets of resonances nearly coincide, and the distance between them is the same as the one frequency case. The maximum possible width is increased by $2^{1/4}$ although the time averaged width is the same as for one frequency. Thus one would expect a small improvement over the one frequency case if $\Delta\omega = 2n\omega_b$.

The idea of interlacing resonances can be extended to more than two waves. Consider J waves whose electric fields are given by $E_j = E_0/(J)^{1/2}$ to maintain constant power input. The half width of the oscillations, Δv_{osc}, about a resonance scale as $E_j^{1/2} \propto (J)^{-1/4}$. If one choses the frequencies such that $\Delta\omega_j = (j - 1)\omega_b/J$, the resonances will interlace evenly, reducing the distance

between them by $1/J$. The ratio of the oscillation width to the half width between resonances, Δv_{rw}, thus scales as

$$\Delta v_{osc}/\Delta v_{rw} \propto J^{3/4} \quad . \tag{12}$$

Stochasticity occurs for $\Delta v_{osc}/\Delta v_{rw} > \pi/2$ [Ref. 4]. Consequently, using more waves (larger J) increases the chance of heating. This effect has been seen in SM-1 where the hot electron beta increases with the number of waves,[1] although no attempt was made to optimize the frequency separations for more than two waves.

Another issue which has arisen in connection with heating is the zeros of the Airy function in the expression for $\Delta v_\perp$ in Eq. (5). These could present barriers to diffusion even for the quasilinear case.[10] If we omit collisions at 10 keV, we clearly see these regions where diffusion is extremely weak. However, we have verified that collisions virtually remove these small accumulation regions where diffusion stops.

In the SM-1 experiment[1] the optimum frequency separation for two waves was $\Delta f \approx 40$ MHz with a rather broad peak. Our optimum is closer to $\Delta f = 25$ MHz shown in Fig. 4; calculations for $\Delta f = 40$ MHz have less overall enhancement of D. We think the reason for this is that our model has a mirror ratio of 2.2 whereas the experiment, owing in part to finite beta enhancement, has a mirror ratio of ~ 3. This would increase the bounce frequency of 13 keV electrons to approximately 25 MHz $\times \sqrt{2}$ = 35 MHz, which is close to the optimum observed in the experiment.

An additional effect that we are beginning to study is that the second harmonic heating at 10-30 keV may also exhibit some superadiabatic limitations which are removed by multiple frequencies in just the same way as for the first harmonic. Then $\ell = 2$ in Eq. (9), and the condition for interlacing resonances is still $\Delta\omega = (2n+1)\omega_b$.

ACKNOWLEDGMENTS

The author thanks R. H. Cohen for several useful discussions.

REFERENCES

1. B. H. Quon, R. A. Dandl, N. H. Lazar, and R. F. Wuerker, Bull. Am. Phys. Soc. 26, 893 (1981).

2. J. E. Howard, A. J. Lichtenberg, M. A. Lieberman, and R. H. Cohen, Bull. Am. Phys. Soc. 26, 1036 (1981).

3. N. C. Wyeth, A. J. Lichtenberg, and M. A. Lieberman, Plasma Phys. 17, 679 (1975), and references therein.

4. G. R. Smith, J. A. Byers, L. L. LoDestro, Phys. Fluids 23, 278 (1980).

5. T. D. Rognlien and T. A. Cutler, Nucl. Fusion 20, 1003 (1980).

6. L. Spitzer, Jr., Phys. Fully Ionized Gases, (Interscience, New York, 1967) p. 132.

7. T. D. Rognlien and Y. Matsuda, Nucl. Fusion 21, 345 (1981).

8. Y. Matsuda, W. M. Nevins, and R. H. Cohen, "Electron Cyclotron Resonant Heated Electron Distribution Functions," Proc. Workshop on EBT Stability Theory, May 13-14, 1981 (Oak Ridge Nat'l. Lab., Oak Ridge, TN) p.211.

9. B. I. Cohen, R. H. Cohen, and T. D. Rognlien, "Influence of Pitch-Angle Collisions and Phase Decorrelation on DCLC Transport in Mirror Machines," Lawrence Livermore Nat'l. Lab. Rept. No. UCRL-86272, June 1981; submitted to Phys. Fluids.

10. T. K. Samec, B. I. Hauss, and G. Guest, Bull. Am. Phys. Soc. 26, 928 (1981).

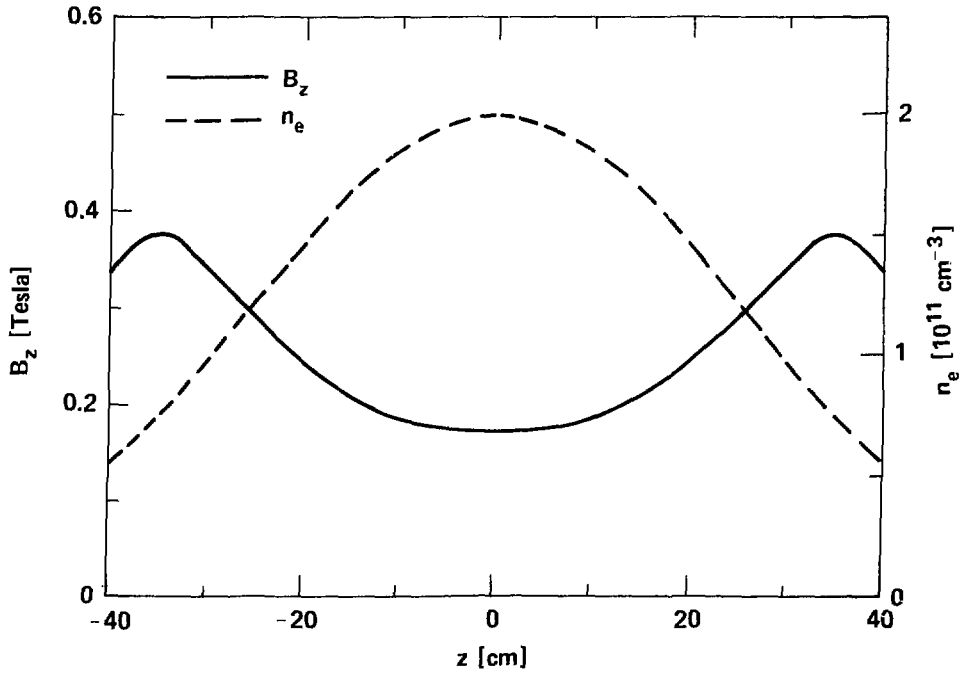

Fig. 1 Axial profiles of magnetic field, B_z, and density, n_e, used in tne simulation modeling SM-1.

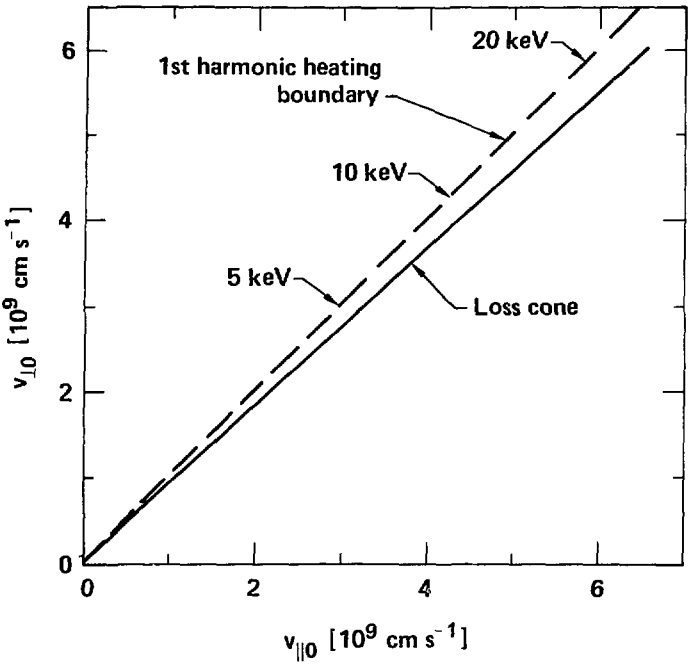

Fig. 2 Electron velocity space showing the wedge region where first harmonic heating occurs with $\omega = 2\omega_{c0}$.

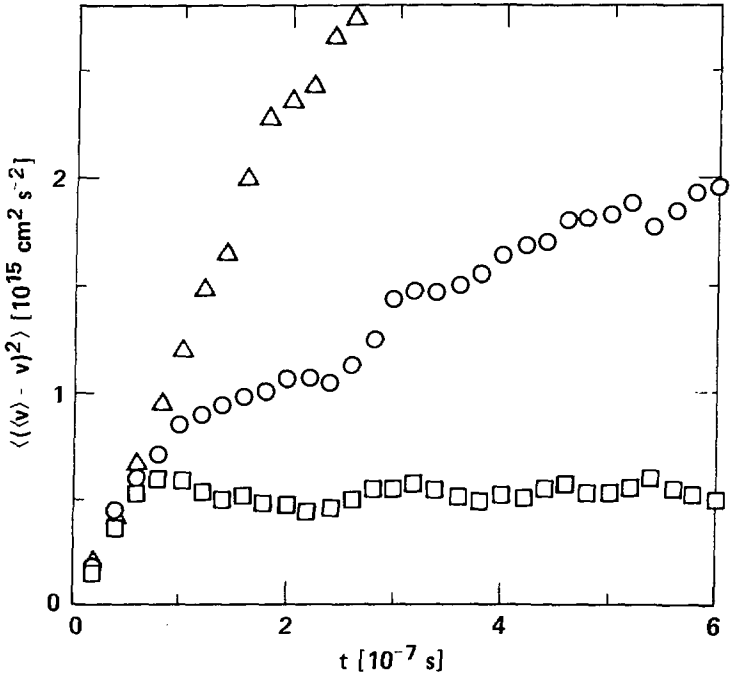

Fig. 3 Variance of the velocity versus time for three cases at ε_e = 15 keV with E = 5 V/cm: Δ, gyrophase artifically randomized on each pass through midplane (quasilinear diffusion); O, Coulomb collisions alone provide gyrophase decorrelation; □, collision omitted resulting in superadiabatic motion.

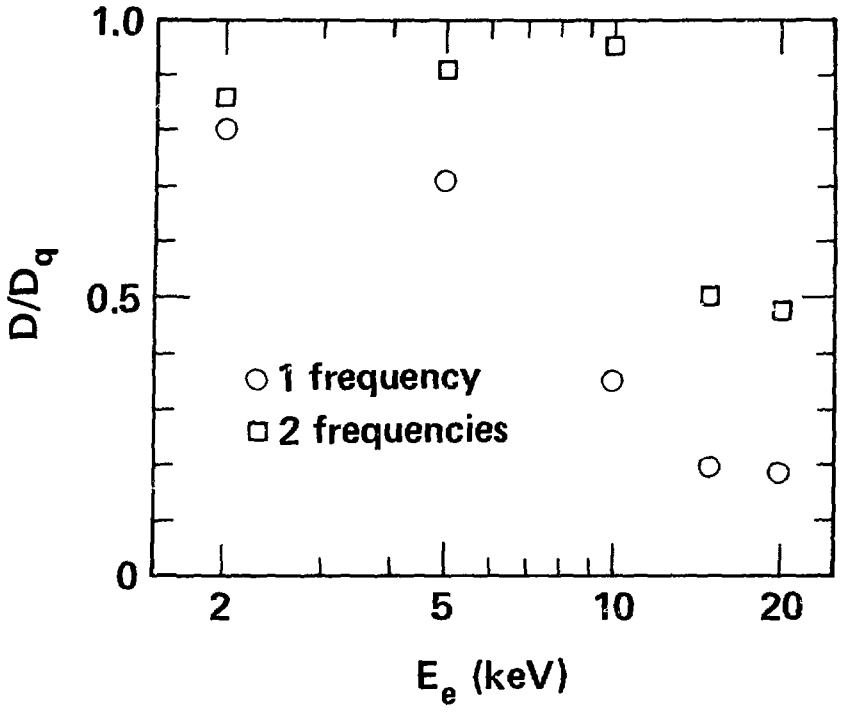

Fig. 4 Ratio of tne measured diffusion D to the quasilinear value, D_q, at various energies for two cases: O, one frequency with $E_1 = 5$ V/cm; □, two frequencies with $E_1 = E_2 = 5/\sqrt{2}$ V/cm and $\omega_1 - \omega_2 = \Delta\omega = 1.5 \times 10^8\ s^{-1}$. The $\Delta\omega$ corresponds to the bounce frequency at 13 keV.

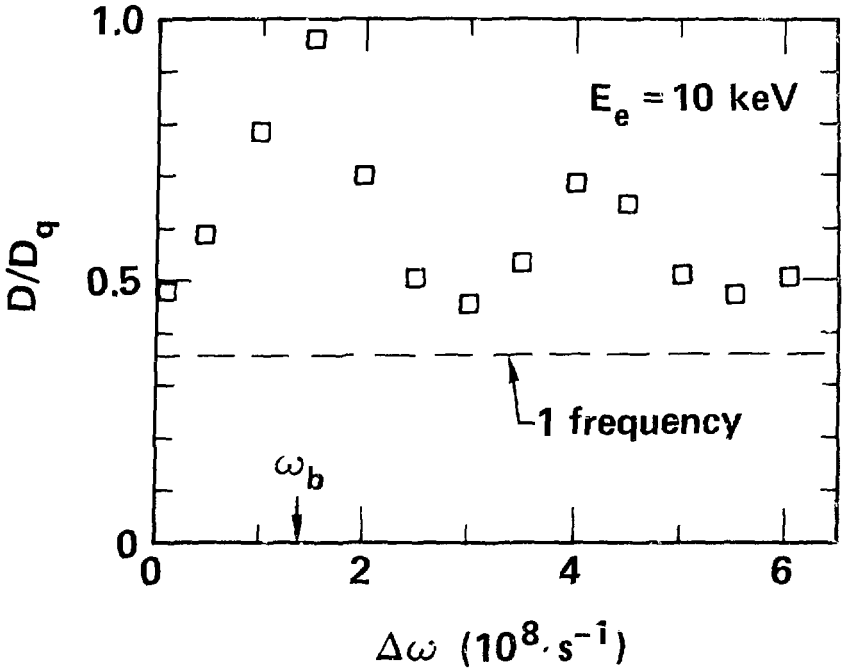

Fig. 5 Ratio of D to D_q at 10 keV for two frequencies as the frequency separation, $\Delta\omega$, is varied. Electric fields are $E_1 = E_2 = 5/\sqrt{2}$ V/cm.

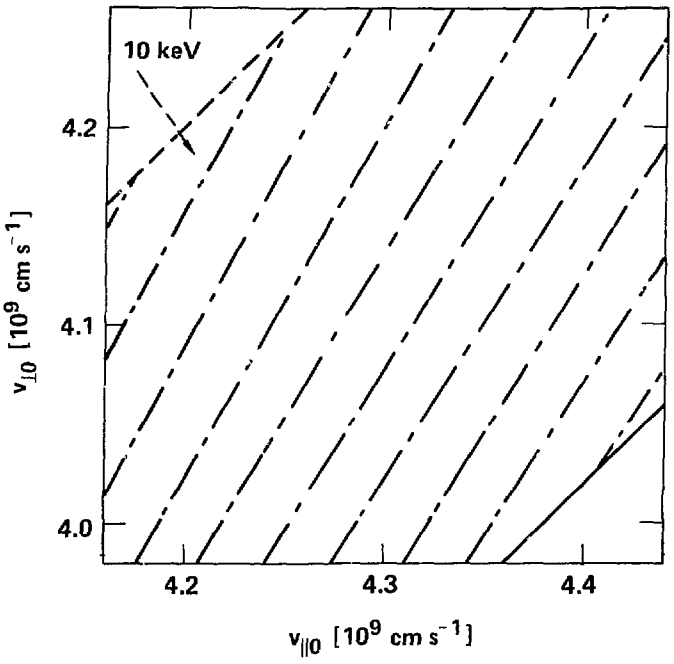

Fig. 6 Location of the bounce resonances near 10 keV from Eq. (5) assuming a quadratic magnetic well with a scale length of z_B = 30 cm. Also shown are the first harmonic heating boundary(- - -) and the loss cone (——) as in Fig. 2.

THEORY OF MULTIFREQUENCY ECRH

J. E. Howard, M. A. Lieberman and A. J. Lichtenberg
Department of Electrical Engineering and Computer Sciences
and the Electronics Research Laboratory
University of California, Berkeley, California 94720

and

R. H. Cohen
Lawrence Livermore National Laboratory
Livermore, California 94550

ABSTRACT

Significant enhancement of ECRH has been demonstrated experimentally by dividing the heating power among several closely-spaced frequencies[1]. This effect may possibly be explained as an increase in the adiabatic barrier via destruction of isolating KAM curves. We have investigated this possibility for two frequencies both analytically and numerically by means of area-preserving mappings. The basic enhancement mechanism of interspersing two sets of phase space islands which can be made to overlap, has been treated in detail for the Fermi acceleration model of particle heating[2]. In general, the ERCH problem requires a four-dimensional phase space, owing to changes in $v_{\parallel}$ between the resonance layers, but reduces to a two-dimensional mapping when the two frequencies are sufficiently close. Linear and nonlinear stability limits are derived and confirmed numerically. Constraints on $\Delta\omega/\omega$ are obtained for optimal island spacing and validity of the mathematical models. Implications for the design of two-frequency experiments are discussed.

1. INTRODUCTION

Recent encouraging ECRH experiments[1] on the SM-1 device at TRW, Inc. have stimulated several numerical and theoretical calculations to model the effects of two or more closely spaced frequencies on the heating rate. In a numerical guiding center simulation, Samec[2] et al. find considerable enhancement in the heating rate over the single frequency value. Rognlien[3], using a Monte Carlo technique, finds a factor of two increase in the diffusion coefficient for heating at the fundamental resonance. The optimal frequency spacing for enhancement is found from numerical simulation to occur at odd multiples of the bounce frequency,

$$\Delta\omega = (2m-1)\omega_b, \quad m = 1,2,3,\ldots \; . \tag{1}$$

A possible mechanism for the observed enchancement is overlap of the phase space islands corresponding to the two heating frequencies, leading to an increase in the adiabatic barrier to heating, as proposed by Howard et al.[4]. In this earlier work we studied the Fermi acceleration mapping as an analog to ECRH in a magnetic trap and found close agreement between the analytic and numerical results. The present paper relates the Fermi model results to ECRH experiments in three stages. We first illustrate the utility of the mapping method by deriving an area-preserving mapping for collisionless single frequency ECRH in a parabolic well. Next we summarize the principal features and results of the two-frequency Fermi mapping study. This relatively simple model retains most of the essential features of the ECRH interaction, while allowing accurate prediction of the position

of the adiabatic barrier for varying admixtures of two driving terms at different frequencies. An expression for the optimal $\Delta\omega$ analogous to Eq. (1) is derived and verified numerically for the Fermi mapping. Finally we discuss our work to date in deriving a valid area-preserving mapping for two-frequency ECRH, and finish with a derivation of Eq. (1).

2. AREA-PRESERVING MAPPING FOR SINGLE FREQUENCY ECRH

Consider single particle motion in a parabolic well

$$B = B_0(1+z^2/L^2), \tag{2}$$

with resonance zones located off-midplane at $\pm z_1$, as illustrated in Fig. 1. In the absence of collisions, an electron intially penetrating the resonance zone will reflect near z_1 after a few transits, especially if $\vec{v}$ is initially small. Under these assumptions the following well-known formula for the velocity kick readily follows from the (non-relativistic) equations of motion[5]

$$\Delta v_\perp = 2\pi a\left(\frac{R_1 L^2}{\gamma\omega_1}\right)^{1/3} \frac{Ai(-x)}{v_{\perp 1}^{2/3}} \sin\Psi, \tag{3}$$

where $a \equiv eE/m$, $R_1 = B_1/B_0$ is the mirror ratio at resonance, $\gamma \equiv (R_1-1)/R_1$,

$$x = \left(\frac{R_1\omega_1^2 L^2}{\gamma}\right)^{1/3} \frac{v_{z1}^2}{v_{\perp 1}^{8/3}} << 1 \tag{4}$$

and

$$\psi = \int_0^t \omega_{ce}dt - \omega_1 t \tag{5}$$

is the phase slip between the wave and the electron gyration. In deriving Eq. (3) we assumed first harmonic heating in the limit $k_\perp \rho_e << 1$. For a parabolic well, the phase slip between turning points is

$$\Delta\psi = \frac{\pi\omega_1 L}{2} \frac{\gamma R_1^{1/2}}{v_{\perp 1}} . \tag{6}$$

After scaling, Eqs. (3) and (6) take the simple form

$$u' = u + \frac{\sin\psi}{(u')^{2/3}} \tag{7a}$$

$$\psi' = \psi + \frac{2\pi M}{u'} , \tag{7b}$$

where $u = v_\perp/V$, with

$$V^{5/3} = 2\pi a \ \mathrm{Ai}(0)\left(\frac{R_1 L^2}{\omega_1 \gamma}\right)^{1/3} .$$

Note that (7) depends on the single dimensionless parameter

$$M = \frac{R_1^{3/10} \ \gamma^{6/5}}{4[2\pi \mathrm{Ai}(0)]^{3/5}} \Lambda^{3/5},$$

where

$$\Lambda = \omega^2 L/a.$$

We shall refer to Eqs. (7), with $x = 0$, as the turning point mapping.

Figure 2 illustrates the result of iterating Eqs. (7) starting from a number of initial conditions for $M = 5$. The dome-shaped void at the bottom left portion of the graph is a consequence of the fact that Eq. (7a), which must be solved implicitly for u', has no solutions for

$$u < -(\frac{5}{2})^{2/5} \left(\frac{5 \sin \psi}{3}\right)^{3/5} \approx -2 \sin^{3/5}\psi.$$

In practice this gap does not present a problem, as it always lies in the stochastic lower region for interesting values of $M \gtrsim 100$.

A more serious drawback to Eqs. (7) is that they are not area-preserving, so that stable fixed points are attractors[6]. This means that phase space trajectories spiral in towards fixed points, rather than forming the closed (KAM) curves characteristic of a Hamiltonian system. The non-area preservation of Eqs. (7) is a consequence of truncating the expansions used in deriving Eqs. (3) and (6). We may easily remedy this flaw by adding a small term to Eq. (7b), to obtain the area-preserving turning point mapping

$$u' = u + \frac{\sin \psi}{(u')^{2/3}} \tag{8a}$$

$$\psi' = \psi + \frac{2\pi M}{u'} - \frac{2 \cos \psi}{3(u')^{5/3}} . \tag{8b}$$

The dramatic effect of this small change is shown in Fig. 3, which reveals much more regular structure in the upper half of the plot. A relatively small price to be paid is a negligible shift in the vertical location of the primary fixed points at $\psi = 0$ and π near $u_0 = 2.5$ and 5.0. The secondary islands near $u_0 = 3.3$ are shifted horizontally as well. Figure 3 illustrates some of the basic properties of area preserving mappings. Primary period-one fixed points which leave u unchanged lie on the lines $\psi = 0$ and π. These fixed points occur in families at $u_0 \approx M/k$, $k = 1,2,3,\ldots$, corresponding to $\Delta\psi = 2\pi k$. The mapping is primarily regular for large u, effectively stochastic for

small u, while islands appear admidst chaos at intermediate velocities. An orbit initialized in the stochastic region will diffuse around the phase plane, but will not rise above the adiabatic barrier, u_B, presented by the lowest KAM curves that spans the entire range of ψ. By changing M, the location of u_B may be raised. The mechanism for this enhancement may be intuitively understood as the destruction of KAM curves lying between contiguous islands which almost overlap.

3. THE FERMI MODEL

3.1 Single Frequency Heating

A mathematical model which has been used as an analog to ECRH is Fermi acceleration[7], depicted in Fig. 4. It may be shown that the motion of a light ball making elastic collisions with a fixed and a sinusoidally oscillating wall is approximately described by the area-preserving mapping

$$u' = u + \sin \psi \tag{9a}$$

$$\psi' = \psi + \frac{2\pi M}{u'} , \tag{9b}$$

where $\psi = \omega t$, $M = \omega L/\pi V$ and V is the maximum wall velocity. Comparing this system with the ECRH mapping Eqs. (8), we see that the phase slip equations are identical, except for the small term added to Eq. (8b) to maintain area preservation. Furthermore, the velocity equations (8a) and (9b) can be put into correspondence locally by Taylor expanding Eq. (8a) about a local velocity. The predicted position of the adiabatic barrier velocity is the same for the two systems once this correspondence is made. The simplicity of the Fermi mapping is very useful in studying its stability properties.

Now consider what happens to these mappings when a second frequency is added. For the ECRH problem, the change in $v_{\parallel}$ between the two spatially separate resonance zones leads to a four-dimensional mapping, which reduces to a two-dimensional system in the limit of small frequency separation. Or the other hand, it is perfectly straightforward to generalize the Fermi mapping to an arbitrary number of frequencies. If the frequencies are rational multiples of one another, then a simple periodic mapping is possible. Since only single collisions with the wall are allowed, regardless of the complexity of the wall motion, we shall always obtain a two-dimensional mapping.

3.2 Two-Frequency Heating

We now briefly review the derivation of the two-frequency Fermi mapping treated in detail in Ref. 4. Let the wall motion be $V_r \sin \omega_r t + V_s \sin \omega_s t$, where $V = \sqrt{V_r^2+V_s^2}$ = constant and the two frequencies are rationally related ($\omega_r/\omega_s = r/s$, with r and s coprime integers). Defining the phase $\phi = \omega_s t/s$ and scaled velocity $u = v/V$, we obtain

$$u' = u + \frac{1}{\sqrt{1+\mu^2}} (\sin s\phi + \mu \sin r\phi) \tag{10a}$$

$$\phi' = \phi + \frac{4\pi M}{(r+s)u'} \tag{10b}$$

where $\mu = V_r/V_s$ is the amplitude ratio and

$$M = \frac{L(\omega_r+\omega_s)}{2\pi V} . \tag{11}$$

Note that the driving terms in (10a) have been normalized to maintain approximately constant input power as μ is varied.

In studying this mapping we hold M and r/s fixed and observe the change in the adiabatic barrier, u_B, as μ is varied. A representative set of mappings is shown in Fig. 5 for r/s = 3/2, M = 125, and μ = 0 and 1. Note the occurence of distinct families of island chains corresponding to the two frequencies. These families occur at velocities[4]

$$u_{or} = \frac{rM_{eff}}{k_r}, \quad k_r = 1,2,3,\ldots \tag{12}$$

$$u_{os} = \frac{sM_{eff}}{k_s}, \quad k_s = 1,2,3,\ldots, \tag{13}$$

where $M_{eff} = 2M/(r+s)$. In addition, there are chains of common islands at

$$u_0 = \frac{M_{eff}}{k}, \quad k = 1,2,3,\ldots \tag{14}$$

The locations of several of these chains are indicated in Fig. 5a, for which $M_{eff} = 50$.

If r/s and M are chosen such that a set of r-fold islands lie between two contiguous chains of s-fold islands near the adiabatic barrier, then this barrier may be broken down for some value of μ. More precisely, the stochastic layer surrounding the r-fold island chain overlaps the stochastic layers of the neighboring s-fold islands, destroying all nearby KAM curves. This process may be clearly seen in Fig. 5, where the growing $k_r = 5$ chain overlaps the $k_s = 3$ and 4 chains, resulting in a significant increase in u_B.

To estimate the value of μ at which island overlap occurs we employ the "two-thirds rule,"

$$\Delta_r + \Delta_s \gtrsim \frac{2}{3} |u_{or}-u_{os}| \tag{15}$$

where Δ_r and Δ_s are the resonance half-widths, depicted in Fig. 6. Intuitively, Eq. (15) says that overlap occurs when the sum of the island widths, their stochastic layers and sets of secondary islands just touch. Expressions for Δ_r and Δ_s are derived in Ref. 4. Generally the criterion (15) agrees well with numerical data for comparable size islands and enables us to predict the location of the adiabatic barrier quite accurately.

Maximum overlap takes place when the r-fold islands fall midway between the s-fold islands, i.e.,

$$u_{or} = \frac{1}{2} (u_{os}+u_{os'}). \tag{16}$$

Restricting $r = s+1$ and taking $k_r = k_s+m$ then gives, for $k_s \gg 1$,

$$k_s \cong \frac{1}{2} (2m-1)s, \tag{17}$$

which requires $s \gg 1$ for moderate values of m. Equation (17) can be put in a more useful form by taking $sM_e \approx M$ and $u_{os} \approx u_B = \alpha\sqrt{2\pi M}$ in (13) to obtain

$$\frac{1}{s} = (2m-1)\, \alpha\sqrt{\frac{\pi}{2M}}\,, \tag{18}$$

where the factor α is the relative increase in the barrier velocity when the second frequency is added. Equation (18) gives the condition for optimum interspersal of r-fold and s-fold islands in the vicinity of the adiabatic barrier. Conversely, the r-fold and s-fold resonances

coincide when $u_{os} = u_{or}$, which leads to

$$\frac{1}{s} = 2m\alpha\sqrt{\frac{\pi}{2M}} \ . \tag{19}$$

Equations (18) and (19) can be combined to give

$$\frac{\Delta\omega}{\omega_s} = \frac{1}{s} = \alpha m' \sqrt{\frac{\pi}{2M}} \ , \tag{20}$$

with maximum enhancement of u_B for odd m' and minima at even m'.

Figure 7 shows the relative change in u_B,

$$\eta = \frac{u_B(1)-u_B(0)}{u_B(0)} \tag{21}$$

versus 1/s, for r = s+1, where $u_B(1) = u_B(\mu = 1) \approx u_{Bmax}$. For large s, the r-fold and s-fold island chains nearly coincide near the adiabatic barrier; the small residual change in u_B is due to the mutual destruction of closely spaced fixed points with incommensurate frequencies and also to a small increase in island width resulting from our normalization. The oscillatory behavior of η at smaller s is a consequence of the interspersal of resonances as expressed by Eq. (20). Using the numerical results in Fig. 7 and knowing the positions of the r-fold and s-fold chains, we estimate the last KAM curves to be destroyed at $\alpha = 1.4$ for the peaks and at $\alpha = 1.1$ for the minimum. The corresponding analytic values of 1/s are indicated in Fig. 7, in good agreement with the numerical data.

4. DISCUSSION

Owing to the similarity of the two mappings, the principal results derived for the two-frequency Fermi mapping are expected to carry over,

at least qualitatively, to the corresponding ECRH problem. Most important, the adiabatic barrier to stochastic heating at the fundamental may increase by as much as a factor of two when two frequencies are used rather than one. For a device such as SM-1, where both first and second harmonic heating are used, using multiple frequencies at the fundamental provides a more efficient source of warm electrons for second harmonic heating.

A formula for the optimal frequency separation, analogous to Eq. (18), may also be derived for ECRH. The condition for resonance with a wave of frequency ω_1 is that the phase slip in one half-bounce time be $2\pi p$, p integer. For an arbitrarily shaped magnetic well (including an arbitrary ambipolar potential) this relation has the form

$$\langle\Omega\rangle - n\omega_1 = 2p\omega_b, \tag{22}$$

where n is the wave harmonic number (1 for first harmonic), ω_b is the bounce frequency, and $\langle\Omega\rangle$ is the bounce-averaged gyrofrequency. In general ω_b and $\langle\Omega\rangle$ are both functions of $v_\perp$ and $v_\parallel$. A criterion for optimal interspersal of resonances is that, as the wave amplitude is increased, a resonance layer for frequency ω_1 first overlaps simultaneously its two neighboring layers for frequency $\omega_1 + \Delta\omega$. In the limit that the resonance layers change insignificantly with p, an approximate criterion is that an ω_1 resonance lie midway between two $\omega_1 + \Delta\omega$ resonances; that is, along any curve $C(v_\perp, v_\parallel) = 0$,

$$v_\perp(\omega_1,p) = \frac{1}{2}[v_\perp(\omega_1+\Delta\omega,p-m) + v_\perp(\omega_1+\Delta\omega,p-m+1)] \tag{23}$$

where m is an integer. If the resonances are closely spaced compared

with the scale lengths of $\langle\Omega\rangle$ and ω_b, then the right hand side of Eq. (23) is approximately $v_\perp(\omega_1+\Delta\omega, p-m+\frac{1}{2})$. Combining this result with Eq. (22) then gives

$$\Delta\omega = (2m-1)\omega_b, \tag{24}$$

which is the empirical result noted at the beginning of this paper. The analogous result for the two-frequency Fermi mapping follows by defining a bounce frequency $\omega_b = \pi u/2L$ corresponding to two mapping periods. Again taking $u = \alpha\sqrt{2\pi M}$ for consistency in Eq. (13) yields Eqs. (23), with $\Delta\omega = \omega_s/s$.

The two-frequency ECRH problem reduces to a two-dimensional system only in the limit of small frequency differences. More generally, the higher-dimensional nature of two-frequency ECRH leads to the phenomenon of Arnold diffusion[8]. When $v_\perp$ is stochastic "thick-layer diffusion" occurs, in which the stochastic gyrophase drives diffusion in the parallel velocity, as measured at the lower frequency resonance layer. Where the motion is mainly adiabatic stochastic motion in the thin separatrix layers will drive "thin layer Arnold diffusion," which allows particles to diffuse slowly to higher energy. We are currently investigating these phenomena.

ACKNOWLEDGEMENT

Research sponsored by the Department of Energy Contract DE-ATOE-76ET53059 and the Office of Naval Research Contract N00014-79-C-0674.

REFERENCES

1. B. M. Quon, R. A. Dandl, N. H. Lazar, and R. F. Wuerker, Bull. Am. Phys. Soc. 26, 893 (1981).
2. T. K. Samec, B. I. Hauss, and G. Guest, Bull. Am. Phys. Soc. 26, 928 (1981).
3. T. D. Rognlien, Bull. Am. Phys. Soc. 26, 1035 (1981).
4. J. E. Howard, A. J. Lichtenberg, and M. A. Lieberman, Univ. of Calif., Electronics Res. Lab. Memo No. M81/86, 1981 (submitted to Physica D).
5. F. Jaeger, A. J. Lichtenberg, and M. A. Lieberman, Plasma Physics 14, 1073 (1972).
6. M. A. Lieberman and A. J. Lichtenberg, Plasma Physics 15, 125 (1981).
7. M. A. Lieberman and A. J. Lichtenberg, Phys. Rev. A 5, 1852 (1972).
8. M. A. Lieberman, Ann. N. Y. Acad. Sci. 257, 119 (1980).

$$\gamma \approx \pi k \; L_B \; (\frac{\omega_p^2}{\omega\omega_c}) \qquad F_0 \tag{15}$$

where

$$F_0 = \int_{\infty}^{V_0} f_1(v_z) \; dv_z \tag{16}$$

The function F_0 is just the fraction of electrons for which $v_z \geq v_0$. That is, as the wave approaches the cold plasma resonance ω_c from the high field side, its energy is absorbed by electrons of lower and lower velocity until it reaches the point z_0, where the resonant velocity is v_0, the e-folding parameter is γ, and the fraction of the electron velocity distribution that has absorbed this energy is F_0. Now solve for F_0 from eqs. (1), (4) and (15)

$$F_0 \approx \frac{\gamma}{\pi k L_B} \; (\frac{\omega}{\omega_p})^2 \; (1 + Nv_z/c) \tag{17}$$

For approximate estimates of the absorption process, we take $N \approx 1$, we use the vacuum value of k, and we set $v_z \approx v_0$:

$$F_0 \approx \frac{1}{2\pi^2} \; \frac{\lambda}{L_B} \; \frac{n_c}{n} \; (1 + \frac{v_0}{c}) \quad \gamma \tag{18}$$

where n is the plasma density and n_c is the ordinary wave cutoff density:

$$n_c = \epsilon_0 \; m\omega^2/e^2 \tag{19}$$

Note that in this low density approximation, the fraction F_0 is independent of the shape of the velocity distribution.

For some numerical examples relevant to current and planned experiments, consider a 28 GHz wave (λ = 1 cm, $n_c = 10^{13}$ cm^{-3}) and put γ = 1, because more than half of the energy absorption occurs during the first e-folding. Parameters typical of the mirror thermal barrier experiments (TMX-U and MFTF-B) would be $L_B \approx 100$ cm, $n \approx 5 \times 10^{12}$, and $(v_0/c) \approx 0.3$ (corresponding to 30 keV parallel velocity). Then one finds F_0 (mirrors) ≈ 0.0013. On the other hand, for a small hot electron ring (such as the STM experiment[4] λ = 3 cm, $n_c = 1.1 \times 10^{12}$ cm^{-3}), one would have $L_B \approx 20$ cm, $n \approx 2.5 \times 10^{11}$, and $(v_0/c) \approx 0.1$ (corresponding to 3 keV parallel velocity). In this case F_0 (STM) ≈ 0.037. In both examples, only a small proportion of the electrons are resonantly absorbing the preponderant amount of wave energy - far "upstream" from the cold plasma resonance.

For the mirror example, the low density approximation is not very good, but in this case F_0 is so small that it is difficult to imagine any other result than $F_0 << 1$.

4. RAY TRACING CALCULATIONS

Although this calculation is one-dimensional, the general effect of Doppler-shifted absorption should happen for a wide range of angles. For example, it appears in recent ray tracing calculations[2] of the thermal barrier region of the large tandem mirror experiment MFTF-B.[5,6] Fig. 2 shows some results for plasma conditions which may be typical of the early buildup stage of this experiment. For both of the cases shown in figure 2, the absorption zone is centered in a region where $\omega \approx 1.1\ \omega_c$, even though the ray is not parallel to the magnetic field. However, there is still a component $k_{\parallel}$ of the wave vector which is sufficient to provoke the Doppler-shifted absorption effect. A rough estimate based on eq. (1) shows that the mean parallel electron energy associated with this 10% frequency shift is 3 keV, which is comparable to the temperature range of the plasma.

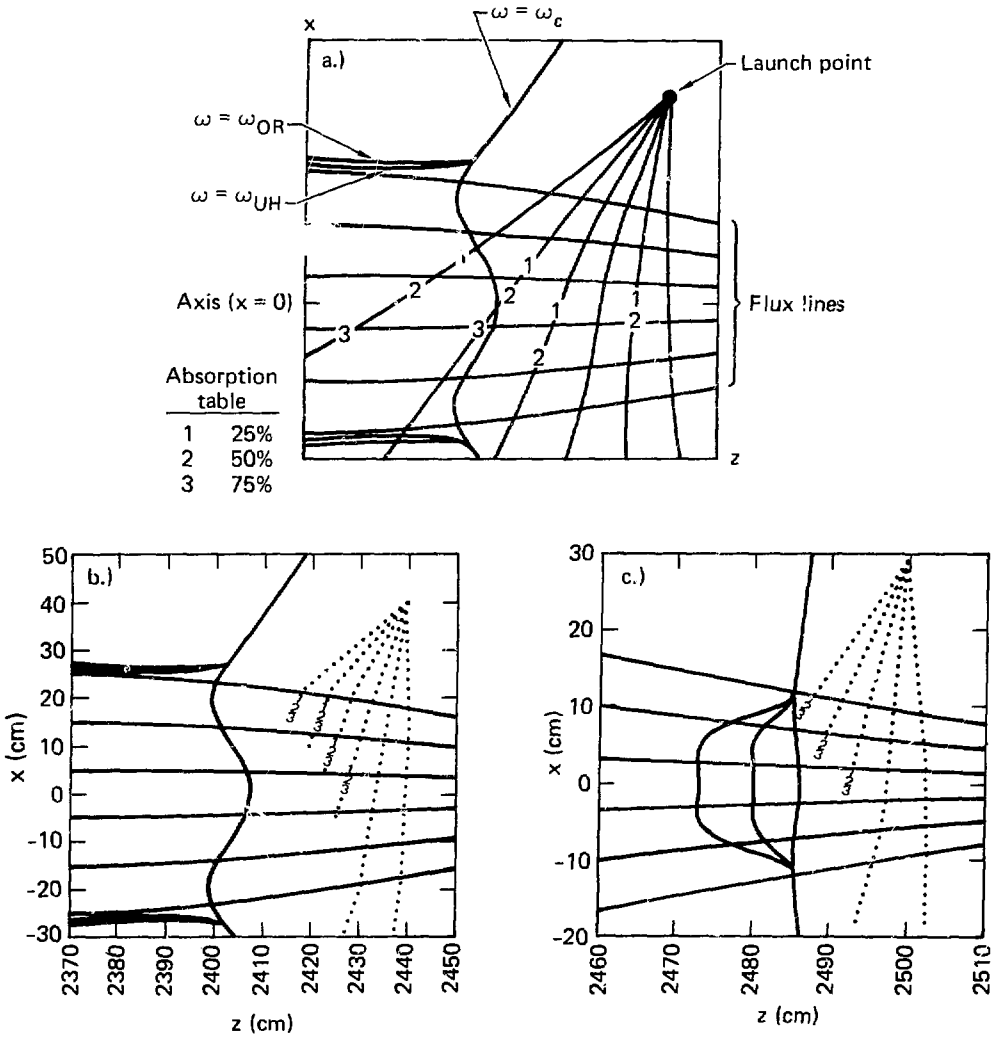

Fig. 2 Examples of ray-tracing code calculations for MFTF-B, showing ray absorption on the high field side of the cold plasma resonance. Extraordinary rays are incident on a Maxwellian plasma of maximum density = 7×10^{12} cm^{-3} and maximum temperature (on axis) = 5 keV, which is contained within the flux lines. (a) is a key to the graphs; (b) is for 28 GHz near the 1 Tesla field minimum of the thermal barrier; (c) is for 56 GHz near 2 Tesla.

The more general absorption equations that are used in this ray tracing code[7] also show similar Doppler-shifted absorption effects for the ordinary wave. However, for this mode the absorption coefficient is so much smaller than for the extraordinary wave that the ordinary wave reaches the cold plasma resonance and passes through it. So in this case the main effect of the Doppler shift is to broaden the absorption zone rather than shifting its center to the edge of the resonance region.

At higher temperature, the Doppler shift effect is even greater, but these results are not shown here because there is still some question as to whether all of the important relativistic electron effects have yet been completely included in the ray tracing code. Certainly, no relativistic corrections were included in the one-dimensional analysis.

5. ABSORPTION ZONE IN VELOCITY SPACE

It is also interesting to examine the position of the Doppler-shifted absorption zone in velocity space. Let v_0 be considered as an appropriate average value of the mean Doppler-shifted parallel velocity in the absorption zone (see fig. 1). Then figure 3a illustrates that all electrons with parallel velocity $v_z > v_0$ will be heated near or on the high field side of point z_0.

It is more customary in mirror systems to use the velocity coordinates $v_{\perp m}^2$ v_{zm}^2 at the midplane. Consider the usual mirror field equations of adiabaticity:

$$\mu B = \frac{1}{2} m v_\perp^2 \tag{20}$$

and of energy conservation:

$$U = \mu B + \frac{1}{2} m v_z^2 \tag{21}$$

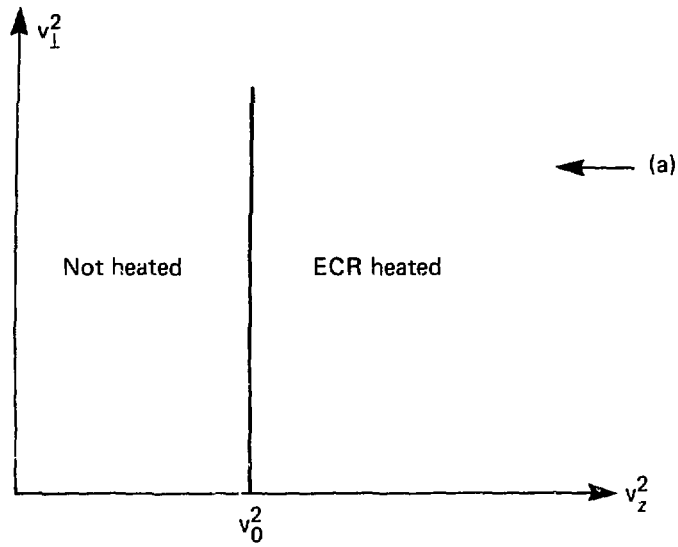

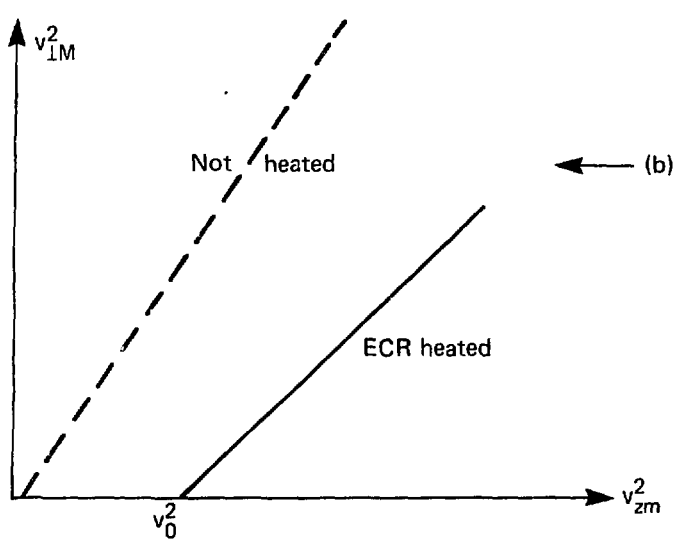

Fig. 3. Velocity Space Diagrams in a Mirror Field for Doppler-shifted ECRH absorption (a) at the absorption zone (b) at the midplane. The solid line is the Doppler-shifted absorption zone boundary, the dotted line is the corresponding cold plasma resonance case.

where μ, the diamagnetic moment, and U, the total energy, are constants. From this starting point, a short derivation yields the relation:

$$v_{\perp m}^2 = \frac{B_m}{B_o - B_m} \left(v_{zm}^2 - v_o^2\right) \tag{22}$$

where the subscript m refers to the midplane values. Equation (22) is plotted in fig. 3b, where it is compared with a similar equation for the cold plasma resonance:

$$v_{\perp m}^2 = \frac{B_m}{B_R - B_m} v_{zm}^2 \tag{23}$$

Note that both the slope and the horizontal axis intercept are different for these two cases. This means that the diffusion coefficients for the Fokker-Planck calculations of the electron velocity distribution must take the Doppler-shifted absorption into account. This has not yet been done in the present Fokker-Planck code.[8] The necessary correction is similar to the effect introduced by a potential difference between the heating zone and the midplane, and it should be possible to incorporate it into future codes.

6. SUMMARY

We have discussed the spatial shift of the resonance absorption region due to the Doppler effect, especially for the extraordinary ray. It appears to be an important effect for electron temperatures greater than 1 keV. It must be taken into account when one is planning the placement of antennas in a mirror experiment such as MFTF-B, where large single-pass absorption is

anticipated. It must also be an important effect in the formation of hot electron rings.

In addition to the spatial shift, the effect leads to selective heating of a small fraction of the electrons - only those which have the largest parallel velocity. The resultant distortion of the electron velocity spectrum, and the subsequent changes in the absorption coefficient, are important issues that remain to be resolved.

ACKNOWLEDGEMENTS

The author is indebted to Karl Audenaerde (Univ. of Wisconsin) for assistance and for the ray-tracing code. Helpful discussions were held with Y. Matsuda, W. M. Nevins, G. D. Porter, and B. W. Stallard.

Work performed under the auspices of the U.S. Department of Energy by the Lawrence Livermore National Laboratory under contract number W-7405-ENG-48.

REFERENCES

1. A. F. Kuckes, Plasma Physics 10, 367 (1968).
2. J. W. Shearer and K. Audenaerde, Bulletin of the Amer. Phys. Soc., 26 (7), 927 (1981).
3. George Schmidt, "Physics of High Temperature Plasmas," 2nd edition, Academic Press, New York (L979) pp 252-254.
4. "Symmetric Tandem Mirror Program Annual Progress Report," TRW Report S/N 35638 (October 1980).
5. K. I. Thomassen and V. N. Karpenko, "Tandem Mirror Fusion Test Facility," LLL-PROP-163, Rev. 1 (Jan. 23, 1980).
6. D. E. Baldwin, B. G. Logan, T. C. Simonen, "Physics Basis for MFTF-B," UCID-18496 - Part 1 and Part 2 (Jan. 16, 1980).
7. K. Audenaerde, J. Scharer, and D. Mancl, Bulletin of the Amer. Phys. Soc., 26 (7), 889 (1981).
8. B. W. Stallard, Y. Matsuda, W. M. Nevins, "Fokker-Planck Calculations of Electron Cyclotron Resonant Heating (ECRH) in Mirror Geometry," companion paper for this workshop.

ENHANCEMENT OF EBT RING PARAMETERS DURING ION CYCLOTRON HEATING*

F. W. Baity, J. C. Glowienka, D. L. Hillis
Oak Ridge National Laboratory
Oak Ridge, Tennessee 37830

and

T. L. Owens
McDonnell Douglas Astronautics Company
St. Louis, Missouri 63166

ABSTRACT

Significant enhancement of the relativistic electron ring parameters during ion cyclotron heating (ICH) on EBT-S has been observed. Even with moderate ICH power absorbed by the plasma ($\lesssim$10 kW), the ring temperature increased by as much as 40%, and the ring density doubled. The ICH power was applied to a single one-third turn antenna located midway between two toroidal field magnet coils; however, under certain conditions, the rings were enhanced all around the torus. (At the same time, the core plasma ion energy was strongly increased, with little effect on other core parameters.) The mechanism responsible for the ring enhancement is not understood.

*Research sponsored by the Office of Fusion Energy, U. S. Department of Energy, under contract W-7405-eng-26 with the Union Carbide Corporation.

1.1 *INTRODUCTION*

In order to achieve a sufficient ion temperature for an EBT reactor plasma, some method of auxiliary ion heating must be employed. Ion cyclotron heating would appear to be the most attractive method since an EBT operates steady-state and the technology for high-power rf generation in the ICH frequency range for a reactor ($\sim$ 100 MHz) has already been demonstrated. Therefore, an ICH program has been initiated on EBT-S, concentrating on so-called fast wave heating, which is the relevant method on EBT-P and subsequent EBT experiments. While ion heating has been the principal reason for initiating these experiments, a number of effects have been observed on other parameters characterizing the plasma. This paper will focus on one of these; namely the observation of an anomalous enhancement in the hot electron ring energy on EBT during ICH.

Fast wave ICH was predicted to be marginal on EBT-S because of the relatively low plasma density and small size of EBT-S. In order to heat the core ions it is necessary to have penetration of the ICH wave fields into the plasma, and in order to heat the ions in more than one cavity with a single antenna it is necessary to have propagation of wave energy through the high magnetic field regions in each mirror throat. For EBT-S these conditions mean operating at ICH frequencies high enough such that the fundamental resonance, and in most cases the second harmonic resonance, do not exist anywhere in the plasma. Classical wave absorption theory predicts very little heating at higher harmonics; however, anomolously strong ion heating has been observed in EBT-S during ICH. Furthermore, at lower ICH frequencies, where wave propagation to adjacent cavities is non-existent, ion heating is still expected to be large in the cavity with the antenna. In fact, local (single cavity) heating is observed in the absence of wave propagation around the torus, but the heating is much less than that observed with propagation.

The radial profile of the ion heating has not been measured yet, due to a lack of diagnostic capability. Other core plasma parameters, including electron density and temperature, impurity radiation, and plasma space potential, have shown very little change at the 10 kW level of ICH.

1.2 MEASUREMENTS

The relativistic electron ring parameters are measured by two principal diagnostics: a hard x-ray detector and diamagnetic loop probes. The former measures both the ring temperature and density separately, while the latter only measure the product, the total stored energy in the rings. There was only one hard x-ray detector in use during the ICH runs, located two cavities away from the antenna. Diamagnetic loop probes were located on all 24 cavities. Wave propagation and absorption was measured by a set of electrostatically shielded magnetic probes, oriented to pick up the wave fields along the toroidal direction. These probes were distributed around the torus toroidally from the antenna cavity to 180° from the antenna.

For the hard x-ray measurements the ICH was operated steady-state in order to accumulate enough signal for good accuracy. In order to improve the resolution of the diamagnetic loops the ICH was pulsed on for about 5 sec, then off again. The rise and decay times of the hard x-ray flux was also measured during the pulsed experiments.

In order to vary the resonance zones spatially in the plasma, it is necessary to vary the frequency of the ICH source, since the ECH gyrotron (28 GHz) is a single frequency device and thus fixes the magnetic field setting. The ICH power source used for these experiments was a 20-kW cw HF-band transmitter. The frequency range of the antenna system was 15-50 MHz; however, the upper frequency limit of the 20 kW transmitter was 30 MHz. As a result the high power experiments were performed primarily at 30 MHz. Measurements at higher frequencies will be attempted following construction of a new rf source covering the 30-60 MHz range.

1.3 RESULTS

ICH power absorption by the plasma is largely dependent on the applied frequency and on the plasma density profile. Figure 1 shows the ratio of the power absorbed by the plasma to the total power applied to the antenna as a function of frequency for a typical C-mode (no electron rings), a typical T-mode (with rings) case, and near the T-M transition in a predominantly deuterium plasma. At 30 MHz in the T-mode approximately 45 percent of the applied power was absorbed in the plasma. This operating condition is just at the onset of wave propagation to other cavities, as

seen in Figure 2, which is a plot of the amplitude of the magnetic probes normalized to the signal in the antenna cavity versus toroidal position. In a hydrogen plasma under the same conditions, the toroidal extent of the wave fields was greatly reduced, but the fractional power coupling was only slightly less.

In Figure 3 is plotted the change in ring stored energy when 2 kW of ICH was applied as a function of toroidal position with respect to the antenna for the deuterium case at 30 MHz. It shows that the increase in ring energy occurs everywhere there is a ring. (Three cavities are not fed with ECH for diagnostic purposes.) Figure 4 is the same plot at 23 MHz. Here the ring enhancement is local. Thus the ring enhancement is dependent on the toroidal extent of wave fields.

For a given ICH input power the hard x-ray and diamagnetic loop diagnostics give the same answer for ring enhancement. The enhancement scales directly with input power, with no saturation apparent at the 10-kW level. With 10 kW of input power the ring in the cavity two cavities from the antenna cavity was enhanced by 40 percent in temperature and doubled in density as shown in Figure 5 (a,b). Figure 5 (a) is the hard x-ray spectrum with ECH only; ring temperature was 475 KeV and density was 6.4×10^{10} cm^{-3}. The spectrum with ICH (15 kW applied or 7 kW absorbed by the plasma) is shown in Figure 5 (b). This variation in the ring parameters for this case is greater than that obtainable with ECH alone by varying the plasma operating conditions.

The ring enhancement closely followed the ion heating behavior. The core ions had a multi-component non-Maxwellian spectrum, and the measurement was complicated by multiple ion species. However, the heating depended on the wave propagation and was linear with power. The observed heating is orders of magnitude larger than predicted by linear theory. Figure 6 shows the effect of varying frequency on the charge-exchange spectrum in the antenna cavity. The ordinate is the uncorrected count rate observed. The power to the antenna was held constant at only 400 W. At 20 MHz the spectrum was essentially the same as without ICH. The power coupled to the plasma and the charge-exchange flux increased steadily as the frequency was increased. The transmitter used had an upper limit of 32 MHz. Plasma loading measurements with a signal generator indicated that power absorption continued to increase between 32 and 48 MHz (the limit of the antenna tunable matching circuit).

The plasma density decreased slightly during ICH. The density reduction occurred uniformly throughout the plasma, with no change in radial profile as measured by a 9-channel microwave interferometer. The magnitude of the density reduction was proportional to the absorbed power but was only about 10% for 10 kW at 30 MHz in the high pressure T-mode operation. This density reduction may play a role in the ring enhancement, although the percentage density reduction increased as the pressure was lowered to approach the TM-transition, while the ring enhancement decreased.

Other core plasma parameters changed little if at all during ICH. Core electron temperature and impurity radiation did not change, and plasma space potential became more positive everywhere, mainly in the center of the plasma, but only slightly at the highest ICH power levels. Plasma space potential plays a major role in EBT confinement, so it may become very important when the ICH power is increased to levels comparable to the ECH power.

1.4 CONCLUSIONS

ICH has proven to be an effective technique for increasing the ion energy in EBT-S. The heating is anomolously large at frequencies near the threshold for wave propagation. An unexpected effect is a substantial enhancement in relativistic ring parameters, which is not understood theoretically. The ring enhancement can be localized to the vicinity of the ICH antenna or can be nearly uniform around the torus, depending on the ICH operating conditions. ICH would appear to be a useful tool in the study of hot electron rings since wide variations in ring density and temperature are possible with moderate amounts of ICH power, and the rings can be enhanced singly or altogether by suitably adjusting the ICH.

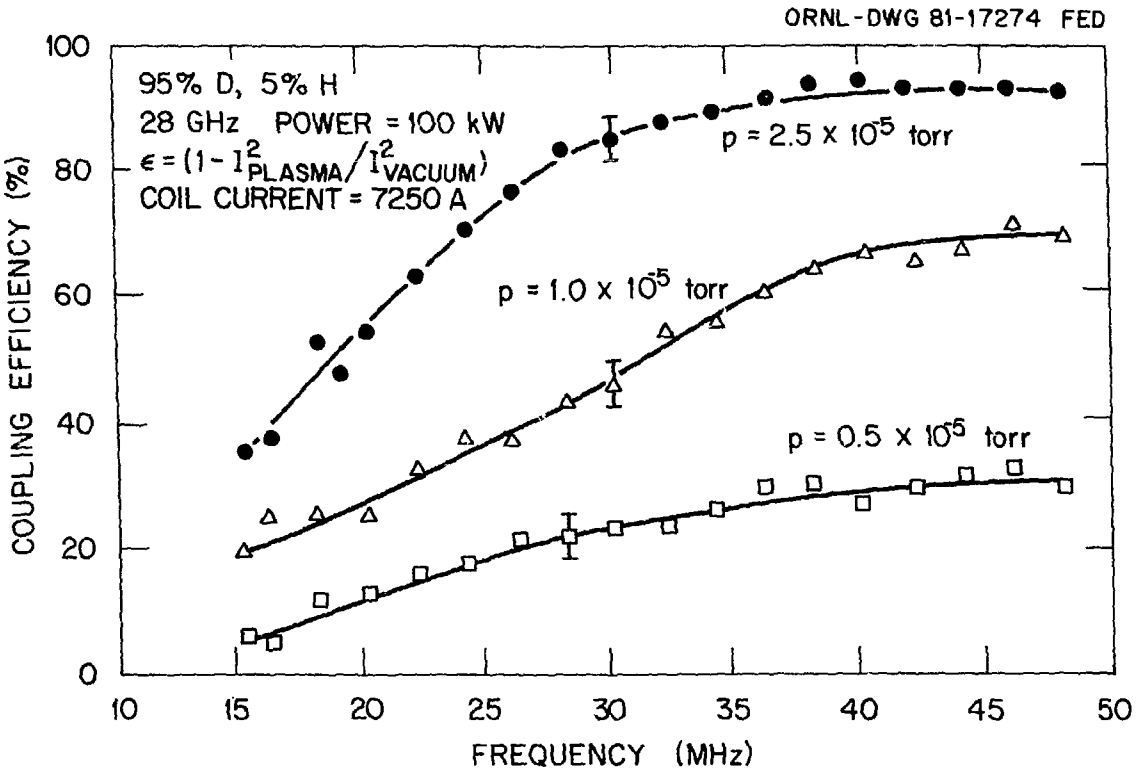

Fig. 1 The antenna coupling efficiency, defined as the ratio of the power, versus frequency for three different EBT-S operating conditions. The top curve is a C-mode condition; the other two are both in the T-mode.

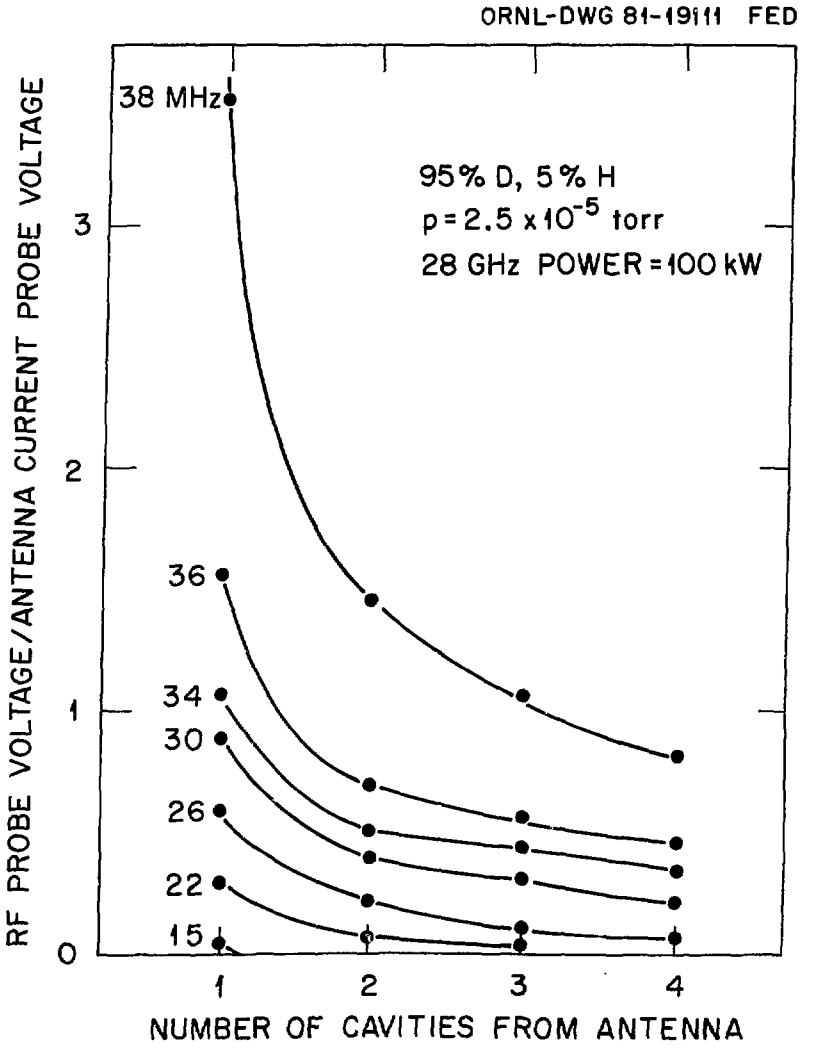

Fig. 2 Amplitude of the ICH wave fields normalized to the signal at the antenna as a function of toroidal position for frequencies ranging from 15-38 MHz for a deuterium plasma in the C-mode.

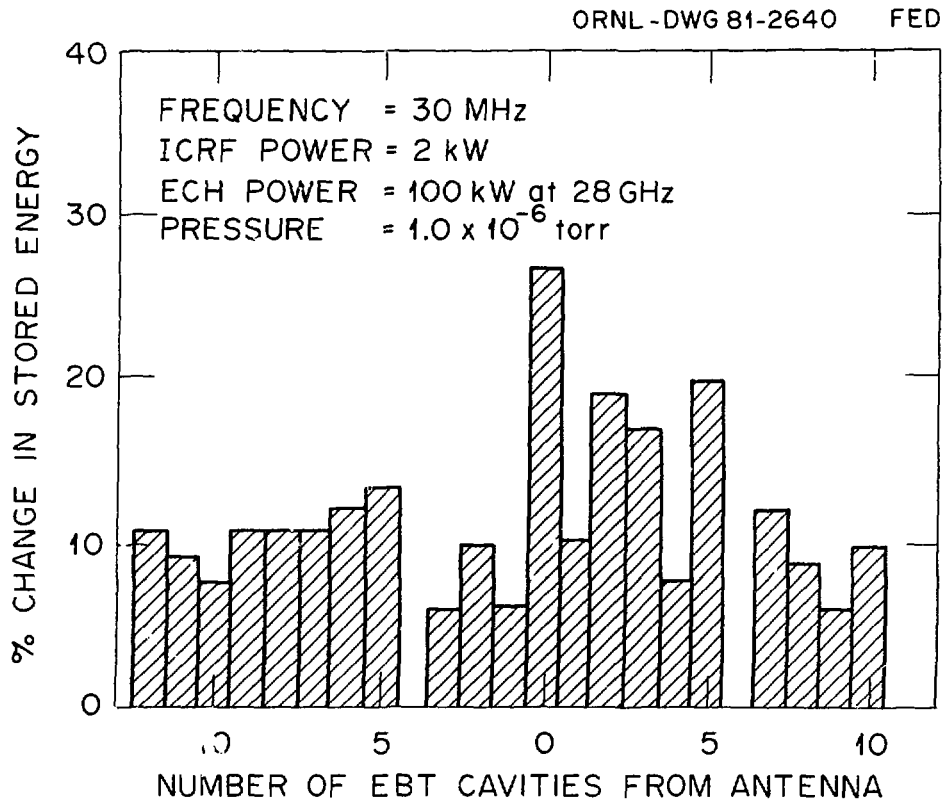

Fig. 3 Percentage change in relativistic electron ring stored energy versus toroidal position with 2 kW at 30 MHz applied to a deuterium plasma in the T-mode. The three cavities showing no change (-4, +6, +11) were not fed with ECH and consequently had no ring.

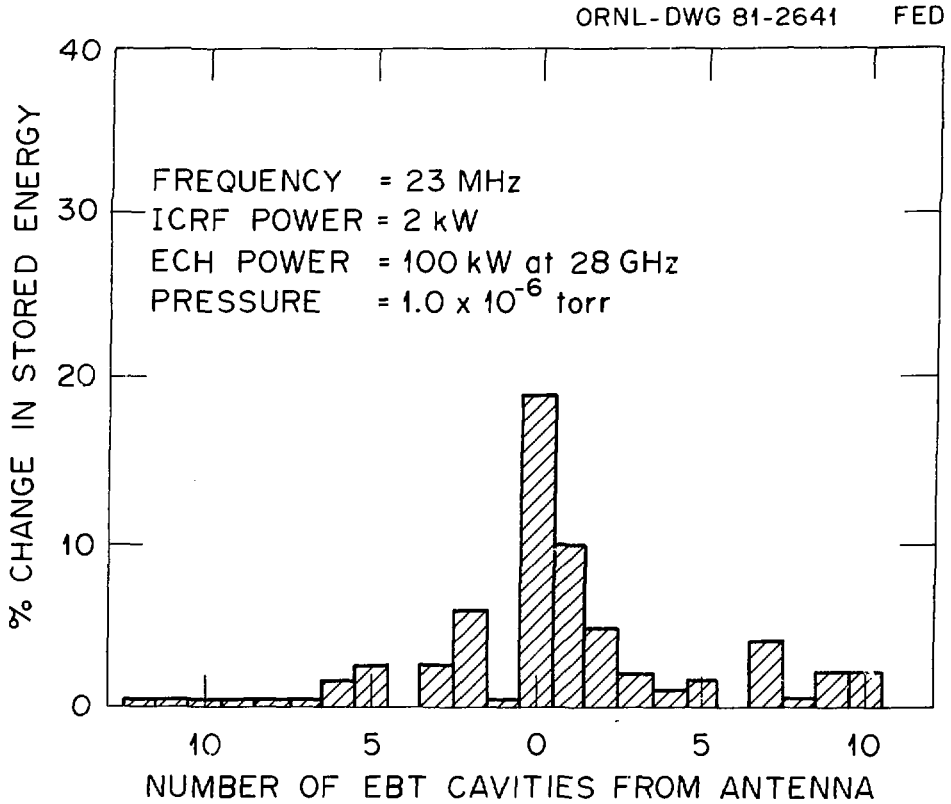

Fig. 4 Percentage change in relativistic electron ring stored energy versus toroidal position with 2 kW at 23 MHz applied to a deuterium plasma in the T-mode.

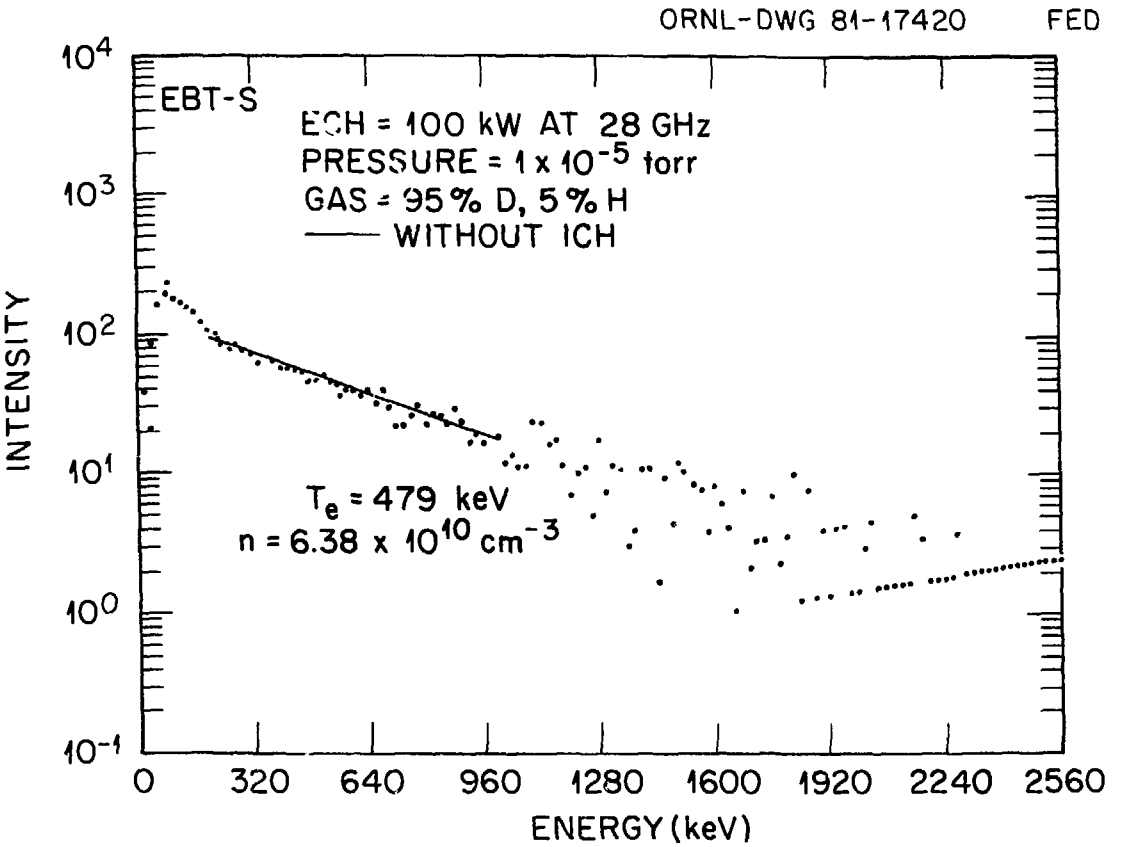

Fig. 5 (a) X-ray intensity versus energy for a deuterium plasma in the T-mode with ECH only (no ICH). The straight line segment corresponds to a ring temperature of 479 keV and a ring density of 6.38 X 10^{10} cm^{-3}.

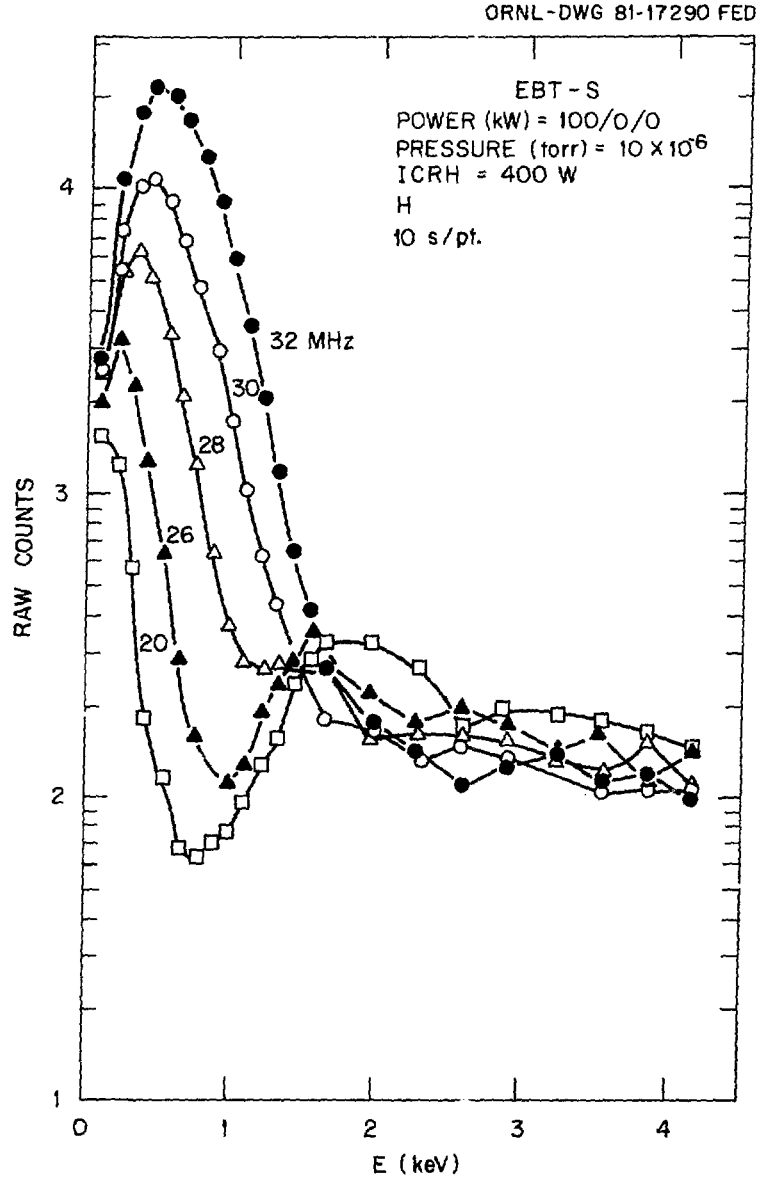

Fig. 6 Charge-exchange neutral counting rate versus energy for ICH frequencies between 20 MHz and 32 MHz.

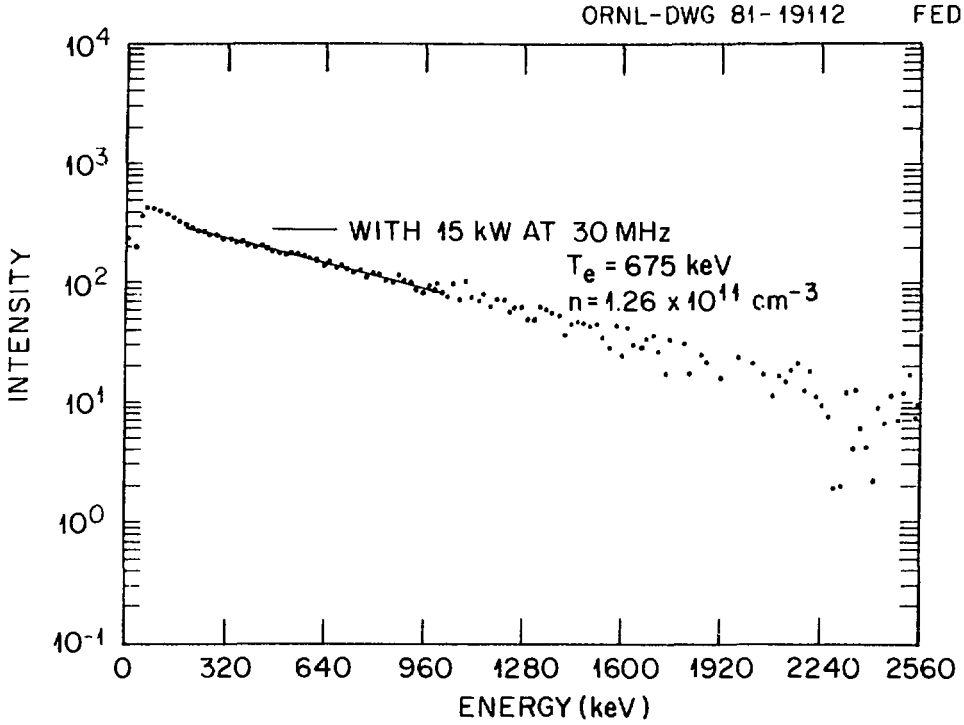

Fig. 5 (b) X-ray intensity spectrum under the condition in 5 (a) with the addition of 15 kW at 30 MHz. The ring temperature increased to 675 keV, and the ring density increased to 1.26×10^{11} cm^{-3}.

NON-STANDARD HEATING EXPERIMENTS IN EBT +

J.C. Glowienka, W.A. Davis, D.L. Hillis, and T. Uckan

Oak Ridge National Laboratory

F.M. Bieniosek and L. Solensten

Rensselaer Polytechnic Institute

+ Research sponsored by the Office of Fusion Energy, U.S. Department of Energy, under contract W-7405-eng-26 with Union Carbide Corporation.

ABSTRACT

The magnetic design of EBT-I/S provides a flexible environment in which to examine various ring and core plasma electron cyclotron heating (ECH) scenarios. The heating occurs when the ECH power, available at three discrete frequencies, 10.6, 18, and 28 GHz, is in resonance with local harmonics of the electron cyclotron frequency. The resonance locations can be moved in a continuous fashion in the cavity sectors by changing the toroidal magnetic field over the range of 0 to 1.4 T. In an EBT, the bumpy magnetic equilibrium is stabilized by the high-beta, hot electron rings formed in the field bumps by proper choice of microwave heating frequency and magnetic geometry. The most commonly utilized heating geometry for ECH is the Standard Resonance (SR) configuration wherein a fundamental resonance exists across the mirror coil throats for bulk plasma heating, and a second harmonic resonance exists in an annular region in the cavity midplane for ring heating. Reported here are the results of two nonstandard heating experiments. In one, the fundamental ECH resonance either at 10.6 or 18 GHz was placed at the usual ring position in an attempt to generate rings solely with fundamental heating (Fundamental Resonance configuration - FR). In a second experiment, an attempt was made to heat the ring and core separately by forming the ring as above with 10.6 GHz and then heating the core with the fundamental and second harmonic of 28 GHz (SCRATCH). In both cases, the hot electron annuli were formed and stabilized the core plasma as in the SR experiments. In FR, the ring is formed at the second harmonic and no significant potential structures were found. In SCRATCH, either a potential well or a potential hill co[illegible] be formed. In both heating regimes, significant ion heating a[illegible]e that [illegible]ound in standard heating experiments was found.

I. Introduction

The ELMO Bumpy Torus[1] is a steady-state, microwave-heated toroidal plasma device consisting of 24 mirror sections with a mirror ratio of 1.9 to 1, a major radius of 150 cm, and a mirror throat radius of 11 cm. The heating occurs when the electron cyclotron heating (ECH) power, available at three discrete frequencies 10.6, 18, and 28 GHz, is in resonance with local harmonics of the electron cyclotron frequency. The resonance locations can be moved in a continuous fashion throughout the cavity sectors by changing the toroidal magnetic field over the range of 0 to 1.4T.

Reported here are the results of two non-standard heating experiments. In one, the fundamental ECH resonance at either 10.6 or 18 GHz was placed at the usual ring position in an attempt to generate rings solely with fundamental heating (Fundamental Resonance configuration - FR). In a second experiment, an attempt was made to heat the ring and core separately by forming the ring as above with 10.6 GHz and then heating the core with the fundamental and second harmonic of 28 GHz (Separately Coupled Ring and Toroidal Core Heating -- SCRATCH[2]). In both cases, the hot electron annuli were formed and stabilized the core plasma as in the standard heating experiments. In FR, no significant potential structures were found although in SCRATCH, either a potential well or a potential hill could be formed. In both heating regimes, significant ion heating above that found in standard heating experiments was found. Section II provides the definitions for the various heating geometries; Section III lists the experimental results, and section IV offers several conclusions about the two new modes of operating EBT.

II. Definition of Heating Geometries

A. Standard Resonance Configuration

The conventional heating procedure in EBT, the Standard Resonance configuration (SR), utilizes a fundamental resonance mod-B contour spanning each magnet near the throat and a second harmonic resonance mod-B contour located in the field bumps. Typical resonance locations for SR in EBT-I/S are plotted in the equatorial plane in Fig. 1. In this manner, a warm electron core of order hundreds of electron volts is generated by the fundamental, and those warm electrons passing through the second harmonic resonance are heated to energies of order hundreds of kiloelectron volts to form the mirror trapped, hot electron annuli necessary for EBT stability. The ions are weakly heated by the electrons through collisions.

B. Non - Standard Heating Schemes - FR and SCRATCH

The ability to vary the magnetic field and/or the microwave frequency provides the opportunity to investigate entirely new heating geometries. The Fundamental Resonance (FR) configuration seeks to generate the the hot electron annuli with a fundamental resonance placed at the ring location as shown in Fig. 2. The higher harmonics are located outside the ring region and can couple energy to electrons but present heating theories predict lower coupling for higher harmonic heating ($n>2$)[3]. If the rings could be formed by the fundamental heating and could provide stabilization for a separately heated core plasma, the microwave frequency requirements for a reactor could be reduced.

An attempt to heat the ring and core plasmas independently (SCRATCH) utilizes rings formed by FR and a core heated by a higher frequency ECH source with its fundamental and second harmonic resonance zones located inside the core plasma. This is illustrated in Fig. 3.

Again, present theories suggest that higher harmonics do not play a significant heating role.

With the various mixtures of microwave frequencies and magnetic fields, a shorthand has been developed to identify the type of heating geometry in EBT. The steady state microwave power in kilowatts is denoted as X/X/X for heating at 28, 18, and 10.6 GHz, respectively. A four digit number following the ECH frequencies identifies the toroidal field magnet current. Table I lists the various possibilities. The values for the TF coil current are nominal values. The details for locating the resonant mod-B contours for arbitrary currents are found in Fig. 4.

III. Results

A. FR

The first FR experiments were conducted on the Nagoya Bumpy Torus with the principle results[4] that the rings were formed and were found to stabilize a toroidal core plasma over an operating range defined by pressure and power with identifiable C-, T-, and M-modes of operation. In addition, the line averaged density in FR was approximately twice that found in SR for comparable power. The NBT experiments utilized 8.5 GHz ECH and 3200 A in the TF coils for a midplane-on-axis field of about 0.32T.

Experiments were conducted in EBT-I FR and EBT-S FR; however, detailed plasma parameter measurements are available only in the higher density EBT-S FR. A plot of line integrated density $n_e l$ as a function of pressure using 50 kW ECH for EBT-I SR, EBT-S SR, and EBT-S FR is shown in Fig. 5a. The stored energy W_{perp} is shown in Fig. 5b for the same conditions. The signature[5] of the C, T, and M operating modes is clearly seen in FR albeit at higher pressure. The ring stored energy does not drop as fast in FR as in SR with increasing pressure. Figure, 6 shows a plot of ring stored energy, ring temperature, and density for 30 kW and 50 kW ECH in EBT-S FR versus pressure. Typical of EBT-I/S SR operation, in T-mode, the ring temperature is fairly constant and the ring density varies inversely with pressure.

Notably lacking in Fig. 5a is a plot of potential well depth[5] in T-mode. As shown in Fig. 7, a quasi-spatial scan of plasma potential obtained with a heavy ion beam probe using a Cs^{+1} primary beam shows a nearly flat profile near zero volts. A detailed look at the Cs^{++} and Cs^{+++} secondary signals indicate that there is little ring formation at the fundamental; most of the ring is formed at the second harmonic resonance as in SR operation. For details of the beam probe's sensitivity to hot electrons, see paper G 4. The low secondary ion

current or sum signal in the core region indicates a hollow density profile and/or extremely cold core electrons (T_e < 10eV). Conventional electron temperature diagnostics suggest a very cold core, and multichord microwave interferometry indicates a relatively flat density profile inside the ring.

In sharp contrast to the electrons, the ions appear to be heated above levels obtained in EBT-S SR. Shown in Fig. 8 are distribution functions for an EBT-S SR 100/0/0 at a presure of 5.5 x 10^{-6} torr and an EBT-S FR 0/50/0 at 7 x 10^{-6} torr. Despite the lower power and higher pressure, a significant ion tail population exists. In an attempt to heat the ions separately with fast wave ion cyclotron heating (ICH), majority heating of hydrogen and minority heating of hydrogen in a deuterium majority were tried at low power but with little success. Higher power and higher frequency experiments are planned in the near term.

B. SCRATCH

SCRATCH experiments were conducted in an attempt to independently heat the ring and core plasmas. In all experiments, ECH at 10.6 GHz was used to establish the rings using 0,10,20, and 30kW, and various levels of ECH at 28 GHz was used to heat the core using up to 110kW. The plots of line integrated density $n_e l$ and ring stored energy W_{perp} versus pressure shown in Fig. 9 show that conditions can be established where the standard hierarchy[5] of C-,T-, and M-modes characteristic of EBT's are found. Ring densities and temperatures remain fairly constant as a function of pressure at fixed power. At fixed pressure, ring densities (of order 10^{11} cm^{-3}) increase with power, whereas ring temperatures vary from about 100 keV with 10.6 GHz power alone to about 500 keV with 28 GHz power alone. The mechanism that determines the ring temperature with combinations of 10.6 and 28 GHz power is not understood. A plot of $n_e l$ versus 28 GHz power at

various levels of 10.6 GHz power, as shown in Fig. 10, shows $n_e l$ increasing with increasing 10.6 GHz power at constant 28 GHz power, but also shows $n_e l$ decreasing with 28 GHz power holding 10.6 GHz power constant. Shown for reference is an EBT-S SR. From Figs. 9 and 10, it is evident that there is no decoupling of ring and core heating. As in FR, the ions are heated above levels in EBT-S SR for comparable powers, as shown in Fig 11. In SCRATCH, it is those ions nearer to the bulk of the distribution that appear to be heated. Calibration problems with the charge exchange analyzer prevent ascribing an actual temperature, although the heating is clear.

SCRATCH differs sharply from FR in that definite potential structures exist. In Figure 12 are plotted two potential profiles, one showing a positive potential hill and the other, the traditional EBT potential well. The difference between the two is the amount of ring heating power at 10.6 GHz. This is the first experimental evidence showing a large positive potential in an EBT T-mode and may be evidence of new transport. The beam probe also supplies indirect evidence of a warmer electron component from the relative signal levels compared to FR. Conventional electron temperature diagnostics indicate temperatures of order 100 eV, consistent with the beam probe signal levels.

IV. Conclusions

It is significant that rings are formed and stabilize a core plasma yielding the familiar C-,T-, and M-modes for both FR and SCRATCH. It is also fairly clear that these heating geometries are not strong candidates to supplant the traditional SR operation. In FR, it appears that the larger line densities can be attributed to a larger line length. Second harmonic heating dominates ring formation in both SR and FR. FR may still provide an interesting vehicle for ICH studies with higher frequencies and higher powers. Both FR and SCRATCH provide interesting contrasts in ion heating that are not understood. SCRATCH may provide valuable insights in potential formation and its effect on transport.

REFERENCES

1. J. C. Glowienka, J. Vac. Sci. Technol.,813 1088(1981) and references contained therein.

2. This acronym was first suggested by L. Bighel.

3. D.B. Batchelor (Fusion Energy Division, ORNL, Oak Ridge, Tn.) Private communication, 1981.

4. M. Fujiwara et al., in Proceedings of the 8th International Conference on Plasma Physics and Controlled Fusion Research (IAEA, Brussels, 1980), Vol I,845.

5. As in reference 1, Fig 4a.

Table I

Shorthand	Name
0/0/X 3500	EBT SR
0/X/0 5000	EBT-I SR
X/0/0 7250	EBT-S SR
0/0/X 5000	EBT-I FR
0/X/0 7250	EBT-S FR
X/0/X 5000	SCRATCH

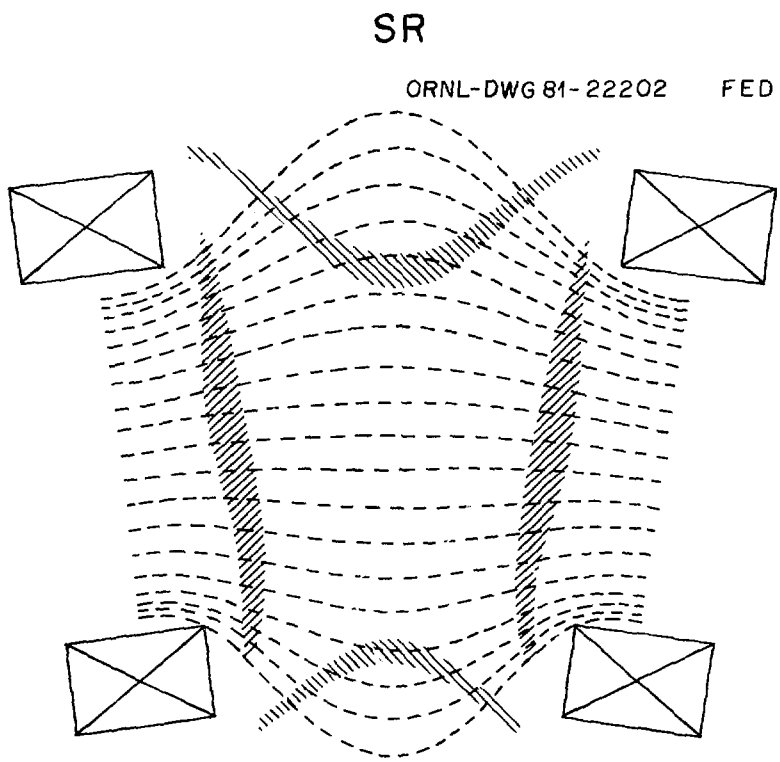

1. Typical resonance locations for Standard Resonance heating in EBT-I/S plotted in the equatorial plane.

FR

ORNL-DWG 81-22205 FED

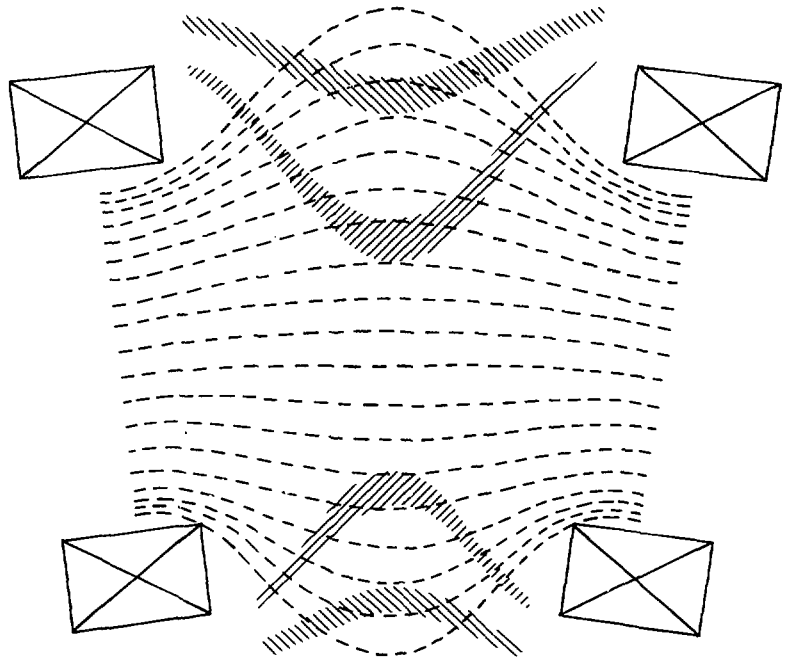

2. Resonance locations for Fundamental Resonance heating plotted in the equatorial plane.

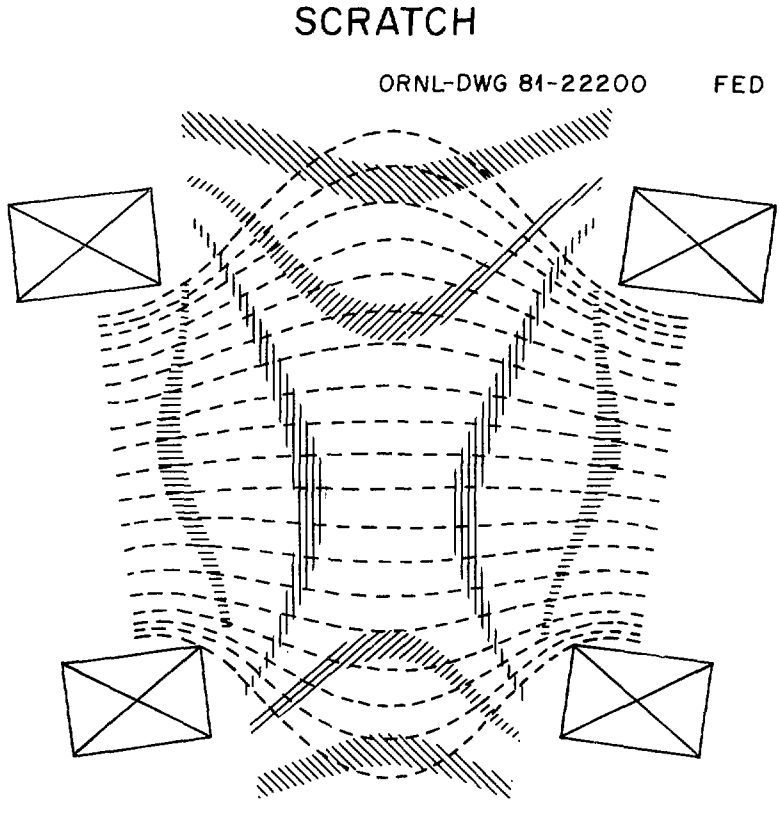

3. Resonance locations for SCRATCH plotted in the equatorial plane.

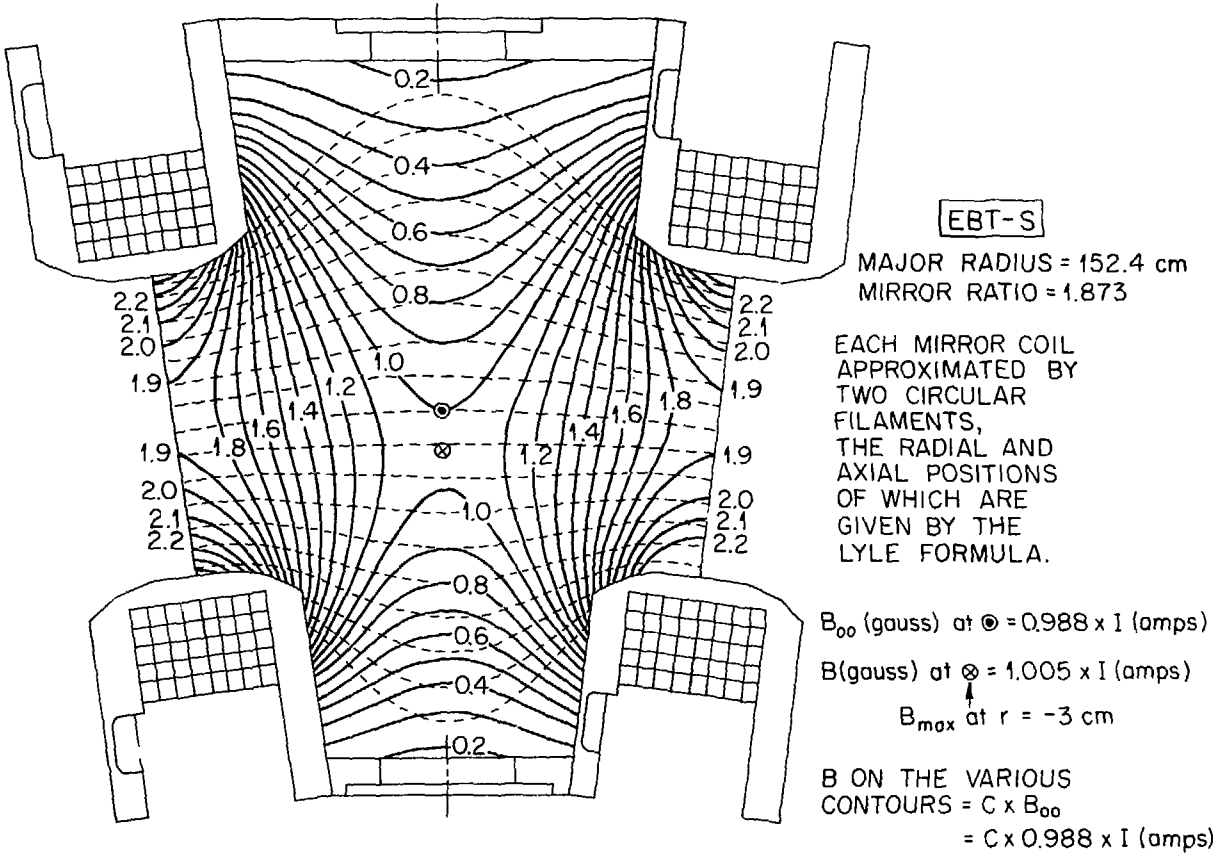

4. Generalized method for locating resonant mod-B contours in the equatorial plane for EBT-I/S.

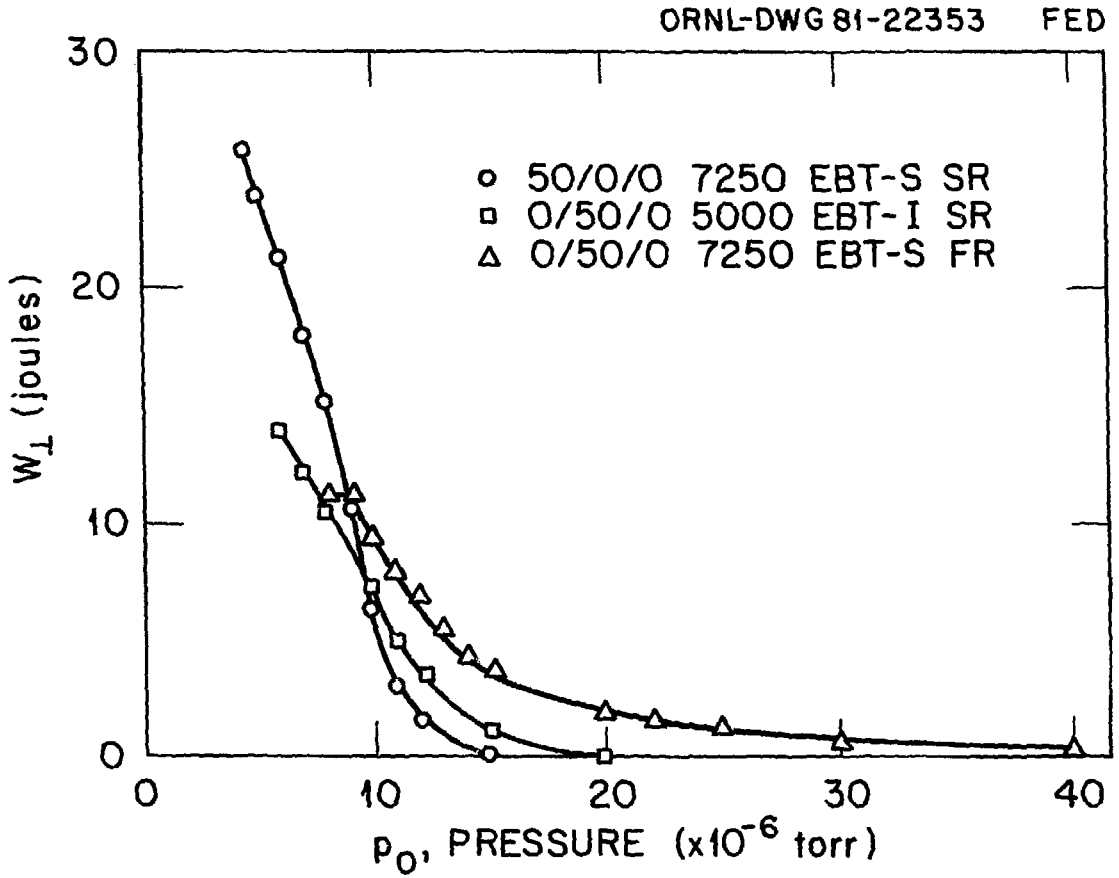

5. b. Average annulus stored energy per ring W_{perp} as a function of pressure using 50 kW ECH for EBT-I SR, EBT-S SR, and EBT-S FR.

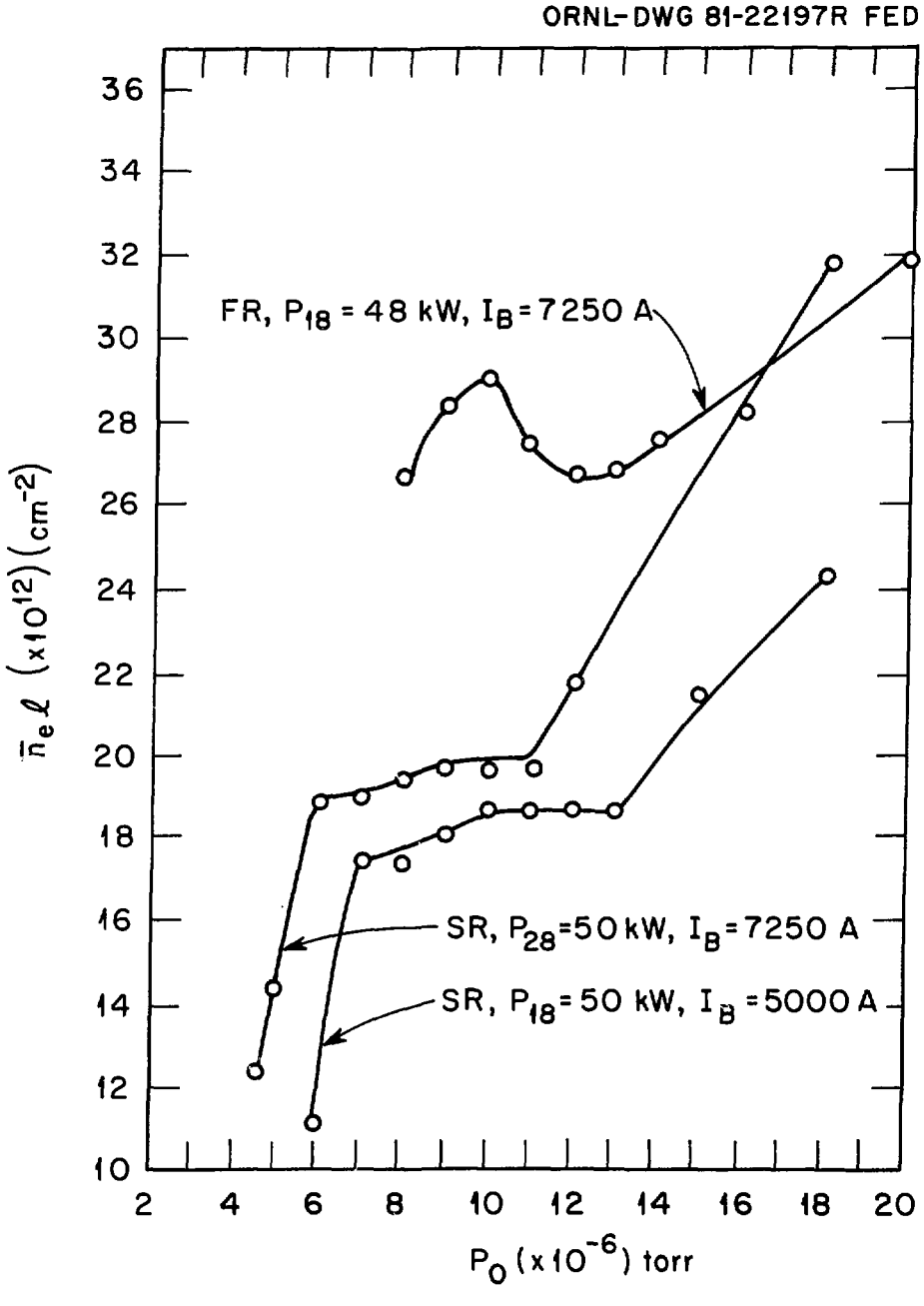

5. a. Line integrated density $n_e l$ as a function of pressure using 50 kW ECH for EBT-I SR, EBT-S SR, and EBT-S FR.

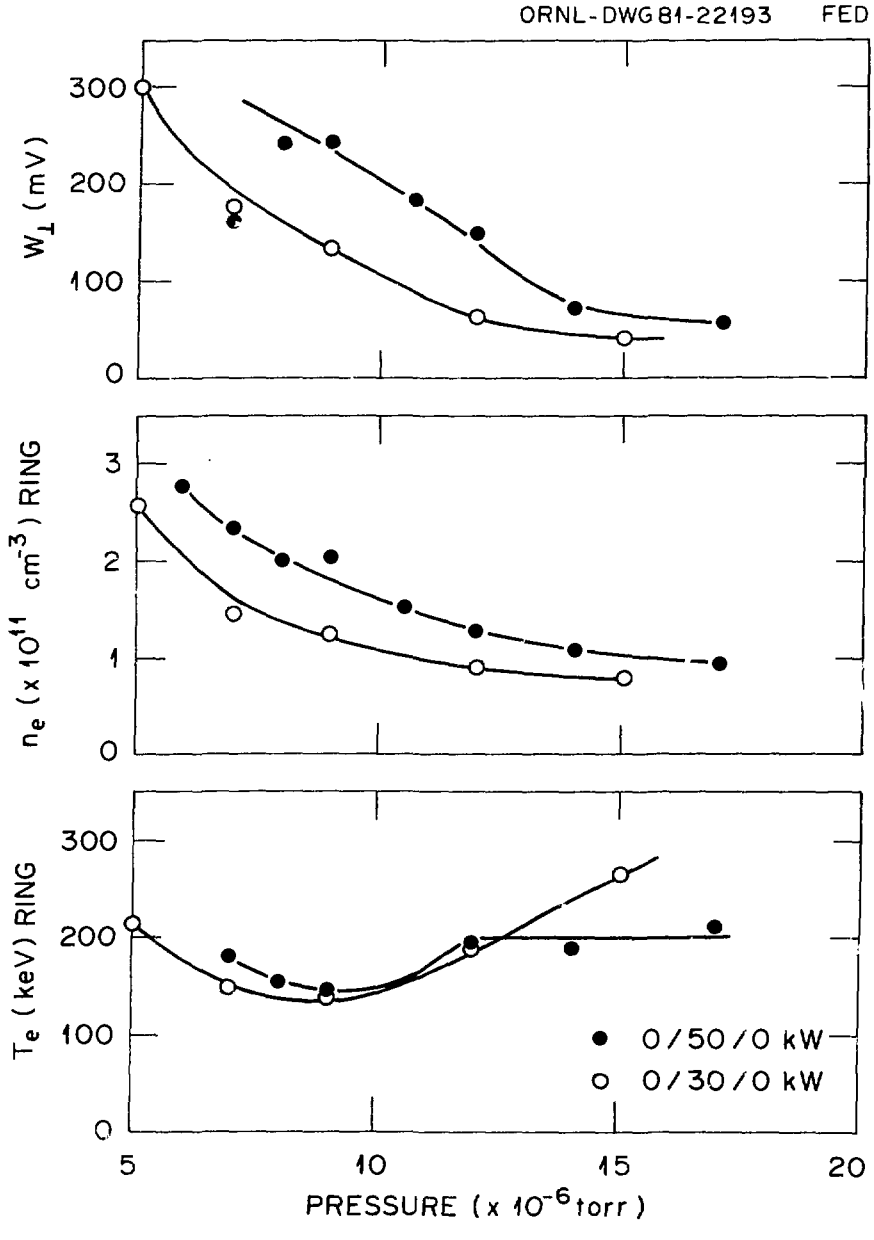

6. Ring stored energy, temperature, and density as a function of pressure for 30 kW and 50 kW in FR.

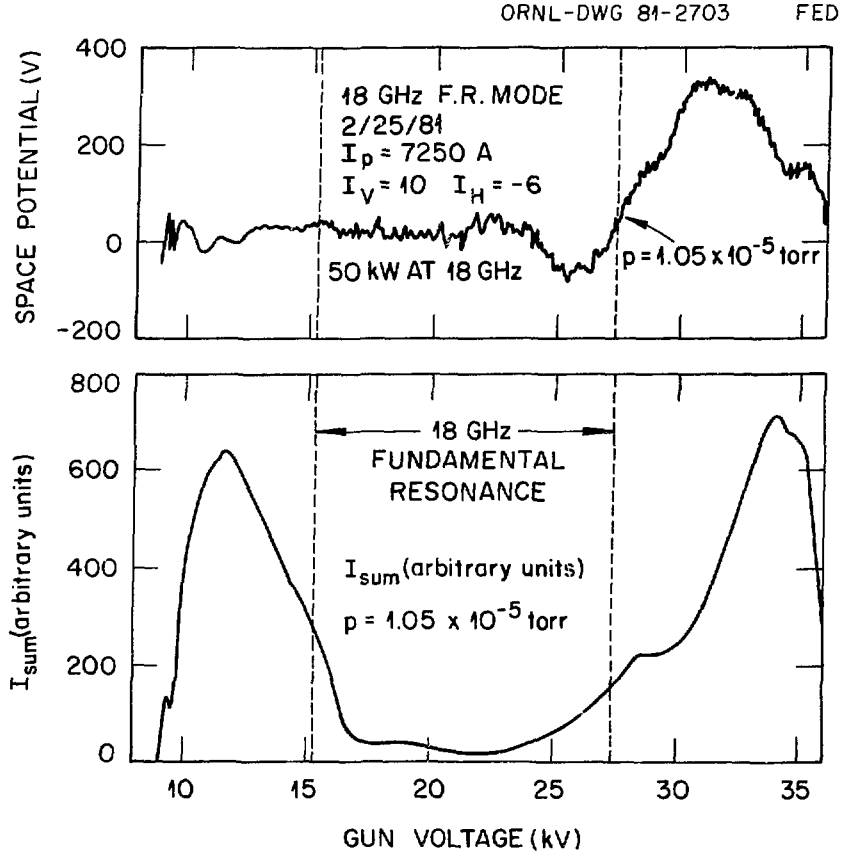

7. *Quasi spatial scan of plasma potential in FR. Structure found* between 25 and 35 cm is caused by small errors in the electronics and in the alignment.

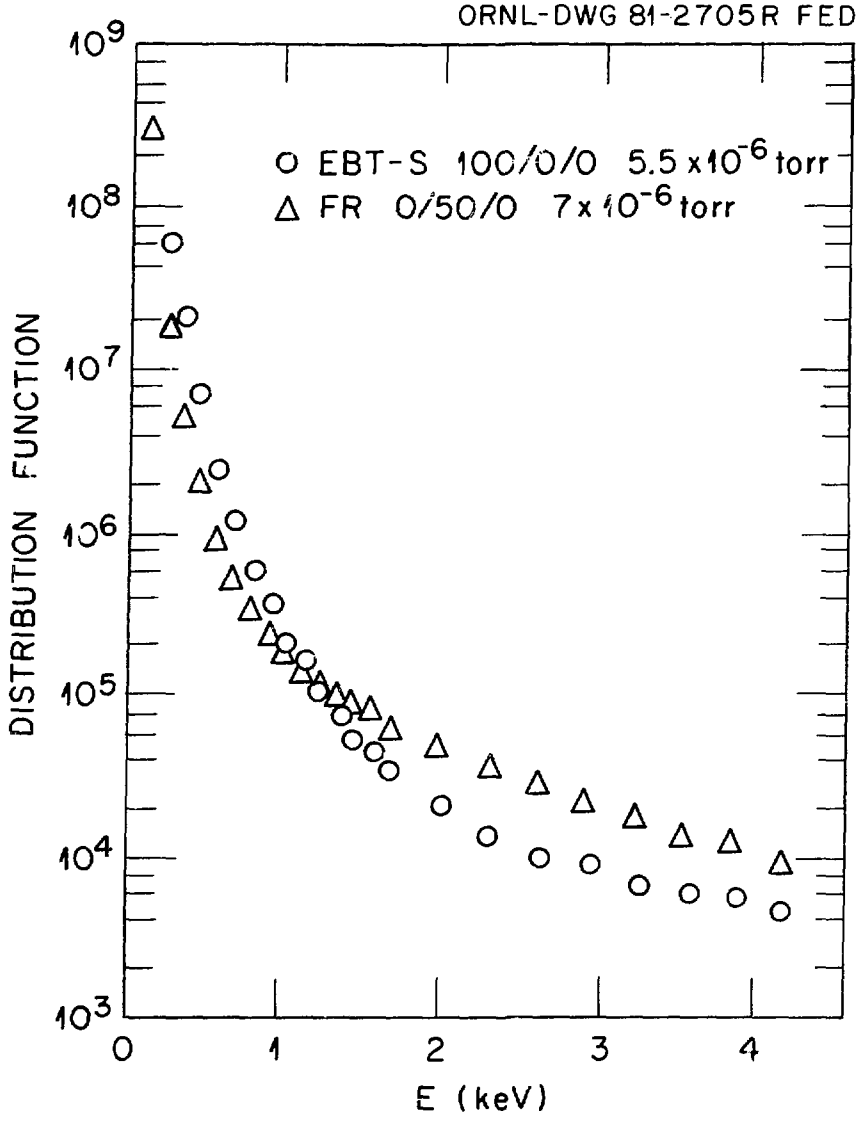

8. Comparison of ion energy distribution functions for EBT-S SR (100/0/0, 5.5 x 10^{-6} torr) and EBT-S FR (0/50/0, 7 x 10^{-6} torr).

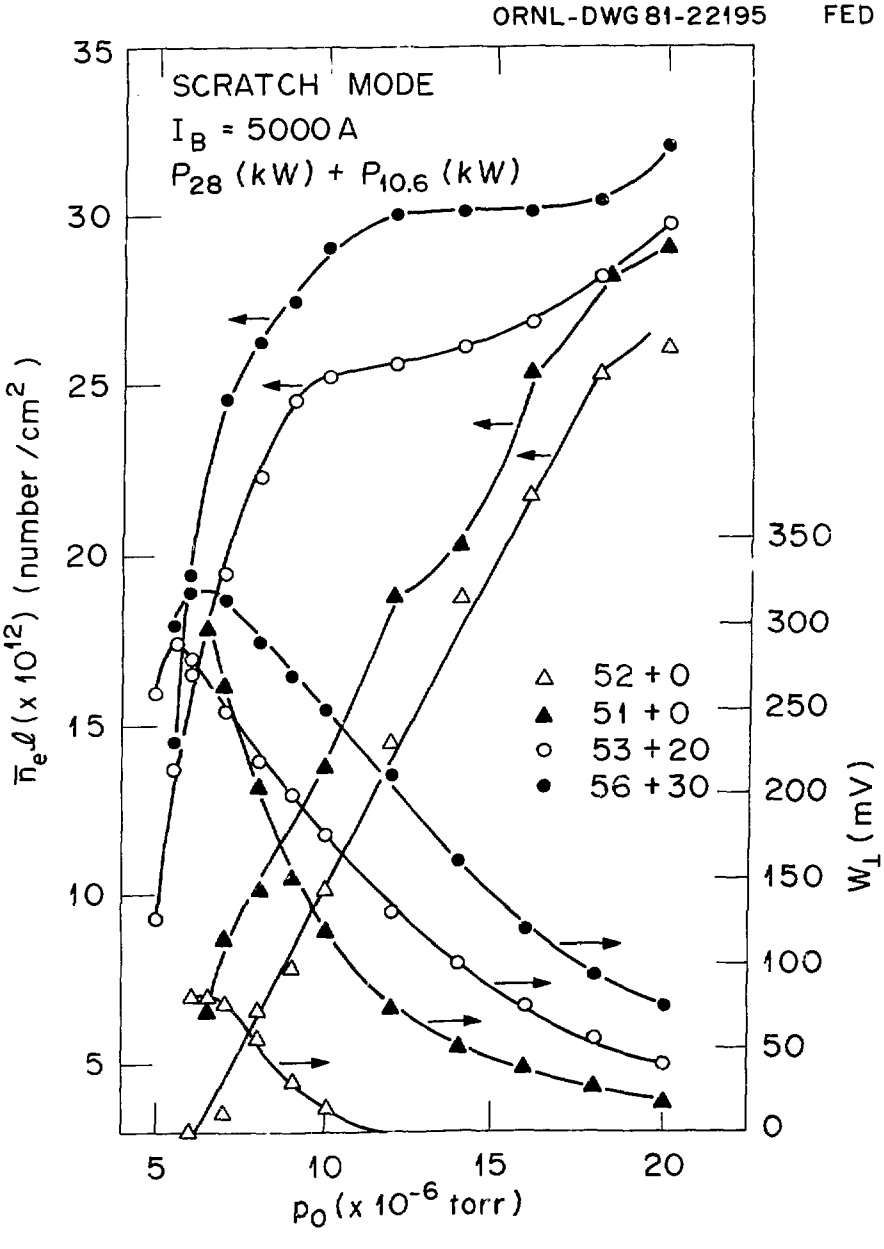

9. Line integrated density $n_e l$ and ring stored energy W_{perp} as a function of pressure and power mixtures in SCRATCH.

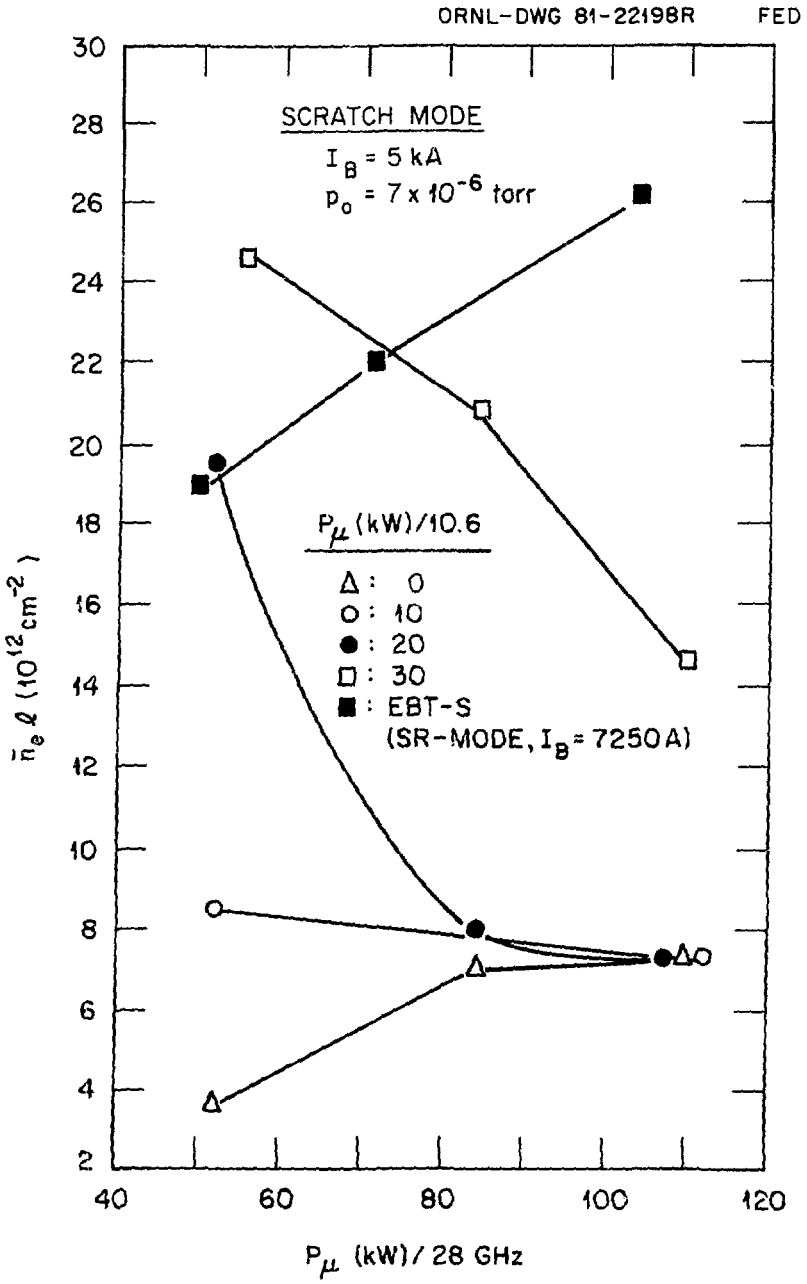

10. Line integrated density $n_e l$ as a function of 10.6 GHz and 28 GHz power in SCRATCH. Shown for reference (black squares) is an EBT-S SR.

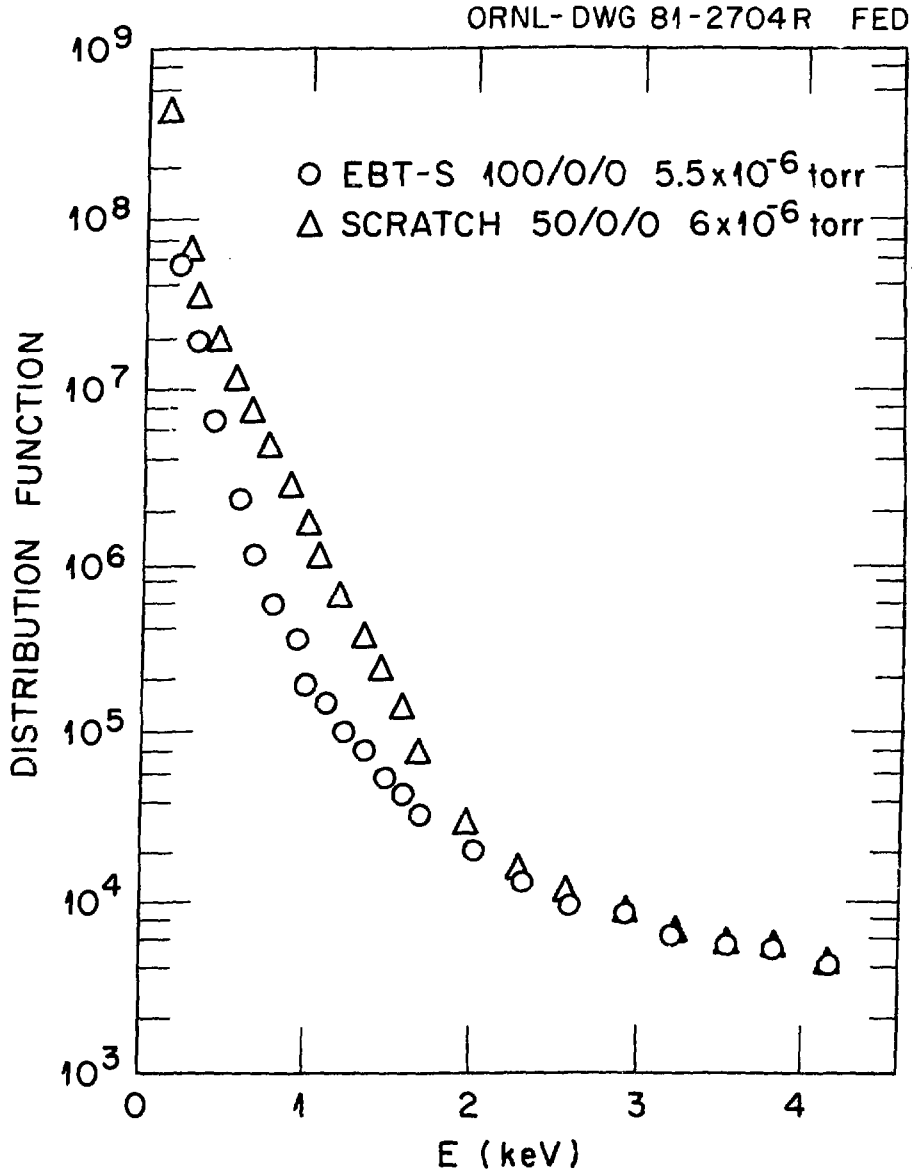

11. Comparison of ion energy distribution for EBT-S SR (100/0/0, 5.5×10^{-6} torr) and SCRATCH (50/0/0, 6×10^{-6} torr).

ORNL-DWG 81-2702R FED

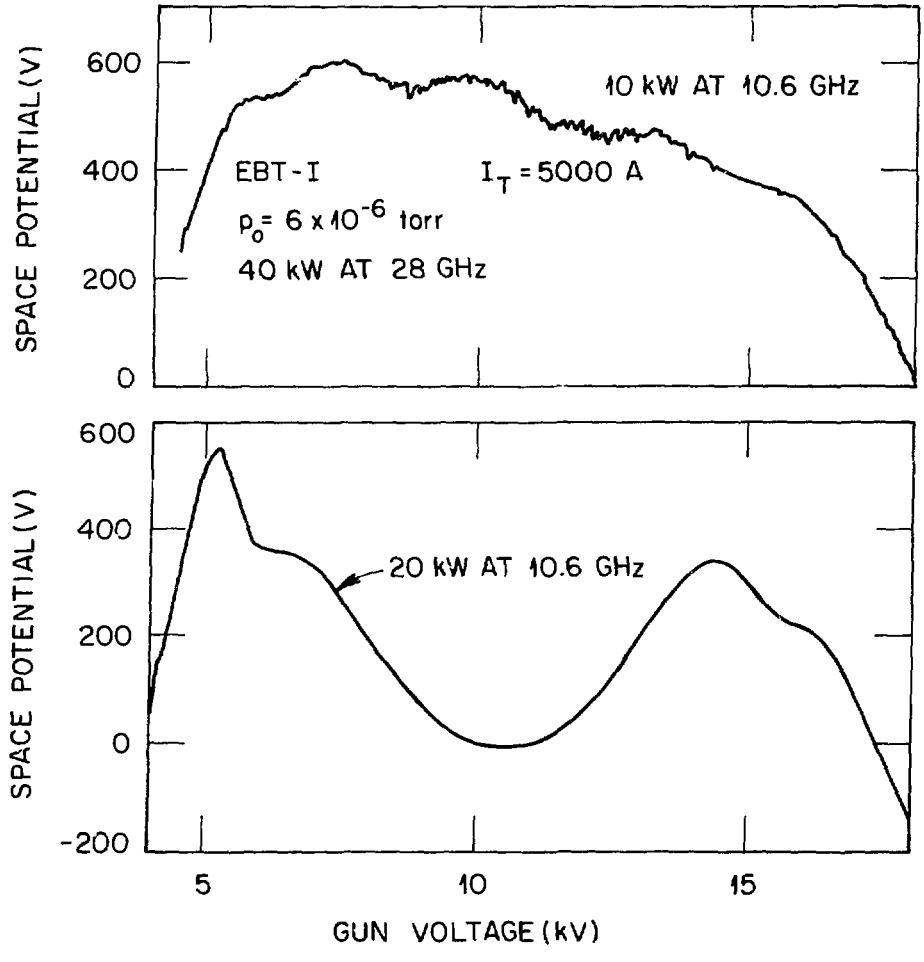

12. Comparison of two plasma potential profiles in SCRATCH: 50/0/10 and 50/0/20.

6. SYNCHROTRON EMISSION

SYNCHROTRON EMISSION MEASUREMENTS FROM THE HOT ELECTRON RINGS IN EBT*

J. Wilgen and T. Uckan

Oak Ridge National Laboratory
Oak Ridge, Tennessee 37830

ABSTRACT

Preliminary measurements of synchrotron emission from the hot electron rings of EBT have been carried out. The purpose of the experiments is to acquire information about the intensity of the radiation as a diagnostic for estimating ring parameters, such as ring density, temperature, and physical size. In the experiment, a conventional, fast-sweeping, superheterodyne receiver was used, and the measurements were performed in the frequency range of 80-110 GHz. In EBT, the hot electron rings are produced by ECH, and their location is at the second harmonic resonance. The microwave heating frequencies are 18 and 28 GHz, the typical hard x-ray ring temperatures are 150 and 500 keV, and the electron densities are 2×10^{11} and 3×10^{11} cm^{-3}, respectively, for EBT-I and EBT-S. Considering the relativistic effects, the estimated fundamental emission frequency is about 7 GHz for both EBT-I and EBT-S. The measured intensity levels and the shape of the spectrum are in good agreement with theoretical estimations which make use of the hard x-ray measurements for the ring parameters; for example, the intensity levels for EBT-S are about a factor of 5 higher than for EBT-I. It is also observed that the radiation

*Research sponsored by the Office of Fusion Energy, U.S. Department of Energy, under contract W-7405-eng-26, with the Union Carbide Corporation.

intensity increases, as expected, with decreasing filling pressure below the C-T transition. The radiation signal, I_ω, follows a trend similar to the $W_\perp$ measurements, which are indicative of the stored energy of the rings. The ring temperature and density behavior may be deduced from I_ω and $W_\perp$ correlation experiments, and the results show the same trend which is obtained from the hard x-ray measurements. The effect of polarization (extraordinary vs ordinary mode) on the measurements is also studied.

1. INTRODUCTION

Exploratory measurements have been carried out using a partially calibrated system which does not use a viewing dump.[1] Since absolute measurements of the synchrotron radiation spectrum are not appropriate with this system, the emphasis has been on relative measurements. Calibration information is not required, for example, to examine changes in the intensity and the slope of the spectrum for EBT-S relative to EBT-I, where EBT-S denotes EBT operation with an ECH frequency of 28 GHz and EBT-I designates 18 GHz heating. It is also of interest to find out how the synchrotron spectrum varies with EBT operating parameters, such as power level and neutral gas pressure, and to examine whether the synchrotron scaling is consistent with other ring diagnostics. It is found that correlations between the synchrotron and diamagnetic diagnostics are particularly interesting, and that the combination of the two diagnostics can potentially provide useful information about changing ring parameters such as temperature and density.

2. MICROWAVE SYSTEM

A block diagram of the heterodyne microwave receiver is shown in Fig. 1. The frequency range is 80-110 GHz, which corresponds to harmonics 9-12 of the nonrelativistic electron cyclotron frequency for EBT-I and harmonics 6-8 for EBT-S. A well-calibrated spectrum analyzer is utilized as a calibrated logarithmic IF detector. By using known and estimated characteristics of various components (the measured gain of the IF preamplifier, the conversion loss of the broadband mixer, and estimated losses for the waveguide components and transmission line),

signal levels in the waveguide at various locations can be inferred. In this way, the synchrotron intensity at the microwave antenna, or equivalently the antenna temperature, can be estimated within a factor of 2.

3. RELATIVE MEASUREMENTS

A relative comparison of the synchrotron spectra for EBT-I and EBT-S is shown in Fig. 2, where the synchrotron intensity over the frequency range of 80-110 GHz is displayed on a logarithmic scale. The intensity measured for EBT-S exceeds that of EBT-I by 7-10 db; this is not unexpected. If the ring parameters, temperature and density, as measured by the hard x-ray diagnostic are used as input, theoretical calculations predict an eight-fold increase in intensity for EBT-S relative to EBT-I.[2] This is to be compared with the experimentally measured ratio of 5-10, depending on the exact operating conditions.

The same calculations also predict that the slope of the spectrum should change, becoming flatter for EBT-S. Unfortunately, it is not very easy to observe small changes in slope when the data is displayed on a logarithmic scale. In order to facilitate such measurements, the logarithmic detector was replaced with a square-law IF power detector. A detailed comparison of the spectra recorded for EBT-I and EBT-S with such a system shows that the ratio of intensities does, in fact, increase with frequency, as shown in Fig. 3, indicating a change in the slope of the synchrotron spectrum. The data shows that the ratio of the intensity measured for EBT-S to that measured for EBT-I is 25% greater at 110 GHz than it is at 80 GHz, in agreement with theory.[2]

Therefore, relative measurements of the type which do not require any calibration information show changes in the intensity and slope of the synchrotron spectrum which are consistent with theoretical calculations.

In addition, the polarization of the synchrotron radiation was checked. With the millimeter-wave antenna oriented to receive the extraordinary mode polarization ($E \perp B$), the intensity is approximately twice the intensity observed with the antenna oriented to receive the ordinary mode ($E \parallel B$), a polarization ratio of 2:1. Theory, in contrast, predicts that the synchrotron radiation should be strongly polarized, with typical polarization ratios of 10:1 and 6:1 for EBT-I and EBT-S, respectively. The weak polarization observed experimentally is probably a consequence of the high reflectivity of the EBT vacuum vessel walls.

4. ABSOLUTE COMPARISONS WITH THEORY

Because of wall reflections and uncertainties in the calibration of the microwave system, precise comparisons of the measured intensity with theoretical calculation are precluded. Nevertheless, meaningful statements can still be made.

The data of Fig. 2 show a gradual falloff in intensity from 80 to 110 GHZ, along with considerable variation in the measured intensity across the frequency spectrum. The variations are instrumental in origin and due to the frequency response of the microwave system. This is demonstrated by the fact that they are identical for both EBT-I and EBT-S, even though the cyclotron frequency has changed substantially. Ignoring these variations, the intensity, as measured in the waveguide,

appears to fall off by roughly a factor of 2 over the frequency range covered by the measurements. Taking into account the frequency dependence of the effective receiving area of the microwave horn antenna ($A \propto f^{-2}$), the measurements are then consistent with a free space synchrotron spectrum which is flat, independent of frequency. This result is in good agreement with calculated spectral shapes for the synchrotron emission, particularly for EBT-S.[2]

Absolute comparisons of the measured synchrotron intensity with theory is limited not by uncertainties in the calibration of the microwave system but instead by wall reflection effects. The EBT device has been designed to effectively contain microwave energy at the principle heating frequencies (10.6, 18, and 28 GHz). As a consequence, it is not too surprising that synchrotron radiation in the 80-110 GHz region is also well confined.

The major consequence of the reflective walls is a buildup of the synchrotron radiation intensity until a power balance is achieved. At each frequency, loss of synchrotron radiation by dissipation in the walls, reabsorption by the plasma, or escape through holes in the wall, is balanced by the rate at which radiation is emitted by the electron rings. In fact, much of the synchrotron radiation escapes through holes in the wall of one sort or another. For example, every cavity has apertures via which the heating frequencies are coupled into the cavity. In addition, many diagnostics utilize large area microwave screens which very effectively reflect the heating frequencies but are essentially transparent for synchrotron radiation at higher frequencies. Because many of the EBT cavities have no diagnostic

losses, whereas others have large microwave screens, it is very likely that the equilibrium synchrotron intensity is not uniform around the torus, but rather builds up to different levels at various toroidal locations.

The experimental configuration consists of a millimeter-wave antenna viewing an optically thin electron ring which is surrounded by a reflective wall. For the case of no wall reflection, the millimeter-wave radiometer should measure an antenna temperature, T_A, given by $T_A = \varepsilon T_R$, where ε is the emissivity of the electron ring and T_R is the ring temperature, for a Maxwellian energy distribution. The ring emissivity is highly anisotropic with most of the radiation concentrated in the direction perpendicular to the magnetic field. When wall reflections are added, the synchrotron intensity is enhanced and isotropized and can be approximated by the expression

$$T_A = \frac{\langle\varepsilon\rangle T_R}{(1 - R)}, \tag{1}$$

where R is the effective reflection coefficient of the walls including the effects of holes, and $\langle\varepsilon\rangle$ is the directionally averaged ring emissivity. The expression $1 - R$ is the fraction of the synchrotron radiation which is lost per transit of the EBT cavity. To compare the measured synchrotron intensity (antenna temperature) with theory, it is necessary to know both $\langle\varepsilon\rangle$ and R, in addition to the calibration of the millimeter-wave radiometer.

The emissivity of the electron ring is inferred from calculations of synchrotron radiation. Basically, the emissivity is given by $\varepsilon = I_R/I_{BB}$, where I_R is the calculated intensity of the synchrotron radiation emitted by the ring and I_{BB} is the blackbody radiation intensity corresponding to the ring temperature. In the direction perpendicular to the magnetic field, synchrotron calculations for typical high β electron rings in EBT-S indicate that $\varepsilon_\perp \simeq 10^{-3}$ at 100 GHz. The directionally averaged emissivity, $\langle\varepsilon\rangle$, is considerably smaller, by perhaps a factor of 4.

The effective reflection coefficient of the walls is not well known. The coupling apertures of the power feeds are relatively small, 25 cm^2, and represent a loss which is comparable to absorption by the cavity walls. The combination of these two losses leads to a reflection coefficient of $R \geq 99$ %. Additional losses resulting from diagnostics apertures and reabsorption by the electron rings are also significant, but smaller.

Using an effective reflection coefficient of $R = 99\%$ for the region of the torus where the measurements are made and an averaged ring emissivity of 2.5×10^{-4}, Eq. (1) predicts an antenna temperature of 10 keV for EBT-S. Experimentally, antenna temperatures in the range of 5-20 keV, depending on operating conditions, are measured with the radiometer. Therefore, within the large uncertainties of the present measurements, due mostly to wall reflections, the measured synchrotron intensities are consistent with those which are calculated.

5. SCALING WITH EBT PARAMETERS – CORRELATIONS WITH OTHER RING DIAGNOSTICS

Further measurements featuring comparisons with other ring diagnostics were carried out with two objectives in mind: to find out how the synchrotron intensity scales with EBT operating parameters and to determine whether the synchrotron intensity is generally consistent with other ring measurements. As is well known, the stored energy of the electron rings increases with applied power and decreases with neutral gas pressure; therefore, it is anticipated that the synchrotron intensity will follow a similar trend. And since these observations require only relative measurements, an uncalibrated system can be utilized very effectively, calibration information being irrelevant.

Scaling information as the heating power level is varied for EBT-I is shown in Fig. 4. The synchrotron intensity, I_ω, is plotted versus the diamagnetic measurement of stored ring energy, $W_\perp$, for various levels of 18 GHz power, ranging from 15 to 46 kW. It is apparent from this data that both $W_\perp$ and I_ω increase almost linearly with the heating power and that the correlation between the two measurements is very good. For EBT-S, heating at 28 GHz, the situation is very similar for power levels up to about 60 kW. At higher power, the synchrotron intensity falls below the level projected by the linear dependence at low power, in spite of the fact that $W_\perp$ continues to increase with power in essentially a linear fashion.

Similar scaling information has also been obtained as the ambient neutral gas pressure is varied. In this case, both the stored energy and the synchrotron intensity increase as the neutral gas pressure is lowered. Data for EBT-I with 40 kW of heating power at 18 GHz are shown in Fig. 5. Here I_ω, the X-mode polarization of the synchrotron intensity at 80 GHz, is plotted versus $W_\perp$ as the neutral gas pressure is scanned over the range of 4.6-20 × 10^{-6} torr. The ratio is not constant, which suggests that ring parameters are changing. Similar data for EBT-S with 100 kW of power at 28 GHz are shown in Fig. 6. However, in this case the correlation is quite different. These observations appear to be explainable on the basis of fairly elementary considerations.

Although the two measurements involve quite different phenomena, both have very similar dependences on ring parameters. The diamagnetic measurement of the stored energy of the electron ring is proportional to the product of the total number of electrons in the ring, N_{TOT}, times the average energy per electron. For a Maxwellian distribution,

$$W_\perp \propto N_{TOT} T_R \quad , \tag{2}$$

where T_R is the ring temperature. The synchrotron intensity is also proportional to the total number of electrons in the ring but has a much more complicated dependence on the ring temperature,

$$I_\omega \propto N_{TOT} F(T_R)(1 - \beta), \tag{3}$$

where F is the functional temperature dependence. There is a finite β correction whereby the synchrotron intensity decreases as the magnetic well created by the ring gets deeper.

In addition, both measurements tend to average over several electron rings. The diamagnetic loops are sensitive to the presence of rings in adjacent cavities to the extent that roughly 35% of the signal is attributable to the neighboring rings. Because of wall reflection, and the resulting toroidal transport of the radiation, the measured synchrotron intensity is also a weighted average over several rings with less than 50% of the radiation originating in the cavity of observation.

So, although there are many similarities between the synchrotron and $W_\perp$ measurements, there are very few differences which can be called upon to explain the lack of correlation which is observed during the pressure scans. The two diagnostics differ principally in the dependence on ring temperature, with a weaker finite β dependence for the synchrotron emission.

Taking the ratio of Eqs. (2) and (3), we find that

$$\frac{I_\omega}{W_\perp} = \frac{(1-\beta)F(T_R)}{T_R} \quad . \tag{4}$$

The function $F(T_R)$ has been examined through numerical calculation of synchrotron intensity as a function of ring temperature, assuming a Maxwellian energy distribution. It is found that the temperature dependence can be approximated by $F(T_R) \propto T^\alpha$, with $\alpha \simeq 2$ for the

temperature range $150 < T_R$ (keV) < 250 which is appropriate for EBT-I operation.[3] Taking $F(T_R) \propto T^{\alpha}$, and solving equation (4) for T_R, it is found that

$$T_R \propto \left[\frac{I_\omega}{W_\perp(1-\beta)}\right]^{\frac{1}{\alpha-1}} . \tag{5}$$

Similarly, solving Eqs. (2) and (3) for N_{TOT}, it is found that

$$N_{TOT} \propto \left[\frac{W_\perp^{\alpha}(1-\beta)}{I_\omega}\right]^{\frac{1}{\alpha-1}} \propto \frac{W_\perp}{T_R} . \tag{6}$$

It appears plausible that from the ratio of the two measurements, I_ω and $W_\perp$, ring temperature and density variations can be inferred. The EBT-I data from Fig. 5 has been analyzed using Eqs. (5) and (6), taking $\alpha = 2$, and the results are shown in Fig. 7. Hard x-ray measurements of ring temperature and density are also shown for comparison. Variations in the ring temperature and density which are inferred from the I_ω and $W_\perp$ measurements follow the same trend shown by the hard x-ray diagnostic, at least over the pressure range of 6-11 $\times$ 10^{-6} torr where hard x-ray data are available. On the basis of these results it is concluded that the synchrotron measurements are consistent with the results of other ring diagnostics.

6. SUMMARY

Relative measurements of the synchrotron radiation spectrum have proven to be very informative. Comparisons of synchrotron emission from EBT-S and EBT-I have demonstrated that the intensity changes by a factor of 5-10, in agreement with theoretical predictions, and that the slope of the spectrum changes, as expected. It is found that the synchrotron intensity increases with heating power and decreases with neutral gas pressure, demonstrating essentially the same behavior as the $W_\perp$ diagnostic. Throughout the parameter scans, the synchrotron measurements seem to be consistent with other ring diagnostics.

These observations support the view that the synchrotron radiation from the energetic electron rings is classical, at least to the extent that it scales as expected from the classical theory. Because of wall reflections, quantitative comparison of theory and experiment is quite difficult. What is required, if this comparison is to be successful, is the ability to separate out and measure only the direct radiation from the electron ring, as opposed to the indirect radiation which has been multiply reflected, enhanced, depolarized, and isotropized by the walls of the EBT cavity. Basically, the measurement requires the use of a viewing dump. Such a synchrotron diagnostic system, enabling greatly improved measurements, is under development by the University of Maryland[4] and will be operational shortly. Within the uncertainties of the present measurements, a factor of 4x, the synchrotron radiation nevertheless appears to be classical and therefore is a promising candidate for diagnostic measurements of the various parameters of the energetic electron rings in EBT.

6. REFERENCES

1. T. Uckan, J. Wilgen, and L. Bighel, Bull. Am. Phys. Soc. 25, 832 (1980).

2. N. A. Uckan, R. G. Spencer, and T. Uckan, Oak Ridge National Laboratory Report #ORNL/TM-7687.

3. T. Uckan and N. Uckan, "Synchrotron Emission from the Ring Electrons in EBT" in these proceedings.

4. Z. S. Wang, G. D. Tsakiris, and D. A. Boyd, Bull. Am. Phys. Soc. 26, 996 (1981).

ORNL–DWG 81-2249R FED

FAST-SWEEPING SUPERHETERODYNE RECEIVER (80-110 GHz)

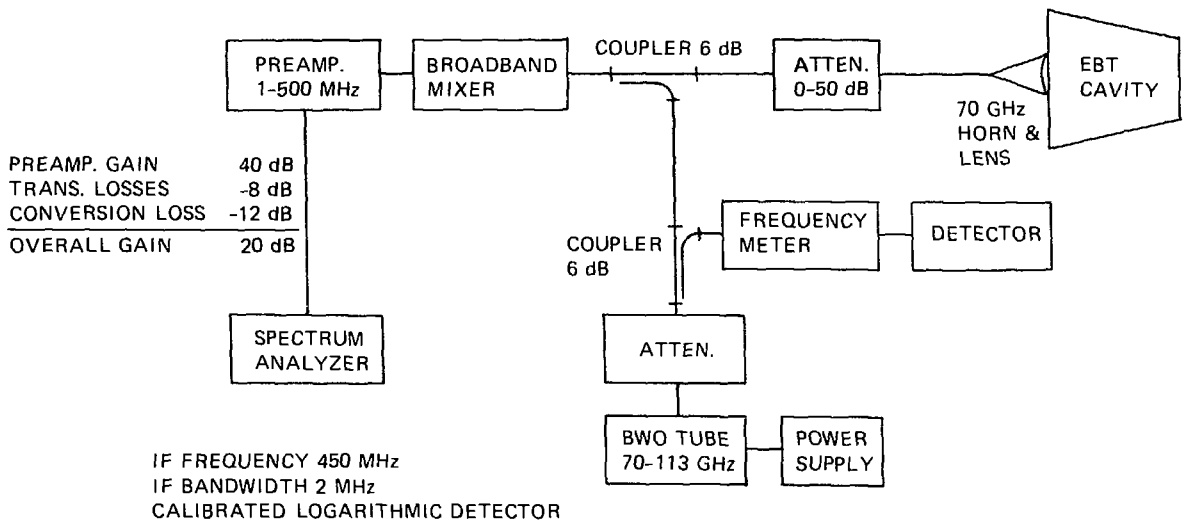

Fig. 1. Block diagram of the millimeter wave radiometer.

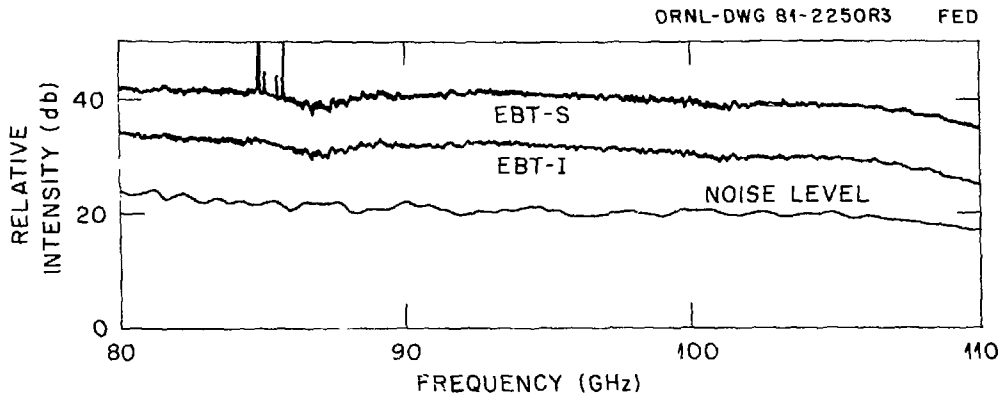

$$\frac{I_\omega^x\,(\text{EBT-S})}{I_\omega^x\,(\text{EBT-I})} \simeq \begin{cases} 8\ (\text{theory}) \\ 5\text{-}10\ (\text{experiment}) \end{cases}$$

POWER 42 kW
PRESSURE 6×10^{-6} torr

Fig. 2. A comparison of the synchrotron emission spectra measured for EBT-I with that measured for EBT-S.

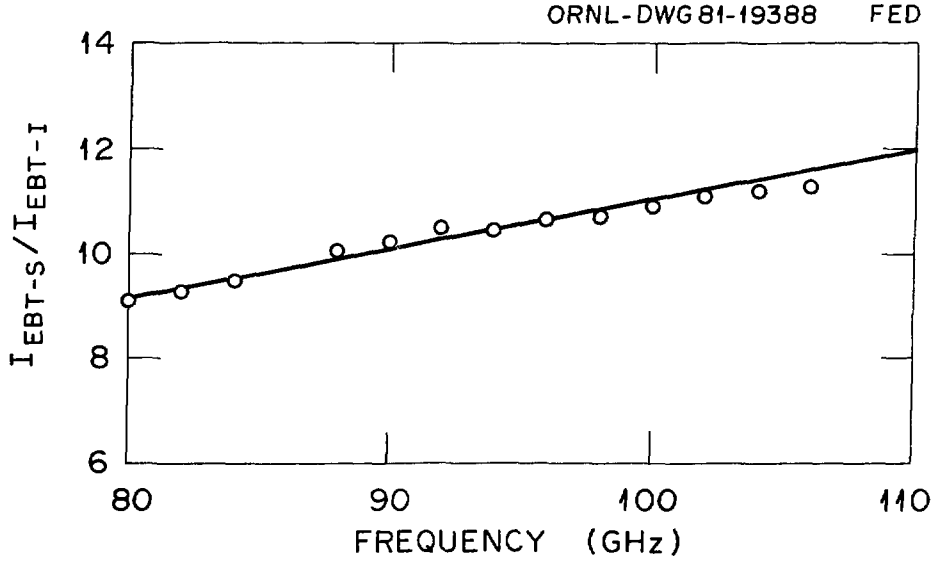

Fig. 3. The ratio of the synchrotron intensity measured for EBT-S to that measured for EBT-I as a function of frequency. The data demonstrates that the slope of the spectrum does, in fact, undergo a change and that the ratio of intensities is 25% greater at 110 GHz than it is at 80 GHz.

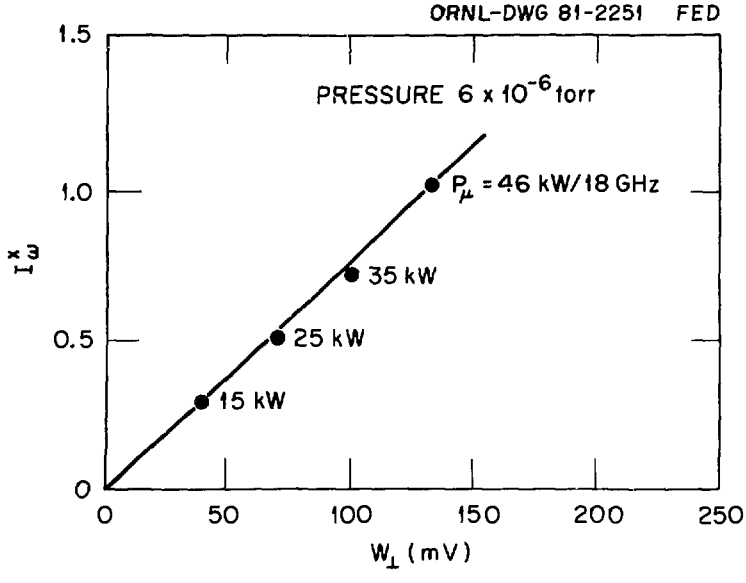

Fig. 4. The synchrotron intensity is plotted vs the stored energy of the electron ring for various levels of heating power in EBT-I. The data demonstrates a strong correlation between the synchrotron and diamagnetic diagnostics.

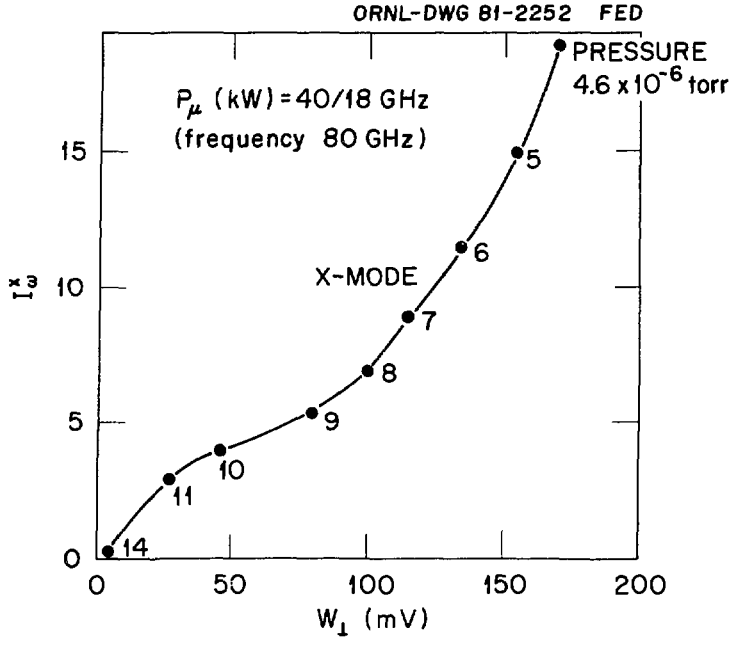

Fig. 5. The synchrotron intensity is plotted vs $W_\perp$ as the neutral gas pressure is varied for EBT-I operated at 40 kW. The ratio of the two measurements is not constant which suggests that the ring parameters are changing.

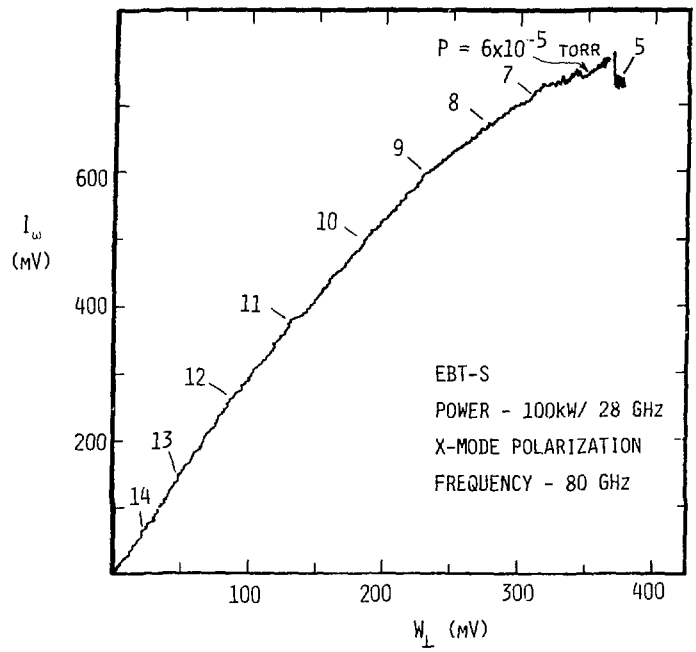

Fig. 6. The synchrotron intensity is plotted vs $W_\perp$ as the neutral gas pressure is varied for EBT-S operated at 100 kW of 28 GHz. The correlation between the two measurements is much stronger for EBT-S, but again the ratio of $I_\omega/W_\perp$ changes significantly in the low pressure range.

ORNL-DWG 81-23429R FED

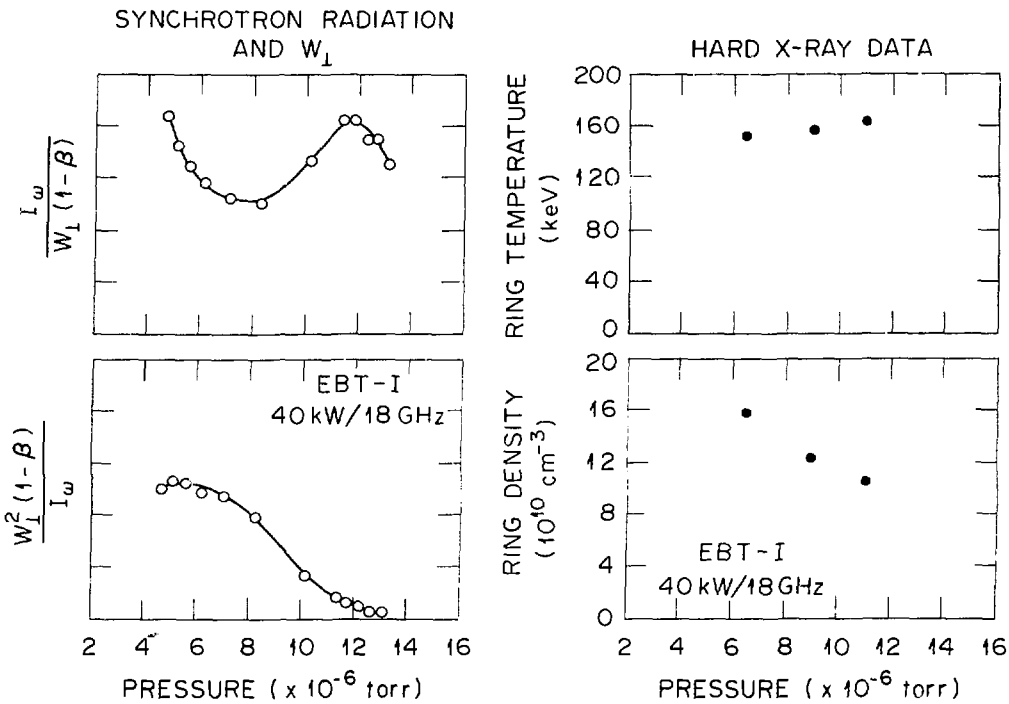

Fig. 7. (a) Variations in the ring temperature [$I_\omega/W_\perp$ (1-β)] and density [$W_\perp^2$(1-β)/I_ω] inferred from the synchrotron intensity (I_ω) and diamagnetic ($W_\perp$) measurements as a function of pressure in EBT-I. (b) Hard x-ray measurements of ring temperature and density are shown for comparison. (Hard x-ray data courtesy of D. L. Hillis and G. R. Haste)

SYNCHROTRON EMISSION FROM THE RING ELECTRONS IN EBT*

T. Uckan and N. A. Uckan
Oak Ridge National Laboratory
Oak Ridge, Tennessee 37830

ABSTRACT

The energy spectrum of the synchrotron radiation emitted by the relativistic ring electrons in ELMO Bumpy Torus (EBT) has been calculated for various classes of isotropic and anisotropic ring electron distribution functions. Calculations have been carried out for present (EBT-I/S) and planned (EBT-P) experiments. The ring temperatures in EBT-I and EBT-S are ~200 and ~500 keV, respectively. The projected ring temperature in EBT-P is ~1000-1500 keV. The calculations indicate that the radiation is predominantly in higher harmonics ($\ell \geq \gamma^2/2$) and the radiation spectrum monotonically decreases and becomes almost flat at high frequencies, as observed in the experiments. With increasing temperature and anisotropy, the total emission increases, the slope of the spectrum decreases, and the peak of the spectrum moves to higher frequency. The ratio of the extraordinary wave intensity to ordinary wave intensity decreases with temperature but increases with anisotropy. Calculated spectra and relative intensity levels of EBT-I and EBT-S are found to be in reasonable agreement with the experimental measurements. Both measurements and calculations show that synchrotron losses are low in EBT-I and EBT-S. However, in future experiments (EBT-P, reactor, etc.), radiation losses will play an important role in determining the ring power balance. Correlations of calculated intensity variations with temperature, density, beta, anisotropy, etc., are given that can be used as a useful tool for comparison of theory and experiment, as well as in the determination of ring properties and scaling of the radiation with ring parameters.

---

*Research sponsored by the Office of Fusion Energy, U.S. Department of Energy, under contract W-7405-eng-26 with the Union Carbide Corporation.

I. INTRODUCTION

The key element of the ELMO Bumpy Torus (EBT) concept[1] is the high-beta, hot electron rings[2] formed in each sector of the torus as a natural consequence of the electron cyclotron heating (ECH). The local magnetic wells produced by these hot electron rings stabilize the toroidally confined plasma,[3] as demonstrated in EBT experiments[2,4] (EBT-I/S) and the Nagoya Bumpy Torus (NBT).[4,5] In addition to other experimentally observed features of the rings (i.e., diamagnetic effects, electrostatic potential, bremsstrahlung distribution, etc.),[4] measurements of the synchrotron emission spectrum emitted by the relativistic hot electrons can be utilized as a useful diagnostic method in determining the ring properties (i.e., distribution function, density, temperature, etc.) and their scaling with operating conditions in different devices. Initial measurements of synchrotron emission in EBT have been carried out using a fast-sweeping superheterodyne receiver in the frequency range 80-110 GHz.[6] Similar measurements have also been made on NBT using a radiometer at frequencies of ~10 and ~35 GHz.[7] In the near future, the University of Maryland will perform experiments on EBT-S at two fixed frequencies (80 and 140 GHz) using two superheterodyne receivers.[8]

In order to make use of the synchrotron emission measurements as a diagnostic tool, theoretical models[9,10] are being developed to analyze the experimental results. In this paper the emission spectra for various classes of isotropic and anisotropic distribution functions are obtained for the parameter range of interest for the EBT ring plasma. In the calculations the plasma dispersion effects ($\omega_p^2 \ll \omega_c^2 < \omega^2$, where ω_p and ω_c are the characteristic ring electron plasma frequency and cyclotron frequency, respectively) and absorption are neglected. Because of the relativistic temperatures ($T \sim 0.2$-2 MeV) of the ring electrons, the emission is in higher harmonics ($\omega = \ell\omega_c$, with $\ell \gg 1$), and the inequality $\omega_p^2 \ll \omega^2$ is satisfied for all but possibly the lowest harmonics. The angular distribution of emission for these relativistic electrons peaks in a direction perpendicular to the magnetic field B (i.e., near $\theta \simeq \pi/2$, where θ is the observation angle

measured from the magnetic axis). Also, the observation angle in the experiments[6] is $\theta = \pi/2$. Therefore, the interest in this paper is restricted primarily to $\theta = \pi/2$, and the expressions developed herein are valid for the purpose of making comparisons of experimental results with the theoretical spectrum. As will be discussed, a deviation from the perpendicular direction ($\theta \neq \pi/2$) could, however, provide additional information on the ring properties (such as anisotropy, etc.).

Spatial profiles of ring electron density and temperature (determined from fits to the experimental data) and a consistent profile for the magnetic field (deduced from the pressure balance) are included in the analysis. The emission spectrum and its dependence on ring parameters and distribution functions are calculated for present (EBT-I/S) and planned (EBT-P) experiments. The measured ring electron temperatures[4] in EBT-I and EBT-S are ~200 and ~500 keV, respectively. The projected ring temperature in EBT-P is ~1000-1500 keV. Calculated spectra and relative intensity levels of EBT-I and EBT-S are in reasonable agreement with the experimental measurements.

Other than the diagnostic interest, there is also an interest in the study of synchrotron emission from the ring electrons in order to determine the total radiation losses and its scaling with ring parameters. The dominant ring power losses are synchrotron radiation, drag cooling, and scattering.[2,4] In EBT-I and EBT-S the ring sustaining power is modest[4] and primarily determined by drag cooling and scattering because the synchrotron losses are calculated (and measured) to be low. However, in future experiments, predicted ring temperatures ($T > 1$ MeV) will be in the synchrotron-dominated regime and radiation losses will play an important role in determining the ring power balance.

In Sec. II, basic expressions for the energy spectrum of the synchrotron radiation are given for isotropic and anisotropic distribution functions. Results for present and planned experiments are presented in Sec. III. Section IV summarizes the findings.

II. EMISSION SPECTRUM OF SYNCHROTRON RADIATION

A. Basic equations and assumptions

The expression for single electron emissivity (i.e., the energy radiated per unit solid angle $d\Omega$, per unit frequency interval $d\omega$, per second) can easily be approximated by Schott-Trubnikov results[11,12] for the frequency range of interest ($\omega_p^2 << \omega_c^2$) and is given by[12] (in mks units)

$$\eta_\omega(\omega,\beta,\theta) = \frac{e^2\omega^2}{8\pi^2\varepsilon_o c} \sum_{\ell=1}^{\infty} \left[\left(\frac{\cos\theta - \beta_\parallel}{\sin\theta}\right)^2 J_\ell^2(x) + \beta_\perp^2 J_\ell'^2(x)\right]\delta(y)$$

$$= \frac{e^2\omega^2}{8\pi^2\varepsilon_o c} \sin^{-2}\theta(1+p^2)^{-1} \sum_{\ell=1}^{\infty} \{[(1+p^2)\cos\theta - p_\parallel]^2 J_\ell^2(x)$$

$$+ p_\perp^2 \sin^2\theta J_\ell'^2(x)\}\delta(y) \quad . \quad (1)$$

Here, $\omega_c = eB/m_o c\gamma = \omega_{co}(1-\beta^2)^{1/2} = \omega_{co}(1+p^2)^{-1/2}$; $\beta_\parallel (= v_\parallel/c)$ and $\beta_\perp$ $(= v_\perp/c)$ are dimensionless velocities parallel and perpendicular to the magnetic field B, respectively; $p_\parallel$ and $p_\perp$ are the electron momenta expressed in units of $m_o c$ (m_o is the rest mass of the electron); ε_o is the permitivity of the free space; J_ℓ and J_ℓ' $\left[\equiv \frac{d}{dx} J_\ell(x)\right]$ are Bessel functions and their derivatives; and θ is the observation angle measured from the magnetic axis. In Eq. (1), the argument of the Bessel function is

$$x = \frac{\omega}{\omega_c}\beta_\perp \sin\theta = \frac{\omega}{\omega_{co}} p_\perp \sin\theta \quad , \qquad (2)$$

and the argument of the δ function is

$$y = \ell\omega_c - \omega(1 - \beta_\parallel\cos\theta)$$

$$= (1+p^2)^{-1/2}[\ell\omega_{co} - \omega(\sqrt{1+p^2} - p_\parallel\cos\theta)] \quad . \qquad (3)$$

Considering the propagation at exactly $\theta = \pi/2$, one finds from Eq. (1) that the emissivity is made up of two parts:[12] one is associated with the ordinary wave ($E \parallel B$, the electric vector oriented along B),

$$\eta_\omega^{(o)}\left(\frac{\pi}{2}\right) = \frac{e^2\omega^2}{8\pi^2\varepsilon_o c} \sum_{\ell=1}^{\infty} \beta_\parallel^2 J_\ell^2(\ell\beta_\perp)\delta(\ell\omega_c - \omega) \quad , \tag{4}$$

and the other with the extraordinary wave ($E \perp B$),

$$\eta_\omega^{(x)}\left(\frac{\pi}{2}\right) = \frac{e^2\omega^2}{8\pi^2\varepsilon_o c} \sum_{\ell=1}^{\infty} \beta_\perp^2 J_\ell'^2(\ell\beta_\perp)\delta(\ell\omega_c - \omega) \quad . \tag{5}$$

For an assembly of electrons, the radiation emitted per unit volume dV, per unit frequency interval $d\omega$, and per unit solid angle $d\Omega$ is then written as

$$j_\omega^{(o,x)} \equiv \frac{d^3P_\omega^{(o,x)}}{d\omega\, d\Omega\, dV} = n_R \int d^3p f(\vec{p})\eta_\omega^{(o,x)}(\vec{p}) \quad , \tag{6}$$

where n_R is the ring electron density and $f(\vec{p})$ [$\int d^3p f(\vec{p}) = 1$] is the ring distribution function. In writing Eq. (6), it is assumed that the total power radiated by all electrons in the plasma is a simple superposition of single-particle emissions, a valid assumption provided collective effects (such as instabilities) do not lead to coherent emission over some spectral bandwidth. Also, under the conditions of interest ($\omega^2 >> \omega_p^2$, where ω is the emission frequency), the refractive properties of the medium are neglected.

Assuming the hot electron ring is a cylindrical shell of finite length L_R (in each sector) and is located at a mean radius of a_R with a half-width of δ_R, one can write the power radiated from the unit axial length as

$$\langle I_\omega^{(o,x)} \rangle \equiv \frac{d^2 P_\omega^{(o,x)}}{d\omega\, d\Omega\, L_R} = 2\pi \int_{a_R-\delta_R}^{a_R+\delta_R} r\, dr\, j_\omega^{(o,x)} \quad . \tag{7}$$

In Eq. (7), the self-absorption of the radiation has been neglected.

The radial profiles of density and temperature are assumed to be parabolic

$$[n_R(r), T_R(r)] = (n_o, T_o)\left[1 - C_{n,T}\left(\frac{r - a_R}{\delta_R}\right)^2\right] \quad , \tag{8}$$

where n_o, T_o represents the peak values of ring density and temperature at $r = a_R$ and C (C_n or C_T) is constant and determined from fits to the experimental data.

From the pressure balance equation, the modification to the magnetic field due to the hot electron rings can be approximated as

$$B(r) \cong B_o(r)[1 - \beta_R(r)]^{1/2} \quad , \tag{9}$$

where β_R is the ring beta and $B_o(r)$ is the vacuum magnetic field and is assumed to be uniform along the magnetic axis z within the ring length L_R. To a good approximation,

$$B_o(r) \cong B_{oo}\left[1 - \alpha\left(\frac{r}{R_B}\right)^m\right] \quad , \tag{10}$$

where B_{oo} is the midplane field (at r = 0), R_B is the magnetic field scale length in the radial direction in the absence of the high-beta ring, and α and m are constants which can be obtained from fits to the exact field calculations. (The magnetic field at the ring location $r = a_R$ is ~0.6-0.7B_{oo} with $\beta_R = 0$.) Here, the neglect of nonuniformity

in the magnetic field in the axial direction z corresponds to the neglect of line broadening of the emitted radiation. This is generally justified[12] because the primary mechanism for line broadening is spread in electron energy, which is fairly large for the ring temperatures of interest in comparison with any other broadening mechanisms.

B. Emission for isotropic and anisotropic distribution functions

In case of perpendicular propagation ($\theta = \pi/2$), expressions for the emission coefficient can be represented by relatively simple and compact formulas for some classes of distribution functions.[9] Among those are any class of isotropic [i.e., $\partial f(p,\psi)/\partial\psi = 0$, where ψ is the angle between $\underline{B}$ and $\vec{p}$] and any anisotropic distribution function of the form

$$f(\vec{p}) = f_{\perp}(p_{\perp})f_{\parallel}(p_{\parallel}) \quad . \tag{11}$$

When f is isotropic (but not necessarily Maxwellian), Eq. (6) reduces to

$$j_{\omega}^{(o,x)} = \frac{e^2\omega}{4\pi\varepsilon_o c}(m_o c)^3 n_R \sum_{\ell \geq \omega/\omega_{co}} f[p_*(\omega)]p_*^3(\omega)S_{\ell}^{(o,x)}[\beta_*(\omega)] \quad , \tag{12}$$

where

$$p_*^2(\omega) = (\ell\omega_{co}/\omega)^2 - 1 \quad , \tag{13}$$

or equivalently

$$\beta_*^2(\omega) = (\omega/\ell\omega_{co})^2 p_*^2(\omega) = 1 - (\omega/\ell\omega_{co})^2 \quad , \tag{14}$$

and

$$S_\ell^{(o,x)}(\beta_*) = \int_o^\pi d\psi \sin\psi \begin{cases} \cos^2\psi J_\ell^2(\ell\beta_* \sin\psi) & (o) \\ \sin^2\psi J_\ell'^2(\ell\beta_* \sin\psi) & (x) \end{cases} . \tag{15}$$

Equation (12) is the final expression for the emission coefficient j_ω for any arbitrary class of isotropic distribution functions. A special case of this class is the Maxwellian distribution and is used in the numerical calculations presented in the next section.

The ring electrons preferentially gain perpendicular energy as a result of electron cyclotron heating. The parallel and perpendicular temperatures ($T_\parallel$ and $T_\perp$) can be different with the result that the momentum distribution will be anisotropic. If one can represent the distribution function in a separable form as in Eq. (11), the emission coefficient is then given by

$$j_\omega^{(o,x)} = \frac{e^2\omega}{4\pi\varepsilon_o c} n_R (m_o c)^3 \sum_{\ell \geq \omega/\omega_{co}} \int_{-p_*(\omega)}^{p_*(\omega)} dp_\parallel f_\parallel(p_\parallel) f_\perp[p_{\perp *}(\omega, p_\parallel)]$$

$$\bullet \begin{cases} p_\parallel^2 J_\ell^2[\ell\beta_{\perp *}(\omega, p_\parallel)] & (o) \\ p_{\perp *}^2 J_\ell'^2[\ell\beta_{\perp *}(\omega, p_\parallel)] & (x) \end{cases} , \tag{16}$$

where

$$\begin{aligned} p_{\perp *}^2(\omega, p_\parallel) &= p_*^2(\omega) - p_\parallel^2 = [(\ell\omega_{co}/\omega)^2 - 1] - p_\parallel^2 , \\ \beta_{\perp *}^2(\omega, p_\parallel) &= \beta_*^2(\omega) - \beta_\parallel^2 = (\omega/\ell\omega_{co})^2 \, p_{\perp *}^2(\omega, p_\parallel) . \end{aligned} \tag{17}$$

In general, one wants an f of the form represented by Eq. (11) that reduces to (a) the isotropic Maxwellian for $T_\perp = T_\parallel$ and (b) the 2-D Maxwellian $f(p) \sim f_\perp(p)\delta(p_\parallel)$ for $T_\parallel/T_\perp \to 0$. Because of the difficulty in finding a simple relativistic equilibrium distribution function f with both of these limiting behaviors and because the ECH plasma is expected to be quite anisotropic in temperature, the second requirement was selected for asymptotic behavior. Hence, the following distribution function is used in the numerical calculations:

$$f(\vec{p}) = f_\perp(p_\perp)f_\parallel(p_\parallel) = A_\perp \exp(-\varepsilon_\perp/T_\perp) \times A_\parallel \exp\left(-\frac{m_o c^2}{2T_\parallel} p_\parallel^2\right) , \qquad (18)$$

where $\varepsilon_\perp = m_o c^2(1 + p_\perp^2)^{1/2}$ and $A_\perp$ and $A_\parallel$ are the normalization constants.[9] In the limiting case of no parallel motion (2-D Maxwellian), Eq. (18) reduces to

$$f(\vec{p}) = f_\perp(p)\delta(p_\parallel) = A \exp(-\varepsilon/T)\delta(p_\parallel) \quad , \qquad (19)$$

and one finds $j_\omega^{(o)} = 0$ and

$$j_\omega^{(x)} = \frac{e^2\omega}{4\pi\varepsilon_o c} n_R (m_o c)^2 \sum_{\ell > \omega/\omega_{co}} p_*^2(\omega) f_\perp[p_*(\omega)] J_\ell'^2[\ell\beta_*(\omega)] \quad . \qquad (20)$$

For a deviation from perpendicular propagation ($\theta \neq \pi/2$), expressions are, in general, quite complex and Eq. (1) should be used in the derivations. It is shown in Ref. 11 that for $\theta \neq \pi/2$ the radiation intensity falls off more rapidly for an anisotropic distribution than for an isotropic one. Thus, the measurements made with $\theta \neq \pi/2$ can provide useful information on the ring anisotropy. In general, radiation intensity has the form

$$j_\omega^{(o,x)}(\theta) = \frac{e^2\omega}{4\pi\varepsilon_o c}(m_o c)^3 n_R \sum_{\ell > \omega/\omega_{co}} \int d\psi \sin\psi \tilde{p}_*^2(\omega,\theta,\psi)$$

$$\cdot\, f[\tilde{p}_*(\omega,\theta,\psi)]\, G_\ell^{(x,o)}[\tilde{p}_*(\omega,\theta,\psi)] \,, \quad (21)$$

where $\tilde{p}_*(\omega,\theta,\psi)$ satisfies the relation

$$\ell\omega_{co}/\omega = (1 + \tilde{p}_*^2)^{1/2} - \tilde{p}_* \cos\psi \cos\theta \quad (22)$$

and

$$G_\ell^{(x,o)}(\tilde{p}_*) = \begin{cases} \dfrac{\tilde{p}_*^2(1 + \tilde{p}_*^2)^{1/2} \sin^2\psi}{|\cos\psi \cos\theta - \tilde{p}_*(\ell\omega_{co}/\omega)|} J_\ell'^2\left(\dfrac{\omega}{\omega_{co}} \tilde{p}_* \sin\theta \sin\psi\right) \\ \\ \dfrac{[(1 + \tilde{p}_*^2)\cos\theta - \tilde{p}_* \cos\psi]^2 (1 + \tilde{p}_*^2)^{1/2}}{\sin^2\theta |\cos\psi \cos\theta - \tilde{p}_*(\ell\omega_{co}/\omega)|} J_\ell^2\left(\dfrac{\omega}{\omega_{co}} \tilde{p}_* \sin\theta \sin\psi\right). \end{cases} \quad (23)$$

A special case of simple loss cone distribution[10,13]

$$f(p,\psi) = A(\psi_o)\exp(-\varepsilon/T)U(\psi,\psi_o) \quad (24)$$

is used for calculations in the next section. Here, $A(\psi_o)$ is the normalization constant, and

$$U(\psi,\psi_o) = \begin{cases} 1 & \psi_o < \psi < \pi - \psi_o \\ 0 & \text{otherwise} \end{cases} \,, \quad (25)$$

where ψ_o is the loss cone angle ($\psi_o = 0$ corresponds to isotropic distribution and limit of $\psi_o \to \pi/2$ represents pure perpendicular motion) and ψ is the angle between $\underline{B}$ and $\vec{p}$ (i.e., pitch angle $\cos\psi = p_\parallel/p$). In limiting the case of $\theta = \pi/2$ and $\psi_o = 0$, Eq. (21) reduces to Eq. (12).

III. RESULTS FOR PRESENT AND PLANNED EXPERIMENTS

Using the experimentally measured ring temperatures and densities,[4,14] the radiation spectra for EBT-I and EBT-S are calculated for several choices of the ring electron distribution functions discussed in the previous section. The projected parameters for EBT-P are deduced from scaling relationships obtained from the present experiments. The typical parameters used in these calculations are given in Table I.

The extraordinary and ordinary wave intensities for EBT-I, -S, and -P are shown in Fig. 1 for the isotropic Maxwellian distribution. Several features of the spectra can easily be seen in Fig. 1. The peaks at low frequencies are mainly the contributions of lower harmonics ($\ell < 10$), and the emission spectrum peaks around a frequency $\omega = \omega_{max} \cong 0.5\ \omega_{co}\gamma^2$. However, the bulk of the emission comes from part of the spectrum $\omega \gtrsim \omega_{max}$. Because of the smearing of successive harmonics and pronounced overlapping, spectra monotonically decrease and become almost flat at high frequencies, as observed in the experiments.[6] The slope of the spectrum decreases with increasing temperature (i.e., spectra for EBT-P are flatter than those for EBT-S, which are flatter than those for EBT-I). There is almost an order of magnitude increase in intensity levels in going from EBT-I to EBT-S and from EBT-S to EBT-P due to hotter and denser ring plasmas. In the frequency range 80-110 GHz, the ratio of the extraordinary wave intensity levels (average) is

$$\langle I^{(x)}\rangle_{EBT-S}/\langle I^{(x)}\rangle_{EBT-I} \cong 8 \quad ,$$

which compares reasonably with the experimental observation of the intensities in this frequency range.[6] (The experimental value[6] is $I^{(x)}_{EBT-S}/I^{(x)}_{EBT-I} \cong 6$.)

As can be seen from from Fig. 1, whereas most of the power is in the extraordinary wave component the ratio of the extraordinary wave intensity to the ordinary wave intensity decreases with temperature. That is, $I^{(x)}/I^{(o)} \approx 10$ in EBT-I, ≈ 6 in EBT-S, and ≈ 4 in EBT-P. The slope of the ordinary wave spectrum is somewhat larger than the extraordinary wave.

The intensity levels and radiation spectra do depend on the distribution function and the anisotropy level. This effect is shown in Fig. 2 for EBT-S. In Fig. 2, one can compare the spectra at the same values of temperature ($T_\perp$ = constant) or average kinetic energy ($\langle W \rangle$ = constant) for three different distribution functions (e.g., isotropic Maxwellian $T_\perp = T_\parallel$, two-temperature $T_\perp/T_\parallel = 5$, and 2-D Maxwellian $T_\parallel = 0$), discussed in Sec. II. While the intensity increases with anisotropy ($T_\perp/T_\parallel$), the slope of the spectrum decreases. The structures of the spectra are found to be similar in all three cases (for both $T_\perp$ = constant and $\langle W \rangle$ = constant); however, the peaks of the intensity move to higher frequencies as the temperature and anisotropy increase. Comparisons of the isotropic and anisotropic cases for EBT-I, EBT-S, and EBT-P are given in Table II for both $T_\perp$ = constant and $\langle W \rangle$ = constant.

Although Fig. 2 is for the extraordinary wave, similar behavior is observed for the ordinary wave. In Fig. 3, the variation of the ratio of these two intensities [i.e., $I^{(x)}/I^{(o)}$] with the temperature and distribution function is given. The ratio of intensities in the two polarizations exhibits a similar dependence on temperature both for isotropic Maxwellian and for two-temperature or bi-Maxwellian (with $T_\perp/T_\parallel = 5$) cases; however, the ratio increases with anisotropy. The dependence on temperature is stronger at low temperatures. That is, $I^{(x)}/I^{(o)} \sim T^{-\alpha}$, where $\alpha \sim 0.5$–1.0 for $T < 500$ keV and $\alpha < 0.1$ for $T > 1500$ keV. The curves in Fig. 3 are deduced from the calculated spectra for EBT-I, -S, and -P in that they are continuous and are found to be nearly independent of device geometry, magnetic field, beta, etc.

The solid curves in Fig. 3 are for ω = 150 GHz; however, the variation of the ratio within the frequency range 80-250 GHz is found to be modest (<20%). Although one can deduce temperature information from the ratio of intensities in the two polarizations at two widely separated frequencies at low temperatures ($\lesssim$200 keV), it is very difficult to obtain a conclusive answer for temperatures characteristic of EBT-S (or EBT-P) unless the resolution of the measurements is better than 10-20%.

In case of loss cone distribution, at $\theta = \pi/2$, the ratio of intensities is found to be insensitive to the loss cone angle for $\psi_o < 60°$ (see Fig. 4). For large angles ($\psi_o > 70°$), however, the intensity ratio in the two polarizations increases drastically (up to a factor of ~2 at $\psi_o \sim 75°$ and ~4 at 80°), as shown in Fig. 4. Again, the ratio is observed to be weakly dependent on the frequency. In comparison with isotropic distribution, at $\theta = \pi/2$, the change in intensity level is less than 50% for $\psi_o < 45°$, and about a factor of 2-4 increase in intensity is found for $\psi_o > 60°$. The effect of loss cone is more pronounced for $\theta \neq \pi/2$, in which emission falls with θ more rapidly for loss cone distribution than for isotropic distribution. In particular, for an observation angle $\theta > \psi_o$, one finds the ratio $I^{(x)}_{isotropic}(\theta)/I^{(x)}_{loss\ cone}(\theta)$ to be more than an order of magnitude.[10]

The intensity also changes with ring beta, as illustrated in Fig. 5. In comparing vacuum field calculations with finite-beta results, about 20% reduction in intensity level is observed in EBT-S (T = 500 keV) for a ring beta of ~35%.

The changes in intensity with temperature and beta are shown in Figs. 6-8 for EBT-I, -S, and -P. In order to eliminate the density dependence, intensities in Figs. 6-8 are normalized with appropriate densities corresponding to each device. Because the ring volume in the experiments is observed to be nearly constant[2,4,14] (i.e., independent of operating conditions), the ring beta is proportional to the ring stored energy (diamagnetic flux). Thus, the correlation of measured radiation intensity with stored energy will yield similar curves to those in Figs. 6-8 from which one can make a comparison of theory and experiment for determining the ring distribution function. For all of

the three distribution functions (see Figs. 6-8), dependence of intensity to temperature is found to be much stronger in EBT-I than in EBT-S. That is, $I^{(x)} \sim T^{\alpha}$, where $\alpha \sim 2.5$-3 for EBT-I, $\alpha \sim 1$-1.3 for EBT-S, and $\alpha \sim 0$-0.3 for EBT-P. Results from Figs. 6-8 are summarized in Table III.

Correlations of intensity with all of the observable (or measurable) quantities in the experiments (i.e., density, temperature, stored energy which is a measure of ring beta, etc.) can be made as they are shown in Figs. 9 and 10. Figures 9 and 10 are for an EBT-S plasma assuming isotropic Maxwellian distribution, though similar behavior is observed for other distribution functions. For a given density (see Fig. 9), intensity first increases with temperature and, after some critical temperature, either saturates or decreases slightly with increasing temperature (and beta). The saturation temperature increases as the density is increased. From the measurements of the radiation intensity (in x-mode in this case) and stored energy (or beta), one can determine the corresponding ring temperature and density from Fig. 9 or 10.

IV. DISCUSSION AND CONCLUSIONS

Expressions for the energy spectrum of the synchrotron radiation emitted by the relativistic, hot electron rings in EBT are presented for several classes of distribution functions. For special cases, these expressions are used to determine scaling of the radiation with ring parameters and to indicate ways to determine ring properties from the measurements of synchrotron emission.

Because of the relativistic temperatures ($T \sim 200$-1500 keV), the bulk of the emission comes from the higher harmonics. In general, the contributions from lower harmonics ($\ell = \omega/\omega_{co} < 10$) are modest (approximately a few percent) and a large number of harmonics are used in the calculations [i.e., $\ell \sim O(10^2)$].

Calculated spectra and relative intensity levels compare reasonably well with the experimental measurements in EBT-I and EBT-S. That is, the radiation spectrum is almost flat at higher frequencies and the slope of the spectrum decreases, but the intensity increases with temperature. In addition, an increase in intensity and a decrease in slope are observed with an increase in anisotropy ($T_\perp/T_\parallel$).

For the isotropic Maxwellian, the emission spectrum peaks around a frequency $\omega \simeq 0.5\omega_{co}\gamma^2$; however, the peak moves to higher frequency as the anisotropy is increased.

The ratio of the extraordinary wave intensity to the ordinary wave intensity decreases with temperature (for isotropic Maxwellian the ratio is ~10 for EBT-I, ~6 for EBT-S, and ~4 for EBT-P) though it increases with anisotropy. (For $T_\perp/T_\parallel = 5$, the ratio is a factor of ~2-3 larger than that for $T_\perp/T_\parallel = 1$.) The dependence of the ratio on temperature is found to be stronger at low temperatures ($I^{(x)}/I^{(o)} \sim T^{-1/2}$ to $\sim T^{-1}$ for $T < 200$ keV); however, it exhibits a very weak dependence on temperature at high temperatures ($\sim T^{-0.1}$). For perpendicular propagation ($\theta = \pi/2$), a significant change in the ratio of intensities is only observed for loss cone angles $\psi_o > 70^\circ$. The effect of loss cone becomes more important for $\theta \neq \pi/2$, especially for $\theta < \psi_o$. In all cases, the ratio shows very weak dependence on the frequency (~20%).

Correlations of calculated emission spectrum, radiation intensity, etc., with a wide range of ring parameters and/or distribution functions are made. Depending on the information sought, these can be used to deduce properties of the ring plasma from the experimental measurements. For example, information on the ring distribution function can be inferred from comparisons of the theoretical result with the measurement of the ring stored energy and radiation intensity. Similarly, ring anisotropy can be deduced from the ratio of intensities in the two polarizations and so on. However, there are also limitations and difficulties in obtaining conclusive results in most cases due to either limitations of the experimental capabilities (e.g., access problem in making measurements for $\theta \neq \pi/2$) or the difficulties

in interpreting the model calculations (i.e., because of the relativistic temperatures, harmonics are all smeared out with a pronounced overlapping, resulting in a featureless spectra with not much to distinguish with frequency).

ACKNOWLEDGMENT

The authors gratefully acknowledge the many useful discussions with S. Tamor on the comparisons of some of the numerical results with an independent code. Thanks are also due to J. B. Wilgen for numerous discussions of the experimental results.

REFERENCES

1. R. A. Dandl et al., in Plasma Physics and Controlled Nuclear Fusion Research (IAEA, Vienna, 1975), Vol. II, p. 141; Oak Ridge National Laboratory Report ORNL/TM-4941, 1975.
2. N. A. Uckan, editor, EBT Ring Physics: Proceedings of the Workshop (Oak Ridge National Laboratory, Oak Ridge, Tennessee, 1980).
3. D. B. Nelson and C. L. Hedrick, Nucl. Fusion 19, 283 (1979); G. E. Guest, C. L. Hedrick, and D. B. Nelson, Phys. Fluids 18, 871 (1975).
4. N. A. Uckan et al., in Plasma Physics and Controlled Nuclear Fusion Research (IAEA, Vienna, 1981), Vol. I, p. 831.
5. M. Fujiwara et al., in Plasma Physics and Controlled Nuclear Fusion Research (IAEA, Vienna, 1981), Vol. I, p. 845.
6. T. Uckan, J. Wilgen, and L. Bighel, Bull. Am. Phys. Soc. 25, 832 (1980); J. Wilgen and T. Uckan "Synchrotron Emission Measurements from the Hot Electron Rings in EBT," in Hot Electron Ring Physics: Proceedings of the 2nd Workshop (to be published).
7. M. Tanaka et al., "Interaction of Microwave with Hot Electron Ring in Bumpy Torus," in Hot Electron Ring Physics: Proceedings of the 2nd Workshop (to be published).
8. Z. S. Wang, G. D. Tsakiris, and D. A. Boyd, Bull. Am. Phys. Soc. 26, 996 (1981).
9. N. A. Uckan, R. G. Spencer, and T. Uckan, Oak Ridge National Laboratory Report ORNL/TM-7687, 1981.
10. S. Tamor, Laboratory for Applied Plasma Studies Report LAPS-73/SAI-023-81-191-LJ, 1981.
11. B. A. Trubnikov, in Plasma Physics and the Problems of Controlled Thermonuclear Reactions (1958), Vol. III, pp. 122-132; B. A. Trubnikov, Phys. Fluids 4, 195 (1961).
12. G. Bekefi, Radiation Processes in Plasmas (Wiley, New York, 1966), Chapter 6.
13. V. K. Tripathi, E. Ott, and C. S. Liu, in EBT Ring Physics: Proceedings of Workshop, (Oak Ridge National Laboratory, Oak Ridge, Tennessee, 1980) p. 305.

14. G. R. Haste, Bull. Am. Phys. Soc. 25, 921 (1980); D. L. Hillis and G. R. Haste, Bull. Am. Phys. Soc. 26, 979 (1981).

TABLE I. Typical EBT ring parameters[4,14]

	EBT-I	EBT-S	EBT-P[a]
B_{oo} (midplane, r = 0) (kG)	5.0	7.2	15.0
B_o (vacuum field at r = a_R) (kG)	3.2	5	10.7
ECH frequency (GHz)	18	28	60
Ring radius, a_R (cm)	12	12	18
Ring half-width, δ_R (cm)	1.5	1.5	2.0
Ring temperature, T_o (keV)	200	500	1000
Ring density, n_o ($\times 10^{11}$ cm^{-3})	2.3	3.0	5.0

[a]Projected parameters.

TABLE II. Comparisons of isotropic and anisotropic distribution functions for EBT-I, -S, and -P for $T_\perp$ = constant (case a) and $\langle W \rangle$ = constant (case b).

ORNL-DWG 81-23430 FED

	EBT-I			EBT-S			EBT-P		
	$T_\perp = T_\parallel$	$T_\perp/T_\parallel = 5$	$T_\parallel = 0$	$T_\perp = T_\parallel$	$T_\perp/T_\parallel = 5$	$T_\parallel = 0$	$T_\perp = T_\parallel$	$T_\perp/T_\parallel = 5$	$T_\parallel = 0$
Case a: $T_\perp$ = constant (keV)	200			500			1000		
$\langle I^{(x)}/I^{(o)} \rangle$ (at 110 GHz)	10	28	–	6	16	–	4	12.5	–
$I^{(x)}_{\omega = 80\ GHz}/I^{(x)}_{\omega = 110\ GHz}$	1.5	1.45	1.4	1.1	1.05	1.4	0.95	0.9	0.85
$\langle I^{(x)}/I^{(x)}_{isotropic} \rangle$ (at 110 GHz)	1.0	1.6	1.9	1.0	1.95	2.3	1.0	2.1	2.4
Case b: $\langle W \rangle$ = constant (keV)	300			750			1500		
$T_\perp$ (keV)	200	275	300	500	675	750	1000	1375	1500
$\langle I^{(x)}/I^{(o)} \rangle$ (at 110 GHz)	10	23	–	6	14	–	4	11	–
$I^{(x)}_{\omega = 80\ GHz}/I^{(x)}_{\omega = 110\ GHz}$	1.5	1.3	1.2	1.1	1.0	0.95	0.95	0.85	0.85
$\langle I^{(x)}/I^{(x)}_{isotropic} \rangle$ (at 110 GHz)	1.0	2.9	4.2	1.0	2.5	3.1	1.0	2.25	2.6

TABLE III. Calculated variation of intensity with temperature [$I^{(x)} \sim T^{\alpha}$]

		$I^{(x)} \sim T^{\alpha}$		
		α		
Device	Operating window	$T_{\perp} = T_{\parallel}$	$T_{\perp}/T_{\parallel} = 5$	$T_{\parallel} = 0$
EBT-I	$T_{\perp} \sim 150$–250	2.5 ∓ 0.2	2.7 ∓ 0.2	3.0 ∓ 0.2
EBT-S	$T_{\perp} \sim 400$–600	0.9 ∓ 0.1	1.1 ∓ 0.1	1.2 ∓ 0.1
EBT-P[a]	$T_{\perp} \sim 1000$–1500	~ 0	0.25 ± 0.05	0.25 ∓ 0.05

[a]Operating window for EBT-P is a projected range for ring temperature.

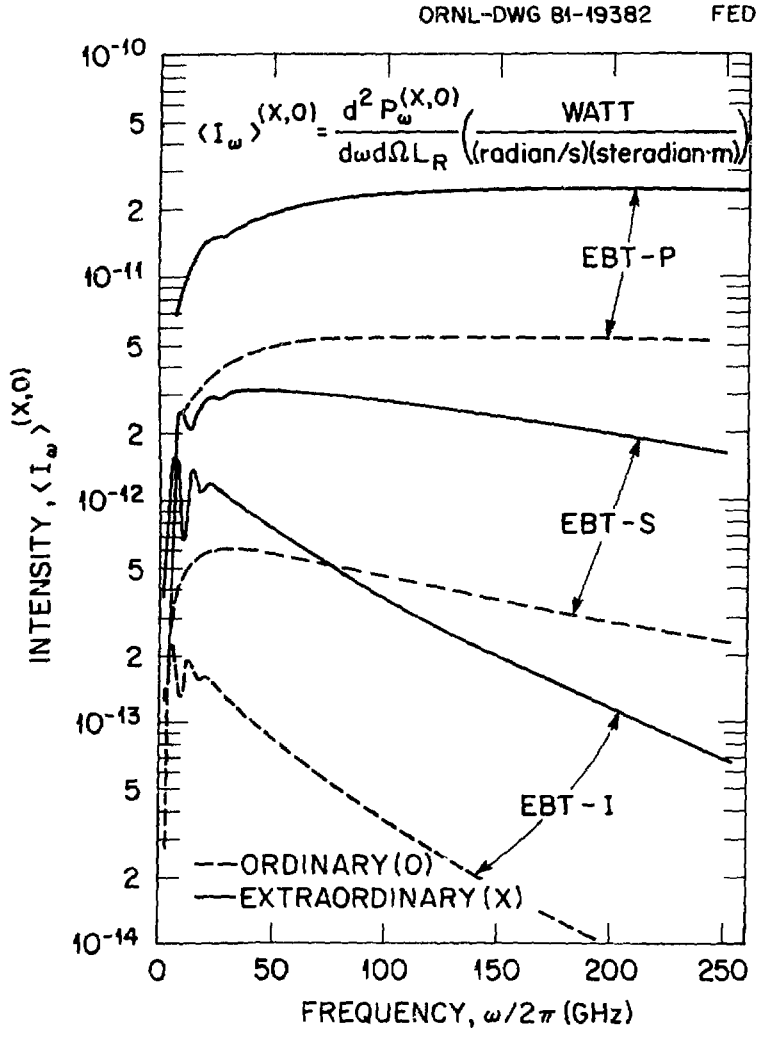

FIG. 1. Synchrotron radiation spectrum of the hot electron rings of EBT-I, EBT-S, and EBT-P. The extraordinary and ordinary wave intensities are shown for the isotropic Maxwellian distribution.

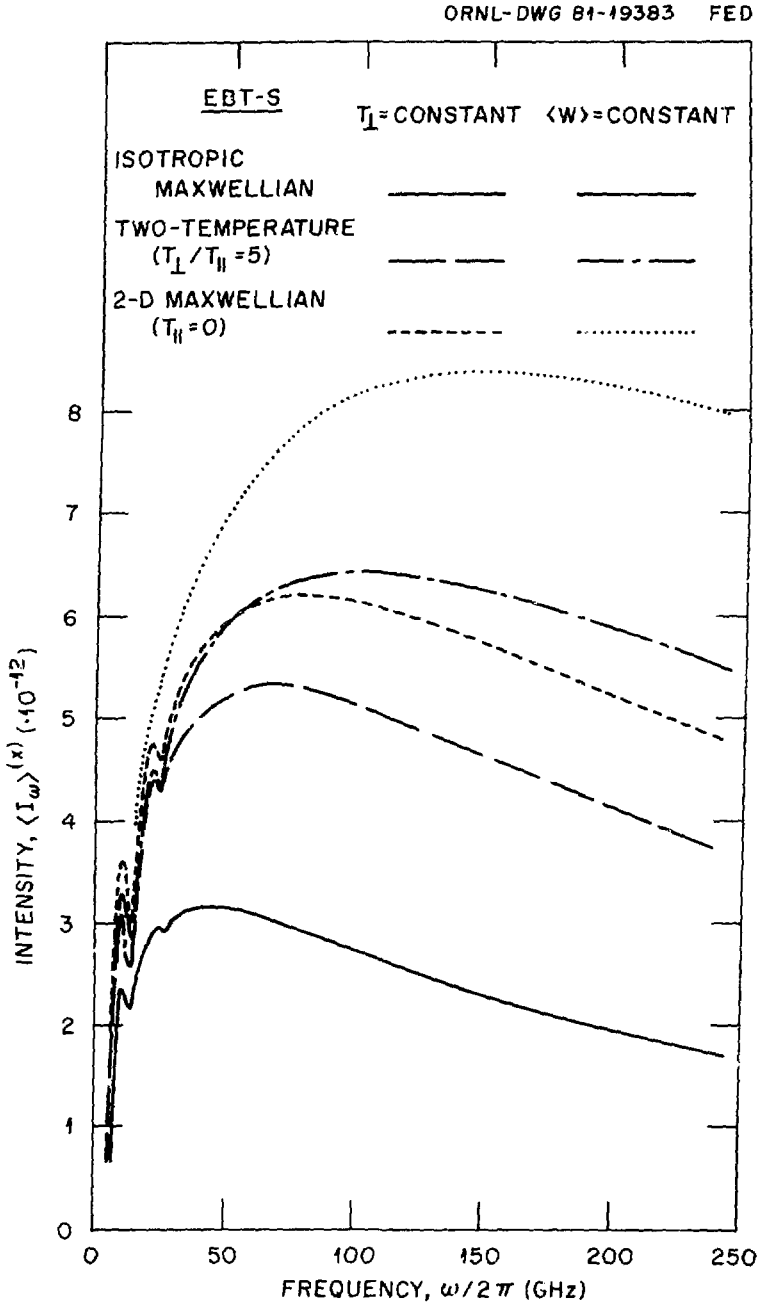

FIG. 2. Radiation spectra in EBT-S for various distribution functions for the same values of temperature ($T_\perp$ = constant) and average kinetic energy (⟨W⟩ = constant). Intensity unit is W/[radian/s)(steradian m)].

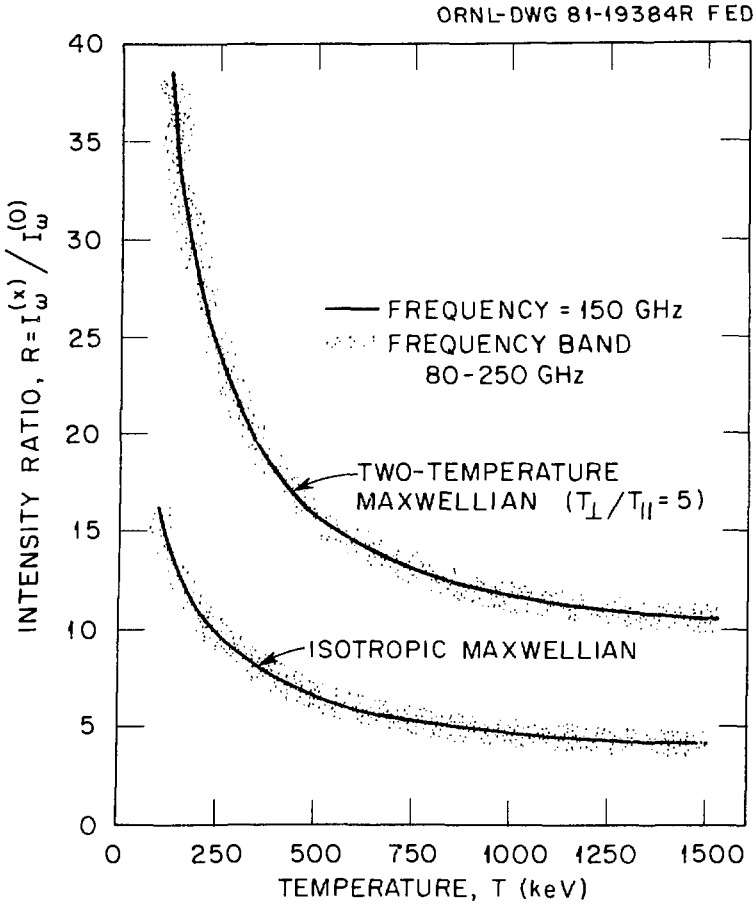

FIG. 3. Computed variation of the ratio of extraordinary wave intensity to ordinary wave intensity with temperature and anisotropy. Solid curve is for 150 GHz. Variation of the ratio within the frequency range 80-250 GHz is shown with dotted band.

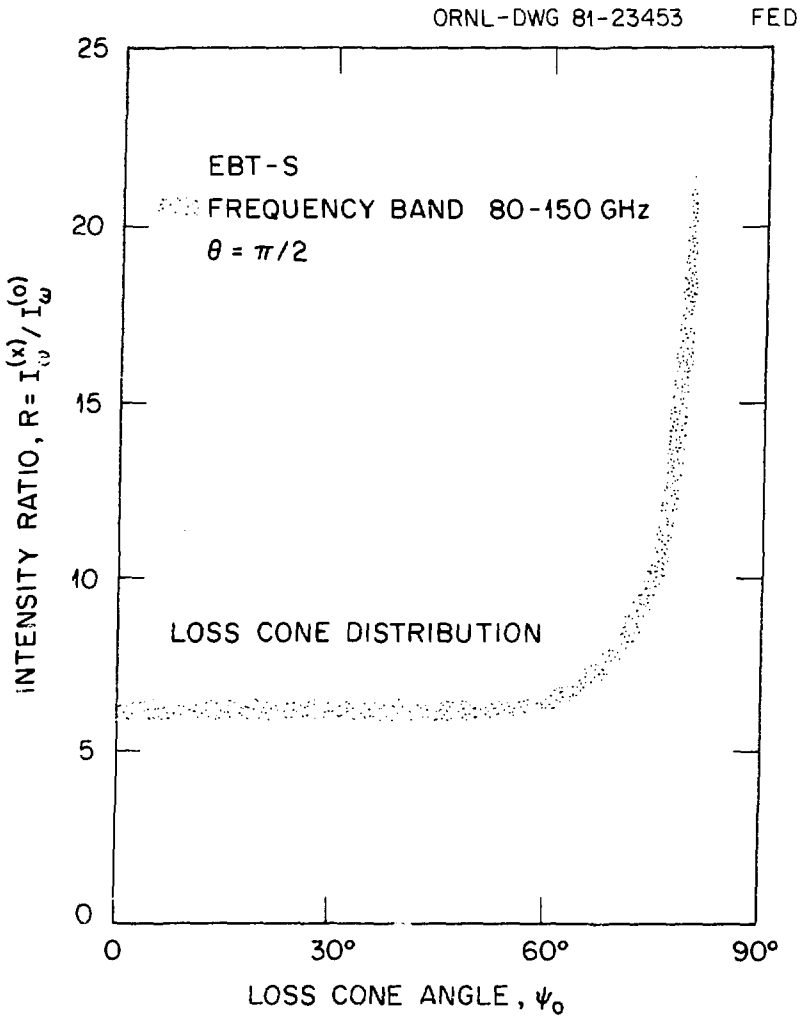

FIG. 4. Ratio of extraordinary wave intensity to ordinary wave intensity as a function of loss cone angle in EBT-S within the frequency range 80-150 GHz. Observation angle $\theta = \pi/2$.

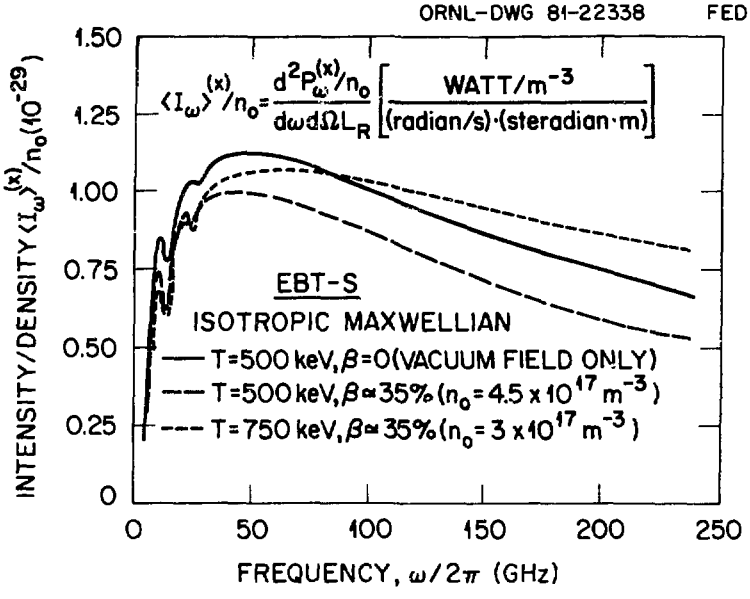

FIG. 5. Comparison of emission spectrum without (β = 0) and with ($\beta \approx 35\%$) beta effects for isotropic Maxwellian distribution.

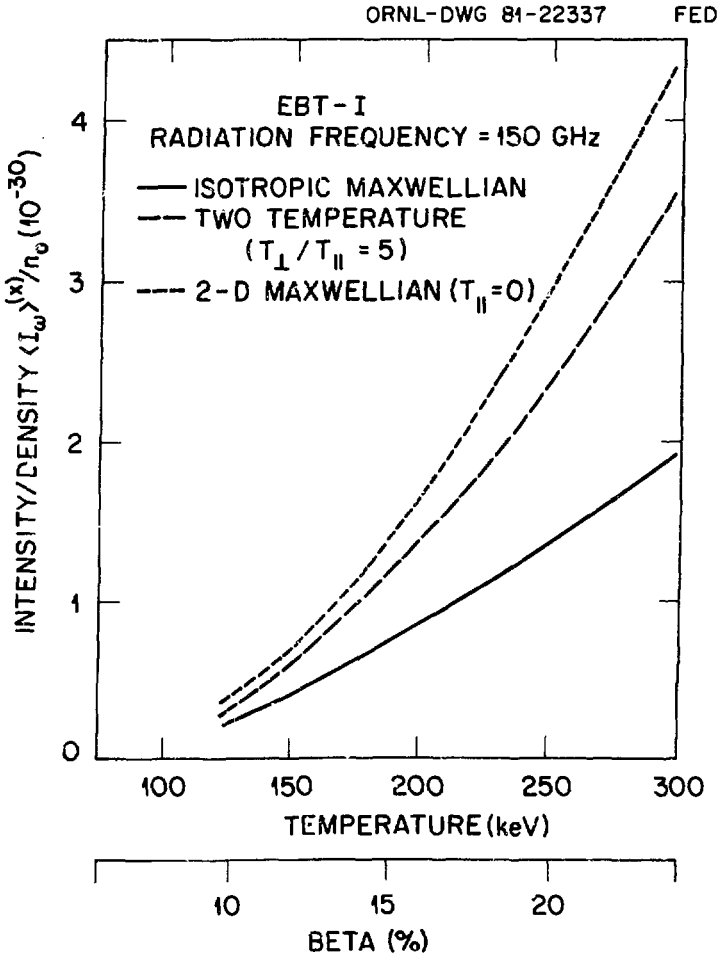

FIG. 6. Computed variation of intensity (normalized to density) with temperature and beta (~stored energy) in EBT-I for various distribution functions.

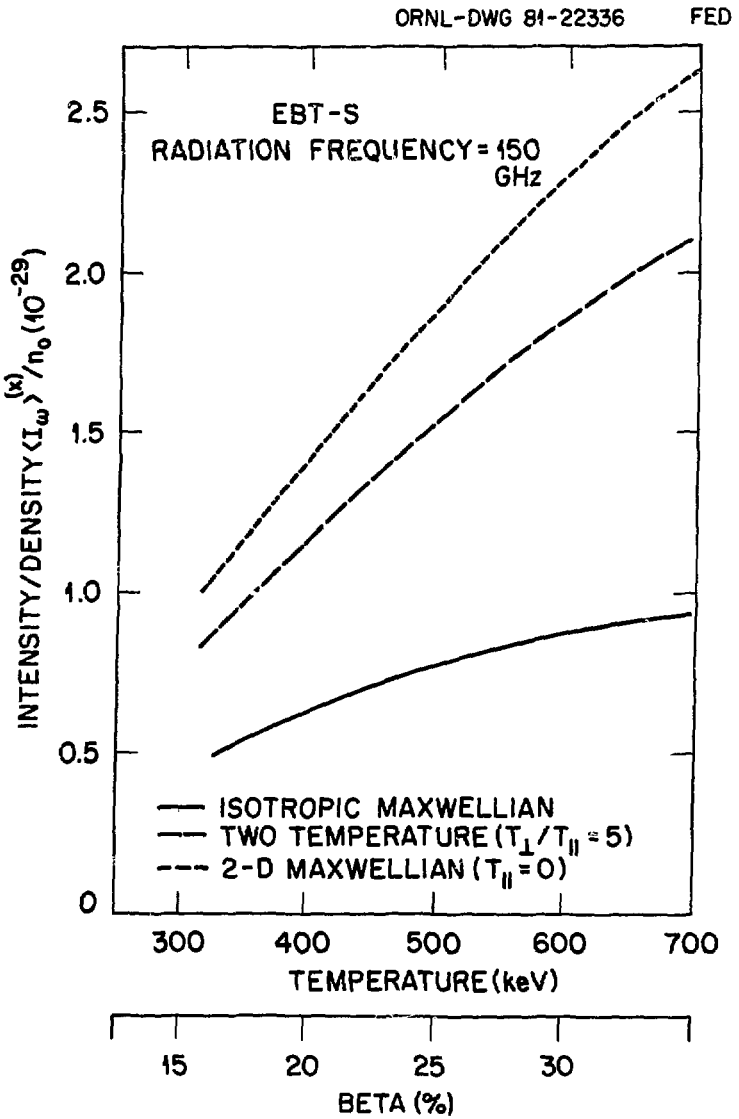

FIG. 7. Same calculations as in Fig. 6 for EBT-S. Intensity shows weaker dependence on temperature in EBT-S than in EBT-I.

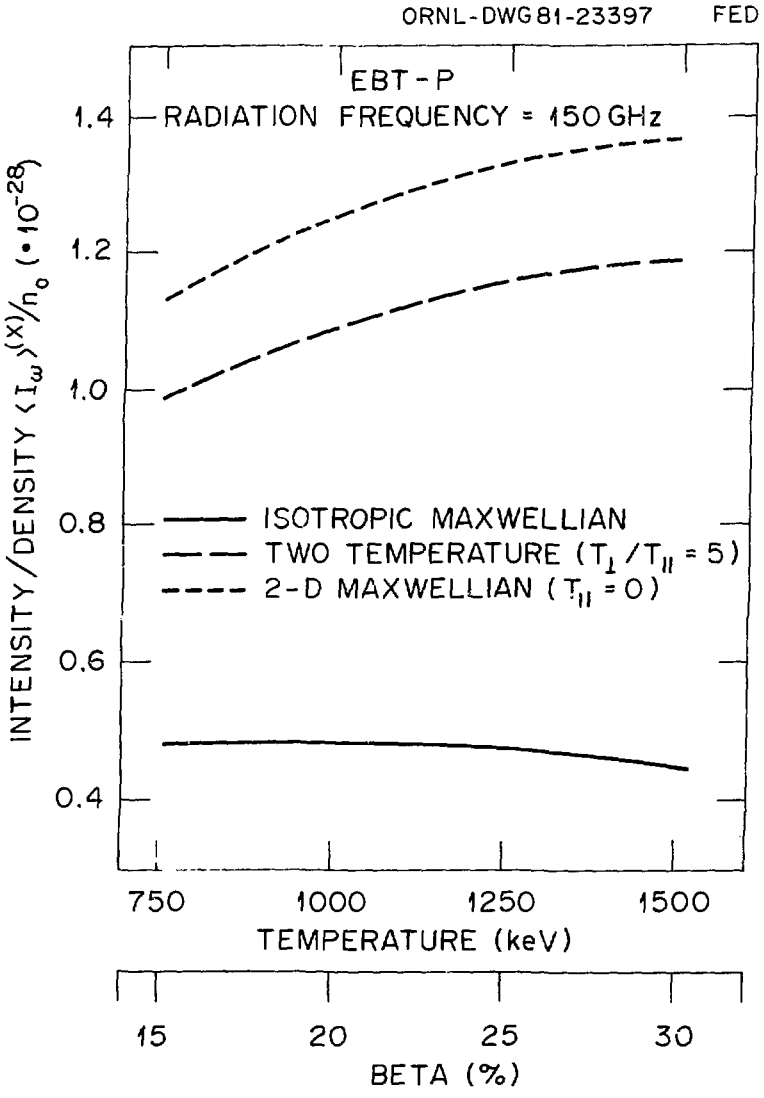

FIG. 8. Same calculations as in Fig. 6 for planned EBT-P experiment. Intensity shows much weaker dependence on temperature in EBT-P than in EBT-S for comparable ring beta.

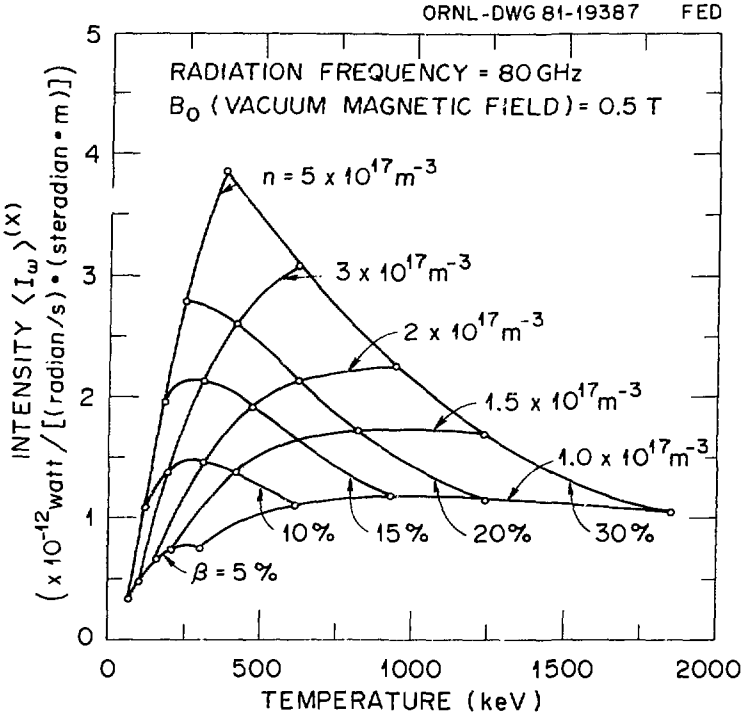

FIG. 9. Computed intensity as a function of temperature and its correlation with density and beta (~stored energy) for isotropic Maxwellian distribution. (Similar correlation is observed for other distribution functions.)

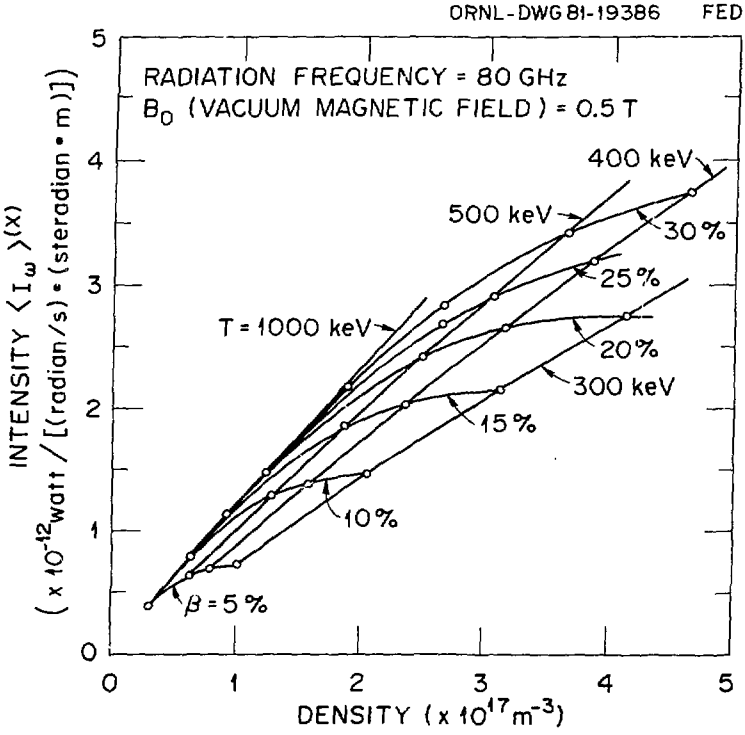

FIG. 10. Correlation of intensity with variations in density, temperature, and beta (same calculations as in Fig. 9 but different representation).

ELECTROMAGNETIC INTERACTIONS OF NON-MAXWELLIAN PLASMAS*

S. Tamor
Science Applications, Inc.
1200 Prospect Street, Suite 480
La Jolla, California 92037

ABSTRACT

The velocity distribution function of the EBT ring electrons is expected to be highly non-Maxwellian, and an investigation of the consequence of this fact with respect to emission, absorption, and transport of radiation is underway. A study of the emission of synchrotron radiation suggests that the angular distribution of the radiation may be a useful diagnostic for studying the anisotropy of the underlying plasma. We are also interested in the absorptive properties of the plasma and have recently developed a computer code which calculates the absorption coefficient for a model class of non-Maxwellian distributions. The first application has been to calculating the absorption coefficients at the first and second harmonics, and initial results indicate that anisotropy tends to increase the absorption coefficient of the extraordinary mode. Further studies both at higher frequencies, and for non-Maxwellian energy distributions will be carried out.

---

*Research sponsored by Oak Ridge National Laboratory.

On the basis of present models for ring heating one would expect the electron distribution function to be non-Maxwellian both with respect to the angular distribution and energy spectrum. Large deviations of this type would, in turn, be expected to modify the electromagnetic interaction of the hot electrons. In this paper we report upon studies of the emission and absorption of radiation by non-Maxwellian electron distributions.

Our studies of the emissivity of an anisotropic plasma were originally motivated by a search for diagnostic applications of synchrotron radiation. It is easy to show that anisotropy of the electron velocity distribution causes a corresponding anisotropy in the emissivity. To show this, first consider as energetic electron with $v_{\parallel} = 0$. In this case the emission is peaked at 90^{0} and at high frequencies the peak is very narrow. The corresponding picture for $v_{\parallel} \neq 0$ is obtained by a Lorentz transformation. If $v_{\parallel}/c = \beta$ then the center of the radiation pattern is shifted to $\cos\theta = \beta$. Similarly the electron orbit pitch angle becomes

$$\cos\theta_e = \frac{p_{\parallel}}{p} = \frac{\sqrt{\beta^2(1+p_{\perp}^2)}}{\sqrt{\beta^2 + p_{\perp}^2}}$$

where p is the relativistic momentum in units of m_0c. In general $\cos\theta_e > \cos\theta$, and the two angles approach each other as $p_{\perp}$ increases.

To exhibit the magnitude of this effect we have modified an existing computer code to describe a loss cause distribution; i.e.,

$$f(p,\theta_e) = \begin{cases} e^{-\mu\gamma} & (\cos\theta_e < \cos\theta_0) \\ 0 & (\cos\theta_e > \cos\theta) \end{cases} \quad .$$

(We do not pretend that this is a realistic distribution, but it does illustrate the essentials of the problem.) Typical results of such calculations are shown in Figs. 1 and 2. The curves show the computed emission per electron as a function of angle for assumed loss cone angles of 0° (isotropic), 45°, 75°, and 85°, and a temperature of 500 keV. Figure 1 is for a frequency $\omega = 10\omega_c$ and Fig. 2 is for $\omega = 20\omega_c$. The most interesting result of this calculation is the large magnitude of the effect; the emission dropping by several orders of magnitude when the angle is much smaller than θ_0, so that even with modest angular resolution a measurement of the intensity distribution should give a good indication of the degree of anistropy.

The proposed experiment is complicated by the need for access to perform an angular scan, and for radiation dumps at each angle to suppress reflected radiation. An experiment which at first appears to avoid this problem would be to measure the polarization at a single angle since the O-mode emission at 90° is very small if the spread in $v_{\parallel}$ is small. Unfortunately, the polarization is strong even for isotropic distributions. Figure 3 displays the computed ratio for the intensities transmitted by plane polarizer parallel to and perpendicular to the plane containing B and the wave vector. We see that at 90° there is essentially no dependence upon θ_0 except for the extreme case of $\theta_0 = 85^o$, and even here detection of the effect puts great demands upon the analyzer system. This situation improves at other angles but, again, unless one knows θ_0 in advance it is necessary to perform an angular scan to find where the polarization ratio changes.

In passing we note that the angle integrated emission in essentially independent of θ_0 so that anisotropy in emission has negligible effect upon the power balance.

Calculations of absorption by a non-Maxwellian distribution is more complicated because it depends upon derivatives of the distribution function. It is, in fact, possible to obtain negative absorption coefficients which would lead to amplification and enhanced losses. A program to investigate these effects was recently begun. It is intended to study both frequencies near the first two harmonics since they are important to ECH, and also at high frequencies because the possibility of anomalies in the reabsorption process could affect the ring energy balance.

The absorption coefficient is proportional to the imaginary part of the propagation vector, which is in turn proportional to Hermitian the part of the conductivity tensor. Treating the absorption as a small perturbation an elementary calculation gives

$$\mathrm{Im}(k) = \frac{4\pi}{c}\,\frac{1}{n}\,\frac{\langle E,\sigma^H E\rangle}{|E_{tr}{}^2|}$$

where E is an eigenmode of the non-dissipative plasma with index of refraction n, and E_{tr} is the part of E transverse to the wave vector.

If the eigenvectors are known, the required expectation value of σ is obtainable from standard expressions for the RF conductivity. Expressing the absorption in terms of an expectation value is useful since, although the general expressions for σ are not very transparent,

the expectation value can be written (in the usual representation)

$$\langle E\sigma^H E\rangle = \frac{-\omega_p^2}{\omega} \int d^3p\ f'(p) \sum_n \delta\left(\gamma\frac{\omega}{\omega_c} - \kappa_\parallel p_\parallel - n\right)$$

$$\cdot \left|\frac{E^x}{2} p_\perp (J_{n-1} + J_{n+1}) + \frac{iE_y}{2} p_\perp (J_{n-1} - J_{n+1}) + E_z p_\parallel J_n\right|^2$$

where

$$f'(p) = \frac{\partial f}{\partial p_\perp} + \frac{\omega_c}{\omega}\frac{\kappa_\parallel}{\gamma}\left(p_\perp \frac{\partial f}{\partial p_\parallel} - p_\parallel \frac{\partial f}{\partial p_\perp}\right)$$

and κ is the wave number in units of c/ω_c. The absence of growing waves is guaranteed if $f' < 0$ everywhere (as for a Maxwellian).

A computer program has recently been completed which computes Im(k) assuming the real part obeys the Appleton-Hartree dispersion relation, and a model class of distribution function of the form

$$f(p,\theta) = \sum_{ijk} a_{ijk} (\sin\theta)^{2i} p^{2j} e^{-\gamma u_k}$$

where the coefficients a_{ijk} are specified. Initial results have been obtained for anisotropic Maxwellian ($j = 0$ and $i = 0, 1,$ or 2) and frequencies in the neighborhood of the first two harmonics. Figure 4 shows the results of one such calculation for the E-mode with k at 90° to B and T = 5 keV. In this case the anisotropy has the effect of increasing the absorption by a factor of 2 or more except for a tiny interval just below $\omega = \omega_c$ where there is evidence of an instability which is harmless since the wave is rapidly reabsorbed as soon as it propagates to weaker fields. At angles other than 90° results for the E

wave are roughly similar. The behavior of the O wave is somewhat more complicated with evidence of bands of growing waves. Similarly, at higher temperature the unstable region at $\omega \sim \omega_c$ is more pronounced and other instability bands appear. These effects are now being explored in greater detail. One would also guess that more drastic effects would appear if the f is not monotone in energy but this has not yet been examined at all. Finally, it remains to study the high frequency region for which some additional code modification will be required.

It is hoped that when results of Fokker-Plank calculations become available it will be possible to carry out these computations with more realistic electron distribution functions.

SUMMARY

We have initiated a systematic study of realistic emission and absorption from complicated electron distribution function such as might occur in EBT rings. Calculations of emissivity from a model loss cone distribution indicate that measurements of angular distribution of synchrotron emission may be a means of directly estimating the degree of anisotropy.

More general codes for calculating absorption coefficients for complex distributions are being developed. Initial results indicate that at low temperatures the record harmonic E wave absorption is somewhat enhanced, but in general the effects of anisotropy are quite complicated and need to be examined in more detail.

FIGURE CAPTIONS

Figure 1. Computed total (summed over polarization) intensity as a function of angle relative to the magnetic field at $\omega = 10\omega_c$ for a temperature of 500 keV and various assumed values of the loss cone aperature, θ_0. Intensity units are watts/electron/ster/GHz.

Figure 2. The same calculation as in Figure 1 but with $\omega = 20\omega_c$.

Figure 3. Computed polarization as a function of angle at $\omega = 10\omega_c$ for a temperature of 500 keV and various loss cone apertures. $I_{\parallel}$ and $I_{\perp}$ are the intensities seen through a plan polarizer with the electric vector lying in or perpendicular to the plane containing the magnetic vector and the propagation vector.

Figure 4. Absorption coefficient (cm^{-1}) for 90^0 propagation vs. frequency for a Maxwellian energy distribution with anisotropy factor $(\sin\theta)^{2j}$. Parameters are:

$T = 5$ keV
$B = 7$ kilogauss
$n_e = 10^{12}$ cm^{-1}

The curves represent: ——— $j = 0$
—·—·—·— $j = 1$
– – – – – $j = 2$

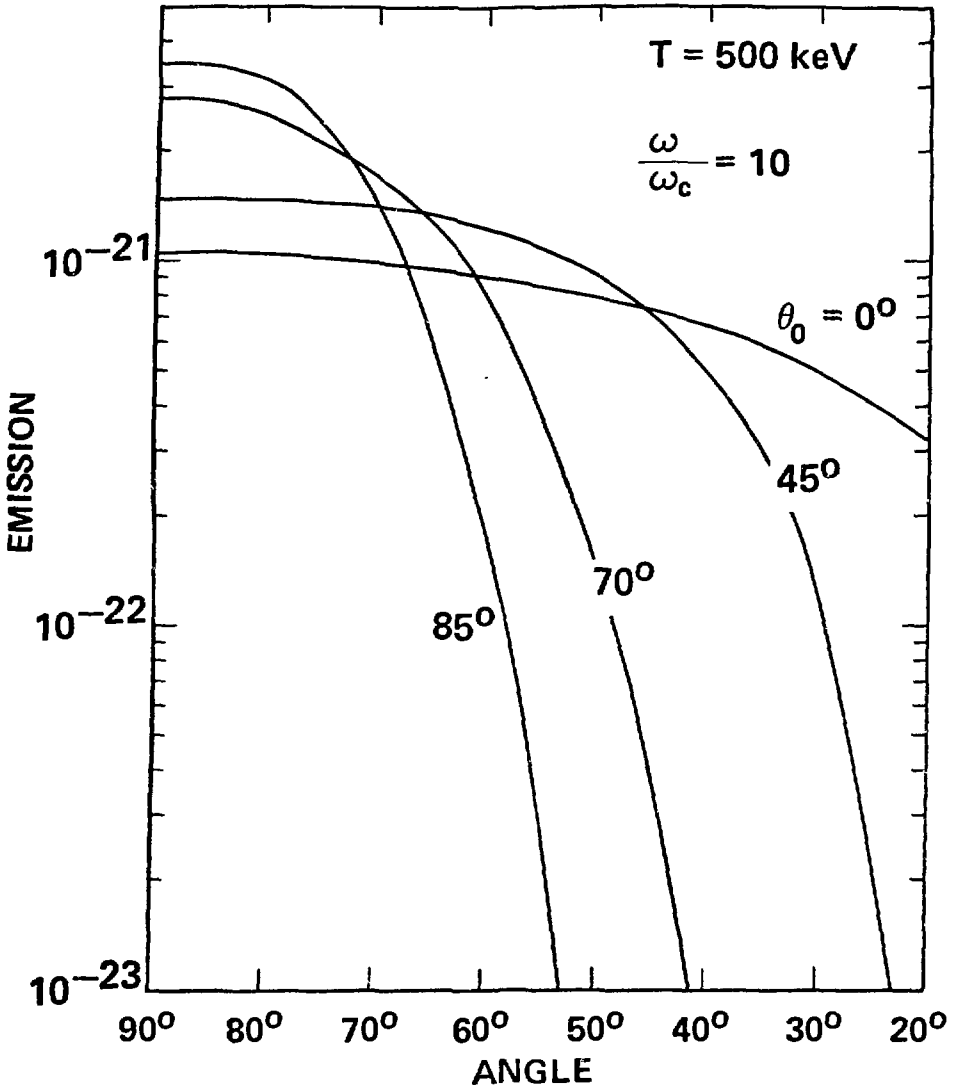
T = 500 keV
$\frac{\omega}{\omega_c} = 10$
$\theta_0 = 0^o$
45°
70°
85°
EMISSION
10^{-21}
10^{-22}
10^{-23}
90° 80° 70° 60° 50° 40° 30° 20°
ANGLE

Figure 1

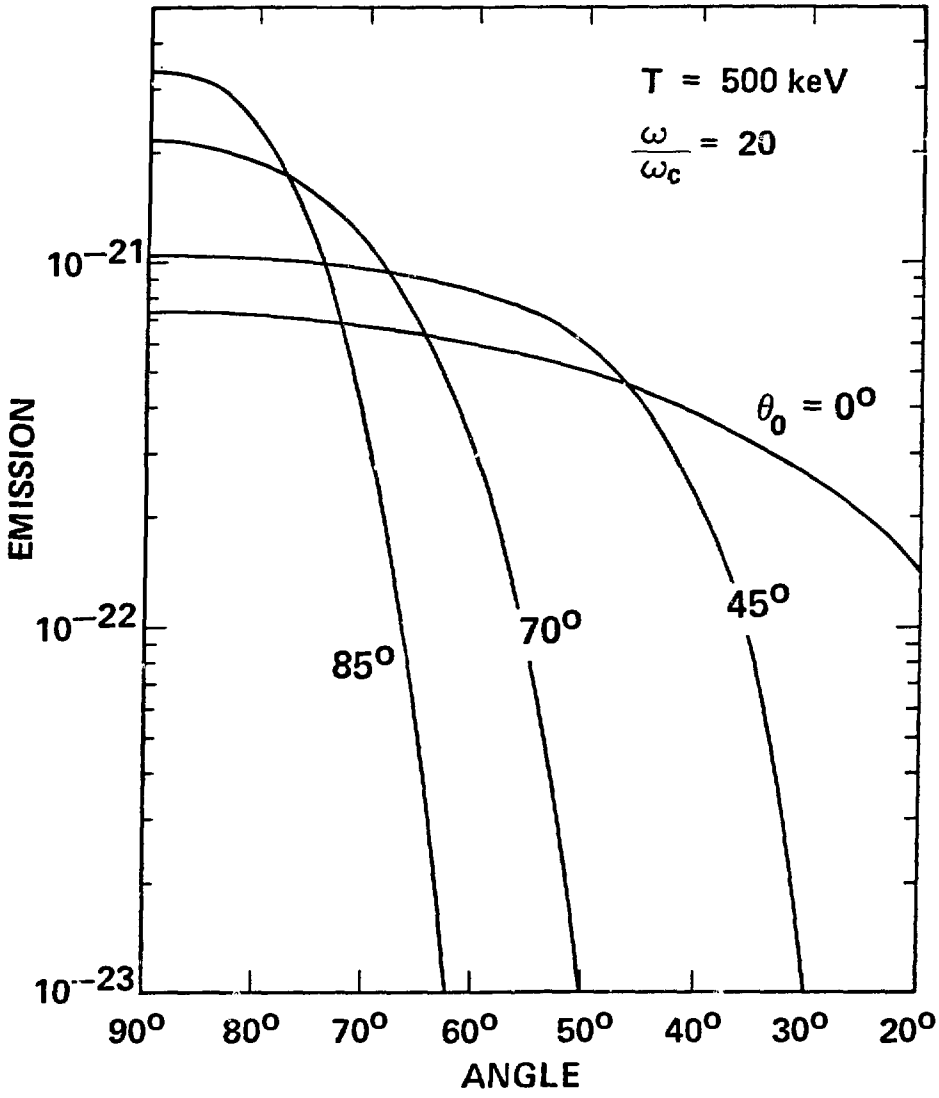
T = 500 keV
ω/ωc = 20
θ0 = 0°
45°
70°
85°
10−21
10−22
10−23
EMISSION
90°
80°
70°
60°
50°
40°
30°
20°
ANGLE

Figure 2

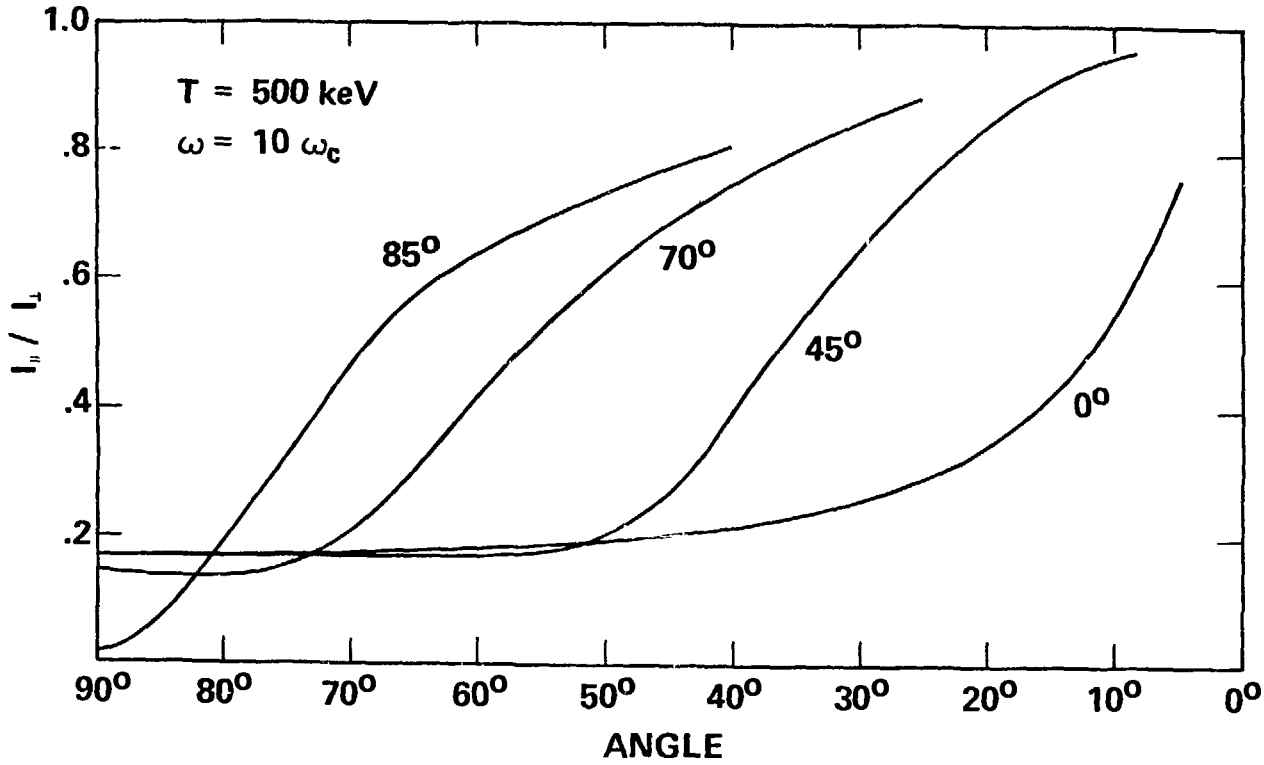
T = 500 keV
ω = 10 ωc
85°
70°
45°
0°
1.0
.8
.6
.4
.2
I∥ / I⊥
90°
80°
70°
60°
50°
40°
30°
20°
10°
0°
ANGLE

Figure 3

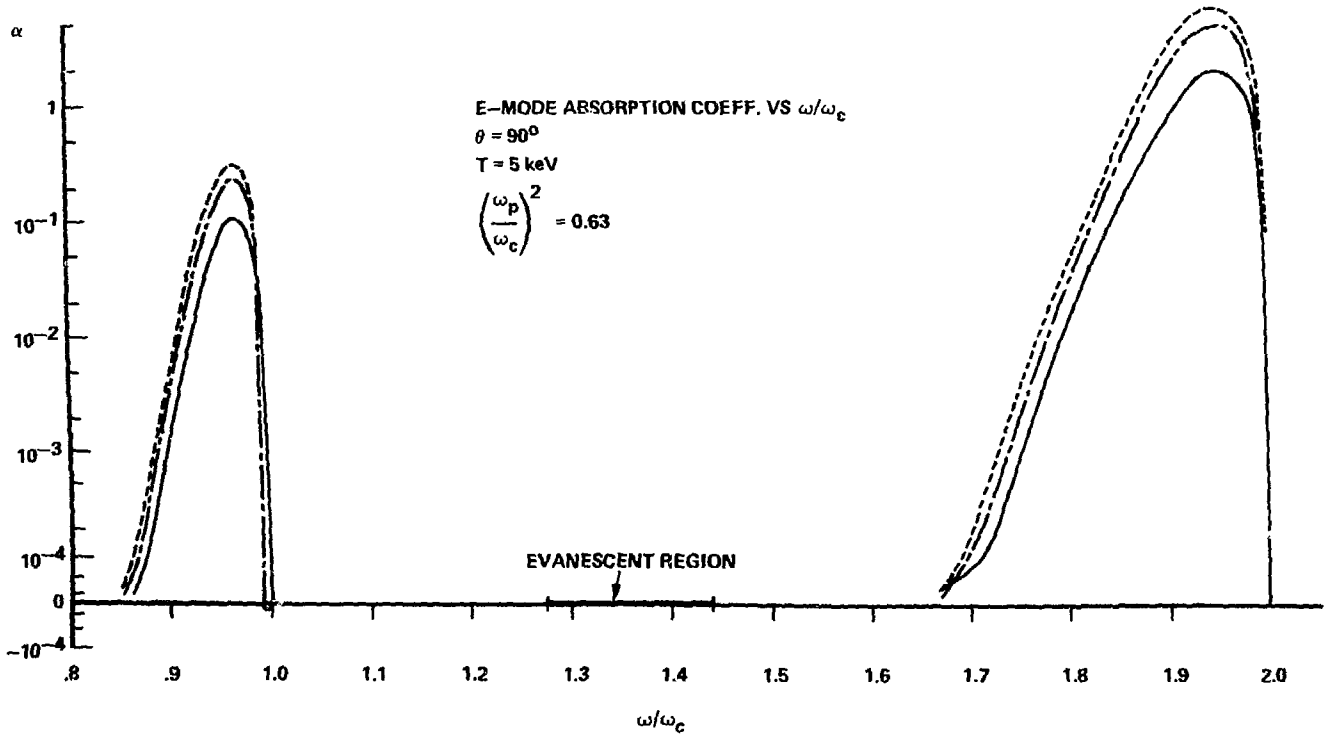
E–MODE ABSORPTION COEFF. VS ω/ω_c
$\theta = 90^0$
T = 5 keV
$\left(\frac{\omega_p}{\omega_c}\right)^2 = 0.63$
EVANESCENT REGION
α
1
10^{-1}
10^{-2}
10^{-3}
10^{-4}
0
-10^{-4}
.8
.9
1.0
1.1
1.2
1.3
1.4
1.5
1.6
1.7
1.8
1.9
2.0
ω/ω_c

Figure 4

ANALYTIC EXPRESSIONS FOR SYNCHROTRON RADIATION FROM EBT

D. Winske, D. A. Boyd, and G. D. Tsakiris
Laboratory for Plasma and Fusion Energy Studies
University of Maryland
College Park, Maryland 20742

Abstract

Analytic expressions for the power emitted per unit volume per solid angle per unit frequency at perpendicular propagation as synchrotron radiation from a relativistic loss-cone distribution of electrons are presented. These expressions are useful for understanding how the radiation scales and for inferring properties of the plasma from measurements of the radiation. As an example, it is shown that the temperature and loss-cone angle of the electron distribution in the EBT ring can be determined in a straightforward fashion from the ratio of radiation in the two polarizations at two frequencies. This method will be used in a forthcoming University of Maryland diagnostic experiment on EBT-S, which is described in some detail.

I. INTRODUCTION

It is well known that the relativistic electron ring in EBT is necessary for the stability of the core plasma. In order to understand how parameters of the ring change with operating conditions and scale in different devices there is a continuing need to develop improved diagnostics for the ring plasma. One such example is the experiment by the University of Maryland to measure the synchrotron radiation from the ring. Synchrotron radiation diagnostics are widely used on tokamaks and are a natural choice for EBT because of the low density and high energy of the ring electrons. Some measurements of the synchrotron emission from the rings have already been made on EBT[1] and NBT.[2]

The relativistic nature of the electrons, however, makes calculations of synchrotron radiation in EBT difficult, since the

contributions of the various harmonics strongly overlap and thus very high harmonics can contribute significantly.[3] In the course of such numerical calculations some rather simple and useful analytic expressions for the radiation at perpendicular propagation for a loss-cone distribution were discovered. These expressions, presented in Sec. II, are valid over a wide parameter regime and hence are helpful in understanding the overall scaling of various quantities. They are also potentially useful in simplifying more complicated computations, such as power loss calculations, where the radiation must be integrated over several spatial variables. In a more restricted parameter regime, such as the operating conditions of EBT-S, the analytic expressions can be simplified further. In this case the expressions are easily inverted to give the ring parameters (temperature and mirror ratio) and an estimate of the uncertainty in the results directly from simple measurements. A specific example of how this will be done in the University of Maryland experiment, which is described in Sec. III, is given in Sec. IV.

II. RESULTS

Expressions for the radiation are easily derived.[3] The energy at frequency ω emitted per electron perpendicular to the magnetic field per unit solid angle $d\Omega$ per unit frequency $d\omega$ per second is:

$$\eta_\omega(o,x) = \frac{e^2\omega^2}{8\pi^2 c\varepsilon_o} \sum_{\ell=1}^{\infty} \begin{cases} \beta_\parallel^2 J_\ell^2(\ell\beta_\perp)\delta(\ell\omega_c - \omega) & \text{ordinary (o) mode} \\ \beta_\perp^2 J_\ell'^2(\ell\beta_\perp)\delta(\ell\omega_c - \omega) & \text{extraord. (x) mode} \end{cases} \tag{1}$$

where $\beta_{\parallel,\perp} = v_{\parallel,\perp}/c$ and ω_c is the cyclotron frequency using the relativistic mass. Then, the power radiated at frequency ω per unit volume dV per solid angle per unit frequency involves an integration over the electron distribution function f(p):

$$j_\omega^{(o,x)} = \frac{d^3P_\omega^{(o,x)}}{d\Omega d\omega dV} = n_r \int d\underset{\sim}{p}\ f(\underset{\sim}{p})\eta_\omega^{(o,x)}(\underset{\sim}{p}) \ , \tag{2}$$

where $\underset{\sim}{p} = m\underset{\sim}{v}$, $m = m_o(1 - v^2/c^2)^{-1/2}$ and n_r is the (ring) electron density. Plasma dispersion effects and absorption have been neglected, as discussed in Ref. 4. A simple relativistic loss-cone distribution[5] is assumed:

$$f(p) = \begin{cases} Ce^{-\varepsilon/T} & \pi/2 - \psi_o < \psi < \pi/2 + \psi_o \\ 0 & \text{otherwise} \end{cases} \tag{3}$$

where the energy $\varepsilon^2 = c^2p^2 + m_o^2c^4$, T is the temperature, ψ is the pitch angle, and ψ_o is the loss cone angle.

After some manipulations, the emission coefficients are obtained:

$$j_\omega^{(o,x)} = \frac{A}{\nu^2\tau^3} \sum_{\ell>\nu} \alpha_\ell^3 e^{-\ell/\nu\tau} \int_0^1 dy \begin{cases} y^2 J_\ell^2(\delta_\ell)/\sigma \\ (1 - y^2/\sigma)J_\ell'^2(\delta_\ell) \end{cases} \tag{4}$$

where $\nu = \omega/\omega_{co}$, $\omega_{co} = eB_o/m_oc$, $\tau = T/m_ec^2$, $\sigma = (\sin\psi_o)^{-2}$, $\alpha_\ell = (\ell^2-\nu^2)^{1/2}$, $\delta_\ell = \alpha_\ell(1-y^2/\sigma)^{1/2}$, and

$$A = 2m_ec^2 \left(\frac{\omega_p}{c}\right)^3 \left(\frac{\omega_{co}}{\omega_p}\right) (4\pi)^{-2} \left[\int_0^\infty dx\ x^2 \exp\{-(\tau^{-2} + x^2)^{1/2}\} \right]^{-1} .$$

In this form the numerical evaluation of the emission coefficients proceeds in a straightforward manner.

In order to derive simplified expressions some approximations are needed. The most important of these simplifications involves suitable replacement of the Bessel functions with complicated arguments. The basic approach is to use known expressions for $J_\ell(\ell z)(z^2 = 1 - \varepsilon^2)$ and its derivative, treating the two factors in the argument $\delta_\ell = (\ell^2-\nu^2)^{1/2}(1-y^2/\sigma)^{1/2}$ separately (and differently). In particular, it is assumed that

$$J_\ell(\alpha_\ell) \sim J_\ell(\ell)(1 - \gamma\nu^2/\ell^{4/3})$$

and

$$J_\ell[\ell(1 - y^2/\sigma)^{1/2}] \sim J_\ell(\ell)\ \exp(-\ell y^3/3\sigma^{3/2})\ .$$

The second approximation is to replace the sum over ℓ by an integral.

The result of these simplications is the following set of expressions (complete derivation with justification in a forthcoming article):

$$j^{(o)} = 8.4 \times 10^{-24} n_r [cm^{-3}] B[kG] (\nu/\tau)^{1/4} \sigma^{1/2} g_1(\sigma,\nu,\tau) e^{-f}$$

$$j^{(x)} = 8.4 \times 10^{-24} n_r B (\nu/\tau)^{1/4} \sigma^{1/2} g_2(\sigma,\nu,\tau)(3.7 + 0.64\nu^{1/2}/\tau) e^{-f}$$

$$R = \frac{j^{(x)}}{j^{(o)}} = \left(3.7 + \frac{0.64\nu^{1/2}}{\tau}\right) \frac{g_2(\sigma,\nu,\tau)}{g_1(\sigma,\nu,\tau)} \tag{5}$$

where

$$g_1 = 1 - e^{-h}$$

$$g_2 = 1 - \Gamma(1/3,h)/\Gamma(1/3)$$

$$h = (2\tau + 2.5)\nu\sigma^{-3/2}$$

$$f = \nu^{1/2}(0.4/\tau + 0.05)$$

$$\nu = \omega/\omega_{co}$$

$$\tau = T/m_e c^2$$

$$\sigma = \sin^{-2}\psi_o = \text{mirror ratio}$$

and $j^{(o,x)}$ has units $Watt/\Delta f(H_z)/\Delta\Omega(ster)/\Delta V(m^3)$.

Examples of these relations (solid curves) and comparisons with exact calculations (circles) are given in Fig. 1. The radiation in the ordinary mode $j^{(o)}$ and the ratio of radiation in the extraordinary mode to that in the ordinary mode R are displayed as a function of frequency (ν), temperature (τ), and mirror ratio (σ) for EBT-S parameters ($n_r = 3 \times 10^{11}$, $\omega_{co} = 14$ GH_z). Generally, there is very good agreement over a sizeable range of parameters.

These curves along with the general expressions (5) indicate the following parametric dependences. The radiation in the ordinary (or extraordinary) mode decreases with frequency (the major dependence is $\exp[-\nu^{1/2}/\tau]$), the decrease with frequency is less as the temperature increases (Fig. 1a). For fixed frequency the radiation increases rapidly at low temperatures, levels off, and eventually decreases slowly as the temperature is further increased (Fig. 1b). As a function of mirror ratio the radiation increases as $\sigma^{1/2}$ for small σ; for large σ it decreases as $\exp(\sigma^{-3/2})$, as shown in Fig. 1c.

Over a rather wide range of parameters the ratio of the radiation in the two polarizations increases primarily as the square root of the frequency at fixed temperature (Fig. 1d) and decreases as T^{-1} for fixed frequency (Fig. 1e). Furthermore, the ratio of radiation intensities is independent of the mirror ratio at small values of σ and increases linearly with mirror ratio at large values (Fig. 1f). It has also been shown that the range of mirror ratios over which R is independent of this quantity increases with increasing frequency and/or temperature. Again, more complete details will be given elsewhere.

III. DESCRIPTION OF EXPERIMENT

The experimental setup, now under construction, is shown schematically in Fig. 2. Measurements of the synchrotron radiation will be performed at two fixed frequencies ($f_1 = 80$ GH_z and $f_2 = 138$ GH_z) using two superheterodyne receivers, in contrast to earlier measurements which were made over a range of frequencies.[1,2]

In selecting these two frequencies the following factors have been considered. Obviously, the two frequencies should be as far apart as possible so that there is an appreciable change in the spectrum intensity at the two measuring points. A lower frequency limit is imposed by the following considerations: (a) the interference from the core plasma and the heating frequencies along with their harmonics should be minimal; (b) refraction effects should be negligible; and (c) quasioptical techniques that can define a spatially isolated viewed volume should be applicable. The only constraints that eventually will impose an upper limit on the frequency are: (a) measurability of the synchrotron radiation intensity level and (b) availability of millimeter and submillimeter microwave technology. The selected frequencies meet these requirements to a satisfactory degree.

The viewing port of the arrangement was designed using Gaussian optics theory. Assuming that the radiation pattern of the receiving antenna resembles that of a Gaussian beam, then, by using a phase-matching dielectric lens, the beam can be transformed to one that has its minimum waist at the center of the EBT cavity. In this way two spatially isolated portions of the electron ring are viewed by the receiving antenna. The metal mirror at the opposite end of the viewing port has a radius of curvature matched to that of the Gaussian beam at this point and its purpose is to insure that only radiation contained within the Gaussian beam will enter the viewing system. It should be noted here that the interference of the metal mirror with the operation of the EBT cavity is expected to be inconsequential.

The heating frequency of 28.0 GH_z is blocked by a honeycomb-type screen some distance from the viewing port. Behind the blocking screen is the vacuum seal. The placement of the blocking screen and window some distance from the viewing port is necessary for two reasons. First, the blocking screen unavoidably generates higher order propagation modes at the measuring frequencies. These higher order modes die out at a short distance from the screen. However, if the screen were positioned right at the port, these higher modes would have

reduced the spatial resolution of the system, since they extend a greater distance from the axis than does the fundamental Gaussian mode. Second, this arrangement allows placing the window behind the screen. This eliminates the necessity of water cooling the window. Furthermore, since the window is removed a distance from the plasma, degradation of the window properties due to particle bombardment and sputtering is avoided.

The receiving antenna is polarized and can be rotated. With the antenna rotated so that its electric field is perpendicular to the magnetic field, the extraordinary mode intensity at the two frequencies is measured. By rotating the antenna by 90°, the ordinary mode intensity for the same two frequencies is measured. Using this scheme the ratios of the intensities in the two polarizations can be experimentally determined.

IV. DISCUSSION

Calculations based specifically on the design of this experiment are presented in this section. Shown in Fig. 3 as circles are exact calculations of the ratio of radiation in the two polarizations at the two frequencies to be used in the experiment: R_1 corresponding to $f = 80$ GH_z and R_2 at 138 GH_z, for EBT-S parameters ($n_r = 3 \times 10^{11} cm^{-3}$, $B_z = 4.5$ kG (assuming the local field is depressed ~10% by β_r ~20%) as a function of temperature ($400 < T < 600$ keV) (Fig. 3a-b) and mirror ratio ($1 < \sigma < 9$) (Fig. 3c-d). The solid curves are simplified versions of the expressions in Sec. II, with the constants slightly adjusted to improve the fit:

$$R_1 = (3.2 + \frac{1100}{T})\ [1 + \exp(-27\sigma^{-3/2})]$$
$$R_2 = (3.4 + \frac{1300}{T})\ [1 + \exp(-54\sigma^{-3/2})]\ . \qquad (6)$$

These expressions are a reasonably good representation of the exact

calculations and are simple enough to manipulate easily. In particular, letting $y = \exp(-27\sigma^{-3/2})$, they reduce to:

$$R_1 = (3.2 + 1100/T)(1 + y)$$
$$R_2 = (3.4 + 1300/T)(1 + y^2) \ . \tag{7}$$

In this form, it is evident that either T or y can be easily eliminated to give an expression relating R_1 and R_2 as a function of only one variable. For example, to eliminate y, let

$$a_1(T) = 3.2 + 1100/T$$
$$a_2(T) = 3.4 + 1300/T \tag{8}$$

then

$$R_2 = a_2(T)\left[1 + \left(\frac{R_1 - a_1(T)}{a_1(T)}\right)^2\right] \ . \tag{9}$$

The result can be expressed in several forms. The first is to write out Eq. (9), obtaining a cubic equation for T, which could easily be solved on a programable hand calculator. Then either equation (7) could be used to obtain y and hence σ.

The second form is a graph of R_1 versus R_2, which consists of a series of parabolas, the curves labelled by different temperatures (Fig. 4a). Keeping the mirror ratio in the range $1 \leq \sigma \leq 9$ then restricts how much of each parabola exists. The results (shown in Fig. 4a as solid lines) indicate that given reasonably accurate measurements of the ratios R_1 and R_2, the temperature can be easily determined. Again, the circles are the superimposed exact calculations. The expression (9) can be further used to give an estimate of the error in the determination of the temperature from the error in the measurements: i.e.,

$$\Delta R_1 = A(T)\Delta T \quad (R_z \text{ fixed})$$
$$\Delta R_2 = B(T)\Delta T \quad (R_1 \text{ fixed}) \ . \tag{10}$$

The construction of this type of graph does not require the simplified expressions. Curves at constant temperature constructed from the exact calculations are presented in Fig. 4b. The existence of the analytic results, however, does make the graph more understandable.

Determination of the ring temperature in this fashion thus provides an independent measurement of the temperature (which is known from x-ray measurements[6] as well as a useful check of the method.

In similar fashion, elimination of T from Eqs. (7) results in either a cubic equation in y or a linear relation of the form

$$R_2 = b(\sigma)R_1 + c(\sigma) \ . \tag{11}$$

Again, the limitation $400 < T < 600$ over which (7) is valid gives a segment of the line defined by Eq. (11). Figure 4c presents this result along with exact calculations for comparison, while Fig. 4d is constructed from the exact results only. The lines, which are labelled by the value of the mirror ratio, are practically indistinguishable at small mirror ratio, implying that this quantity cannot be obtained from these measurements very accurately. However, for mirror ratio greater than three, the various lines are well separated and an accurate estimate of the loss-cone angle should be possible. Again, the expression (10) permits a simple estimate of the error in the results based on the error in the measurements.

If the mirror ratio is indeed small ($\sigma < 3$), it could perhaps be determined from a measurement of the power in either polarization separately (both $j^{(o)}$ and $j^{(e)} \sim \sigma^{1/2}$ for small mirror ratios), although in this case estimates of the various geometric factors (which cancel out when considering ratios) must be included. Alternatively, the method suggested by Tamor could perhaps be employed.[7]

Other calculations, for EBT-I parameters, exhibit similar behavior and will not be shown here. Again, the temperature can be rather easily determined as can the mirror ratio, provided it is not too small ($\sigma > 3$).

In summary, the analytic expressions for synchrotron radiation presented here are useful in their general form for understanding how the radiation scales over a wide range of parameters. In a more simplified form over a more restricted parameter regime, such as the operating conditions of EBT-S, the expressions can be inverted to give the temperature and mirror ratio of the ring in terms of quantities that will be readily measured by the University of Maryland experiment.

ACKNOWLEDGMENTS

This work was supported by the U. S. Department of Energy.

REFERENCES

1. T. Uckan, J. Wilgen, and L. Bighel, "Synchrotron emission measurements from the hot electron rings in EBT," Bull. Am. Phys. Soc. 25, 832 (1980).
2. M. Tanaka, R. J. Parosa, M. Fujiwara and NBT Group, "Radiation and Transmission Experiments in Nagoya Bumpy Torus," Joint Workshop on Electron Cyclotron Emission and Electron Cyclotron Resonance Heating, Oxford, 1980.
3. G. Bekefi, Radiation Processes in Plasmas, (Wiley, New York, 1966), Ch. 6.
4. N. A. Uckan, R. G. Spencer, and T. Uckan, "Synchrotron radiation from the hot electron rings in EBT," Oak Ridge National Laboratory Report ORNL/TM-7687 (May 1981).
5. V. K. Tripathi, E. Ott, and C. S. Liu, "Synchrotron radiation from the ring and nonlinear effects in microwave heating of EBT," U. of Maryland Preprint PL-80-025 (December 1979).

6. N. A. Uckan et al., "Physics of hot electron rings in EBT: theory and experiment," in Plasma Physics and Controlled Nuclear Fusion Research (Proc. 8th Int. Conf. Brussels 1980) Vol. I, p. 831, IAEA, Vienna (1981).

7. S. Tamor, "On the direct measurement of anisotropy of hot electron rings using synchrotron emission," SAI report LAPS-73/SAI-023-81-191-LJ (June 1981).

FIGURE CAPTIONS

Fig. 1. Comparison of analytic expressions (lines) and exact numerical calculations (circles) for radiation in the ordinary mode $j^{(o)}$ and the ratio $R = j^{(x)}/j^{(o)}$ as a function of frequency ($\nu = \omega/\omega_c$), temperature ($\tau = T/m_e c^2$), and mirror ratio (σ).

Fig. 2. Schematic diagram of the experiment.

Fig. 3. Ratio of radiation in the two polarizations at 80 GH_z (R_1) and 138 GH_z (R_2) as a function of temperature (a-b) and mirror ratio (c-d); circles are exact calculations, lines are the expressions (6).

Fig. 4. Contours of constant temperature (a-b) and mirror ratio (c-d) as a function of the ratios R_1 and R_2. Curves in (a-c) are derived from simplified expressions with exact results superimposed; curves in (b-d) are constructed from the numerical calculations directly.

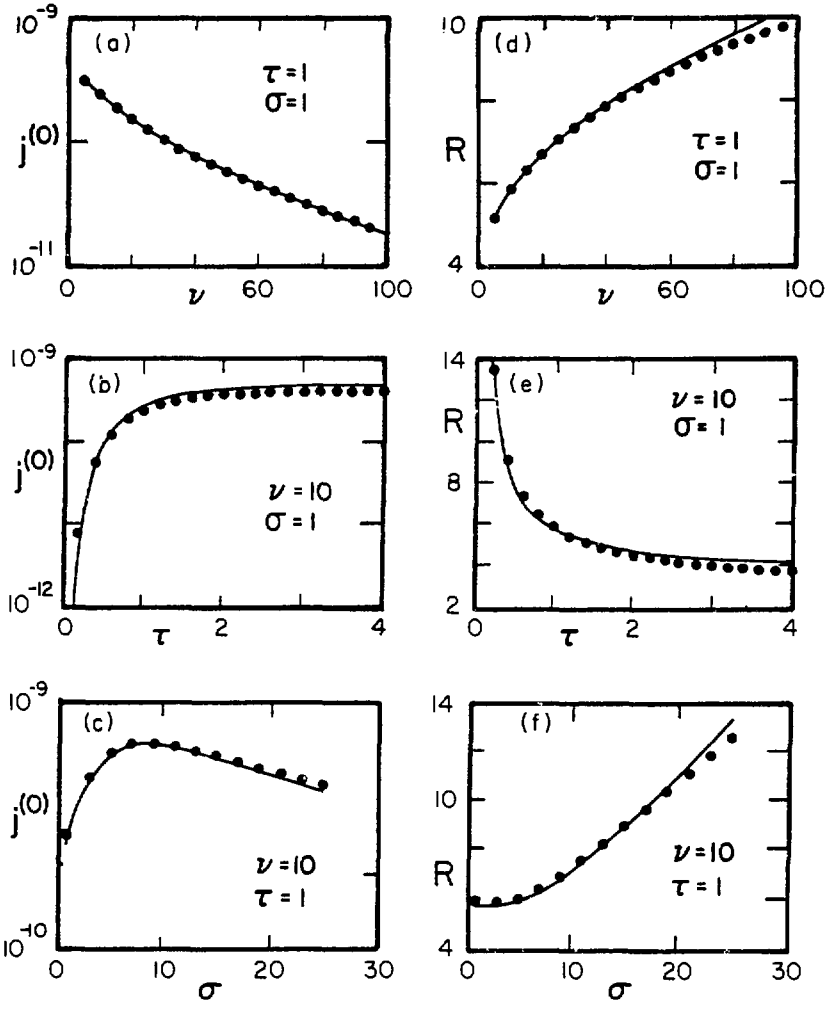

Figure 1

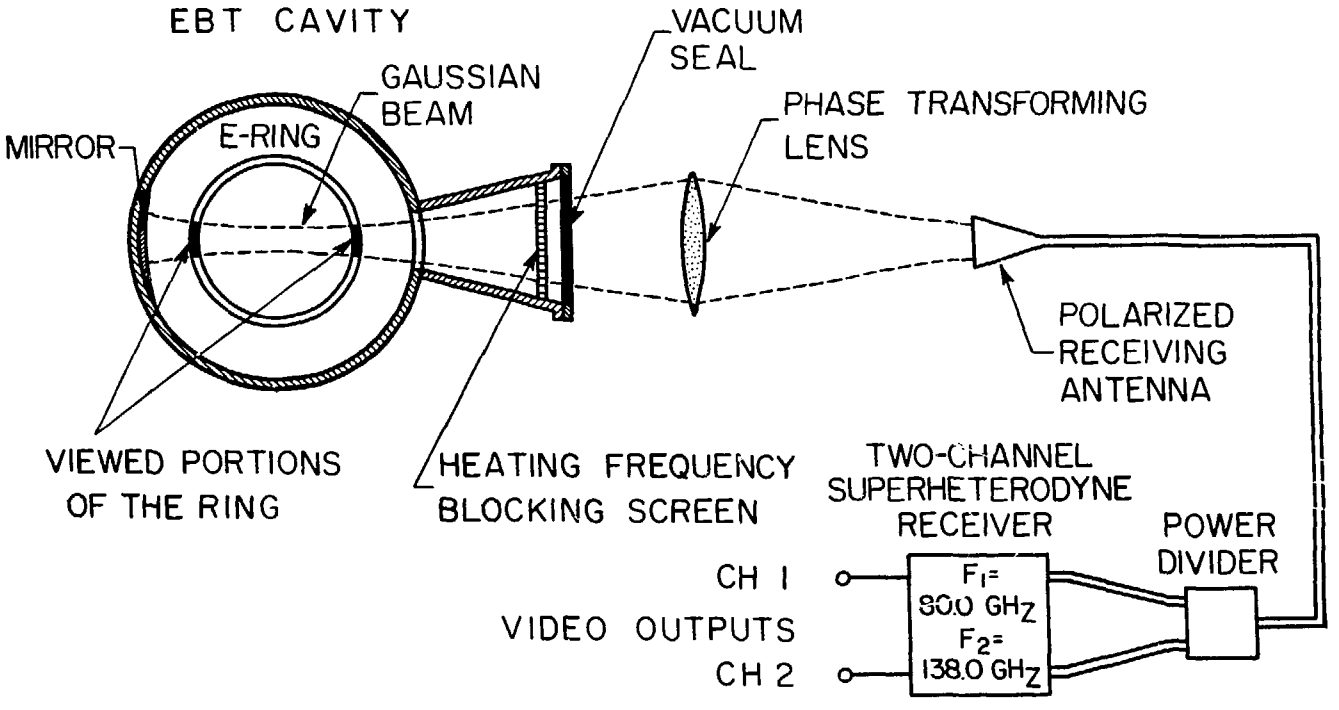
EBT CAVITY
VACUUM SEAL
GAUSSIAN BEAM
PHASE TRANSFORMING LENS
MIRROR
E-RING
POLARIZED RECEIVING ANTENNA
VIEWED PORTIONS OF THE RING
HEATING FREQUENCY BLOCKING SCREEN
TWO-CHANNEL SUPERHETERODYNE RECEIVER
POWER DIVIDER
CH 1
VIDEO OUTPUTS
CH 2
F1= 80.0 GHz
F2= 138.0 GHz

Figure 2

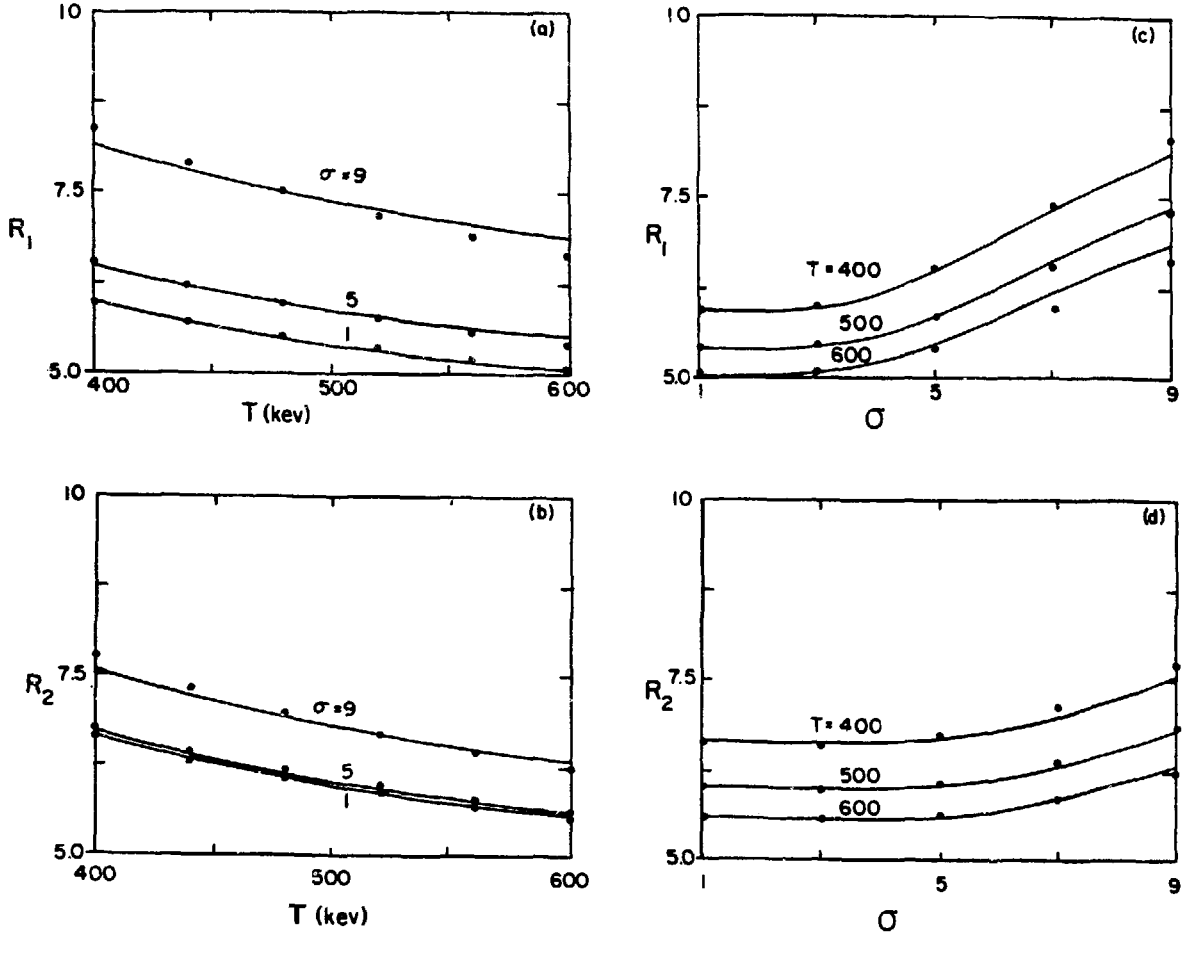

Figure 3

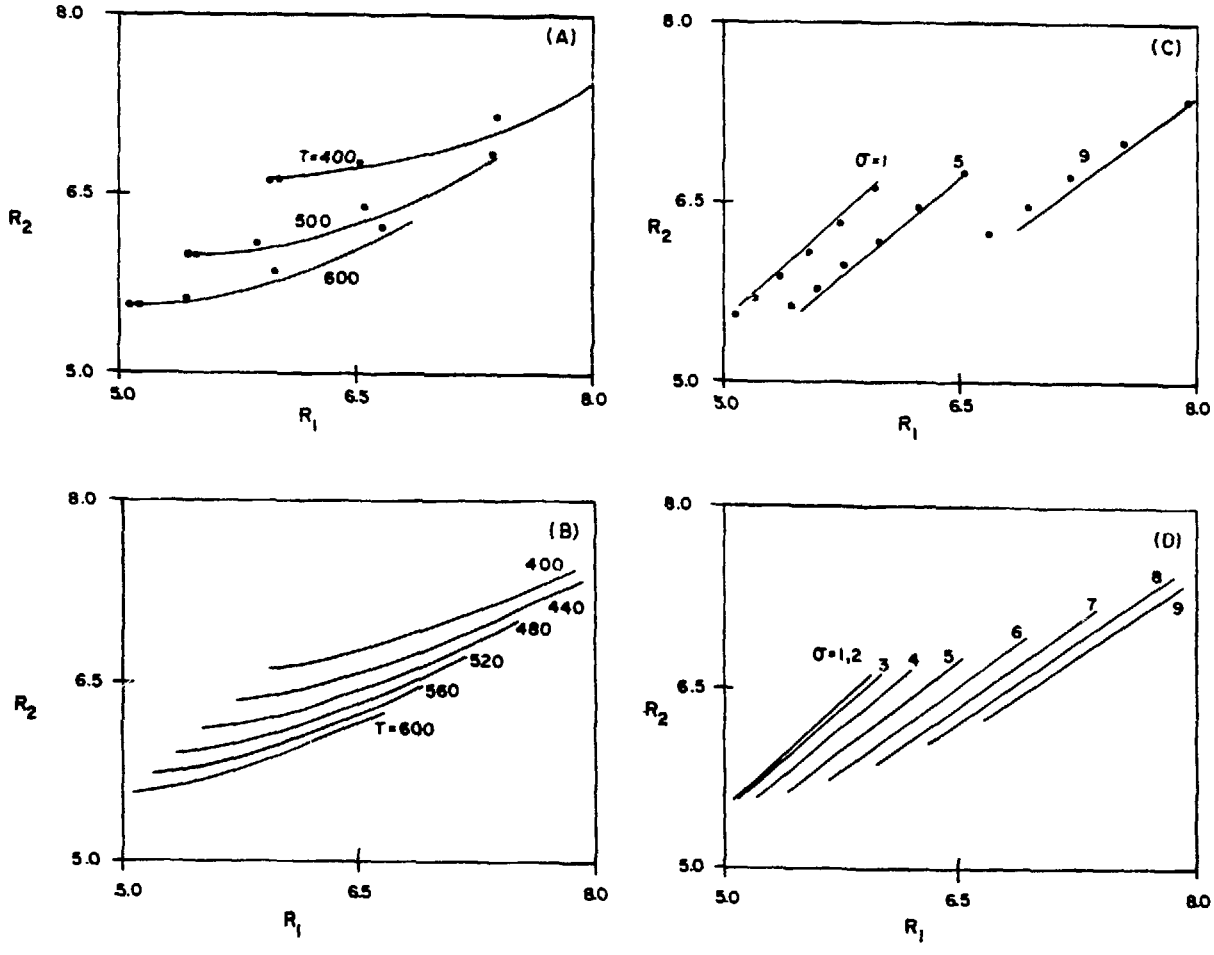
(A)
T=400
500
600
(B)
400
440
480
520
560
T=600
(C)
σ=1
5
9
(D)
σ=1,2
3
4
5
6
7
8
9
8.0
6.5
5.0
R2
R1

Figure 4

ELECTRON SYNCHROTRON EMISSION FROM THE EBT RING PLASMA*

C. M. Celata
Dartmouth College

Calculations will be presented of the electron synchrotron radiation spectrum emitted by the ring plasma in the present and planned EBT experiments. Dependence of the spectrum on parameters of the electron distribution function and the angle of emission with respect to the magnetic field direction will be displayed. Calculations of the total power loss from the ring plasma due to this mechanism will be presented, and its dependence on the dimensions of the ring and ring plasma parameters will be discussed.

*Work supported by the U.S. Department of Energy.

7. IONS, TANDEMS, EQUILIBRIA, AND POWER BALANCE

ION RING SCALING STUDIES FOR AN EBT REACTOR

M. R. Gordinier and R. J. Kashuba
McDonnell Douglas Astronautics Company
St. Louis, MO 63166

The Nelson-Lee-Van Dam ring-core stability criteria constrains the maximum core beta at the annulus to a value proportional to the ratio of the ring thickness to the radius of curvature. Since a substantial core beta is desireable for an economic reactor, thick rings may be necessary if beta is to be increased consistent with the ring-core stability relation. Therefore, the power balance of large gyroradii ion rings in an EBT reactor is investigated. Previous calculations have demonstrated that charge-exchange is the dominant energy loss mechanism for ion rings. A model for the ion rings has been coupled to SPUDNUT, a neutral transport code, in order to evaluate the total ring power loss for a variety of ring radii, thicknesses, temperatures, and neutral densities. Results will be presented indicating that a broad window exists in which the goal of ring thickness, acceptable power losses, and sufficient ring beta can be simultaneously achieved.

INTRODUCTION

The essential feature of an EBT is the stabilization of the toroidal plasma by the presence of high beta annuli which form in the midplane between coils. These annuli perform their stabilizing function by modifying the magnetic field gradient near the plasma edge. In all EBT experiments to date, the annulus has consisted of hot relativistic electron rings. However, due to synchrotron losses, the electrical power required to maintain these high beta electron rings in an EBT reactor could result in a circulating power fraction large enough to seriously impact the economics of the device. In light of this problem, we have examined the power lost by ion annuli of sufficient beta to perform the field modification.[1] For a wide variety of conditions, high beta ion rings with more favorable power balances are found to exist.

In addition to the improved power balance, ion rings also offer the potential of higher core beta. The Nelson-Lee-Van Dam ring/core stability criteria [2,3] constrains the maximum core beta at the annulus to a value proportional to the ratio of ring thickness to the magnetic radius of curvature. Thus, by their inherently larger gyroradii, ion rings may provide a mechanism by which core beta can be increased consistent with the ring/core stability relation.

The energy loss processes appropriate to ion rings are very different from those encountered in the analysis of electron rings. The major energy loss mechanisms for ring ions are: (1) drag losses on core electrons, (2) drag losses on core ions, and (3) charge-exchange and ion impact ionization between ring ions and core neutrals.

In general, these losses decrease with increasing ring ion energy, leading to an unstable increase in ring temperature. The ring ion energies are, however, limited by the size of their Larmor orbits and by the onset of severe adiabatic losses.

In the present EBT-S device the electron ring temperature is about 500 kev, a value consistent with the temperature being limited by the adiabaticity relation ρ_e/R_c = constant. Using this relation and estimates for an EBT reactor, i.e., a magnetic field at the annulus of about 2 Tesla and a plasma radius of 120 cm, the maximum temperature of a D^+ ion ring would be about 1 MeV. In this temperature regime the major ion energy loss mechanism is charge-exchange. Therefore, a model for the ion rings has been coupled to SPUDNUT[4], a two species, two temperature transport code, in order to evaluate the total ring power loss for a variety of ring radii, thicknesses, temperatures and neutral densities.

The Neutral Model

As neutral atoms of energy E_o enter the plasma edge, they are attenuated by their interaction with the plasma via electron impact ionization, ion impact ionization, and ion-neutral change exchange. As a function of position within the plasma, the neutral flux is given by:

$$\Gamma(X) = 2\Gamma_o E_3(\beta_o(x)) \tag{1}$$

where Γ_o is the neutral flux at the plasma edge (x=0), E_3 is the third exponential integral, and β_o (x) is the "optical depth", defined as:

$$\beta_o(X) = \int_o^x \frac{\mu_o(X', E_o)}{V_o} \, dx' \tag{2}$$

where: $\mu_o(x, E_o) = n_e(X)\langle\sigma V\rangle_e + n_i(X)\,[\langle\sigma V\rangle_i + \langle\sigma V\rangle_{cx}]$

$$V_o = (2kT_o/m_i)^{1/2}$$

The reaction rates $\langle\sigma V\rangle$ depend upon the coordinate x through the electron and ion temperatures, Te(x) and Ti(x). Here $n_e(X)$ and $n_i(X)$ refer to the electron and ion densities, respectively.

The total absorption rate of the neutral flux at each point in the plasma is:

$$A\ (x) = -\frac{d\Gamma}{dx} \tag{3}$$

Since a charge-exchange absorption event produces a new neutral in the plasma, the charge-exchange source rate for first generation internally born neutrals is given by:

$$S_1\ (X) = A\ (X)\ \frac{n_i\ (x)\ \langle\sigma v\rangle cx}{\mu_o\ (x,E_o)} \tag{4}$$

The flux of neutrals born at a position x' which reach a point x is given by:

$$\Gamma\ (X) = 1/2\ S_1\ (X')E_2\ (\beta(x,x'))dx' \tag{5}$$

$$\beta\ (x,x') = \int_{X'}^{X} \frac{\mu\ (x'',x')}{V\ (x')}\ dx''$$

Differentiating $\Gamma(x)$ with respect to x to obtain the absorption rate and then multiplying by the probability that the absorption was due to a charge-exchange event gives the source rate at x of second generation charge-exchange neutrals. By generalizing the process, the total change-exchange source rate for the (P+1) generation is related to the (P) generation by the integral equation.

$$S_{p+1}\ (x) = \int_o^d K\ (x,x')\ S_p\ (x')dx' \tag{6}$$

where: $$K(x,x') = \frac{\frac{1}{2} \cdot n_i(x)\ \langle\sigma v\rangle\ cx}{V(x')}\ E_1\ (\beta(x,x'))$$

d = Plasma width

Note that the kernel K (x,x') is independent of generation P, and need only be evaluated once.

Symbolically this integral equation can be written:

$$S_{p+1}(x) = K\, S_p(x) \tag{7}$$

The total charge-exchange source area S(x) is given by summing over all generations:

$$S(x) = \sum_{p=1}^{\infty} S_p(x) = (1 + K + K^2 + ---)S_1(x) \tag{8}$$

$$= \frac{S_1(x)}{1-K}$$

or:

$$S(x) = S_1(x) + \int_0^d K(x,x')\, S(x')\, dx' \tag{9}$$

Here the inhomogeneous term $S_1(x)$ is given by equation (4). Once S(x) is determined, such quantities as the ionization rate due to electron impact ionization, $S_e(x)$, and the energy lost by the ions due to charge-exchange, W_{cx}, can be determined:

$$S_e(x) = \frac{n_e(x)\ \langle\sigma v\rangle_e}{n_i(x)\ \langle\sigma v\rangle_{cx}}\ S_1(x) + \int_0^d \frac{n_e(x)\ \langle\sigma v\rangle_e}{n_i(x)\ \langle\sigma v\rangle_{cx}}\ K(x,x')\, S(x')dx' \tag{10}$$

$$W_{cx}(x) = [3/2kT_i(x)-E_0]S_1(x) + \int_0^d \frac{3}{2}k\ [T_i(x) - T_i(x')]K(x,x')\, S(x')dx' \tag{11}$$

Equation (9) is solved by a finite-difference technique which recasts the integral equation into a matrix equation. Comparative calculations have been made with sophisticated Monte Carlo neutral transport codes and excellent agreement has been obtained.

Two Species Generalization

The preceeding derivations have assumed a plasma composed of electrons and one species of ions. However, in order to use the code to model hot ion rings, the model must be generalized to two distinct ionic species (core and ring) with two distinct temperature profiles. Labelling the core and ring ions by C and R, respectively, by analogy:

$$S^c(x) = S_1{}^c(x) + \int_0^d [K_{cc}(x,x')\, S^c(x') + K_{rc}(x,x')\, S^r(x')]dx'$$
$$S^r(x) = S_1{}^r(s) = \int_0^d [K_{cr}(x,x')\, S^c(x') + K_{rr}(x,x')\, S^r(x')]dx' \qquad (12)$$

where: $$K_{ij}\,(x,x') = \frac{1/2\; n_i^j(x)\; \langle\sigma v\rangle_{cx}^{ij}}{V^i(x')}\; E_1\;(\beta^i(x,x'))$$

Note that these equations are coupled due to interspecies charge-exchange. The two integral equations for the charge-exchange source rates of core and ring ions are discreetized into a "super-matrix" equation which is easily solved:

$$\begin{bmatrix} \bar{\bar{I}} - \bar{\bar{K}}_{cc} & -\bar{\bar{K}}_{rc} \\ -\bar{\bar{K}}_{cr} & \bar{\bar{I}}-\bar{\bar{K}}_{rr} \end{bmatrix} \begin{bmatrix} \vec{S}_c \\ \vec{S}_r \end{bmatrix} = \begin{bmatrix} \vec{S}_1{}^c \\ \vec{S}_1{}^r \end{bmatrix} \qquad (13)$$

The energy lost from the ring ions is then determined by analogy to equation (11).

Ion Ring Model

Two models for potential ion ring geometry have been investigated: (1) a "shielded" ring model (Fig. #1) and (2) an "unshielded" model (Fig. #2).

In the shielded model, the incoming neutral gas encounters a layer of core plasma before interacting with the ring ions. This offers the potential of a reduced neutral flux in the ring region and thus, lower ring losses. In the unshielded case, the ring sees the total unattenuated neutral flux.

For the assumed EBT reactor parameters given in Table #1, the ring temperature and thickness in addition to the ring/core density ratio and edge neutral density were varied to parameterize the ring losses.

RESULTS

The results for each ion ring geometry are presented in Figs. #3-6. In each case, the ring losses per unit axial length are plotted as a function of ring temperature for a variety of ring thicknesses. Tables #2, 3 contain a summary of the ring parameters. For each ring geometry, two ring ion species are considered, D^+ and H^+.

Note that in all cases, the ring losses decrease with increasing ring temperature, since $\langle \sigma v_{CX} \rangle$ falls rapidly in this temperature regime. As expected, thicker rings suffer more losses than thinner rings, but the relationship is not a linear function of annulus width.

The desirability of a shielded ring geometry is demonstrated by comparing shielded and unshielded ring loss curves. Shielded rings can provide a factor of 10 reduction in ring losses, since

the neutral population in the vicinity of the ring is reduced due to the interaction and attenuation of the neutral flux with the shielding plasma.

Assuming D^+ rings at 800 kev for the reactor configuration in Table #1, the ratio of ring power per unit axial length for a variety of ring half-widths is presented in Table #4. Note that in these absolute terms both the shielded and unshielded scenarios have acceptable efficiencies, ranging from .2 percent to 6 percent. By comparison, the losses associated with a comparable electron ring would exceed 10 watts/cm^3, while for a D^+ ion ring the losses are about 5×10^{-2} watts/cm^3, a clearly superior result.

It is important to note that for all of the ion ring power loss calculations presented here, an edge neutral density of 2×10^9 cm^{-3}, has been assumed. Since ring losses are directly proportional to neutral density, a reduction of the neutral density to 2×10^8 cm^{-3} would decrease the already low ring losses by an order of magnitude. This ease with which the ion ring losses can be controlled contrasts sharply with the corresponding actions necessary to reduce electron ring losses and highlights the flexibility of the entire ion ring scheme.

SUMMARY

A brief description of a two species, two temperature ion ring/core model has been given and preliminary ion ring power losses presented for a variety of hypothetical ring geometries. These results demonstrate: (1) that based on power balance considerations, a rather broad window exists in ring thickness, temperature and neutral density for which the power supplied to the rings comprises an acceptable fraction of overall reactor electrical output, (2) that the shielding of the ion rings by a layer of cool core plasma can reduce overall ring losses by an order of magnitude over the unshielded case, and, (3) that the magnitude of ion ring losses can be easily manipulated by controlling the edge neutral density, a feature not available for electron rings.

ACKNOWLEDGMENT

This research was supported by McDonnell Douglas Independent Research and Development Funds and United States Department of Energy under project 80-MF-3.

REFERENCES

[1] R. J. Kashuba and W. B. Ard, "Annulus Power Losses in EBT," EBT Ring Physics, Proceedings of the Workshop, Oak Ridge National Laboratory, CONF-791228 (1980).

[2] D. B. Nelson, "Effects of Hot Electrons on Magnetohydrodynamic Modes in ELMO Bumpy Torus," Phys. Fluids, 23 1850 (1980); J. W. Van Dam and Y. C. Lee, "Stability Analysis of a Hot Electron EBT Plasma," EBT Ring Physics, Proceedings of the Workshop, ORNL CONF-791228 (1980).

[3] EBT Stability Theory, Proceedings of the Workshop. Ed. N. A. Uckan, Oak Ridge National Laboratory CONF-810512 (1981).

[4] K. Audenaerde, G. A. Emmert, and M. Gordinier, "SPUDNUT: A Transport Code for Neutral Atoms in Plasmas," J. Comp. Phys. 34, 268 (1980).

Table 1. EBT Reactor Parameters

MAJOR RADIUS	30 m.
MINOR RADIUS	1.5 m.
NUMBER OF COILS	36
CENTRAL T_e	30 kev; PARABOLIC
CENTRAL T_c	30 kev; PARABOLIC
CENTRAL	1.5×10^{14} cm^{-3}; PARABOLIC
CORE/ANNULUS DENSITY RATIO	10
THERMONUCLEAR POWER	3433 MW_{th}, 1144 MW_e
EDGE NEUTRAL DENSITY	2×10^9 cm^{-3}.
ANNULUS LENGTH/SECTOR LENGTH RATIO	.2

Table 2. Unshielded Ring Parameters

ΔX (cm)	R_{Ring} (cm)	n_a (cm^{-3})
4.7	145.3	1.2×10^{12}
9.7	140.3	1.9×10^{12}
19.3	130.7	3.5×10^{12}

Table 3. Shielded Ring Parameters

ΔX (cm)	R_{Ring} (cm)	$n_a (cm^{-3})$
4.6	126.0	4.5×10^{12}
9.3	126.0	4.5×10^{12}
20.0	126.0	4.5×10^{12}

Table 4. Comparison of Electrical Consumption of Shielded and Unshielded D+ Rings per unit axial length for several ring half-thickness.

APPROXIMATE ΔX (cm)	P_{Ring}/P_{el} (%)	
	UNSHIELDED	SHIELDED
20	6	1
10	4	.3
5	2	.2

FIGURE 1 SHIELDED RING MODEL

13-4753

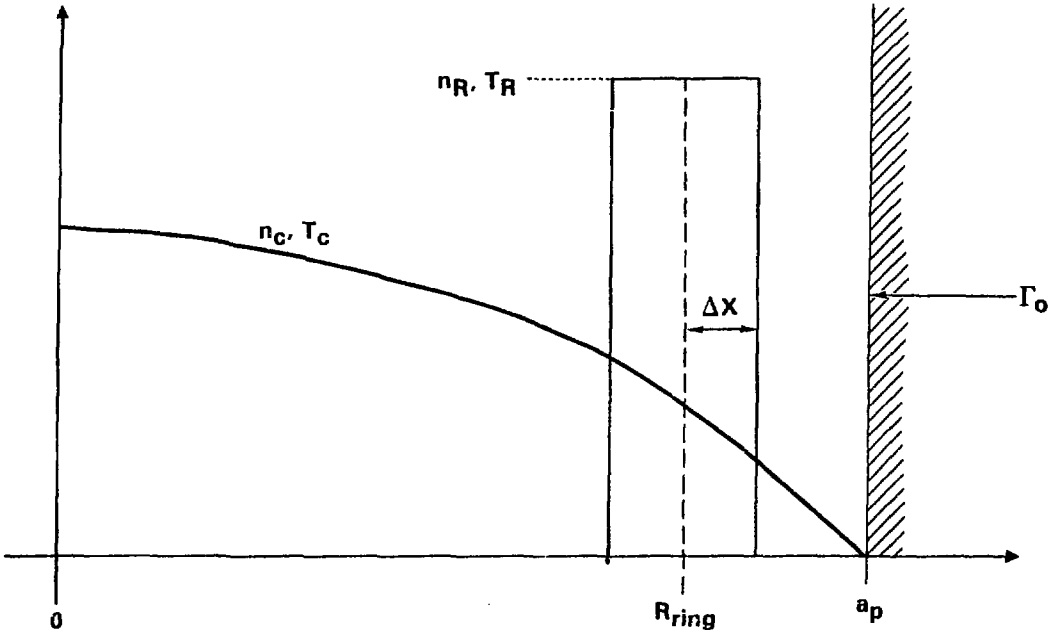

FIGURE 2 UNSHIELDED RING MODEL

13-4784

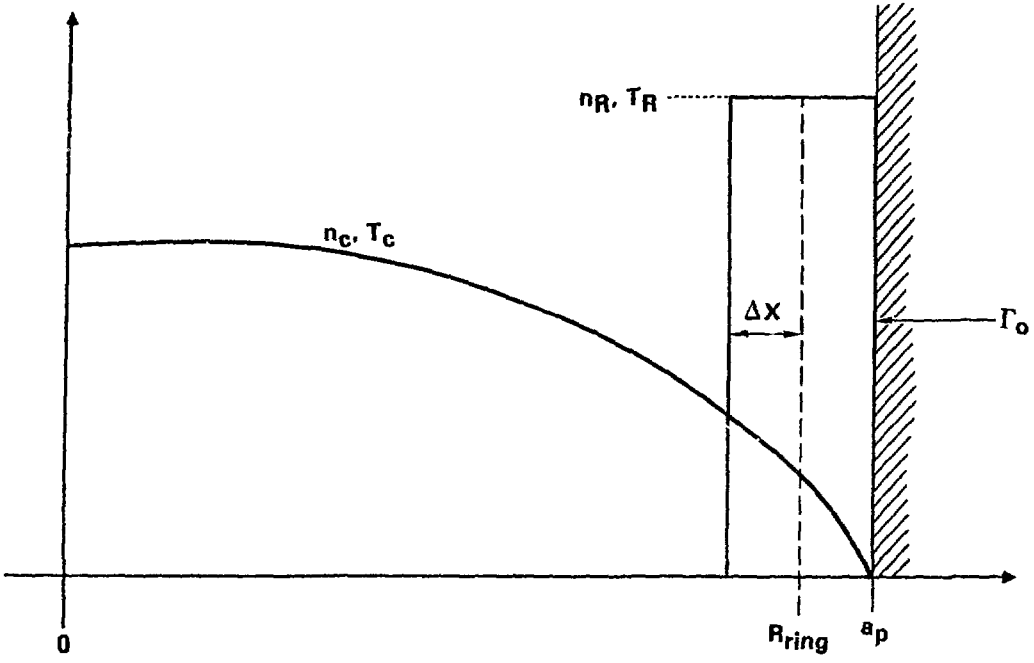

FIGURE 3 UNSHIELDED D^+ RING

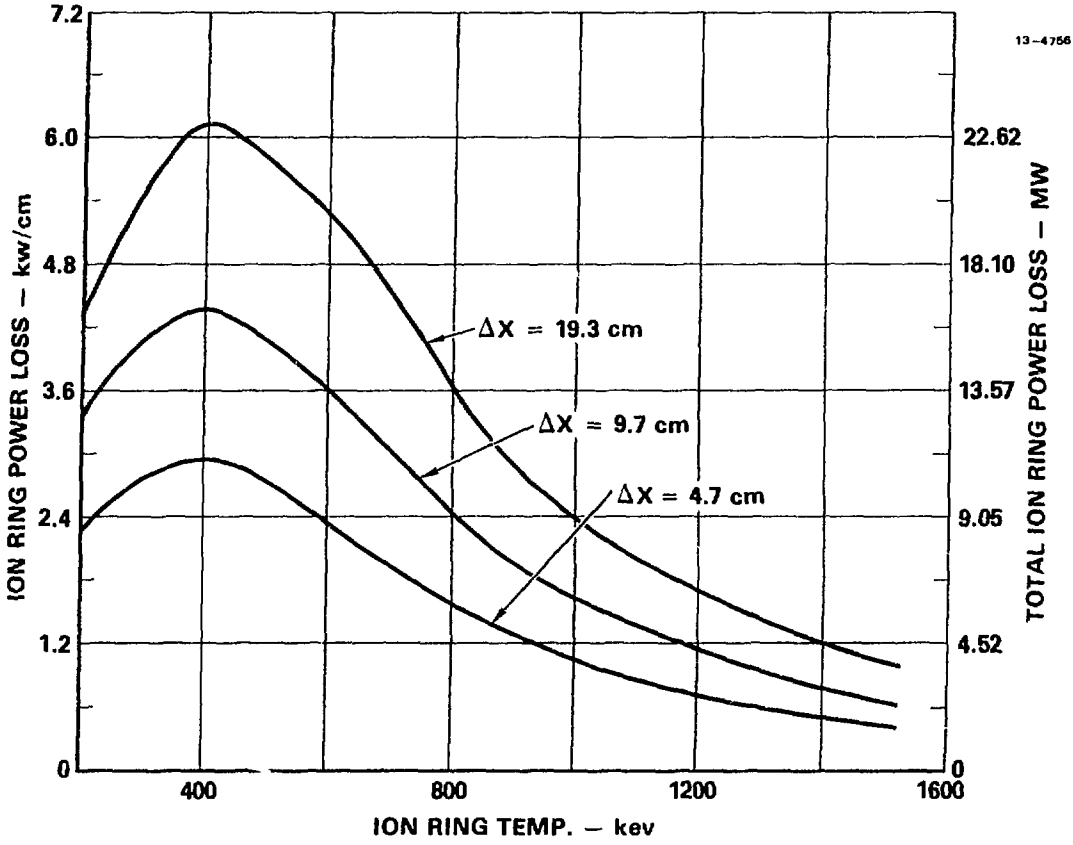

FIGURE 4 UNSHIELDED H^+ RING

13-4767

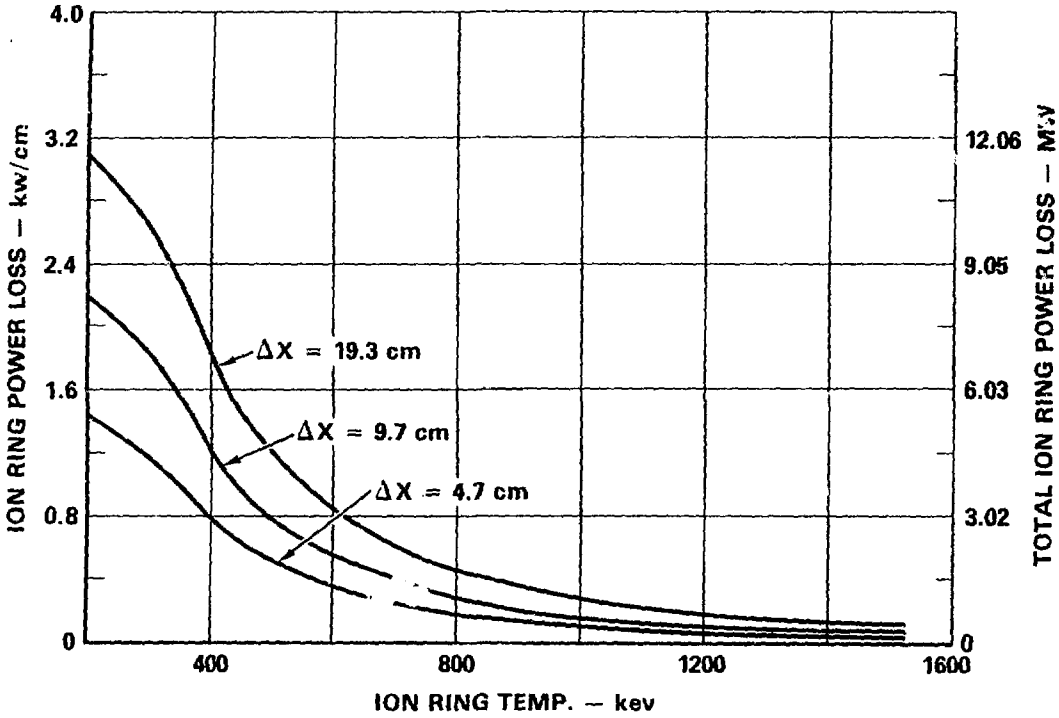

FIGURE 5 SHIELDED D^+ RING

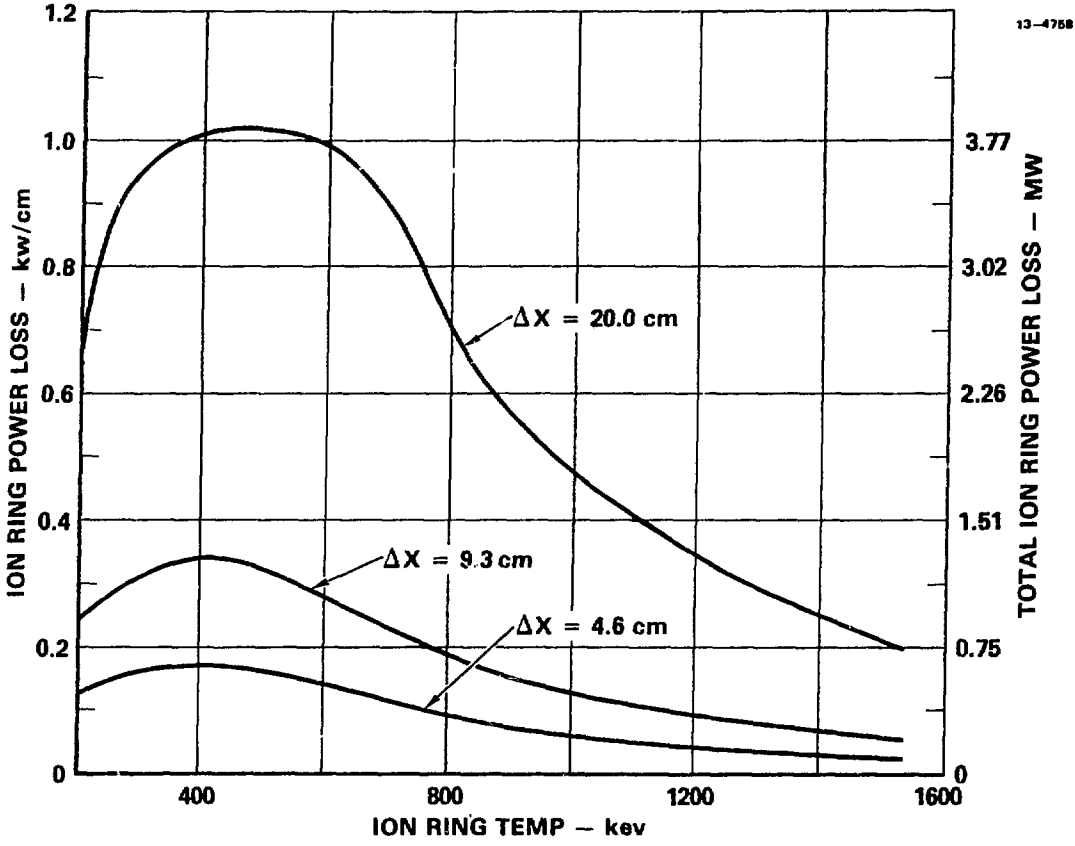

FIGURE 6 SHIELDED H^+ RING

13-4759

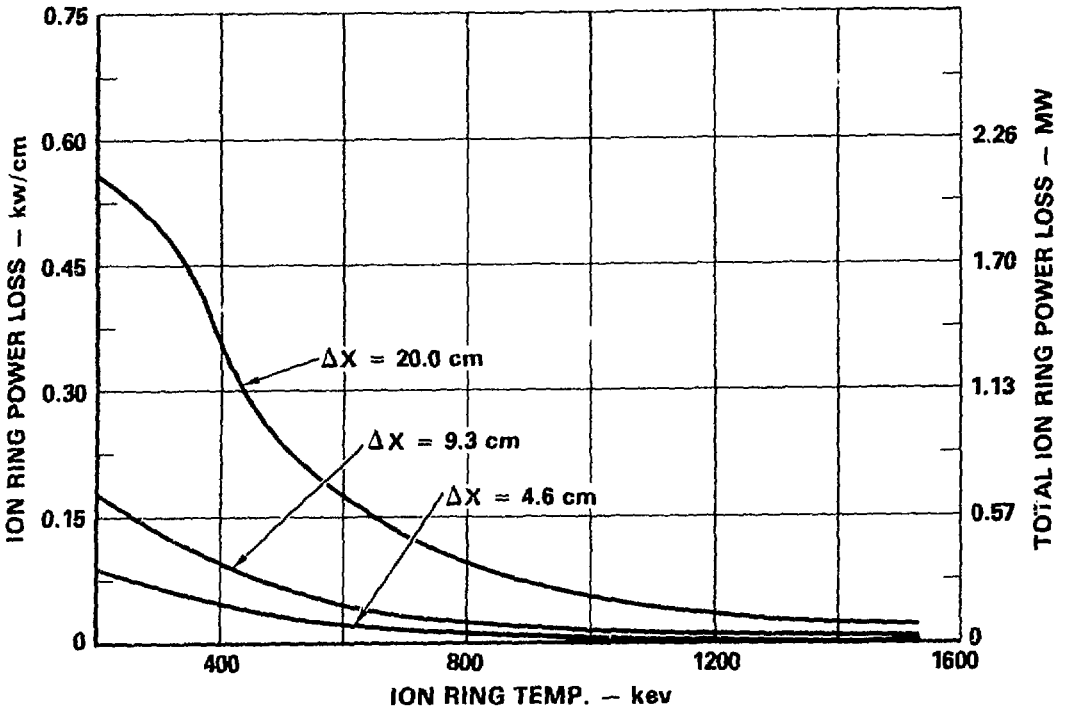

RING POWER BALANCE OBSERVING PLASMA STABILITY CONSTRAINTS*

R. B. Campbell
TRW, Incorporated
Redondo Beach, California 90278

B. G. Logan
Lawrence Livermore National Laboratory
Livermore, California 94550

ABSTRACT

Ring power balance is performed for an E-ring stabilized tandem mirror reactor, taking into account constraints imposed by plasma stability. The two most important criteria are the stability of the core interchange and hot electron interchange modes. The former determines the ring thickness, the latter determines the minimum hot electron temperature; both quantities are important for power balance. The combination of the hot electron interchange constraint and the fact that the barrier density is low places the operating point on the synchrotron dominated branch of power balance. The reference case considered here requires a reasonable 34 MW of heating power deposited in the rings. We also have examined the sensitivity of the required ring power on uncertainties in the numerical coefficients of the stability constraints. We have found that the heating power is strongly affected.

*Work sponsored by DOE Contract W-7405-ENG48, and TRW IR&D

1. INTRODUCTION

Progress in the finite-beta theory of the Elmo Bumpy Torus (EBT) concept[1] suggests the possibility of using hot electron rings to stabilize the inner field lines of the modified-cusp TMR and also the axisymmetric axicell TMR without a quadrupole anchor. (An EBT-stabilized axi-cell TMR has also been referred to as a Symmetric Tandem Mirror, or STM, at TRW[2]). Compared to EBT, E-ring stabilized TMR's would need fewer rings (minimum of two) because of linear geometry, thus reducing electron cyclotron resonant heating (ECRH) power. The most important physics issue for E-ring TMR's, besides plug microstability common to all TMR's, are the same issues concerning EBT; namely, interchange stability of the hot electron ring itself and of the plasma within the ring, and the energy losses by the relativistic ring electrons. To mitigate the latter, the rings can be located in thermal barriers where the field is low (minimizing synchrotron radiation loss), and the density is low (minimizing electron drag loss).

There are certain aspects of the ring stabilized TMR problem which make it different from EBT. The thermal barrier electron density is about a factor of ten lower than the density of the fusion grade plasma in the central cell, which is comparable to that in an EBT reactor. The minimum ratio of cold to hot density at the ring is fixed by requiring stability of the hot electron interchange mode. The lower cold density implies a lower hot density and for the same beta, higher ring temperature, T_h, than in a corresponding EBT case. This suggests that the power balance of a ring stabilized TMR will be synchrotron dominated, rather than drag dominated. This will be quantified later in the paper. Note that this conclusion is based on the use of an axially local hot electron interchange criterion. Since flutes extend into the central cell, a field line average criterion might be the correct one to use. In that case, the barrier electron density would be replaced by the central cell density. Correspondingly, the ring temperature would be in the range of that anticipated for EBT, perhaps improving the power balance from that presented here.

2. MOTIVATION AND CONTENT

In this paper, we examine the power balance of a hot electron ring in a ring stabilized TMR. The new feature of this calculation is to include both macro- and micro- stability constraints of the hot and cold plasma components in the vicinity of the ring. The recent work of Uckan, Spong, and Nelson[3] on EBT ring beta limits and power balance includes parametrically the effect of adhering to the core interchange mode, but does not include the limitation imposed by the hot electron interchange mode, since n_c/n_h and T_h were left as free parameters. In our work, we emphasize the parameter range of interest for tandem mirrors (i.e. low background density and high background temperature), as well as apply additional stability constraints. The constraints we shall use have been documented in the proceedings of the recent EBT stability workshop[4]. The stability constraints and parameters they determine are listed below:

(1) Diamagnetic well creation - determines the minimum hot electron beta, $\beta_h(r_A)$ to create good dl/B on the outside of the ring.

(2) Core interchange - determines ring half thickness, Δ, for a given core beta at the ring, $\beta_c(r_A)$.

(3) Hot electron interchange - determines the minimum value of n_c/n_h, and for a given hot electron beta, $\beta_h(r_A)$, determines the minimum T_h.

(4) Compressional Alfven mode - determines the maximum value of n_c/n_H, not usually important unless T_h is greater than 100MeV.

(5) Temperature anisotropy - determines upper bound on barrier electron density, $n_c(r_A)$, at the ring.

(6) Loss cone w/ anisotropy - determines a lower bound on the barrier electron density at the ring.

(7) Whistler mode - in some cases can determine maximum ring beta for a given degree of anisotropy of the ring electrons, $T_\perp/T_\parallel$.

(8) Mirror mode - usually determines the maximum ring beta for a given $T_\perp/T_\parallel$.

The power balance here includes terms for synchrotron radiation, frictional drag between barrier and ring electrons, pitch angle scattering of ring electrons, and bremmstrahlung. The equations are the same as those used by Borowski, et.al.[5] in solving the unconstrained EBT ring power balance problem. These terms will not be presented here, having had ample coverage in reference 5. Explicit functional forms for the constraints 1-8

above will be presented in Section 4 of this paper. We do not include terms in the power balance which account for enhanced pitch angle scattering due to non-adiabatic behavior of ring electrons, having assumed that for reactor sized rings, the classical loss processes dominate in temperature ranges of interest.

The majority of the constraints 1-8 are derived using an approximate treatment of a very complicated theory[4]. As a consequence, there is uncertainty in their exact form. Usually, the uncertainty lies in the numerical value of the leading coefficients of the formula, but in certain cases the functional form may change. These uncertainties, as we will show in this paper, can effect the required power to the rings quite dramatically

Another feature of our model not treated previously is the inclusion of axial and radial profiles of hot ring electron temperature and density, and magnetic field strength. The radial profile of core pressure, p_c, on the inner half of the ring is derived from the well known MHD marginal stability criterion, $p_c' > -2\gamma pc/R_c$, where γ is the ratio of specific heats and R_c is the (radially dependent) radius of curvature. We find that including the profile of hot pressure is important for determining the required power, and results will be presented in Section 5 to support this claim.

3. TANDEM MIRROR CONFIGURATIONS

The EBT-stabilized axicell (STM) and the modified-cusp TMRs are shown in Figure 1(a) and 1(b) respectively. We examine only the power balance of the former configuration in this paper, but both are now briefly described for the sake of completeness. For the axi-cell configuration, we put the hot electron ring in a barrier electron layer radially outside the flux tube mapping to the central cell. This is necessary so that sloshing ions will remain adiabatic on flux lines plugging the central cell, and so that the ring electrons are at lower magnetic field than nearer the axis. There is a power balance tradeoff between short barriers with high field and longer barriers with lower field, lengths and fields chosen in order to satisfy hot ion adiabaticity. The reference case considered here was optimized in this regard in the absence of ring electrons; it is not clear whether this is the optimum length/field combination in their presence, and requires further study.

Since the electron ring is outside the flux tube connecting to the central cell plasma, the central cell plasma pressure gradient must be stabilized by having the axiplug barrier pressure gradient smaller than that allowed by local marginal stability. For the purposes of this paper, we shall take it to be half the maximum allowable gradient.

In the modified cusp TMR, shown in Figure 1(b), the electron ring occupies the indicated hatched region just inside the annular flux tube connecting to the central cell. Since the internal plasma pressure gradient in the central cell is stable with respect to the local field gradient, the annulus parameters need only be designed to locally stabilize the inside of the plug region. This means that the full marginally stable pressure gradient can be supported, unlike the ring stabilized axi-cell. This has important consequences with respect to power balance, since for a given on-axis barrier electron beta, the barrier beta (density) at the ring can be smaller with larger gradient, thereby reducing power requirement. In addition, the electron ring need only exist in a thin layer inside the edge of the annulus of flux, to stabilize the last bit of pressure drop. Putting the annulus inside the flux tube, and allowing the barrier electrons to extend inward to the ring, we can allow the local ring magnetic field to

drop below the adiabatic limit ($\sim$2.6T) for sloshing ions at 600keV, since lower energy ions can be permitted within the ring. Then the local ring vacuum field can be reduced to 2T, lowering synchrotron power, and corresponding to second harmonic heating at 120 GHz. The annulus field and axial field scale length should be large enough so that the ring electron adiabatic energy limit ($\gtrsim$ 50 MeV) is well above that which is limited by synchrotron radiation. (This is also true of the axi-cell TMR case.)

4. BASIC EQUATIONS AND ANALYSIS

In this section, we present the analytic forms for the stability constraints used in the analysis, and how these constraints are applied and parameters varied. The equation for the required ring power is identical to that given in equation 2.2 of reference 5, with the exception that the densities and temperatures of the ring, the barrier electron density, and the magnetic field strength are spatially dependent, which requires that the volume integral be evaluated numerically.

These profiles of $n_h(r,z)$, $T_h(r,z)$, $n_c(r,z)$ and $B(z)$ are shown pictorally in Figure 2, and are given by:

$$n_h(r,z) = n_h(r_A,0) \exp\left[-(r-r_A)^2/\Delta^2 - (2z/r_A)^2\right] , \tag{1}$$

$$T_h(r,z) = \frac{n_h(r,z)}{n_h(r_A,0)} \; T_h(r_A,0) \quad , \tag{2}$$

$$n_c(r) = n_c(r_A) \begin{cases} \exp\left[-\gamma X (r^2-r_A^2)/r_A R_c(r_A)\right] & \text{for } 0 < r < r_A \\ \exp\left[-\tfrac{1}{2}(r^2 - r_A^2)/(\Delta r_A)\right] & \text{for } 0 < r < r_A + \Delta \end{cases} , \tag{3}$$

and for $B(r,z)$ we take the standard bumpy cylinder model. Here, r_A is the annulus radius, also taken as the ring length, Δ is the ring half thickness, $R_c(r_A)$ is the radius of curvature at the ring, and X is a measure of how much less the pressure gradient is than the marginally stable one. For the baseline axicell case, $X = \frac{1}{2}$, and we shall examine the sensitivity of changing this variable from $\frac{1}{2}$ to 1 in Section 5.

The constraint functions have been obtained from the recent literature on EBT stability[4]. We now present and discuss these constraints in the order in which they were introduced in Section 2.

To dig a diamagnetic well which will stabilize the barrier plasma from interchange modes, the total beta must exceed:

$$\beta_h(r_A) + \beta_c(r_A) \geq \frac{4\Delta}{\langle R_c \rangle} \tag{4}$$

for $\beta_h\ (r_A) \geq \beta\ (r_A)$, where $\langle R_c \rangle$ is a field line averaged radius of curvature. The answer obtained for $\langle R_c \rangle$ depends upon how one does the average. To test the sensitivity of the power balance result to $\langle R_c \rangle$, we replace $\langle R_c \rangle$ with $R_c(r_A)/C_{gb}$ and allow C_{gb} to vary between the plausible limits of $\frac{1}{2}$ to 1.

The core interchange criterion, also called the Nelson, Van Dam, Lee (NVL) criterion is given by:

$$\beta_c \lesssim 2\, C_{ci}\ \frac{\Delta}{R_c(r_A)}\ \frac{1}{(1+\beta_h)} \tag{5}$$

where C_{ci} can vary between 1 and 2, depending upon the details of the hot electron distribution function.

The stability of the hot electron interchange mode and the compressional Alfven mode places lower and upper limits on the ratio n_c/n_h at the ring. The criterion can be compactly written[6]:

$$\frac{2\ \alpha\left(\frac{k_\theta}{k_\perp}\right)^2 \frac{R_c}{\Delta}\ \beta_h}{\left(1-\alpha\left(\frac{k_\theta}{k_\perp}\right)^2 \left|\frac{V_{k_\perp}}{\omega_{ci}\Delta}\right|\right)^2} < \frac{V_A^2}{V_{k_\perp}^2} < \frac{\alpha^2\ K_\perp^2\ \Delta\ R_c}{2\ \beta_h\left(1+\alpha\left(\frac{k_\theta}{k_\perp}\right)^2 \left|\frac{V_{k_\perp}}{\omega_{ci}\Delta}\right|\right)} \tag{6}$$

where $V_{k\perp}$ is the hot electron curvature drift velocity evaluated with the perpendicular temperature, $k_\perp$ and k_θ are the perpendicular and poloidal wave vectors, ω_{ci} is the cyclotron frequency, and V_A is the Alfven speed. The left hand limit is the compressional Alfven, and the right hand limit is the hot electron interchange. The choice we make for the mode spectrum here is that $k_\perp \sim \pi/\Delta$, and $k_\theta/k_\perp \sim \Delta/r_A$. The parameter α is given by:

$$\alpha = 1-\frac{\beta c}{2C_{ci}}\ \frac{R_c(r_A)}{\Delta}\ (1+\beta_h)\,. \tag{7}$$

Note that at the NVL limit, $\alpha \to 0$, which in turn yields from the hot electron interchange constraint that $n_c/n_h > \infty$ for stability. This means that for a given β_h, $T_h \to \infty$ as well. We shall not retain this functional form for α here, but instead treat it as a parameter with the reasonable range of (1/5, 1). Power balance is very sensitive to the value of α.

Stability of modes driven unstable by temperature anisotropy and loss cone/anisotropy defines a window in cold electron density given by

$$1.34\,\frac{T_{\parallel}}{T_{\perp}} + 0.45\left(\frac{T_{\parallel}}{T_{\perp}}\right)^2 \leq \frac{\omega_{pe,c}}{\Omega^2_{ce}} \leq \frac{1}{4} \tag{8}$$

where the anisotropy factor $T_{\parallel}/T_{\perp}$ is given by:

$$\frac{T_{\parallel}}{T_{\perp}} \lesssim \frac{B_{\mu}}{B_o} - 1 \tag{9}$$

where $B\mu$ is the resonant plasma magnetic field, and Bo is the midplane plasma magnetic field. The constraint eqn. (8) can usually be satisfied by picking the proper resonant frequency. In eqn. (8), $\omega_{pe,c}$ is the cold electron plasma frequency and Ω_{ce} is the electron cyclotron frequency.

The more restrictive of the whistler mode and the mirror mode determine the maximum ring beta, $\beta_h(r_A)$:

$$\beta_h(r_A) \leq \min\Big[\underset{\text{Mirror}}{\underset{\uparrow}{0.8}},\ \underset{\text{Whistler}}{\underset{\uparrow}{2(T_{\parallel}/T_{\perp})^2}}\Big] - \beta_c(r_A) \tag{10}$$

In all cases tried so far, the mirror mode is the most restrictive.

The solution of the power balance problem is conceptually quite straightforward. The inputs to the problem are: center line barrier beta, $\beta_c(o)$, barrier electron energy, E_{eh}, $R_c(r_A)$, r_A, vacuum field at the ring, $B_{v,A}$, and microwave frequency, $f\mu$. Using eqn. (3), the value of $\beta_c(r_A)$ is obtained, and from eqn. (5), a ring half thickness, Δ, is computed, for a given hot electron beta, $\beta_h(r_A)$. Then, by using the hot electron interchange branch of eqn. (6), and the definition of $\beta_h(r_A)$, a minimum hot electron temperature is calculated. This temperature always seems to lie to the right of the minimum of the power drain curve ($\sim$ 2.3 MeV), so this is the temperature which minimized power, subject to the stability constraint. Using this temperature in the power equation, the volume quadrature is performed, with a radial extent of 4Δ and an axial extent of $2r_A$, to pick up the tails of the hot electron spatial distribution. The total power, P_A, is then computed for a series of hot electron betas within the bounds given by eqns. (4) and (9) to pick out the minimum power. Usually, the minimum power occurs when $\beta_h(r_A)$ is at the mirror mode limit, although in some cases when C_{gb} and C_{ci} are not at their nominal values $\beta_h(r_A)$ optimizes at lower values. This procedure is repeated for different

assumptions regarding α, C_{gb}, C_{ci}, and X, to see the effect on the required heating power.

5. RESULTS AND DISCUSSION

Table 1 shows the results of the baseline case for the ring-stabilized axicell. Three cases are shown, the first with hot electron pressure and B profiles, the second with flat hot electron pressure, and the third with all profiles flat. Flat profiles extend radially 2Δ and axially r_A. Powers shown are for one ring. Note that with all profiles flat, the power does not differ appreciably from the full set of profiles, but keeping the B profile with pressure flat results in quire a large increase in power, due primarily to the contribution from the ring volume at high field. Note that case 3 does not minimize power at the mirror mode limit.

Figure 3 shows the sensitivity of several ring parameters on changes in α defined in eqn. (7). P_{norm} is the ring power required normalized to the power of case 1 of table 1. The change in P_{norm}, n_c/n_h, and T_h are quite dramatic when α is changed from 1/5 to the nominal value $\alpha = 1$. This suggests there is great incentive to understand theoretically the limit of $\alpha \rightarrow 0$ in the hot electron interchange criterion.

Figure 4 shows the change of ring characteristics when the core interchange criterion is modified by different velocity space distributions. One can see that the power requirement drops by a factor of five when the more optimistic $C_{ci} = 2$ (see eqn. (5)) is used. The reason n_c/n_h decreases beyond a critical value of C_{ci} is because for $C_{ci} \geq 1 + \beta_c$, β_h is fixed at β_c. For fixed β_h, n_c/n_h scales like Δ/T_h, and Δ is seen to decrease faster than T_h in this region. The reason β_h has to be fixed beyond $C_{ci} = 1+\beta_c$ is because at this point $\beta_h < \beta_c$ from eqn. (4). The careful calculation of a realistic value of C_{ci} seems critical to determine power balance.

Figure 5 shows the sensitivity of ring parameters to incertainties in C_{gb}. A C_{gb} value of ½ would correspond to the case when the ring is axially distributed and would see a line averaged R_c of $\langle R_c \rangle = 2\, R_c(r_A)$; the case when C_{gh} is unity corresponds to the case when the ring electrons see only the midplane curvature $R_c(r_A)$. By adopting the more optimistic result, power can be reduced by a factor slightly greater than two. The reason that greater benefit cannot be realized by reducing C_{gb} is that for $C_{gb} \leq (1 + \beta_c)^{-1}$, eqn. (4) would predict $\beta_h < \beta_c$, so for C_{gb} below

this, $\beta_h = \beta_c$ must be invoked.

Figure 6 shows what happens when we allow the magnitude of the barrier electron pressure gradient to increase above the nominal $X = \frac{1}{2}$. The point $X = 1$ would correspond to the EBT case where no excess interchange stability is required to stabilize pressure gradients elsewhere. By going from $X = \frac{1}{2}$ to $X = 1$, the power requirement goes down by slightly under a factor of five. This tells us that the power required to produce rings in the axi-cell TMR might be more than in an EBT by virtue of something other than the higher ring temperature.

Figure 7 combines the results of the preceeding figures into a diagram similar to that presented in reference (3). Here we use P^{-1}_{norm} rather than $Q_E/(n_c/n_h)$. The reference case is shown (case 1 of Table 1) as a point on a curve generated with baseline parameters but allowing T_h to be unconstrained. Also shown is the spread in possible values of P^{-1}_{norm} by assuming a reasonable variation in the uncertainty parameters. For the α uncertainty, it was assumed that the smallest α could get would be $\frac{1}{2}$ instead of the 1/5 assumed in Figure 3.

The conclusions which can be drawn from the analysis presented in this paper are:

(1) The power requirement for the hot electron ring for the E-ring stabilized axi-cell TMR is a reasonable 34 MW. It is likely that some of the radiated power will be absorbed by the barrier electrons, thereby reducing the total ECRH power delivered to the end cell.

(2) The power requirement can change by up to a factor of five by changing the stability constraints within the bounds consistent with the uncertainty in the theory.

(3) Efforts should be made to make the theories of plasma stability more definitive. Of particular interest is the determination of the α factor in the hot electron interchange criterion, eqn. (6), in the vicinity of the core interchange β_c limit, eqn. (5).

TABLE 1 - PARAMETER FOR THREE BASELINE AXICELL CASES

Common Input:

$R_c(r_A) = 2.5m$, $r_A = 1.76$ m, $\beta_c(0) = 0.36$,

$E_{eh} = 240$ keV, $B_{V,A} = 1.65T$, $\alpha = 1$, $C_{ci} = 1$, $C_{gb} = 1$,

$X = 0.5$, $L_{mir} = 8.6$ m, $B_{mir}/B_o = 4$.

Output:

Parameter	1	2	3
P_A (MW)	17	38	21
$\beta_h(r_A)$	0.52	0.52	0.33
T_h (MeV)	9.5	9.5	7
Δ (m)	0.53	0.53	0.33
n_c/n_H	4.3	4.3	8.2
$\beta_c(r_A)$	0.28	0.28	0.2
$n_c(r_A)$ ($10^{18}m^{-3}$)	1.6	1.6	2.6

6. REFERENCES

1. R. A. Dandl, et. al. in Plasma Physics and Controlled Nuclear Fusion Research Vol. 2, p. 435 (1969).
2. Symmetric Tandem Mirror Program, Annual Progress Report. TRW Report No. S/N 35638, October 1980.
3. N. A. Uckan, D. A. Spong, D. B. Nelson, "Beta Limits in EBT and Their Implication for a Reactor", ORNL Report ORNL/TM-7857, August 1981.
4. N. A. Uckan, ed. Proceedings of the Workshop. "EBT Stability Theory", ORNL Report CONF-810512, May 13 - 14, 1981.
5. S. K. Borowski, N. A. Uckan, E. F. Jaeger, and T. Kammash. "Ring Power Balance" presented at the first Ring Physics Workshop, Dec. 3 - 5, 1979. Published in ORNL Report CONF-791228, p. 319.
6. J. W. Van Dam, H. L. Berk, and M. N. Rosenbluth. "Eigenmode Stability Analysis for a Bumpy Torus" in reference 4, p. 97.

FIGURE 1(a). ELECTRON-RING STABILIZED AXICELL TMR

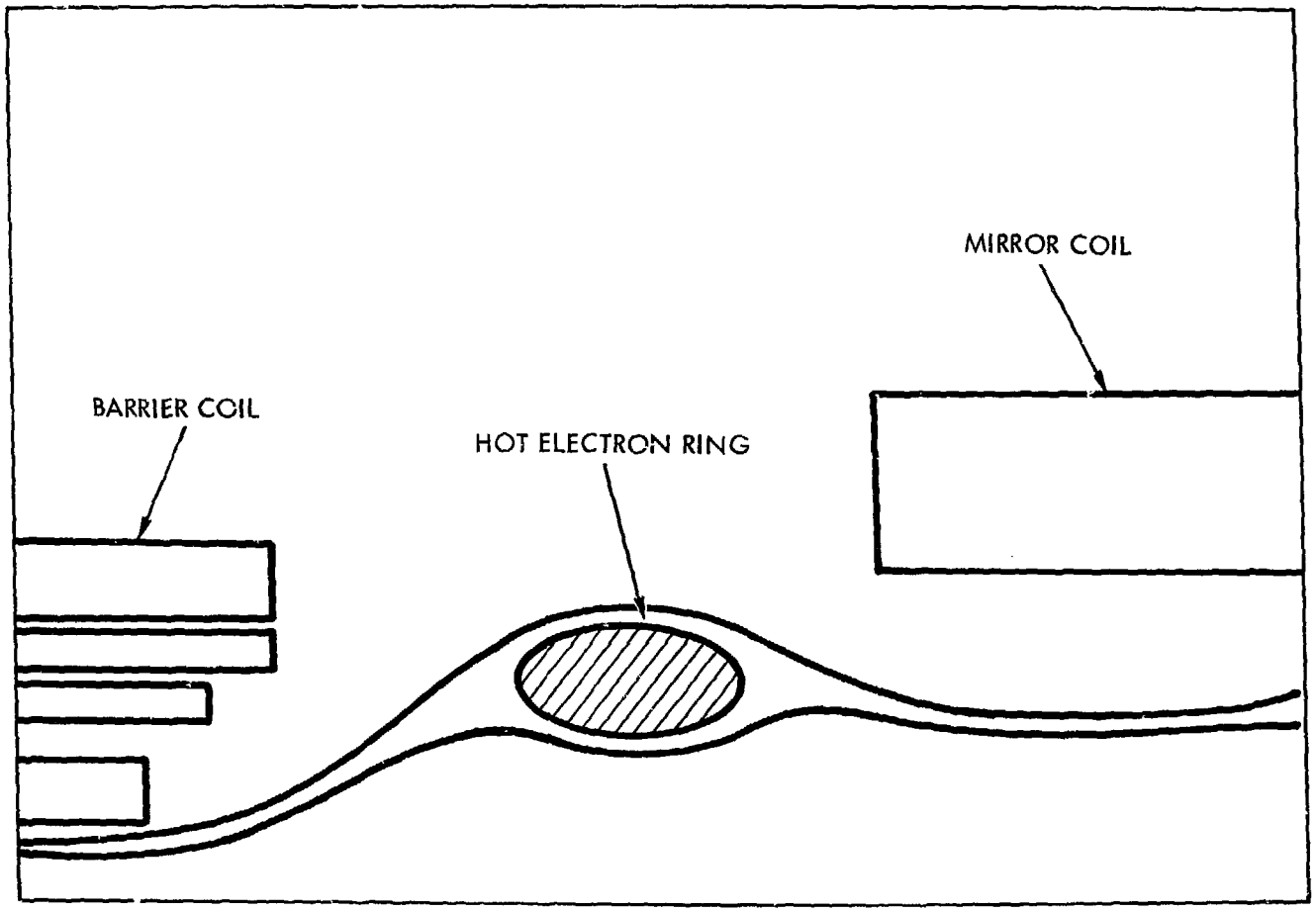

FIGURE 1(b). ELECTRON-RING STABILIZED MODIFIED-CUSP TMR

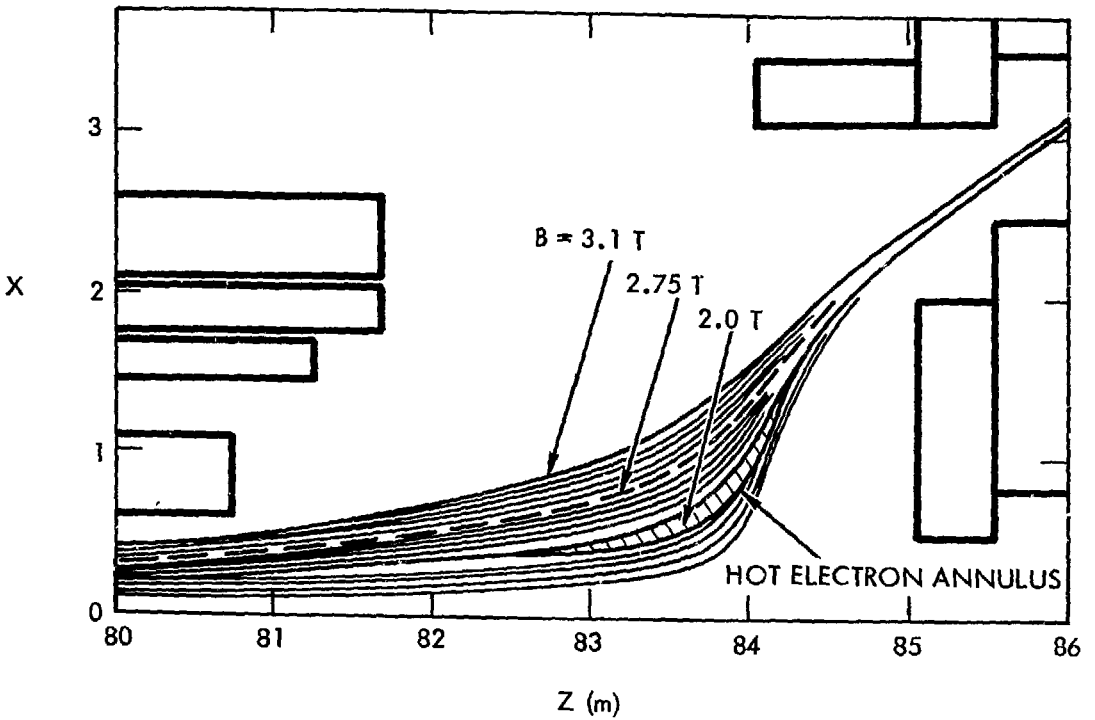

FIGURE 2. RADIAL PLASMA PROFILES

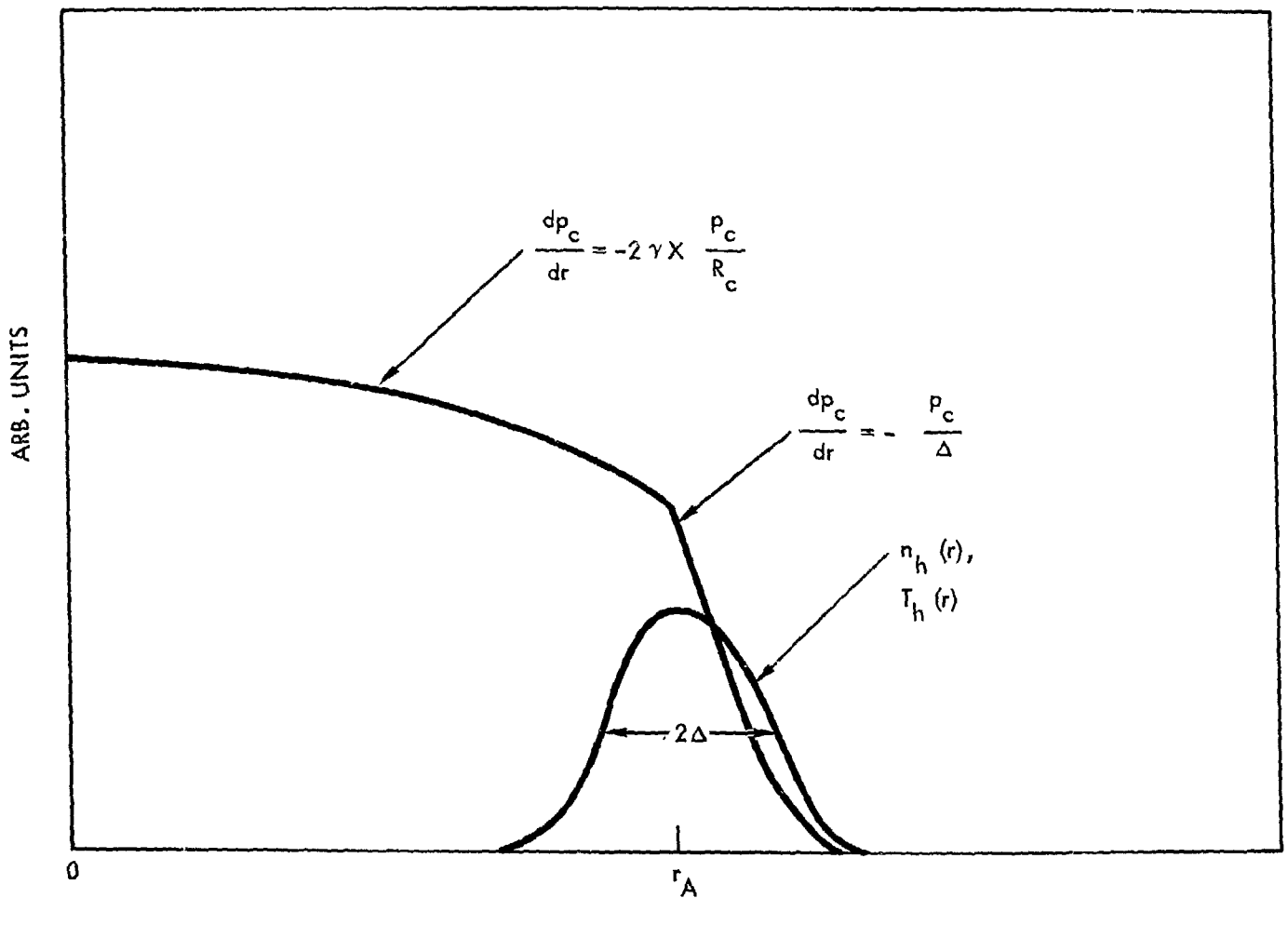

FIGURE 3. SENSITIVITY OF KEY RING PARAMETERS TO CHANGES IN α

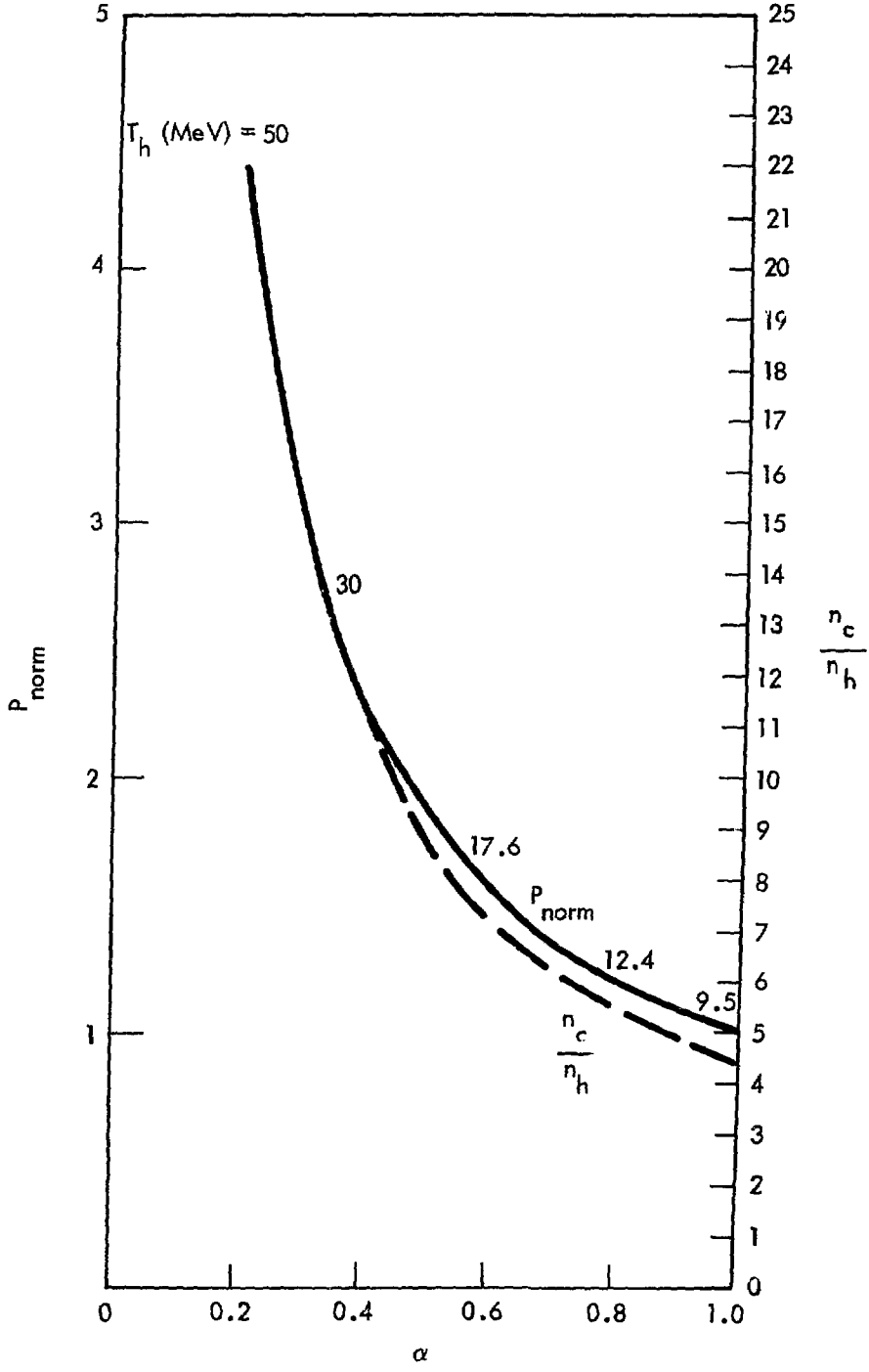

FIGURE 4. SENSITIVITY OF KEY RING PARAMETERS TO CHANGES IN C_{ci}

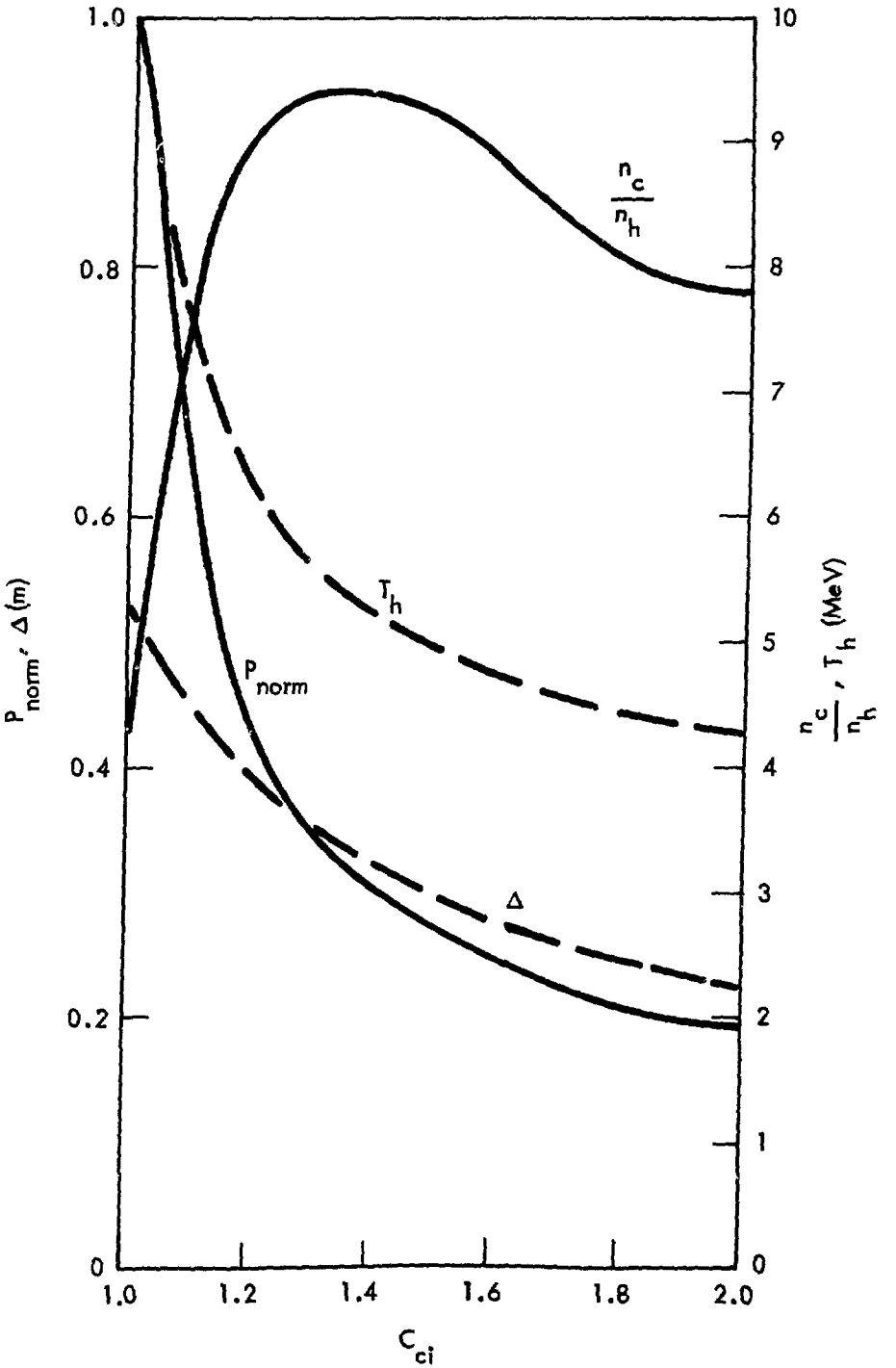

FIGURE 5. SENSIVITY OF KEY RING PARAMETERS TO CHANGES IN C_{gb}

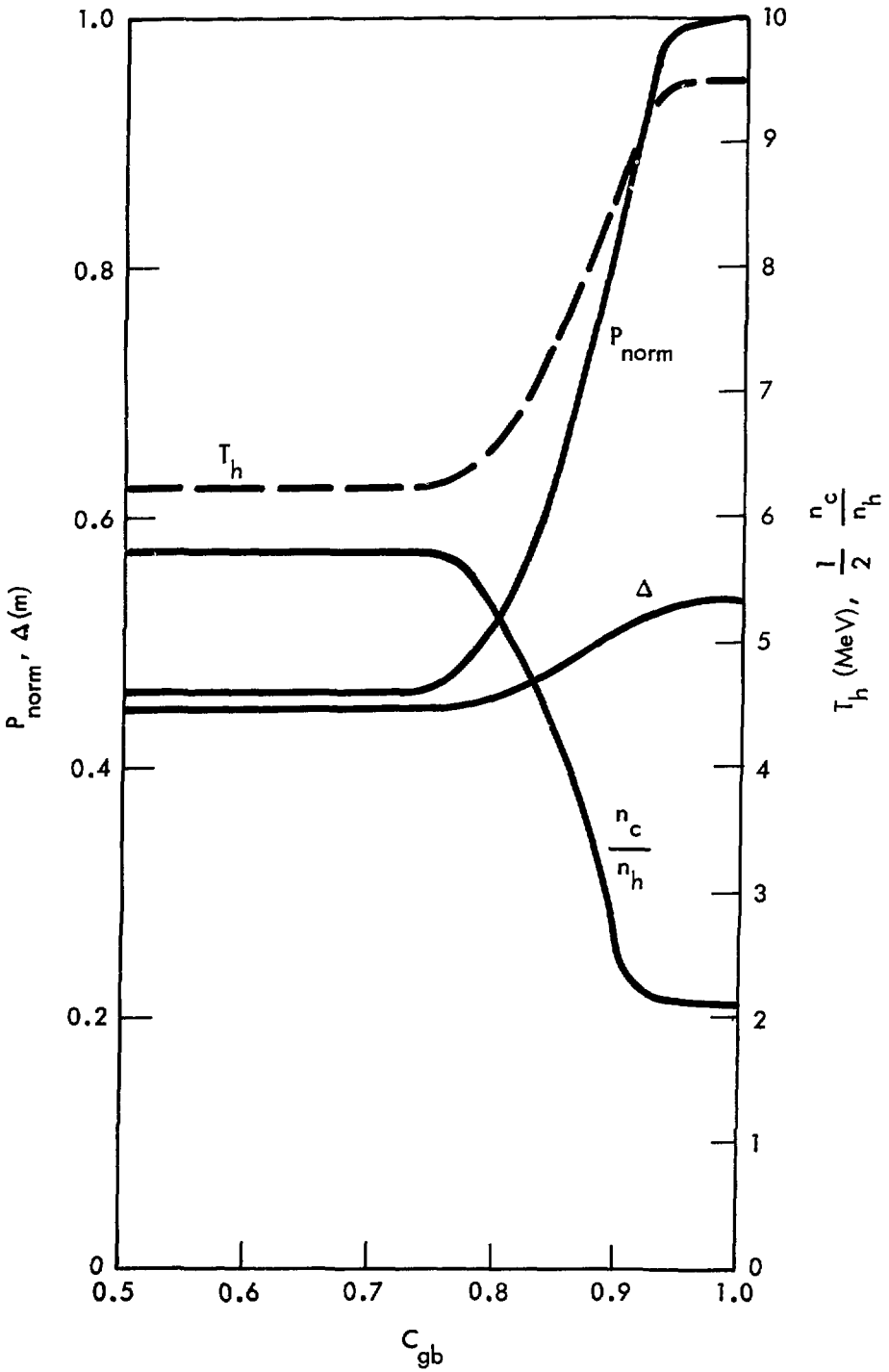

FIGURE 6. SENSITIVITY OF KEY RING PARAMETERS TO CHANGES IN X

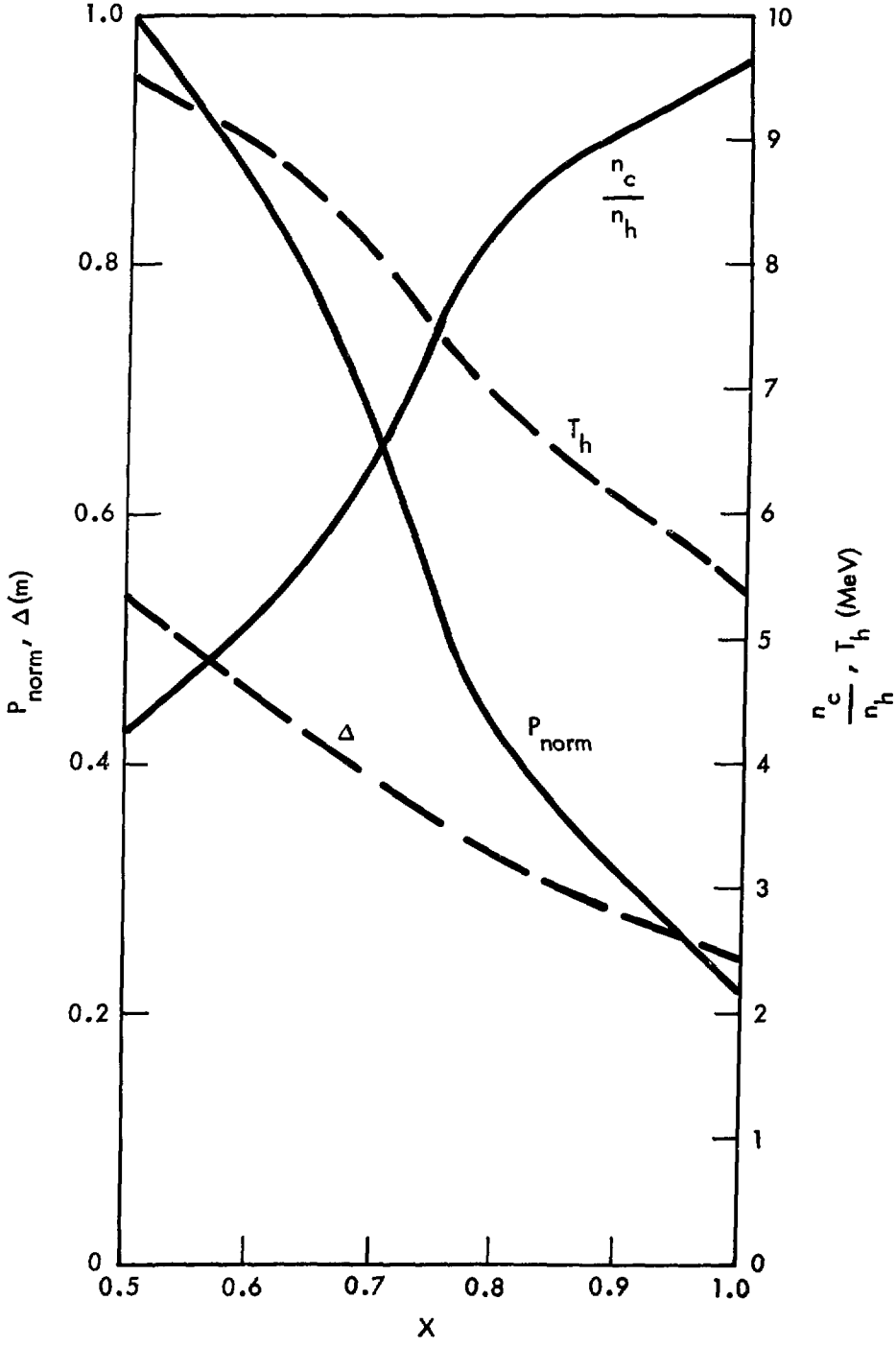

FIGURE 7.

IMPACT OF HOT ELECTRON INTERCHANGE CONSTRAINT AND UNCERTAINTY IN COEFFICIENTS

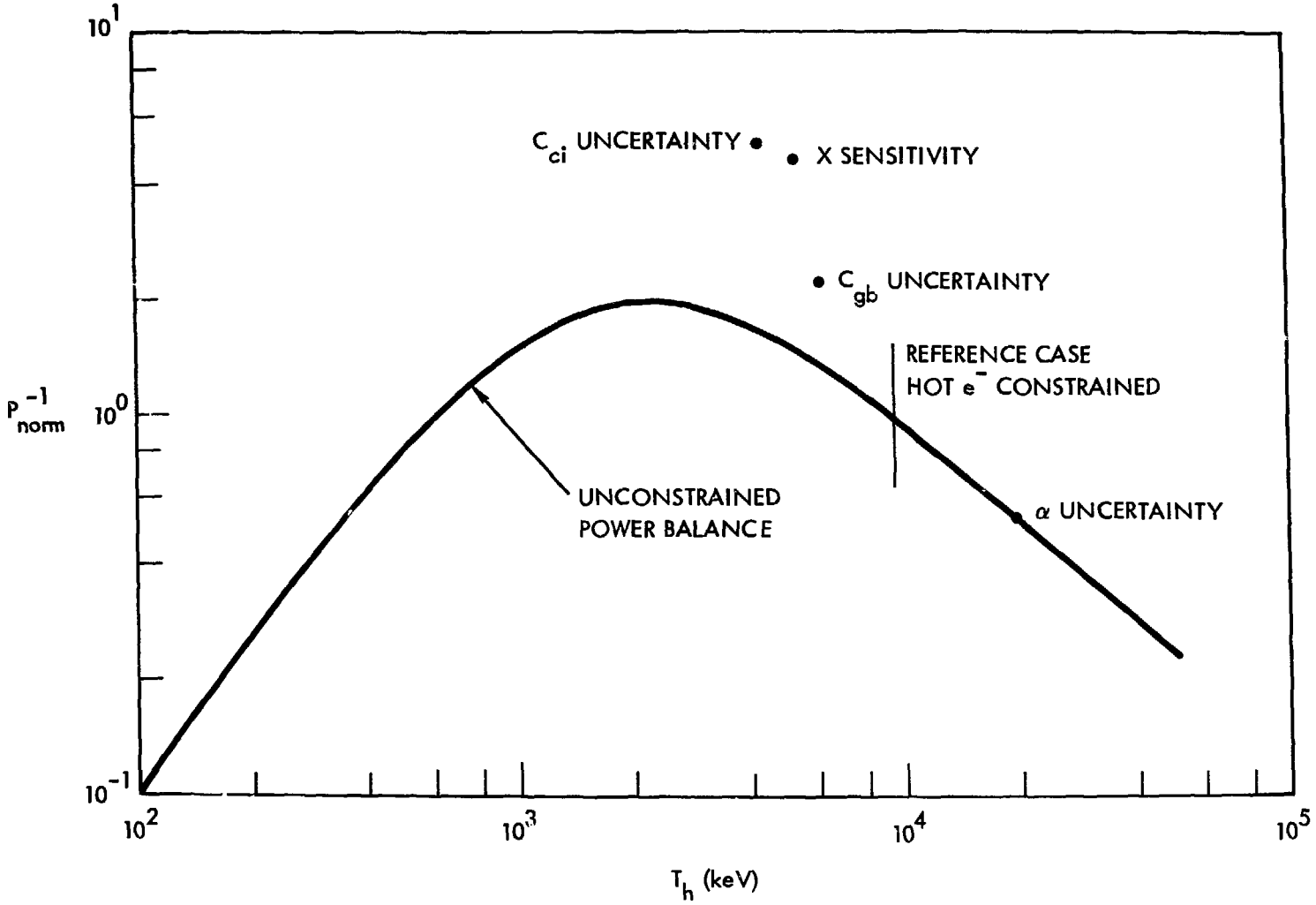

NUMERICAL STUDY OF VLASOV EQUILIBRIUM FOR BUMPY CYLINDER PLASMA WITH HOT ELECTRON RINGS

T. Watanabe, K. Hamamatsu, J. W. Van Dam*, and Kyoji Nishikawa
Institute for Fusion Theory, Hiroshima University, Hiroshima, Japan

ABSTRACT

Equilibrium for an axisymmetric periodic bumpy cylinder plasma with hot electron rings is studied numerically. Each plasma species is described by a Vlasov distribution function whose functional dependence on the single-particle energy, magnetic moment, and angular momentum is appropriately specified so as to include the effects of temperature anisotropy, mirror trapping, and finite gyroradius. The equilibrium magnetic field, together with the electrostatic potential, is then self-consistently obtained by numerically solving the Poisson and Ampere equations as a nonlinear boundary value problem.

*Permanent address: Institute for Fusion Studies, University of Texas, Austin, Texas 78712.

I. INTRODUCTION

The bumpy torus confinement device[1,2] is characterized by the presence of a high-beta hot electron ring in each mirror sector. These rings provide the average-minimum-B configuration necessary for stability of the toroidal core plasma.

Experimental measurements[3] have shown that an electrostatic potential exists in the hot electron rings, which affects particle confinement, stability, and transport in the bumpy torus. To study these effects, the structure of the ambipolar potential in a bumpy torus system must be calculated.

Traditionally, equilibrium for the bumpy torus has been investigated by use of the magnetohydrodynamic (MHD) equations with an anisotropic pressure.[4] Within the framework of the MHD model, however, the electrostatic potential plays no role in the determination of equilibrium.

In the work presented here, equilibrium for an axisymmetric bumpy cylinder plasma is studied numerically on the basis of a kinetic, rather than a fluid, description. The plasma is assumed to be composed of three species: core ions, core electrons, and energetic ring electrons. Whereas in the fluid approach the pressure components are specified as functions of the magnetic flux and field strength, in our Vlasov approach we specify the functional form of the particle distribution function for each species. Because of their relatively

low temperatures, the ions and electrons of the core plasma will be assumed to be isotropic in temperature. On the other hand, the distribution function for the hot ring electrons is taken to be of the mirror-trapped type with temperature anisotropy. With this kinetic approach, the electrostatic potential can be self-consistently included in the determination of equilibrium.

Furthermore, the Vlasov equilibrium solution of this study includes finite gyro orbit effects, whereas they are neglected in the MHD fluid description. This feature of the kinetic model is especially appropriate to the bumpy torus device, since its hot electron rings are considered to be only several Larmor diameters in radial width.[5]

In Sec. 2, the model for the Vlasov equilibrium is described, with the numerical results presented in Sec. 3. A brief conclusion is given in Sec. 4.

2. EQUILIBRIUM MODEL

The model that is adopted in this work to study the equilibrium of a hot electron plasma is based on a collisionless Vlasov description. Thus, each plasma species is described by an equilibrium particle distribution, which should be a function of the constants of particle motion. In this study, we will make use of the fact that the bumpy torus is a large-aspect-ratio device in order to reduce the study of equilibrium to that for a periodic bumpy cylinder.[4] Then as

constants of the motion we have the particle energy E, magnetic moment μ, and angular momentum P_Θ (in the direction of azimuthal symmetry):

$$E_j = m_j v^2/2 + q_j \Phi \tag{1}$$

$$\mu_j = m_j v_\perp^2/2B \tag{2}$$

$$P_{\Theta j} = m_j r v_\Theta + q_j \psi/c \tag{3}$$

Here, m_j and q_j are the mass and charge for the jth species, where j=i (ions), e (electrons), or h (hot electrons); $\vec{v}$ is the particle velocity; c is the speed of light; and Φ is the electrostatic potential, with ψ the magnetic flux function. The magnetic field $\vec{B}$ is given by

$$\vec{B} = \begin{cases} \frac{1}{r}\frac{\partial\psi}{\partial z} \\ 0 \\ B\frac{1}{r}\frac{\partial\psi}{\partial r} \end{cases} , \tag{4}$$

where the three components correspond to the usual (r,Θ,z) coordinates of cylindrical geometry. The perpendicular velocity $\vec{v}_\perp$ is given by

$$\vec{v}_\perp = \vec{B}x(\vec{v} \times \vec{B})/B^2 = rv_\Theta\vec{\nabla}\Theta + (\vec{v} \cdot \vec{\nabla}\psi)\vec{\nabla}\psi \; r^2B^2 \quad . \tag{5}$$

In the present work, we have assumed that the functional form of the equilibrium mirror-trapped particle distribution is given by

$$f_j(r,z,\vec{v}) = n_j(m_j/2\pi T_j)^{3/2} \exp[-E_j/T_j - (m_j/2T_j\lambda_j^2)(P_{0j} - R_{0j})^2] \times [\exp(\alpha_1\mu B_0/T_j) - \delta_j \exp(-\alpha_2\mu B_0/T_j)]. \quad (6)$$

The various parameters in Eq. (6) have the following significance: n_j is a measure of the particle density; T_j is the parallel temperature (assumed to be constant); R_{0j} and λ_j determine the peak position and half width of the radial density profiles; B_0 is the magnetic field strength on axis at the midplane of a mirror sector; and α_{1j}, α_{2j}, and δ_j determine the degree of temperature anisotropy and mirror trapping. Note that the effective perpendicular "temperature" $T_\perp$ is given by

$$T_{\perp j} = \begin{cases} T_j[1-\alpha_{ij}B_0/B(r_1z)]^{-1} \\ T_j[1+\alpha_{2j}B_0/B(r_1z)]^{-1} \end{cases} \quad (7)$$

for the two parts of the dependence on $v_\perp^2$: $T_\perp$ for the first part (involving α_{1j}, where α_{1j} is required to be less than the mirror ratio) is peaked at the midplane, corresponding to mirror trapping, whereas $T_\perp$ for the subtracted second part (involving α_2) peaks at the mirror throats, corresponding to a passing plasma component. Thus, δ_j is related to the fraction of passing particles; more precisely, it is the fraction of particles having $v_\perp^2 = 0$ at any position. For the core plasma ions and electrons, we take $\alpha_1 = \alpha_2 = \delta = R_0 = 0$; that is, we assume that the core plasma is centered on the magnetic axis (r=0) and is isotropic.

The equilibrium density and current distributions are readily calculated from the distribution function of Eq. (6) as

$$n(r,z) = \sum_j \int d^3v\ f_j(r,z,\vec{v}) = \sum_j [N_j(\alpha_{ij}) - \delta_j N_j(\alpha_{2j})] \tag{8}$$

and

$$\vec{j}(r,z) = \sum_j q_j \int d^2v\ \vec{v}\ f_j(r,z,\vec{v}) = \begin{cases} 0 \\ r\sum_j [J_j(\alpha_{1j}) - \delta_j J_j(\alpha_{2j})] \\ 0 \end{cases} \tag{9}$$

The quantities N_j and J_j are given by

$$N_j(\alpha) = n_j(1+\alpha B_o/B)^{-1/2}(1+\alpha B_o/B + r^2/\lambda_j^2)^{-1/2}\exp[-q_j\Phi/T_j - (q_j\psi/c - R_{oj})^2(1+\alpha B_o/B)(1+\alpha B_o/B+r^2\lambda_j^2)^{-1}(2T_j\lambda_j^2)^{-1}] \tag{10}$$

and

$$J_j(\alpha) = -q_j N_j(\alpha)\ (q_j\psi/c - R_{oj})(1+\alpha B_o/B+r^2/\lambda_j^2)^{-1}(m_j\lambda_j^2)^{-1} \quad . \tag{11}$$

The density distribution of Eq. (8) and the current distribution of Eq. (9) are now substituted into Poisson's equation and the θ-component of Ampere's law, respectively, to obtain the coupled system of equations that determine the structure of Φ and ψ:

$$\frac{1}{r}\frac{\partial}{\partial r}(r\frac{\partial\Phi}{\partial r}) + \frac{\partial^2\Phi}{\partial z^2} = -4\pi \sum_j q_j[N_j(\alpha_{1j}) - \delta_j N_j(\alpha_{2j})] \qquad (12)$$

$$\frac{\partial}{\partial r}(\frac{1}{r}\frac{\partial\psi}{\partial r}) + \frac{1}{r}\frac{\partial^2\psi}{\partial z^2} = -(\frac{4\pi}{c})r \sum_j [J_j(\alpha_{1j}) - \delta_j J_j(\alpha_{zj})] \quad . \qquad (13)$$

We have solved the nonlinear boundary value problem of Eqs. (12) and (13) numerically. The numerical procedure is a combination of methods. The finite difference technique is used to handle the axial variation. The radial variation is solved by a shooting method together with the Newton iteration procedure. The system is required to be periodic in z, with fixed boundary conditions employed in the radial direction. The details of the numerical procedure will be reported elsewhere.[6]

3. NUMERICAL RESULTS

In the figures, we exhibit results from numerical computations for the following five cases --

(a) Low density plasma (Figs. 1-9): $n_h = 5 \times 10^7$ cm^{-3}, $n_e = n_i = 5 \times 10^6$ cm^{-3};

(b) High density plasma (Figs. 10-16): $n_h = 5 \times 10^{12}$ cm^{-3}, $n_e = n_i = 5 \times 10^{11}$ cm^{-3}, with the ambipolar field neglected;

(c) High density plasma (Figs. 17-22): same parameters as for (b), but with effects of the ambipolar field included;

(d) High density plasma (Figs. 23-30): $n_h = 5 \times 10^{12}$ cm^{-3}, $n_e = 1 \times 10^{11}$ cm^{-3}, $n_i = 5 \times 10^{11}$ cm^{-3};

(e) Hot electrons only (Figs. 31-36): $n_h = 5 \times 10^{12}$ cm^{-3}, no core plasma. The other parameters are fixed in value to be the same for all cases: $\alpha_{1h} = 0.02$, $\alpha_{2h} = 0.01$, $\delta_h = 1.0$, $\alpha_{1i,e} = \delta_{i,e} = 0$, $R_{oh} = 5 \times 10^4$ cm^2/sec, $R_{oi,e} = 0$, $\lambda_h = 3$ cm, $\lambda_e = 916$ cm, $\lambda_i = 21.5$ cm, $T_h = 10^6$ eV, $T_e = T_i = 500$ eV.

For each of these five cases, we show plots of the magnetic field lines, $|B|$ contours, radial $|B|$ profile, potential contours, radial potential profile, radial hot electron density profile, hot electron density contours, and core electron and ion density profiles.

Case (a) corresponds to the case of an low beta plasma. Using the peak density values $\bar{n}$ from Figs. 6 and 9, we can estimate $\beta_i = 8\pi\bar{n}_i T_i/B_o^2 \cong 4 \times 10^{-9}$ and $\beta_h \cong 1.6 \times 10^{-6}$. (Note, incidentally, that the value of the parameter n_j in the distribution function for a given species does not correspond to the peak density value.) Clearly, the magnetic field configuration is nearly identical to that for a vacuum.

Cases (b)-(d) correspond to a high beta plasma. Using peak values as before, we can estimate $\beta_i \cong 4 \times 10^{-4}$ and $\beta_h \cong 0.5$. The magnetic field configurations for cases (c) and (d) are nearly identical to that for case (b) and hence are not shown. This indicates that the magnetic field structure is fairly insensitive to the shape of the electrostatic potential.

The potential profile, on the other hand, is quite sensitive to the details of the density distributions. In case (c), the core ions and electrons have nearly the same density distributions as in case (b) where the potential is absent. Thus, in case (c), the hot electrons play the role of excess charge, and a negative potential well is created at the location of the hot electron ring. However, this potential is largely shielded by the core plasma and almost vanishes on the magnetic axis. The radial profile of the potential changes in case (d) where the ion density is about five times greater than the core electron density.

Case (e) is for the equilibrium of the hot electron ring without any core plasma. In this case, a very large electrostatic potential, comparable in magnitude to the ring temperature, is formed, and the density difference between throat and midplane is small.

4. CONCLUSION

A numerical technique has been developed for studying self-consistent Vlasov equilibria for a periodic bumpy cylinder plasma. This technique includes the high-beta diamagnetic and finite gyroradius effects of the hot electron rings and also the electrostatic potential.

This technique can also be applied to calculate equilibria for a sloshing ion distribution of the type that has been suggested for the end cells of a tandem mirror device.

The structure of the ambipolar field, however, depends on the electron and ion densities in each mirror cell. To study the development of the electrostatic potential in an actual plasma, it is therefore necessary to take into account the plasma transport processes.

ACKNOWLEDGEMENTS

Instructive comments on these results were received from Dr. H. Sanuki, Dr. C. L. Hedrick, and Dr. H. L. Berk.

This work was supported by the Japan Ministry of Education; also, one author (JVD) received support from the Japan Society for the Promotion of Science.

REFERENCES

1. R.A. Dandl, H.O. Eason, P.H. Edmonds, and A.C. England, Nucl. Fusion 11, 411 (1971).

2. H. Ikegami, H. Ikezi, M. Hosokawa, S. Tanaka, and K. Takayama, Phys. Rev. Lett. 19, 779 (1967).

3. P.L. Colestock, K.A. Connor, R.L. Hickok, and R.A. Dandl, Phys. Rev. Lett. 40, 1716 (1978).

4. D.B. Nelson and C.L. Hedrick, Nucl. Fusion 19, 283 (1979).

5. R.A. Dandl *et al.*, "Summary of EBT-1 Experimental Results", ORNL TM-6457 (1978).

6. T. Watanabe, K. Hamamatsu, J.W. Van Dam, and Kyoji Nishikawa, to be published.

case a) low density plasma case

Parameters

	n_j (cm^{-3})	T_j (eV)	α_{1j}	α_{2j}	δ_j
hot electron	5.0×10^{7}	10^{6}	-0.02	0.01	1.0
core electron	5.0×10^{6}	500	0	0	0
core ion	5.0×10^{6}	500	0	0	0

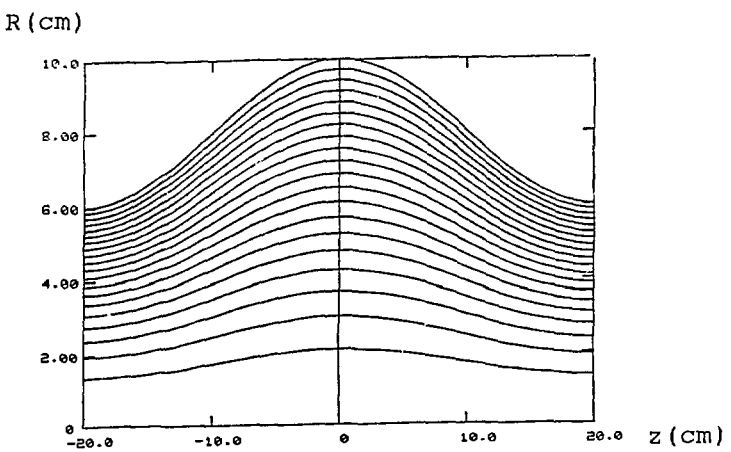

Fig.1 Magnetic field lines

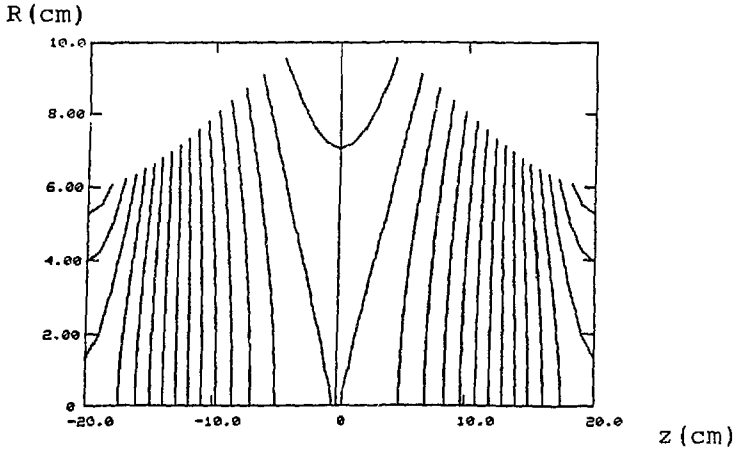

Fig.2 Mod-B contour

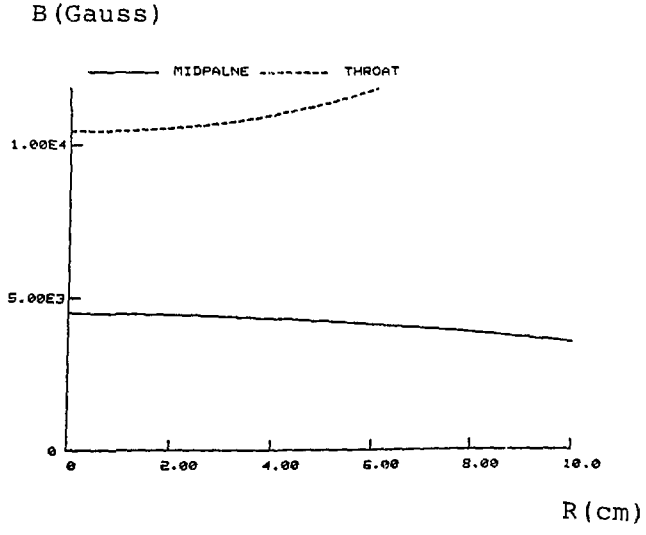

Fig.3
Mod-B at midplane
and at throat

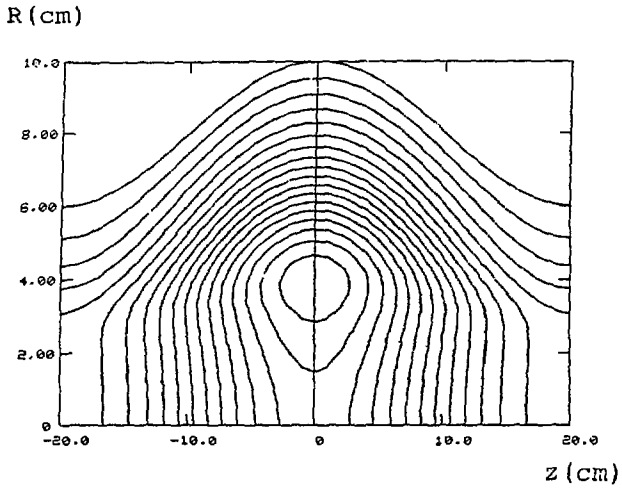

Fig.4
Contour map of
electrostatic potential

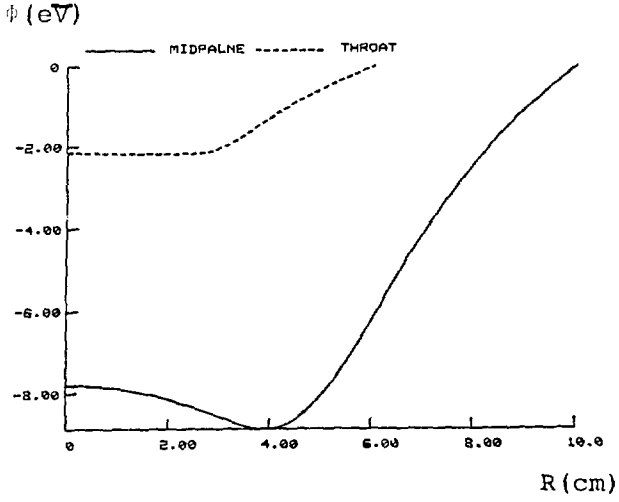

Fig.5
Electrostatic potential
at midplane and at throat

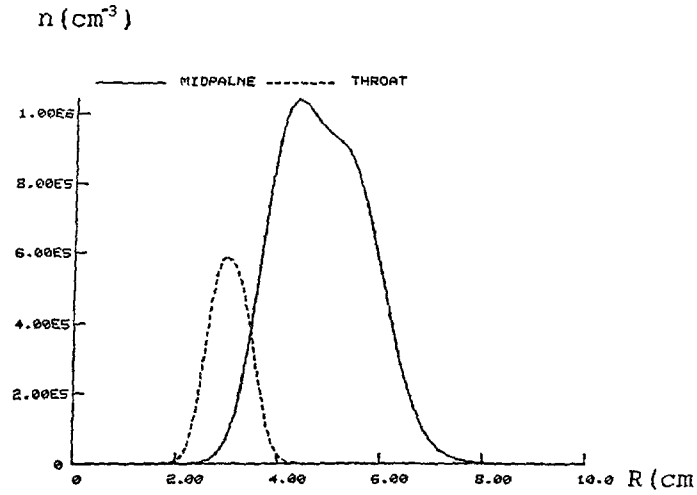

Fig.6 Hot electron density distribution at midplane and at throat

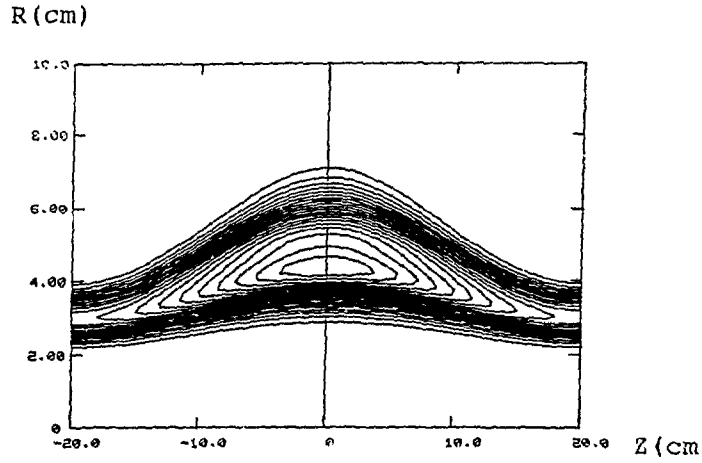

Fig.7 Contour map of hot electron density

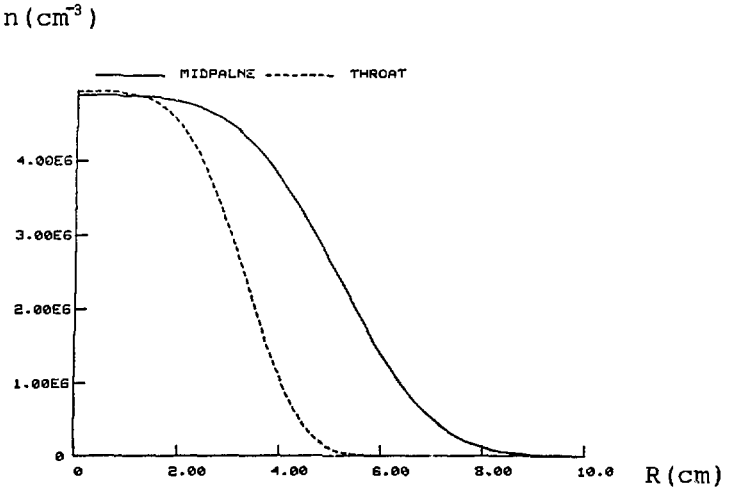

Fig.8 Core electron density distribution at midplane and at throat

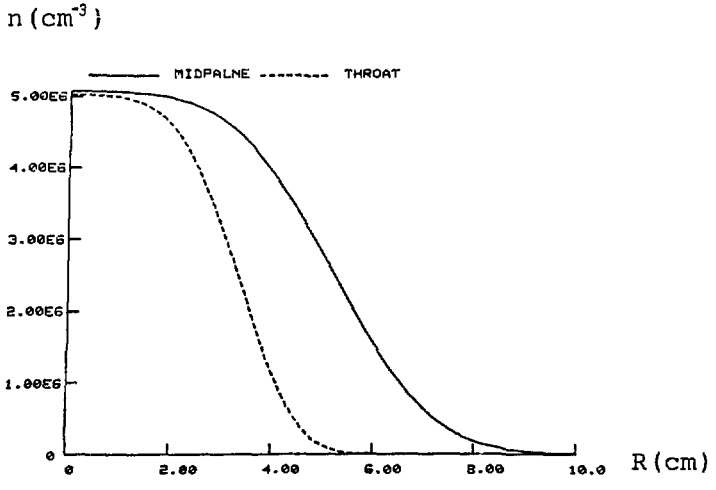

Fig.9 Core ion density distribution at midplane and at throat

case b) high density plasma case -1-

(effects of ambipolar field are neglected)

Parameters

	n_j (cm^{-3})	T_j (eV)	α_{1j}	α_{2j}	δ_j
hot electron	5.0×10^{12}	10^6	-0.02	0.01	1.0
core electron	5.0×10^{11}	500	0	0	0
core ion	5.0×10^{11}	500	0	0	0

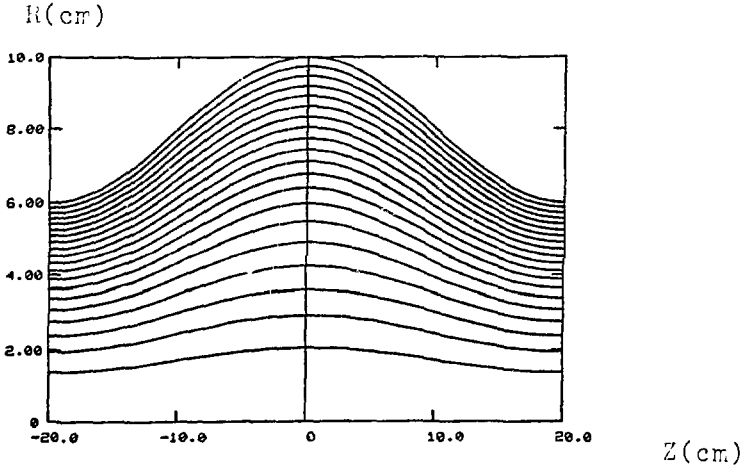

Fig. 10 Magnetic field lines

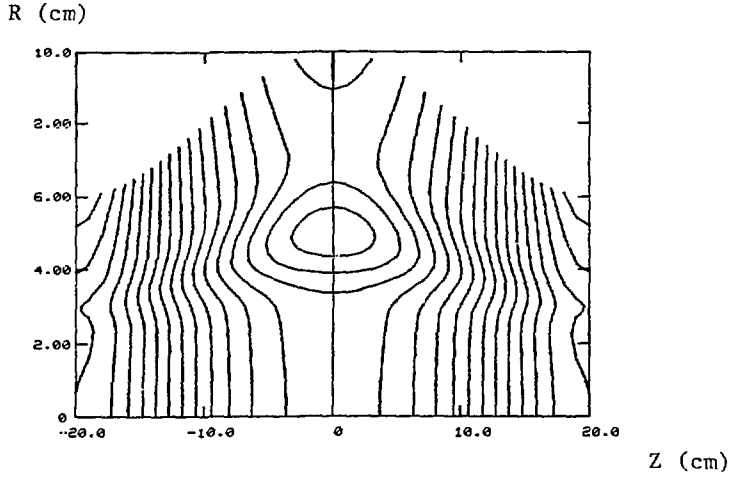

Fig. 11 Mod-B contour

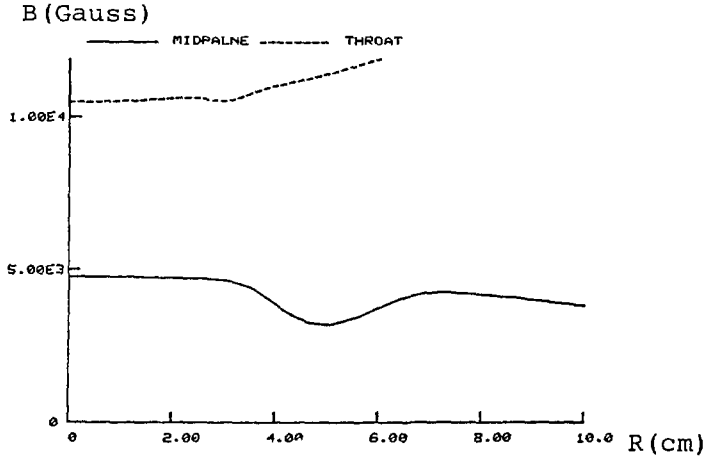

Fig.12
Mod-B at midplane
and at throat

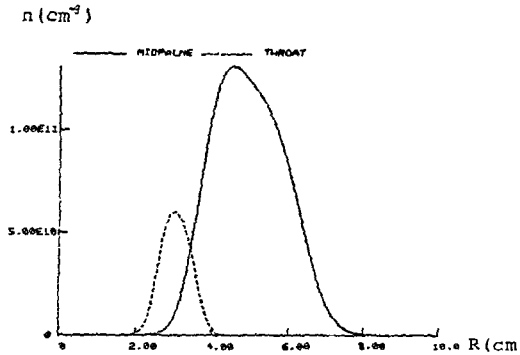

Fig.13
Hot electron density distribution at midplane and at throat

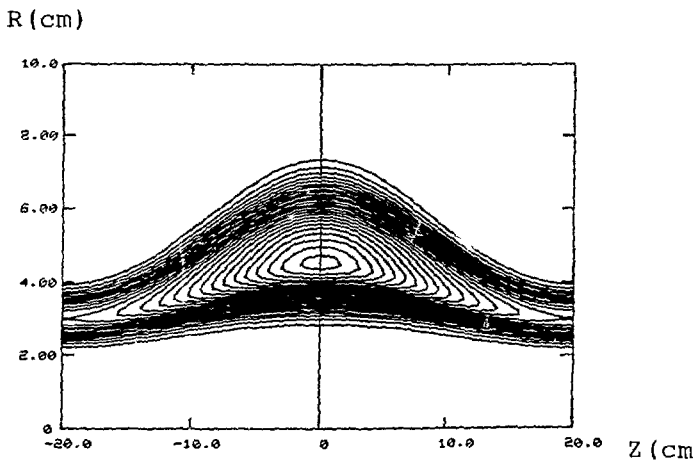

Fig.14
Contour map of hot electron density

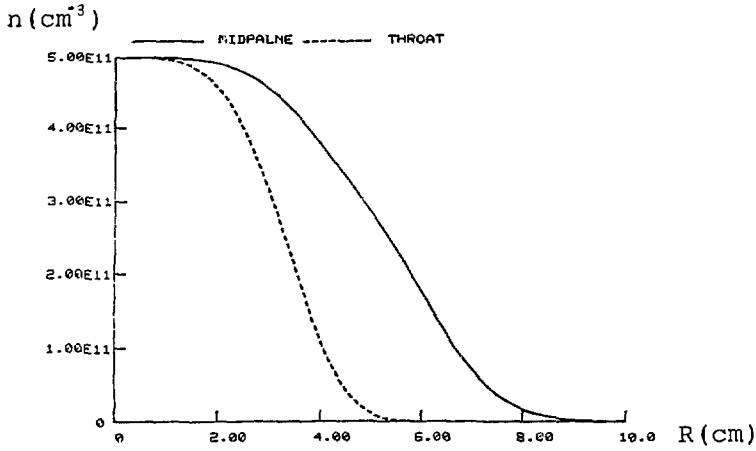

Fig.15 Core electron density distribution at midplane and at throat

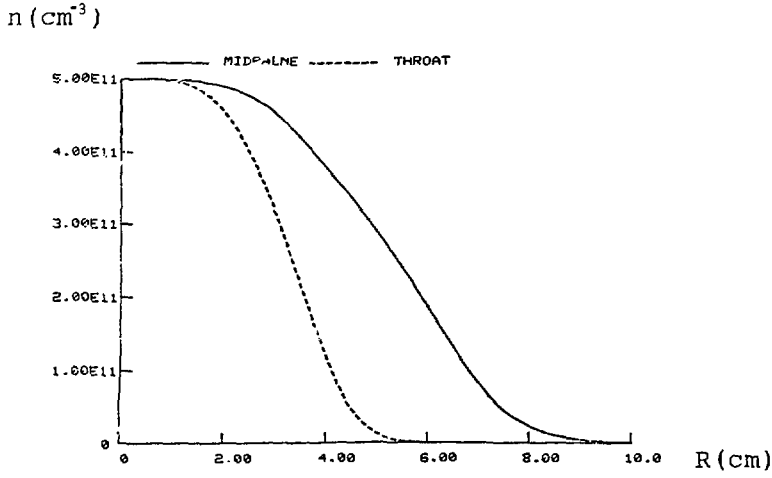

Fig.16 Core ion density distribution at midplane and at throat

case c) high density plasma case
(effects of ambipolar field are included)

Parameters are same with the parameters of case b).

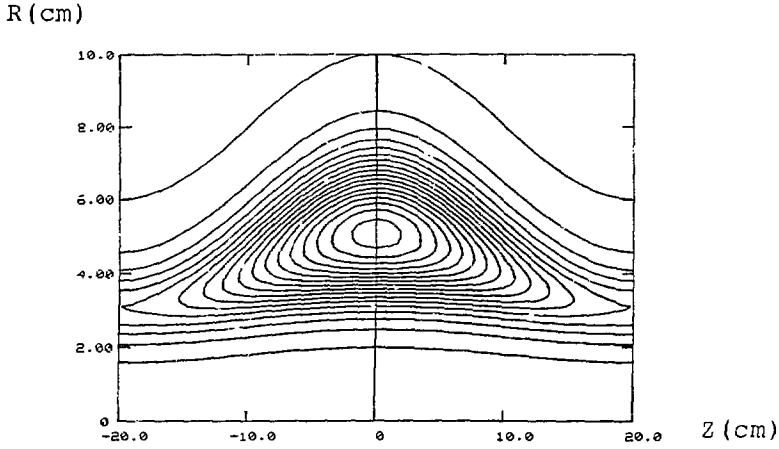

Fig.17 Contour map of electrostatic potential

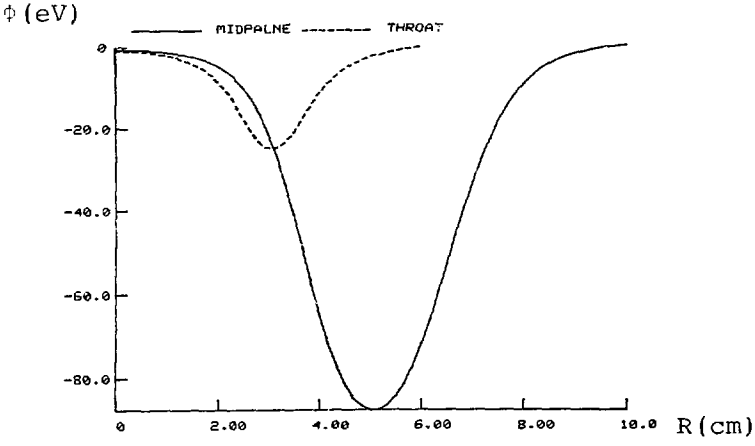

Fig.18 Electrostatic potential at midplane and at throat

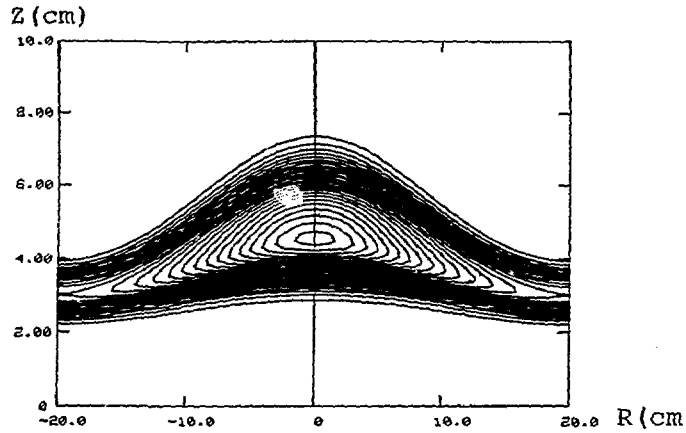

Fig.19 Contour map of hot electron density

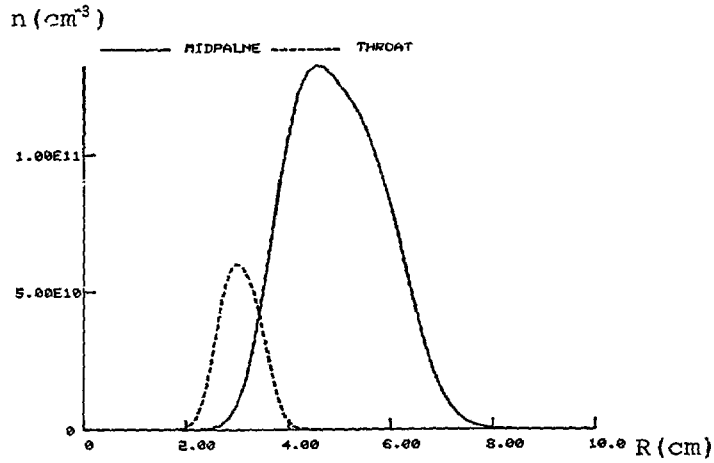

Fig.20 Hot electron density distribution at midplane and at throat

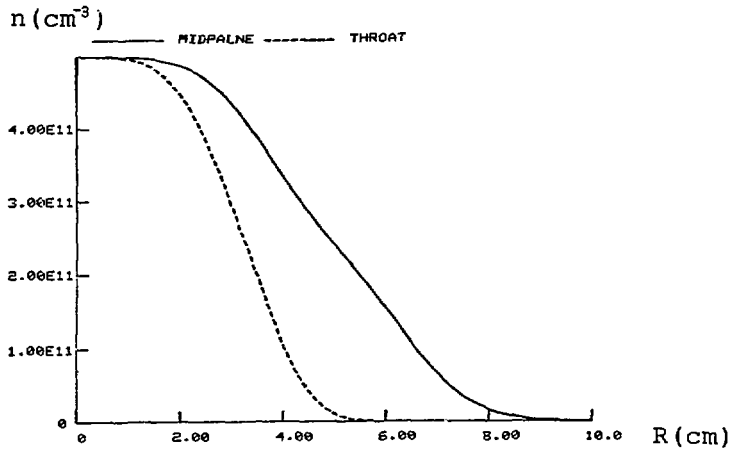

Fig.21 Core electron density distribution at mid plane and at throat

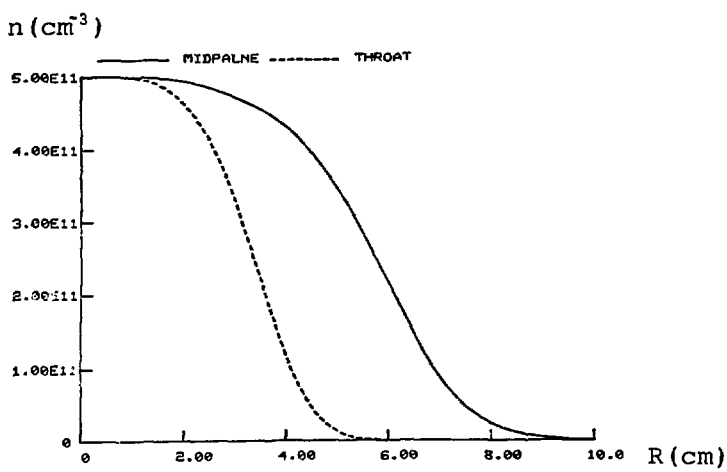

Fig.22 Core ion density distribution at midplane and at throat

case d) high density case

(Effects of ambipolar field are included)

Parameters

	n_j (cm^{-3})	T_j (eV)	α_{1j}	α_{2j}	δ_j
hot electron	5.0×10^{12}	10^6	-0.02	0.01	1.0
core electron	1.0×10^{11}	500	0	0	0
core ion	5.0×10^{11}	500	0	0	0

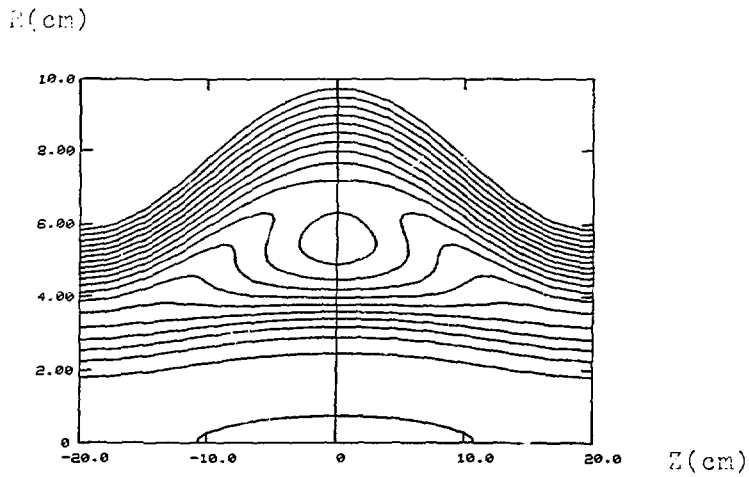

Fig. 23 Contour map of electrostatic potential

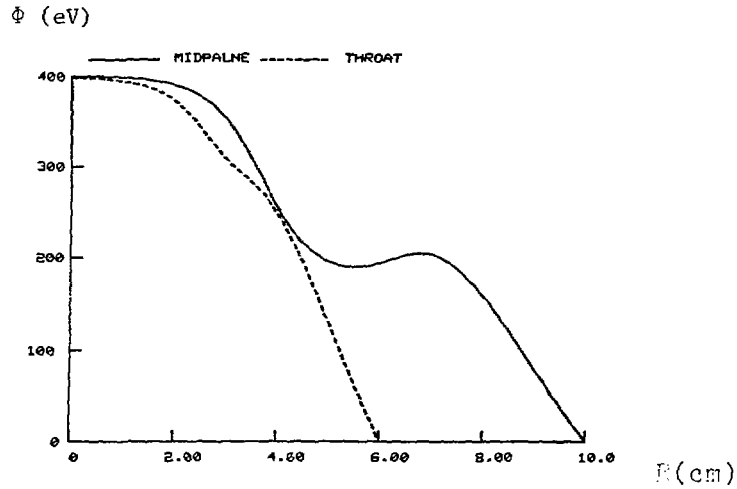

Fig. 24 Electrostatic potential at midplane and at throat

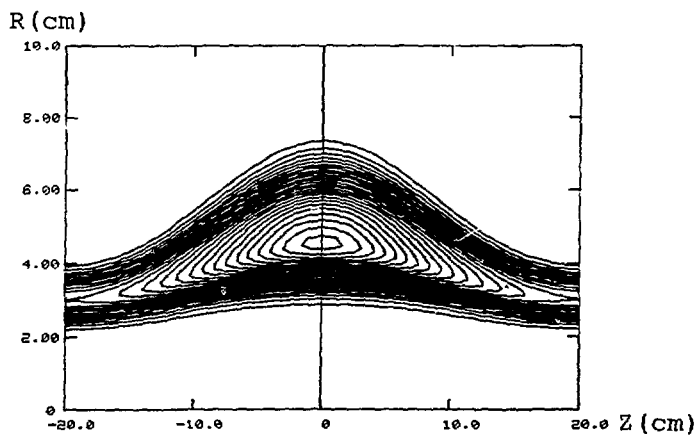

Fig.25 Contour map of hot electron density

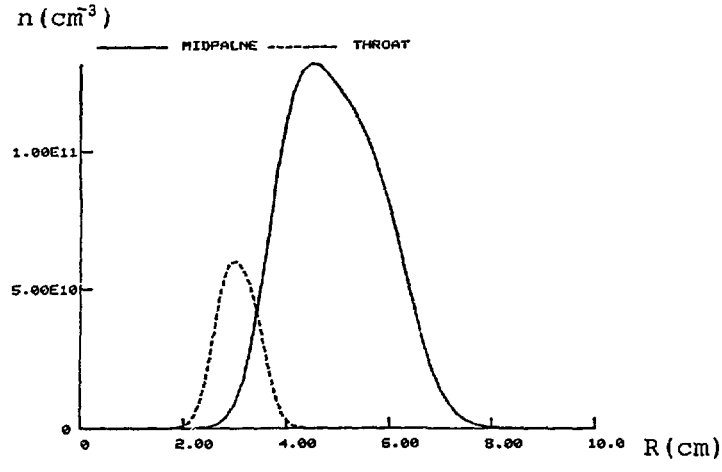

Fig.26 Hot electron density distribution at midplane and at throat

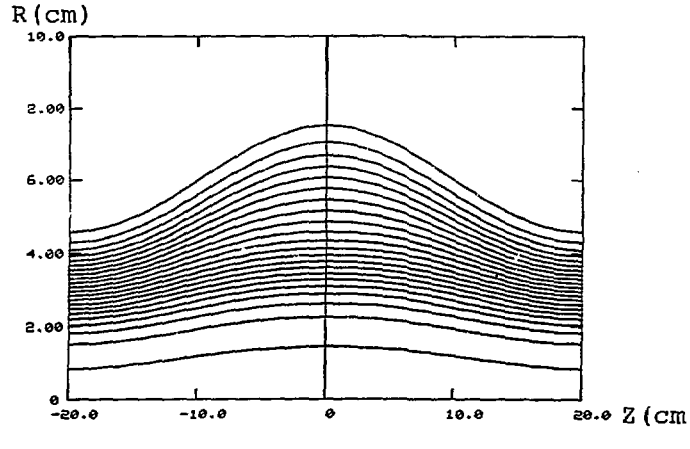

Fig.27 Contour map of core electron density

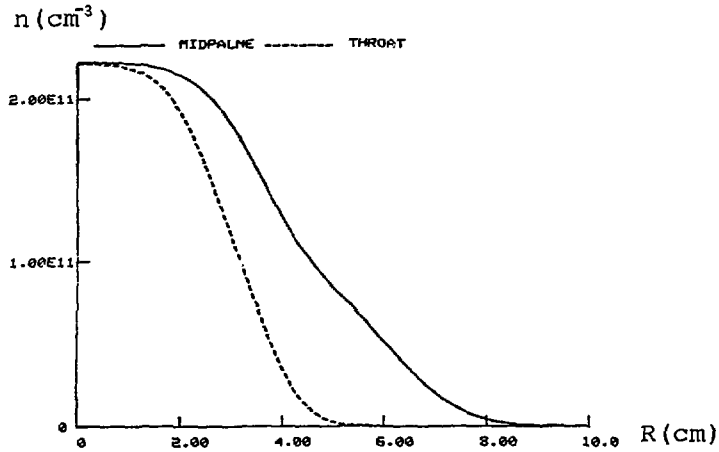

Fig.28 Core electron density distribution at midplane and at throat

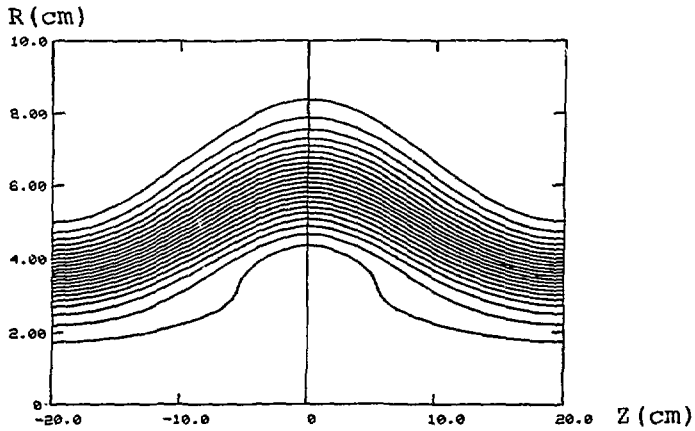

Fig.29 Contour map of core ion density

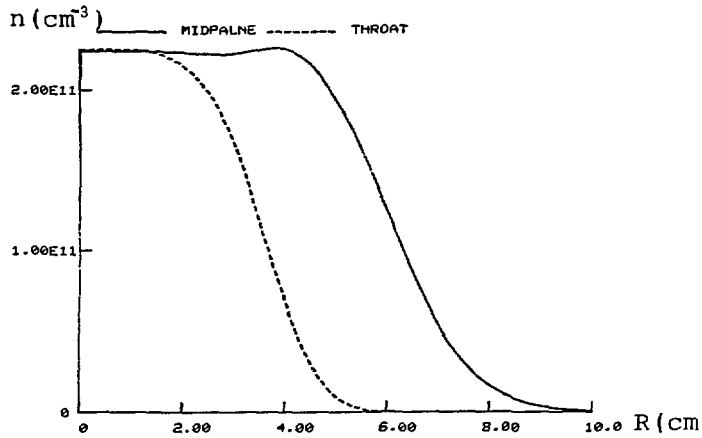

Fig.30 Core ion density distribution at midplane and at throat

case e) Equilibrium of hot electron without core plasma

Parameters

n (cm^{-3})	T (eV)	α_1	α_2	δ
5.0×10^{12}	10^6	-0.02	0.01	1.0

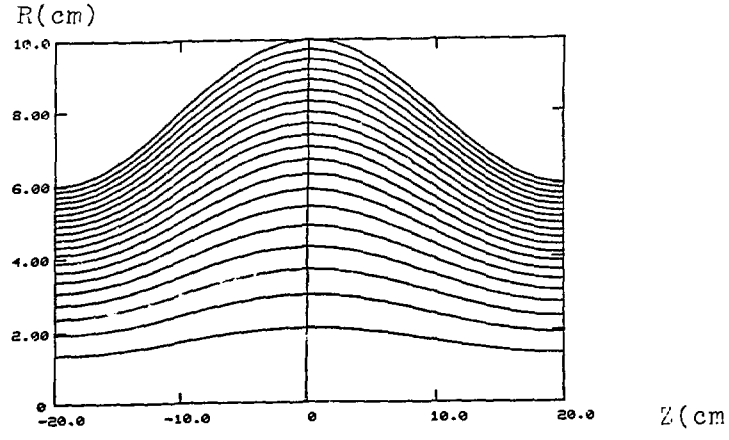

Fig. 31 Magnetic field lines

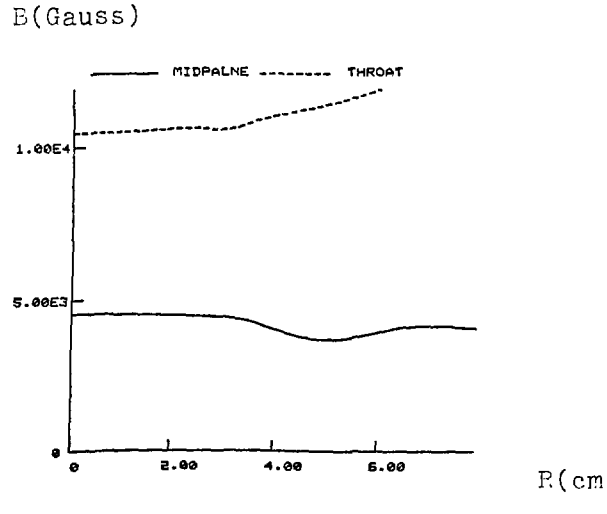

Fig. 32 Mod-B at midplane and at throat

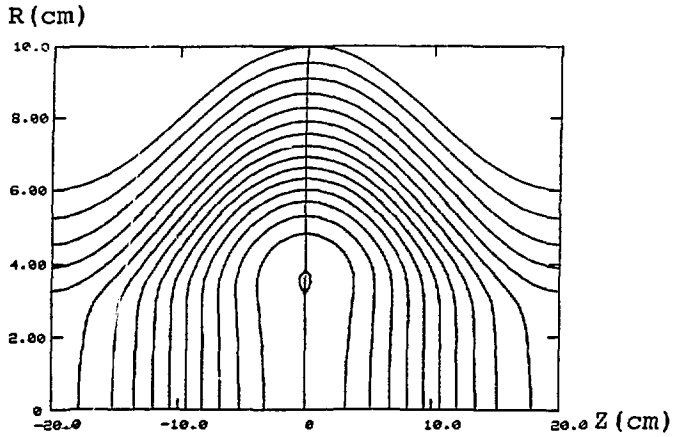

Fig.33 Contour map of electrostatic potential

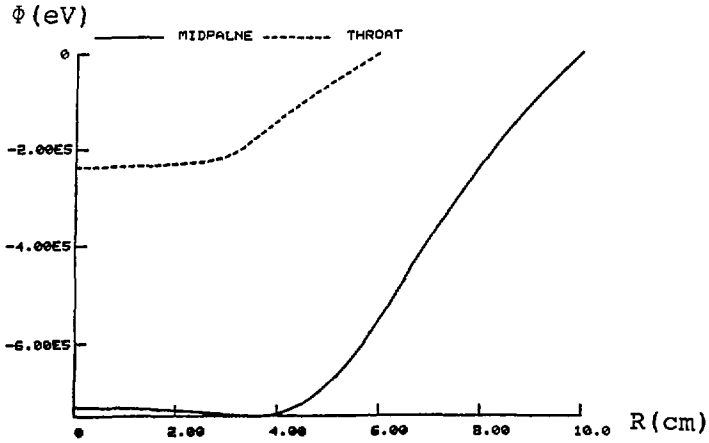

Fig.34 Electrostatic potential at midplane and at throat

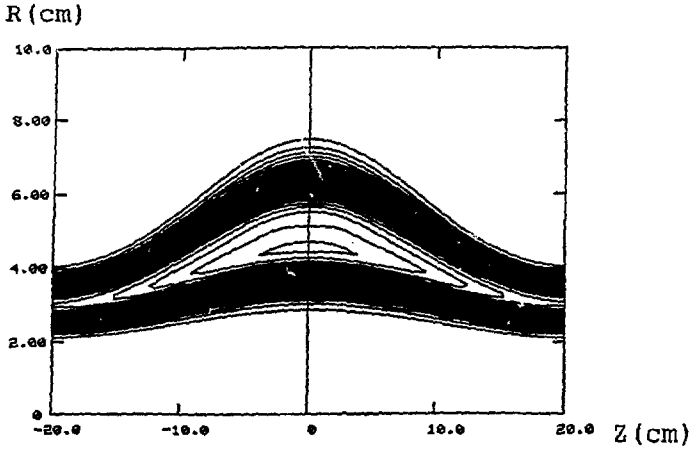

Fig.35 Contour map of hot electron density

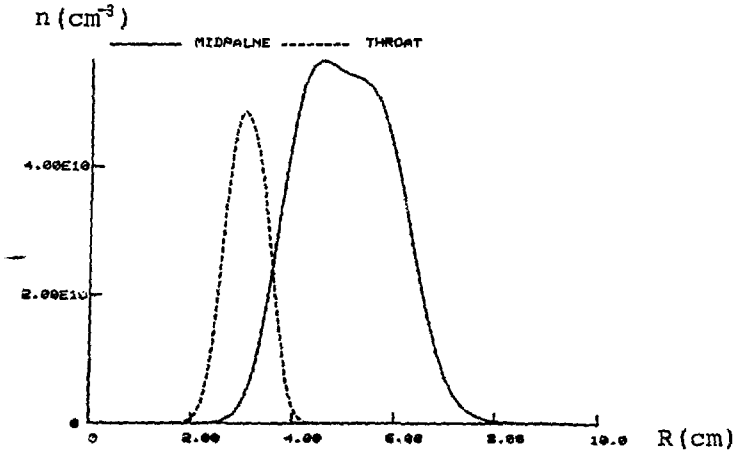

Fig.36 Hot electron density distribution at midplane and at throat

Sensitivity of Heavy Ion Beam Probe to Hot Electrons in EBT*

by

F. M. Bieniosek
McDonnell Douglas Astronautics Company, St. Louis, MO 63166

and

K. A. Connor
Rensselaer Polytechnic Institute, Troy, N. Y. 12181

This paper discusses a method of studying the radial position of locally heated hot electrons in EBT. The heavy ion beam probe on EBT is sensitive to all three electron components--those of the cold surface plasma, the warm core plasma, and the hot electron ring. The total detected signal is proportional to the local electron density at the point of ionization and to the beam ionization rate, which is in turn a function of the local electron temperature. Use of the total detected signal enables qualitative profile measurements of this product known as $nf(T_e)$. The function $f(T_e)$ peaks at several hundred eV, and falls slowly for electron temperatures up to several hundred keV. Especially useful in studies of the hot electrons are the triply ionized Cs^{3+} ionization products. Observations of Cs^{3+} signals with and without 18 GHz microwave power input to the beam probe cavity in EBT-I show a sensitivity to a locally heated hot electron component. Measurements of this component show that it is spatially localized near the 18 GHz second harmonic resonance surface. The hot component is observed at both the upper and lower edges of the plasma and its radial position is observed to vary as the toroidal magnetic field is changed.

*Research performed for Union Carbide Corporation under contract W-7405-eng-26 for the U.S. Dept. of Energy under Subcontract #7044 with Rensselaer Polytechnic Institute.

I. Introduction

An important part of the operation of EBT is the stabilization of the core plasma provided by the hot electron ring. This ring is resonantly heated by microwaves to form a spatially localized distribution of relativistic electrons. These electrons have been studied by a number of diagnostics, including hard X-ray detectors, ionization chamber probes, skimmer probes, diamagnetic loops, and synchrotron radiation detectors, which provide information about their spatial distribution and energy distribution. However, these diagnostics either lack true spatial resolution, requiring an inversion to produce the ring distribution, or are destructive in nature. The heavy ion beam probe, on the other hand, has the advantage that it provides a non perturbing spatially resolved measurement. Hence, the possibility exists of diagnosing the ring by observing the beam ionization products produced locally by interaction with the ring. This paper presents a study of the radial positions of the hot electro produced by microwave heating.

II. Sensitivity to Hot Electrons

Figure 1 shows a cross sectional view of the EBT heavy ion beam probe[1], which is located in the midplane between a pair of mirror coils. A low intensity energetic Cs^+ beam is formed by the ion gun and injected into the plasma chamber. The multiply-charged reaction products (Cs^{2+}, Cs^{3+}) are separated from the beam by the magnetic field and are detected at the secondary detector. This detector is a feedback controlled electrostatic energy analyzer, used to obtain the space potential at the point of ionization by measuring the energy of the reaction products. At the same time, the total signal collected at the detector is proportional to the local electron density at the point of ionization and to the beam ionization rate, which is in turn a function of the local electron temperature.

A plot of the effective cross section

$$\sigma_{eff} = \frac{\langle \sigma v \rangle}{v_b}$$

integrated over a Maxwellian electron distribution at temperature T_e for a fixed beam velocity v_b corresponding to a 10 kV Cs^+ beam is shown in Figure 2 for the two electron impact reactions $Cs^+ \rightarrow Cs^{2+}$ and $Cs^+ \rightarrow Cs^{3+}$. The electron impact ionization cross sections σ as measured by Feeney[2] are used in this calculation. Since the cross sections have not been measured beyond 2 keV, an extrapolation is necessary in the very high energy regions. Most

calculations tend to agree in the high energy range, showing a falloff of 1/E log E in σ^3. For the sake of concreteness the extrapolation used here is based on the theoretical method of Gryzinski.[4] This extrapolation does not take into account the detailed structure of the probing ion, which may be complicated for cesium, especially in the higher charge states (as shown for rubidium in Reference 3). In fact, the most likely difficulty is not that the actual cross section may be too low compared to that given by the approximations, but rather that it might be too high, since other ionization mechanisms, such as excitation and autoionization, may increase the ionization rate at high energies.[5] The cross section ratio Cs^{2+}/Cs^{3+} may be in principle used as a measure of the electron temperature, especially where the ratio is a steep function of temperature. Because of the uncertainty in the numbers, however, these curves cannot be relied upon to give precise temperature measurements. Of particular interest is the fact that the Cs^{3+} cross section on the ring electrons is approximately the same as the Cs^{3+} cross section on cold surface plasma electrons. Since the hot electron ring is immersed in just this cold surface plasma, the beam probe should be sensitive to the hot electrons.

The beam probe system is capable of probing nearly any point in the plasma, including the region of the hot electron ring. Particular locations in the plasma cross section are selected by setting the appropriate gun energy and injection angle. Figure 3 shows the measurement geometry used in this set

of experiments. The gun voltage is varied with no voltage on the sweep plates. The locus of points in the plasma obtained is a curved line called the zero sweep scan as shown in Figure 3. There is a small difference in the location of the zero sweep scan, depending on whether Cs^{2+} or Cs^{3+} ions are being detected. In this figure the ion gun voltages are indicated for measurements with Cs^{+} ions in the standard EBT-I magnetic field (B-field coil current = 5000 A). This information can be scaled for other magnetic fields or ion masses by noting that the voltage required to probe a given point in the plasma scales as B^2/M_i (where M_i = the mass of the probing ion) so that, for example, to probe the center of the plasma with Cs^{2+} requires 10 kV accelerating voltage at 5000 A, but 21 kV at 7250 A.

In this study we use the capability in EBT of turning off the 18 GHz microwave power to a given mirror section without affecting the power input to any of the other sections. This is done with a ferrite switch, either as a manually operated switch, or in a pulsed mode.[6] When this is done, little perpendicular energy remains in the cavity. At the same time, gross stability of the toroidal plasma is not affected, presumably due to the continued presence of the other rings around the torus. The microwave interferometer $\langle n_e \ell \rangle$ drops 6 - 8%, which is the change one would expect if the hot electron ring vanished but the core plasma remained unchanged. Since continuity of the electron temperature and density of the toroidally circulating plasma should be maintained along field lines, any substantial change

observed in the beam probe signal when power is removed from the cavity is interpreted as due to the loss of locally heated electron

III. Ring Turn-Off Experiments

Figure 4 shows data taken during a zero sweep scan from 4 kV to 16 kV while monitoring the Cs^{3+} I_{sum} and ϕ_{sp} signals. Low accelerating voltages correspond to the lower edge of the plasma; high accelerating voltages approach the center of the plasma. (The sharp localized jump in the space potential signal is due to noise and is not plasma related). Each scan was taken twice to ensure repeatability of the data, both with power to the cavity and without power to the cavity. When power was removed from the cavity the $W_{\perp}$ signal on the diamagnetic loop dropped to 37% of its previous value in this case. Such a level is comparable to that signal expected only from the rings in the adjacent cavities;[7] hence little perpendicular energy remained in cavity E-6.

Two observations can be made about the effect of this experiment on the beam probe signals. First, the space potential profile showed little change ($\leq$ 10V) when the power to E-6 was turned off, even outside the potential well. This supports the continuity assumption, that is, that the potential is not directly due to local heating but instead is determined from continuity of the potential along the field lines. The second observation is twofold: over most of the plasma cross section, the total detected Cs^{3+} signal dropped slightly (about 10%) when power to

E-6 was turned off. The Cs^{2+} signal (not shown) showed a similar drop in this case. However, in a small range from 6 to 8 kV, the Cs^{3+} signal showed a larger (20-50%) drop localized in this region ($r \approx 12$-15cm). This reduction in signal level was also observed at the upper edge of the plasma. Because Cs^{3+} is much more sensitive to hot electrons than Cs^{2+}, this indicates the presence of a localized halo of hot electrons, which are hotter than the background electrons in this region and directly dependent on microwave power to the cavity.

This second observation is interpreted in terms of the electron energy distribution model developed from the soft X-ray diagnostic [8]: that there are two Maxwellian components to the electron distribution, one of which is due to the background plasma, and the other due to the hot electron ring. The background plasma should remain essentially unchanged on those field lines which are toroidally connected; hence the large localized change observed at $r \approx 12$-15cm must be identified with the hot electron ring. Figure 5 shows a plot of the space potential profile (from Cs^{2+}) and the relative halo intensity in the Cs^{3+} signal:

$$\text{"relative halo intensity"} = \frac{I_{3+}\ (\text{E-6 on}) - I_{3+}\ (\text{E-6 off})}{I_{3+}\ (\text{E-6 off})}$$

with (in this figure) the approximately 10% background drop subtracted from the result. The 18 GHz second harmonic resonance surface in the vacuum field is indicated by the hatched vertical

line at r = 12.2cm. The rim of the space potential well falls slightly inside the radius of the expected resonance, while at the same time the peak of the relative halo intensity falls slightly outside that radius. No correction has been made for any distortion in the apparent position of the halo due to a possible electron temperature gradient in the background plasma through the ring.

A small difference was also observed on the Cs^{2+} signal profile at r ≈ 12-15cm when the local microwave heating was removed. Comparison of the measured halo profiles allows an estimation of the background temperature at the ring location, because of the different dependencies of their production rates on the electron temperature. The cross section ratio of Figure 2 leads to an estimate of $T_e \approx 80$ eV at the ring location for this case. This estimate can in turn be used to calculate the ratio of ring density to background density from the data of Figure 5, (For $T_{ring} \approx 150$ keV) $n_{ring}/n_{background} = 0.5$. Hence for a typical background density at the ring of 5×10^{11} cm^{-3}, the ring density becomes $n_{ring} = 2.5 \times 10^{11}$ cm^{-3}, comparable to the hard X-ray results.[9]

As the toroidal magnetic field is varied, the resonance $\omega = 2\Omega_{ce}$ moves, and the radial structure of the plasma moves with it. An illustration of this effect is shown in Figure 6. This is a study of the radial position of the rim of the potential well on the bottom of the zero sweep scan. Also plotted is the resonance position as a function of toroidal field current. This figure shows the potential well increasing in size as the

magnetic field increases. The rim of the potential well followed, but remained slightly inside of, the second harmonic resonance surface, implying that the hot electron ring, which defines the edge of the core plasma, also falls near the second harmonic resonance. Similar results were obtained earlier with a skimmer probe.[8]

A study of the effect of moving the resonance surface on the hot electrons observed with Cs^{3+} has also been made. Figure 7 shows the results of a pulsed ring experiment (1 second on, 1 second off) at 4000 A field current. The relative change in the Cs^{3+} signal as the power to the cavity was turned on is plotted for both the top and bottom of the plasma along the zero sweep path (with negative radius being those points below the horizontal axis). As expected, the hot electrons moved inward from the 5000 A case: the peak change on the bottom of the plasma moved from 13cm to 11cm radius. At both the top and bottom, the peak is near $\omega = 2\Omega_{ce}$ (hatched region). The effect of the pulsed ring is less than 10% in the core. It is larger in the surface plasma, probably because the hot electrons are easier to see relative to the cold surface electrons than relative to the warm core electrons. This fact distorts the apparent shape of the ring. Neglecting temperature gradients in the background plasma the apparent thickness of the ring is about 5-8cm for both the 4000 A and the 5000 A cases. However, although the background T_e is not well known in this region, the presence

of any positive temperature gradient, as expected through the boundary between the warm core plasma and the cold surface plasma, would reduce the apparent thickness of the ring by about 1-3cm, depending upon the steepness of the gradient in T_e.

In Figure 8 a similar experiment at 7250 A field current is shown together, for comparison, with the 4000 A and 5000 A data for the lower half of the plasma. The 7250 A case is a fundamentally different heating topology, the so called FR-configuration, in which the magnetic field is high enough to move the $\omega = \Omega_{ce}$ fundamental resonance for 18 GHz onto the mid-plane.[10] The hatched regions in the figure correspond to the radial positions of the second harmonic, and the cross hatched region (at 7250 A) corresponds to the radial position of the fundamental. The 4000 A and 5000 A cases have similar radial structure, but the 7250 A case looks different. In this case the $W_\perp$ signal dropped to 45% of its previous value when the ring was turned off, so that most of the stored energy, or hot electron density, in cavity E-6 was lost. Here the largest observed effect on the Cs^{3+} signal was near the second harmonic, despite the fact that it was near the outer edge of the plasma. However it is difficult to separate the local heating of the surface plasma from the formation of the hot electron ring because the field lines at the edge of the plasma are not toroidally connected. In contrast to the lower field cases, the relative change in Cs^{3+} signal did not drop to 10% inside of the second harmonic position, but remained close to 40% up to the first harmonic

surface. Finally, inside of the $\omega = \Omega_{ce}$ surface there was no Cs^{3+} signal at all due to the very low core T_e in the FR-configuration. Similar, but smaller amplitude, hollow profiles were also observed on the relative change of the Cs^{2+} signal. The 7250 A profile shows evidence of heating from the fundamental surface out to nearly the wall, especially near the second harmonic. Hence, the position of the hot electron ring is not clear from this experiment.

IV. Summary

The ring turn-off experiments using the heavy ion beam probe described in this paper have studied the continuity of the toroidal plasma and the radial distributionof the locally heated hot electrons. The space potential did not appreciably change during a ring turn off, thus implying that the potential is determined from continuity along the field lines around the torus. Applying this result to the continuity of the density and temperature of the toroidal plasma, the sensitivity of the ion beam signal Cs^{3+} to the locally heated hot electrons (hot electron ring) was used to study their distribution. This study confirmed the existence of a spatially localized distribution of hot electrons near the 18 GHz second harmonic resonance, consistent with the hot electron ring observed with the X-ray diagnostic and with a radial thickness of about 3-5cm. The radial position of the hot electrons was observed to vary with

magnetic field as the resonance surface moved. However, the data from the 7250 A FR-configuration are difficult to interpret because of the presence of a significant change in the Cs^{3+} signal during a ring turn off over a wide range of radii.

REFERENCES

1. F. M. Bieniosek, P. L. Colestock, K. A. Connor, R. L. Hickok, S. P. Kuo and R. A. Dandl, Rev. Sci. Instrum. 51, 206 (1980).

2. R. K. Feeney and D. R. Hertling, "Absolute Experimental Cross Sections for Electron Impact Ionization of Cs^+ Ions, Single, Double, Triple, and Quadruple". Research Report ORNL/SUB-7802/X07/1, Oak Ridge, Tennessee, February, 1981.

3. D. W. Hughes, R. K. Feeney, "Absolute Experimental Cross Sections for the Electron Impact Ionization of Rubidium", U. S. Department of Energy Technical Report ORO-3027-52, Oak Ridge, Tennessee (1980).

4. M. Gryzinski, Phys. Rev. A. 138, 341 (1965).

5. G. H. Dunn, IEEE Trans. Nucl. Science NS-23, 929 (1976).

6. J. Wilgen and D. L. Hillis, Bull. Am. Phys. Soc., 26, 979 (1981).

7. K. H. Carpenter, "Diamagnetic Measurements for Experimental Determination of EBT Ring Parameters", Proc. EBT Ring Physics Workshop, Oak Ridge National Laboratory, CONF-791228 page 143 (1980).

8. R. A. Dandl, et.al., "Summary of EBT-I Experimental Results, Oak Ridge National Laboratory Report ORNL/TM-6457 (1978).

9. N. A. Uckan, et.al., "Physics of Hot Electron Rings in EBT: Theory and Experiment, Oak Ridge National Laboratory Report ORNL/TM-7585 (1981).

10. J. C. Glowienka, et.al., "Nonstandard Heating Experiments in EBT", these proceedings.

FIGURE CAPTIONS

Figure 1: Schematic diagram of heavy ion beam probe hardware with typical primary and secondary ion trajectories

Figure 2: Effective electron impact cross sections for a 10 k Cs^+ ion beam.

Figure 3: Measurement geometry for Cs^+ ions in EBT-I.

Figure 4: Effect on Cs^{3+} signals of removing microwave power to the beam probe cavity (E-6).

Figure 5: Radial profile of space potential and relative halo intensity of Cs^{3+} signal.

Figure 6: Position of the rim of the potential well on a single scan, in comparison to the vacuum resonance position $\omega=2\Omega_{ce}$, as a function of toroidal field current.

Figure 7: Radial profile of the relative change in the Cs^{3+} signal for a ring turn off experiment at 4000 A.

Figure 8: Radial profile of the relative change in the Cs^{3+} signal for ring turn off experiments at 4000 A, 5000 A and 7250 A.

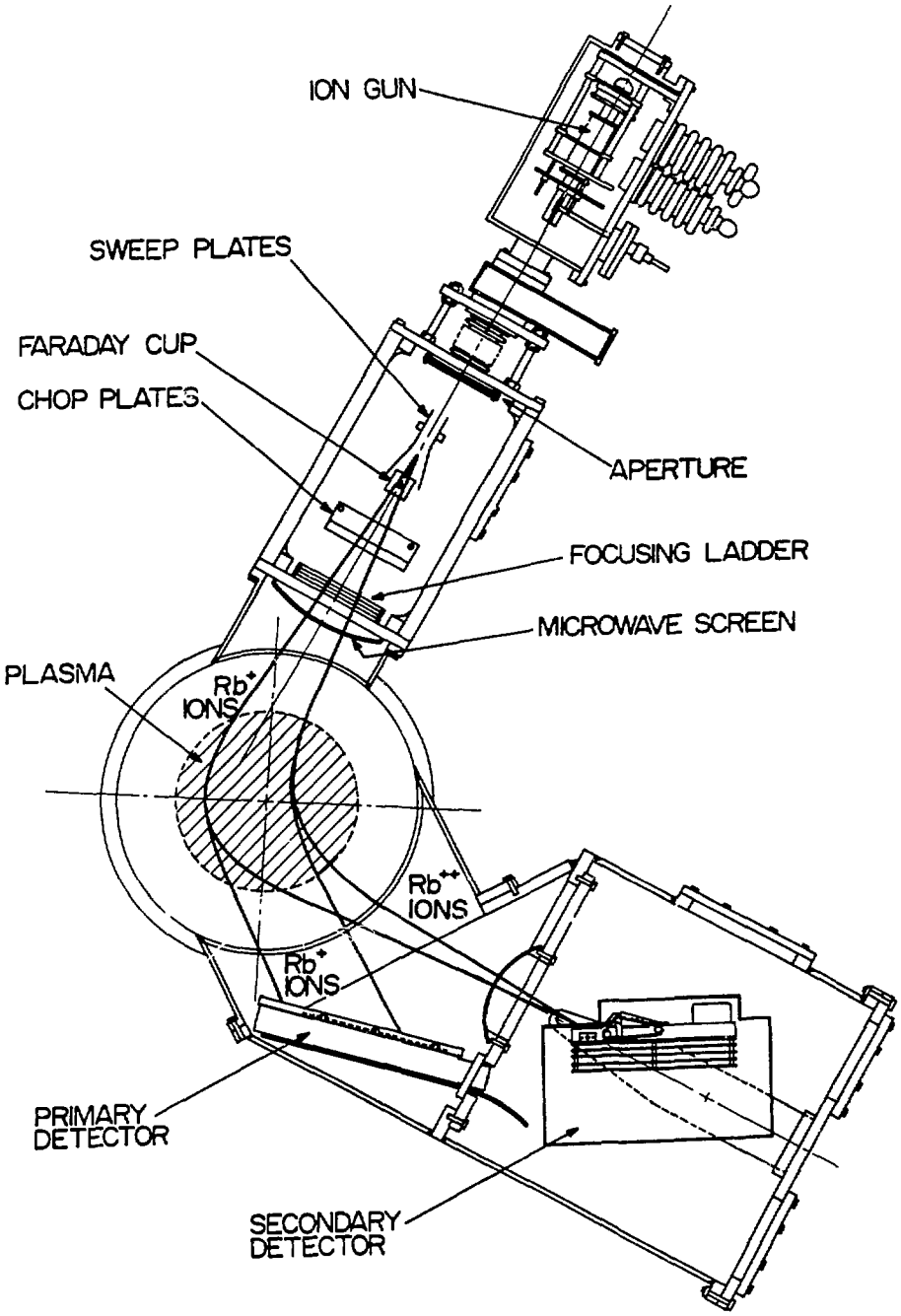
ION GUN
SWEEP PLATES
FARADAY CUP
CHOP PLATES
APERTURE
FOCUSING LADDER
MICROWAVE SCREEN
PLASMA
Rb+ IONS
Rb++ IONS
Rb+ IONS
PRIMARY DETECTOR
SECONDARY DETECTOR

Fig. 1

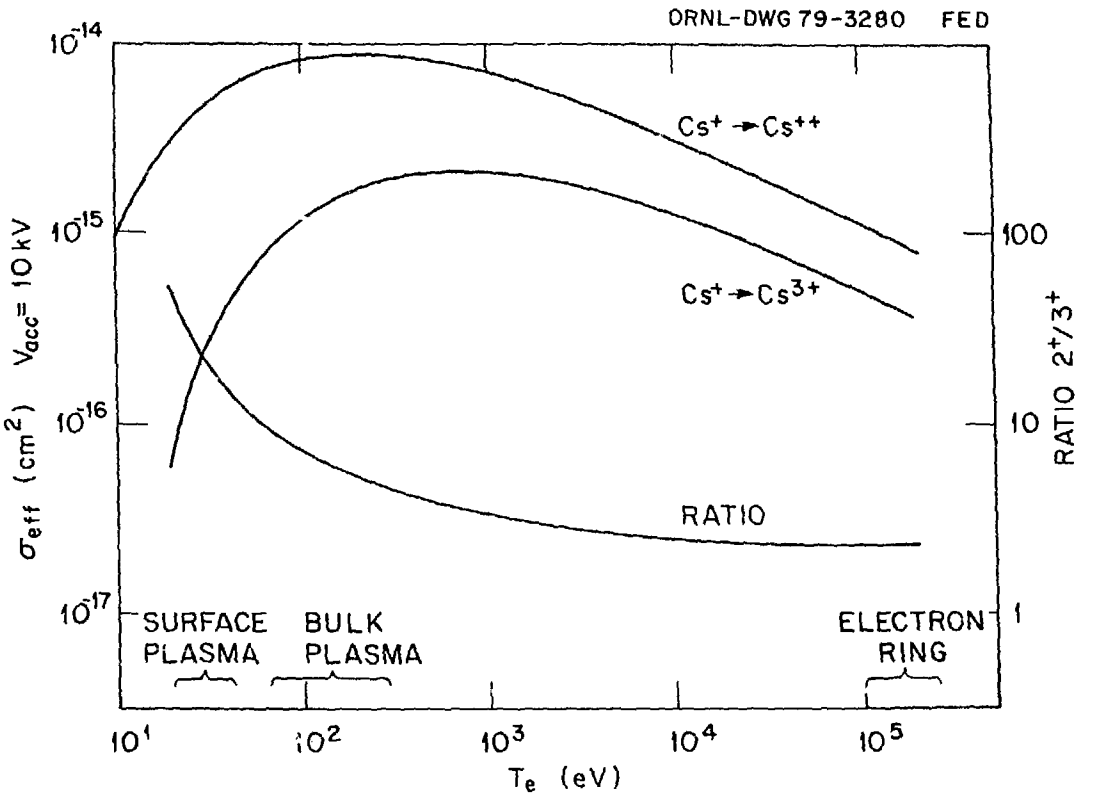
ORNL-DWG 79-3280 FED
10^{-14}
10^{-15}
10^{-16}
10^{-17}
σ_{eff} (cm^2) V_{acc}= 10 kV
$Cs^+ \rightarrow Cs^{++}$
$Cs^+ \rightarrow Cs^{3+}$
RATIO
100
10
1
RATIO $2^+/3^+$
SURFACE PLASMA
BULK PLASMA
ELECTRON RING
10^1
10^2
10^3
10^4
10^5
T_e (eV)

Fig. 2

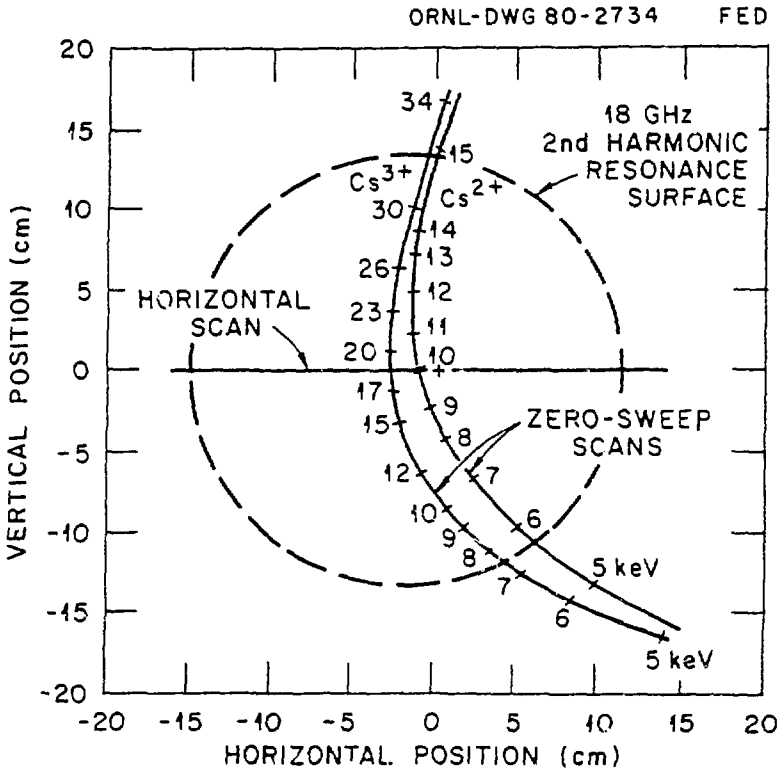
ORNL-DWG 80-2734 FED
18 GHz
2nd HARMONIC
RESONANCE
SURFACE
HORIZONTAL
SCAN
ZERO-SWEEP
SCANS
Cs3+
Cs2+
5 keV
5 keV
VERTICAL POSITION (cm)
HORIZONTAL POSITION (cm)

Fig. 3

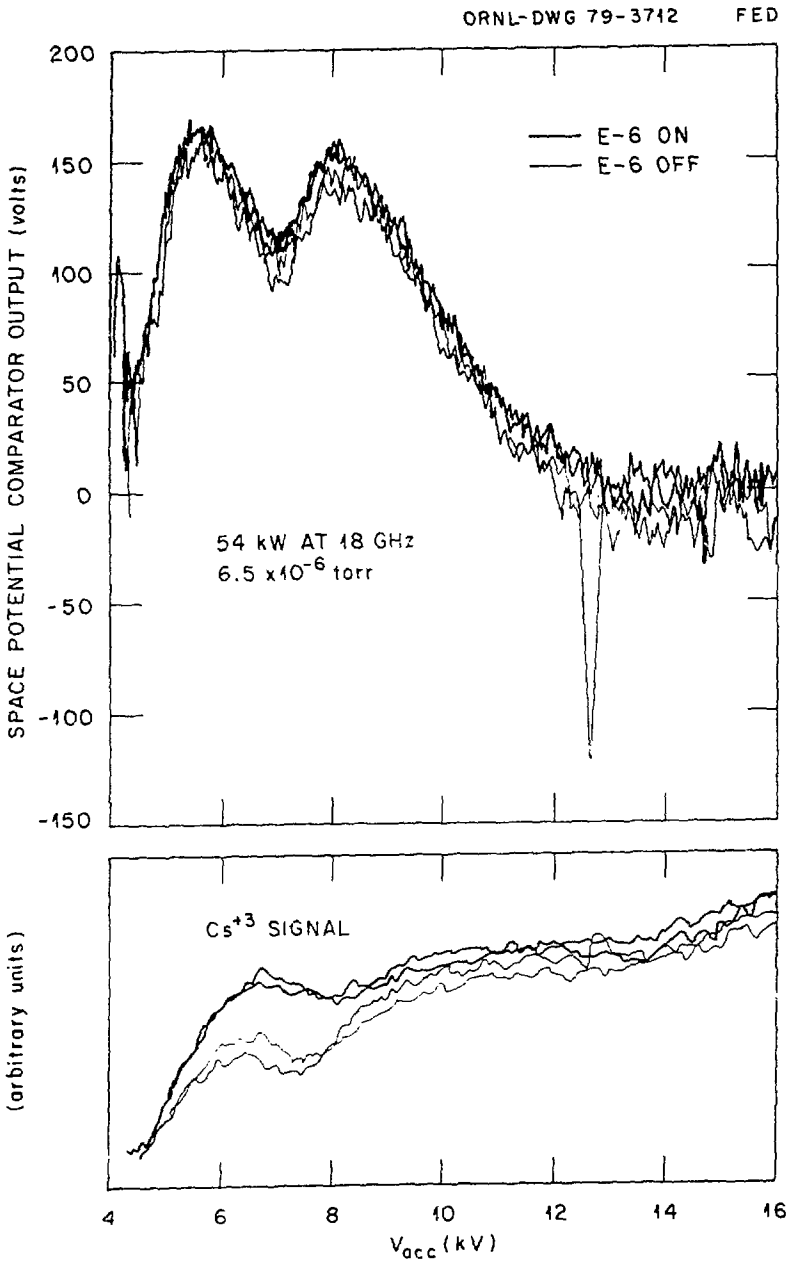
ORNL-DWG 79-3712 FED
SPACE POTENTIAL COMPARATOR OUTPUT (volts)
200
150
100
50
0
-50
-100
-150
E-6 ON
E-6 OFF
54 kW AT 18 GHz
6.5 x10^-6 torr
(arbitrary units)
Cs+3 SIGNAL
4
6
8
10
12
14
16
Vacc (kV)

Fig. 4

ORNL-DWG 79-3459 FED

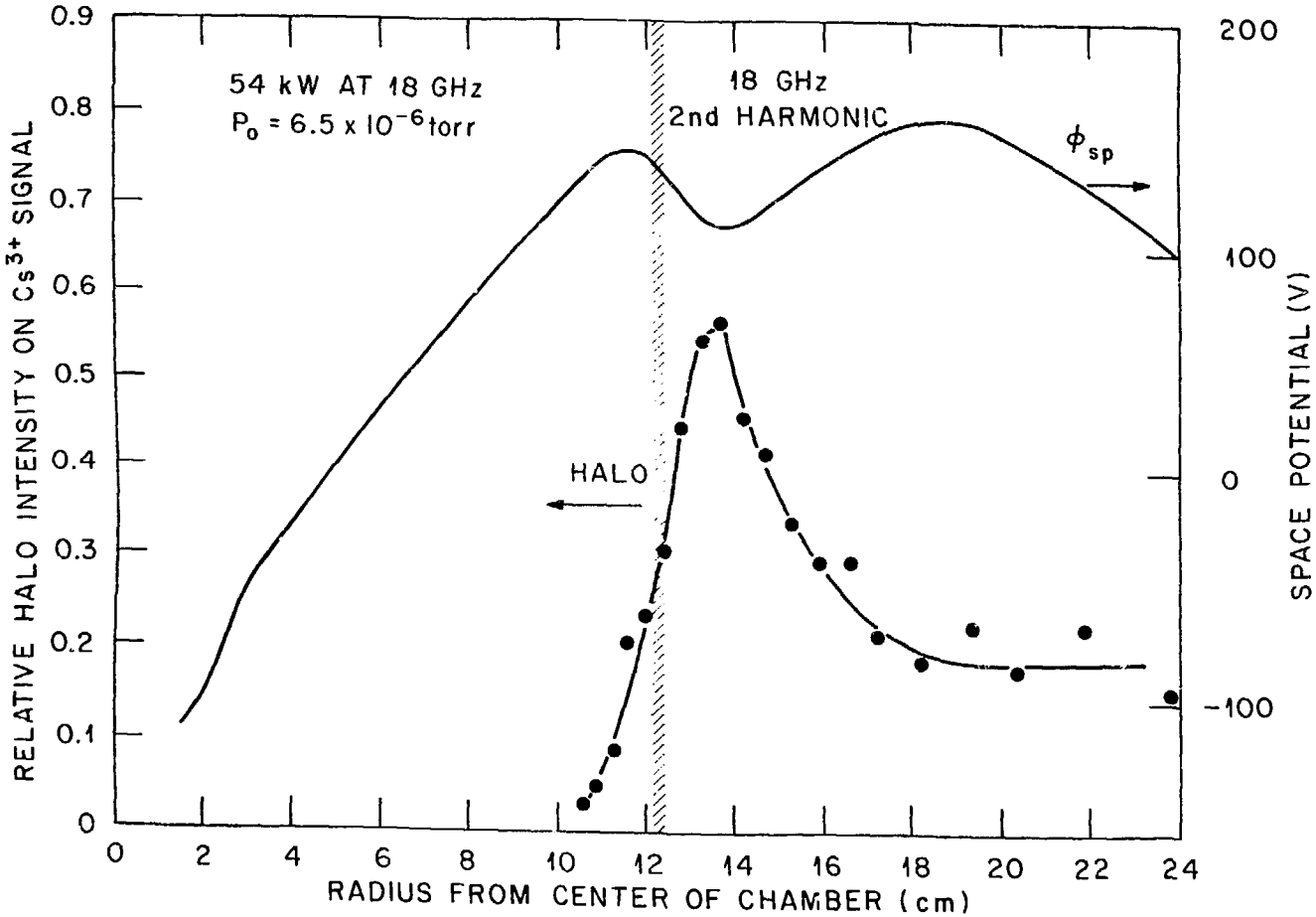

Fig. 5

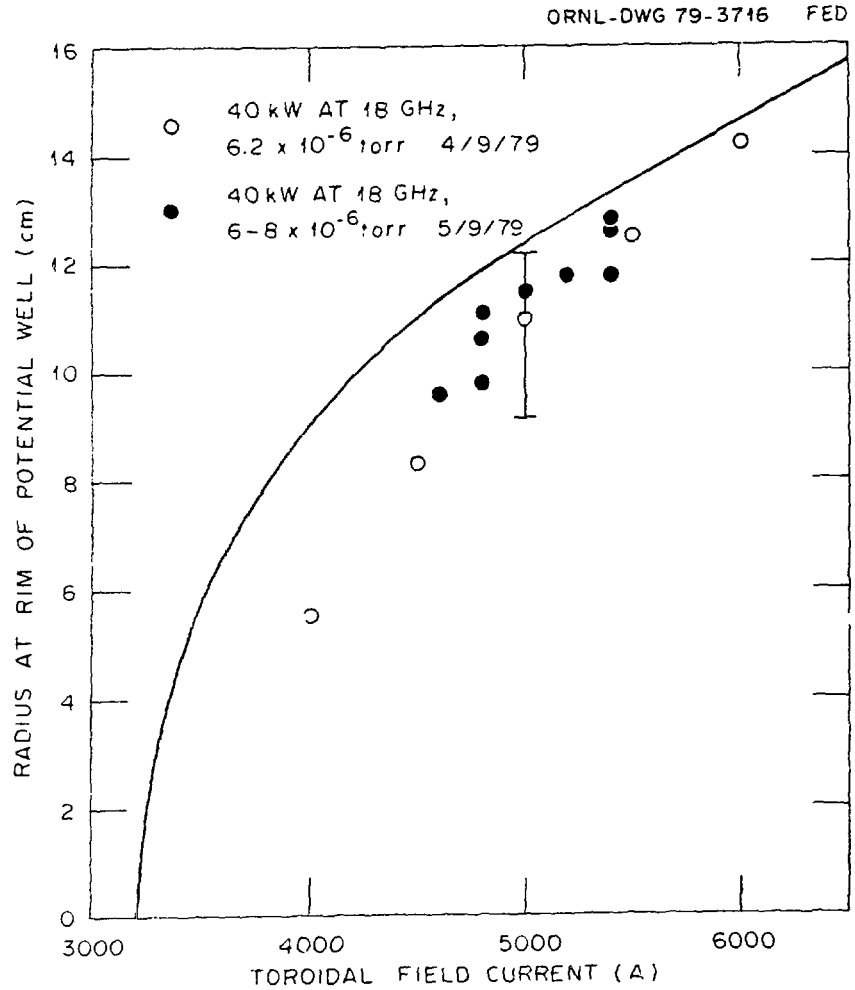
ORNL-DWG 79-3716 FED
40 kW AT 18 GHz,
6.2 x 10^-6 torr 4/9/79
40 kW AT 18 GHz,
6-8 x 10^-6 torr 5/9/79
RADIUS AT RIM OF POTENTIAL WELL (cm)
TOROIDAL FIELD CURRENT (A)
0
2
4
6
8
10
12
14
16
3000
4000
5000
6000

Fig. 6

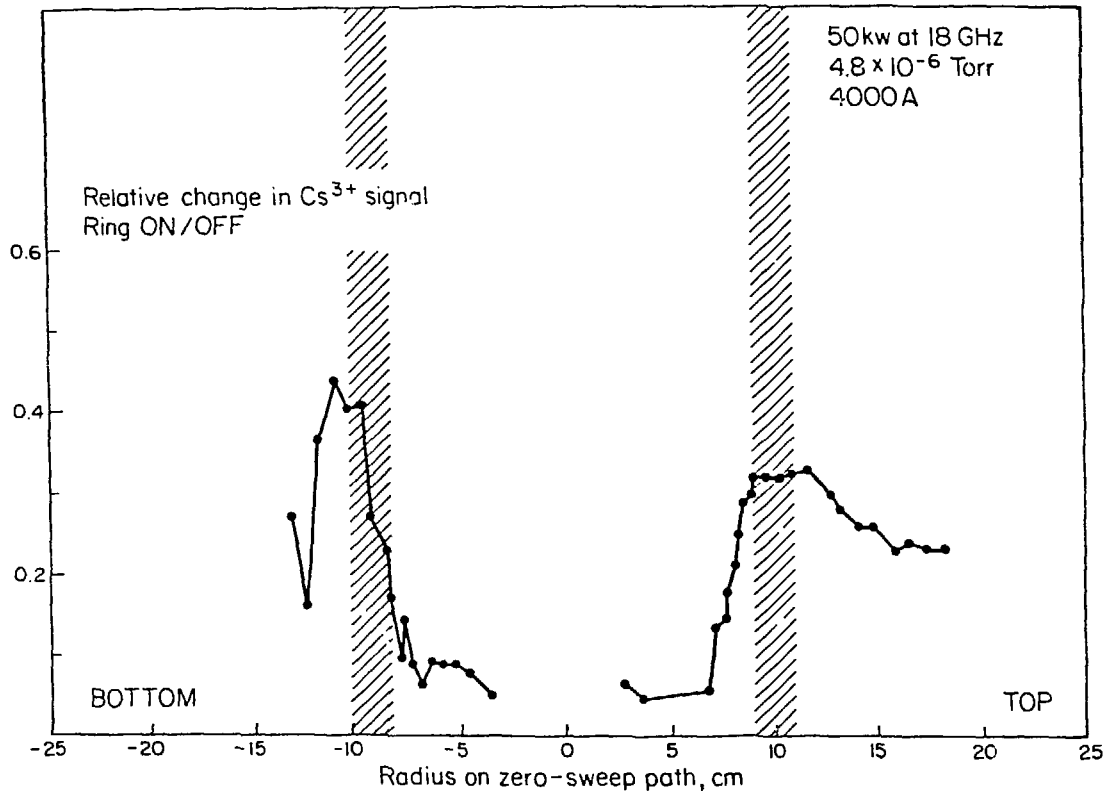
50kw at 18 GHz
4.8 x 10^-6 Torr
4000 A
Relative change in Cs3+ signal
Ring ON/OFF
0.6
0.4
0.2
BOTTOM
TOP
-25
-20
-15
-10
-5
0
5
10
15
20
25
Radius on zero-sweep path, cm

Fig. 7

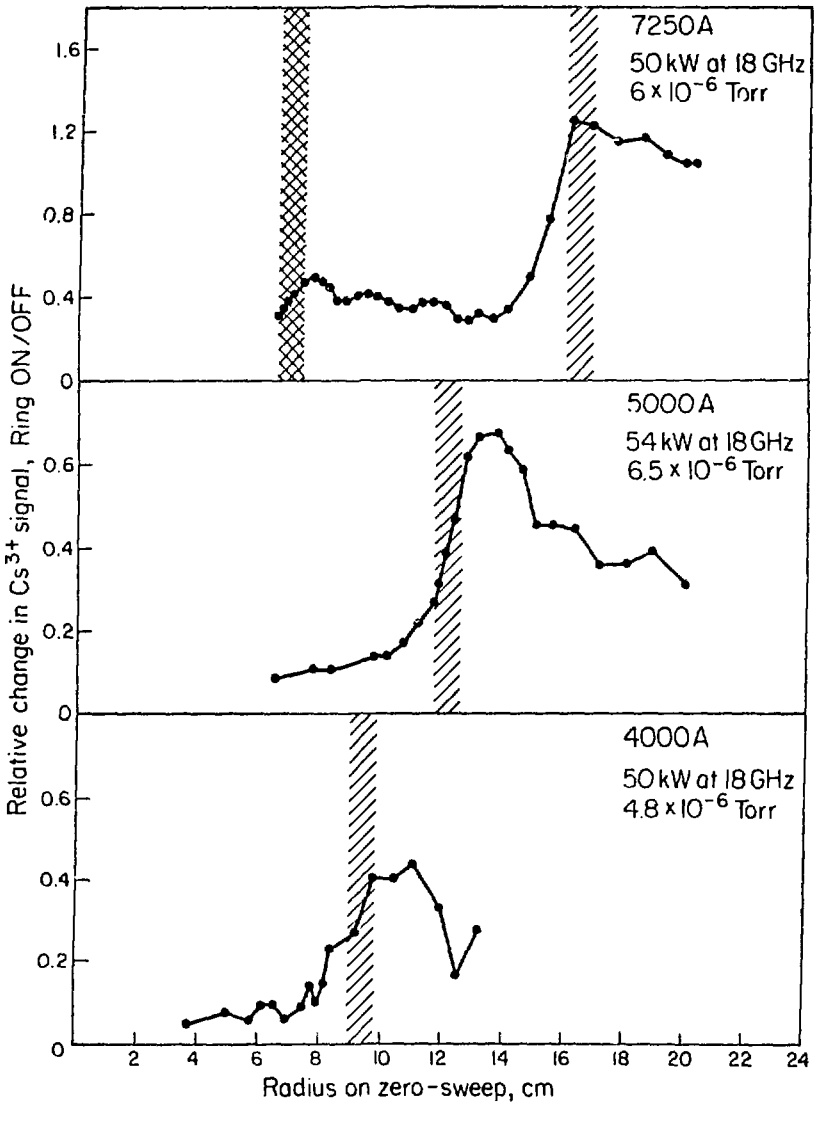
7250A
50 kW at 18 GHz
6 x 10^-6 Torr
5000A
54 kW at 18 GHz
6.5 x 10^-6 Torr
4000A
50 kW at 18 GHz
4.8 x 10^-6 Torr
Relative change in Cs3+ signal, Ring ON/OFF
Radius on zero-sweep, cm
0
0.2
0.4
0.6
0.8
1.2
1.6
2
4
6
8
10
12
14
16
18
20
22
24

Fig. 8

THE "NEGATIVE" TANDEM MIRROR*

P. Poulsen, S. L. Allen, T. A. Casper, D. P. Grubb, R. A. Jong,
W. E. Nexsen, G. D. Porter, and T. C. Simonen
Lawrence Livermore National Laboratory, University of California
Livermore, CA 94550

ABSTRACT

A tandem mirror configuration can be created by combining hot electron end cell plasmas with neutral beam pumping. A region of large negative potential formed in each end cell confines electrons in the central cell. The requirement of charge neutrality causes the central cell potential to become negative with respect to ground in order to confine ions as well as electrons. We discuss the method of producing and calculating the desired axial potential profile, and show the calculated axial potential profile and plasma parameters for a negative configuration of TMX-Upgrade.

*Work performed under the auspices of the U.S. Department of Energy by the Lawrence Livermore National Laboratory under contract number W-7405-ENG-48.

1. THE NEGATIVE TANDEM CONFIGURATION

1.1 SIMPLE TANDEMS

The tandem mirror machines confine plasma in a large volume central cell by creating a difference in potential between the central cell and small volume end cells. In TMX,[1] it was shown that a mirror confined ion population in each end cell produced an end cell potential that was positive with respect to the central cell. Ions were therefore confined in the central cell, and the plasma potential of the central cell was positive in order to confine electrons equally as well as ions.

The negative machine is also possible, i. e. a machine in which end cell electron rather than ions are mirror confined. This option has been considered earlier by Fowler. In this machine, the hot electron density in the end cells exceeds the central cell density; since the lifetime of the end cell electrons is enhanced by mirror confinement, the end cell plasmas develop a negative potential in order to enhance the ion lifetime by potential confinement and maintain charge neutrality. It was found, however, that the central cell to end cell potential difference required to confine central cell electrons demanded that the density difference between the central cell and end cells be large. As a consequence, the end cell density was found to be excessive in terms of power loss and required microwave frequencies.

1.2 PUMPED TANDEMS

A later development enabled the construction of a large negative end cell potential without employing hot electron end cell plasmas much denser than the central cell. It was found that if ions were removed (pumped) at a sufficient rate from the region of the mirror confined, hot electrons, a large negative potential could be produced even in end cell plasmas having densities less than the central cell density.[2] The negative potential develops as a

response of the plasma to maintain charge neutrality in the end cells. Thus, if the end cell electron lifetime is enhanced by mirror confinement, and ions are removed from the end cells by a pumping mechanism described below, the loss of ions by scattering from the region is reduced by the formation of a deep potential well untill the charge flows are equal. This mechanism can be employed to create the thermal barrier for positive tandems,[3] and it can be employed to create the electron confining potential of a negative tandem mirror. An example is shown in Fig. 1.

One method of pumping ions out of a potential well is by passing a beam of energetic neutral atoms through the plasma. If the conditions for magnetic and potential confinement are not satisfied for ions that are produced by charge exchange of the neutrals with potential trapped ions, the net effect is the removal of trapped ions from the potential well. The neutrals that are produced by neutralization of the trapped ions escape the plasma across the field lines.

The density of the end cells in which the negative potentials are located can be substantially less than the density of the central cell. It is this feature that makes the negative tandem attractive from the point of view of making a fusion reactor. The lower density of the hot electron end cell plasma decreases the power and frequency requirement for the microwave heating. In the experimental design discussed below, the density of the hot electron plasma is less than the central cell plasma. Increasing the end cell mirror ratio and decreasing the ratio of the thermal electron temperature to the ion temperature further decreases the end cell density and the ECRH power requirement.

2. *AXIAL POTENTIAL PROFILE AND CONFINEMENT*

2.1 DETERMINATION OF THE POTENTIAL PROFILE

The axial confinement of the negative tandem is determined by the confinement of the thermal central cell electrons by the negative

potential in each end cell. The shape and magnitude of the axial potential is determined by the quasi-neutrality requirement and the dependence of the ion and electron densities on the electrostatic potential and the magnetic field. In calculating the axial potential profile, it is convenient to identify four separate populations of ions and electrons:

a. Thermal, Maxwellian ions in the central cell having temperature T_i; this population flows through the inner mirror into the low potential region of each end cell, is reflected, and returns to the central cell. This is the passing ion population, with a local density n_p depending on both the potential ϕ and the magnetic field B.

b. A fraction of the passing population becomes trapped by collisions in the end cell potential well. This is the trapped ion population. Its local density n_T depends upon the potential ϕ, the magnetic field B, the temperature T_i, and the rate of removal ν of the trapped ion population from the well. It is the dependence of this population on the pumping strength ν that enables the formation of large negative potentials in end cell regions with densities less than the central cell density. The dependence has been found through extensive Fokker-Planck calculations[4] and has been modeled in analytic form.[5]

c. The thermal electron population, assumed to be Maxwellian with temperature T_e within the regions of potential confinement. Outside of this region, the electrons accelerate rapidly, and their density decreases and becomes negligible compared to the mirror confined electron density.

d. The mirror confined electron population, with density n_H assumed to depend only on the magnetic field strength.

The functional dependence, except for the electron and ion temperature, can be written

$$n_H(B) + n_e(\phi) = n_p(\phi,B) + n_T(\phi,B,\nu)$$

It is seen that the potential ϕ is a function of the magnetic field and the pumping strength ν. The axial distribution of the

electrostatic potential $\phi(z)$ is obtained through the axial distribution of the magnetic field intensity $B(z)$. The axial profile shown in Fig. 1(a) and (b) are similar to those of TMX-Upgrade. The magnitude relative to the central cell of the positive potential near the outer mirror points is determined by requiring the loss of ions to equal the total outflow, thermal and hot, of electrons. The axial loss of thermal electrons is determined by a Pastukhov relation.[6] The ion loss is the sum of Pastukhov loss, radial transport, and pumping losses. The density profiles of ions and electrons are shown in Fig. 2 and 3, respectively.

2.2 TMX-UPGRADE PARAMETERS

The TMX-Upgrade confinement device can be operated in a "negative" mode. This mode employs the pumping beams and central cell heating beams only, with no sloshing beams. The calculations are done for an axial $(n\tau)_p = 10^{12}$ cm^{-3} s. The plasma parameters are given in Table I. Cases A and B correspond to different estimates of the radial transport. Case C shows the effect of heating the central cell plasma with ICRH rather than neutral beams. A diagram of the power flow is given in Fig. 4. We note that the axial $(n\tau)_p$ can be increased considerably by increasing the depth of the electron confining potential. This can be accomplished by increasing the neutral beam pumping or increasing the end cell mirror ratio.

3. SUMMARY

Our calculations show that an effective tandem mirror confinement configuration with hot electron end cell plasma densities of 2 to 5 x 10^{12} cm^{-3} can be constructed. Two primary issues in the design of an experiment or a fusion reactor are discussed elsewhere in this workshop: (1) The power required to support the hot electron density, and (2) the MHD stability of the plasma.

Initial analysis of both the microstability[7] and MHD stability[8] is encouraging, and detailed work is in progress.

4. ACKNOWLEDGMENT

We acknowledge the work of G. Logan, T. K. Fowler, and D. Baldwin in conceiving the ideas and doing much of the detailed work, and F. H. Coensgen for initiating this work.

REFERENCES

1. Coensgen, F. H. et al., Phys. Rev. Lett. 44 (1980) 1132.
2. Mirror League Workshop, LLNL, March 1979.
3. Coensgen, F. H. et al., TMX Upgrade Major Project Proposal, Lawrence Livermore National Laboratory Report LLL-PROP-172.
4. LoDestro, L., Mirror Theory Monthly, May 15, 1980.
5. Cohen, R. H., UCRL-84535.
6. Cohen, R. H. et al., Nuclear Fusion 18, 1229 (1978).
7. Casper, T. A., Bull. Am. Phys. Soc., post deadline session, New York, N.Y., October 1981.
8. Baldwin, D. E., personal communication, September 1981.

Table I. TMX upgrade parameters.

Parameter	TMX-U (positive) Thermal barrier (reference case)	TMX-U (negative) Case A	Case B	Case C
Central cell				
Density, n_c (10^{12} cm^{-3})	23	20	16.4	10.6
Ion density, n_{ic} (bulk) (10^{12} cm^{-3})	16.7	10.6	10.6	10.6
Ion temperature, T_{ic} (keV)	0.90	1.0	1.0	1.0
Electron temperature, T_{ec} (keV)	0.60	0.45	0.43	0.24
Beta, β_c ($\perp$)	0.25	0.18	0.12	0.05
Ion confining potential, ϕ_i (keV)	2.2	2.5	2.5	2.5
Electron confining potential, ϕ_e (keV)	2.6	2.4	2.4	1.3
Axial confinement, $(n\tau)_{c\parallel}$ (10^{11} cm^{-3} s)	10	10	10	10
Radial confinement, $(n\tau)$ (10^{11} cm^{-3} s)	5	2	∞	∞
Beam ionization fraction, f^c_{ion}	0.15	0.13	0.11	-
Beam charge-exchange fraction, f^c_{cx}	0.30	0.28	0.22	-
Beam current, I^c_{beam} (incident) (A)	180	162	107	-
Gas feed, I_{gas} (H equiv.) (A) (ionized)	42	67	35	46
ICRH power (absorbed) (kW)	-	-	-	250
Plugs (per plug)				
Density, n_p (10^{12} cm^{-3}) (at electron feed)	7	7	7	7
Confinement, $(\tau n_a)_p$ (cx) (10^{10} cm^{-3} s)	5	-	-	-
Perpendicular beta, $\beta_\perp$	0.33	0.32	0.32	0.32
Parallel beta, $\beta_{p\parallel}$	0.01	0.08	0.08	0.08
Barrier electron energy, E_{eh}(b) (keV)	50	50	50	50

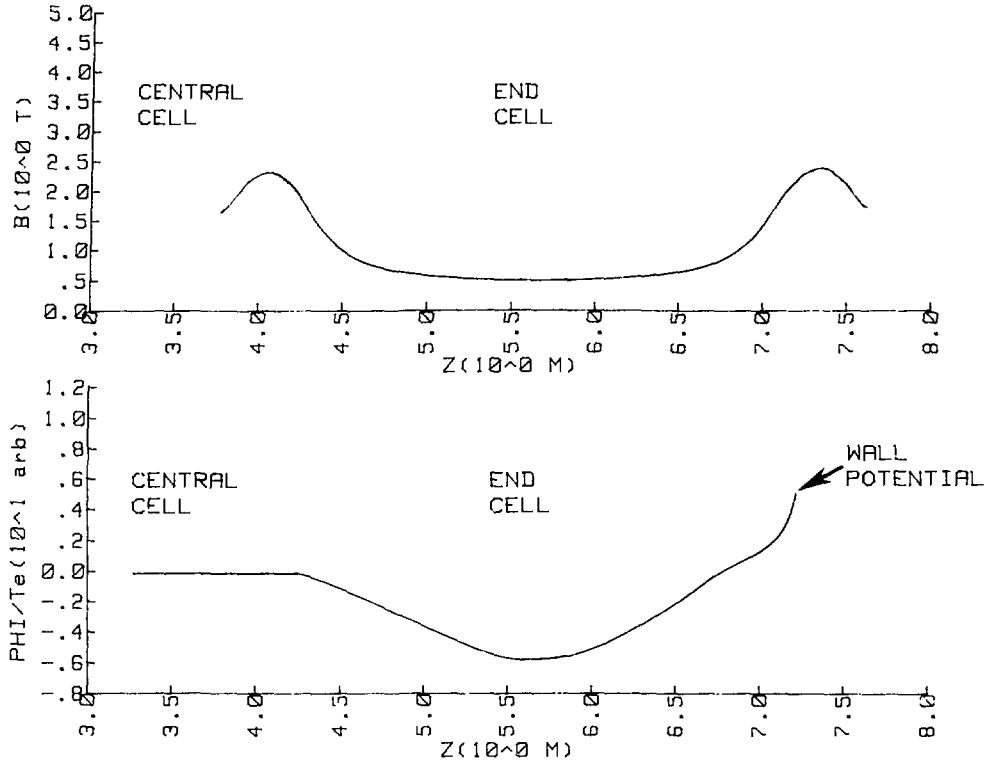

Fig. 1. Axial profiles of magnetic field (top figure) and electrostatic potential (bottom figure). The field and potential models TMX-Upgrade operated in a negative mode.

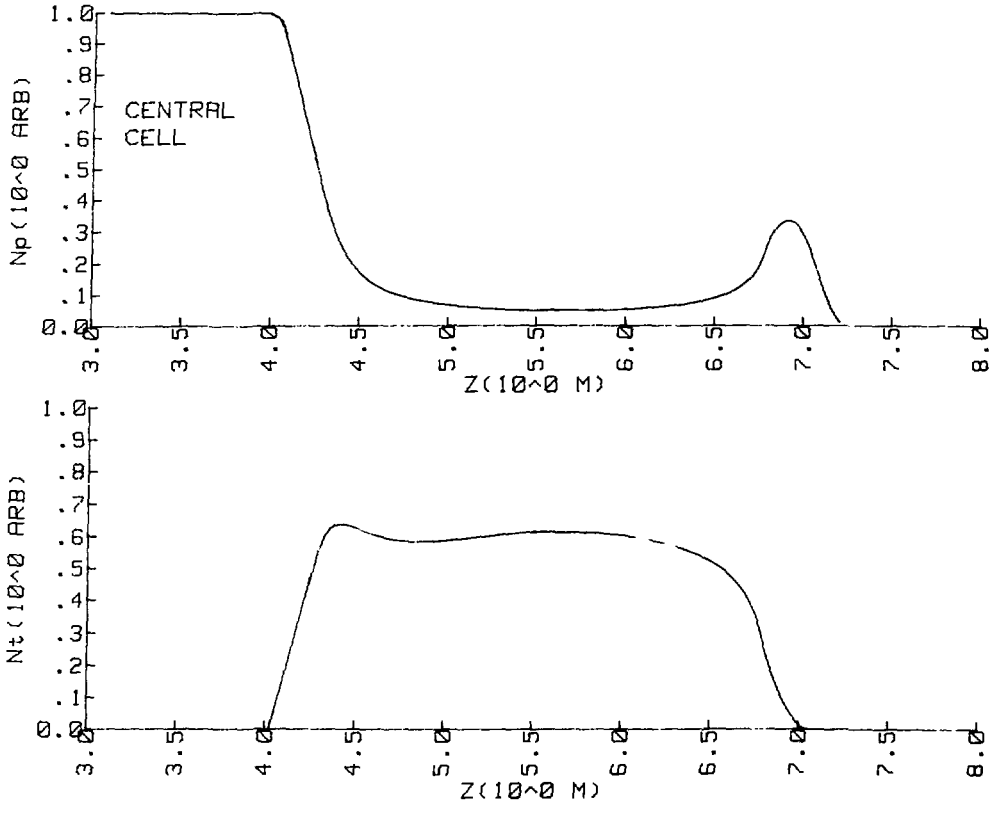

Fig. 2. Axial profiles of n_p, the density of passing ions in the end cell, originating from the Maxwellian central cell ion population (top figure), and n_T, the density of ions trapped in the potential well as a consequence of ion-ion collisions (bottom figure).

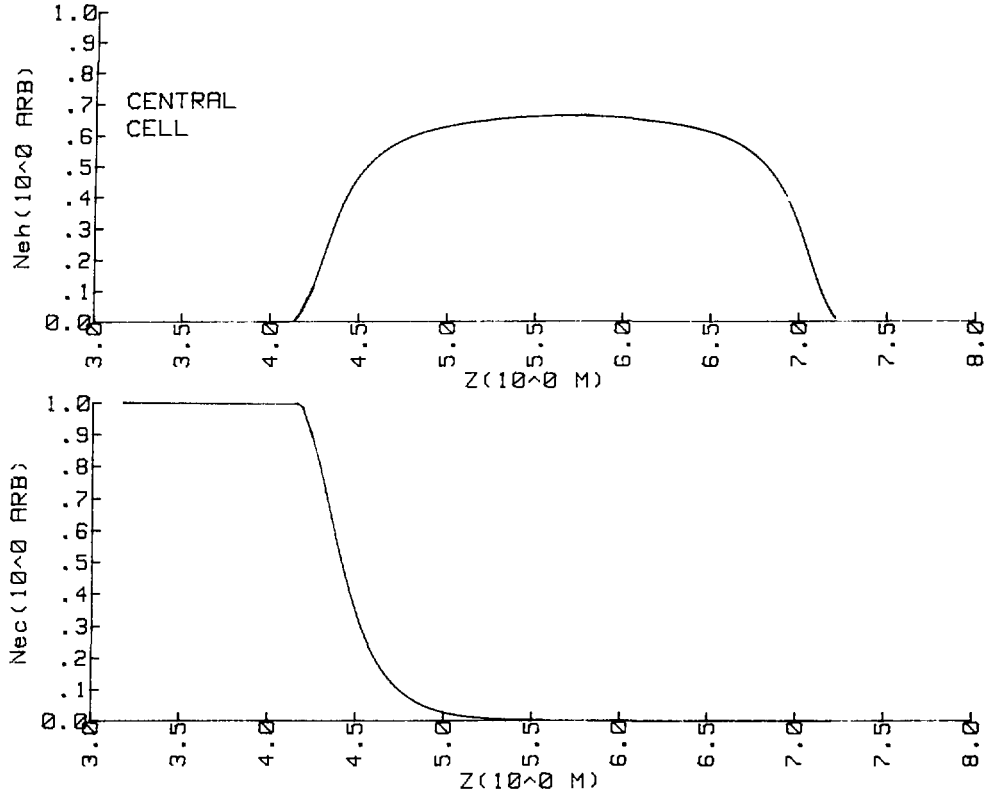

Fig. 3. Axial profiles of n_e, the density of Maxwellian electrons confined between the low potential end cells (top figure), and n_H, the density of energetic, mirror confined electrons in the end cell (bottom figure).

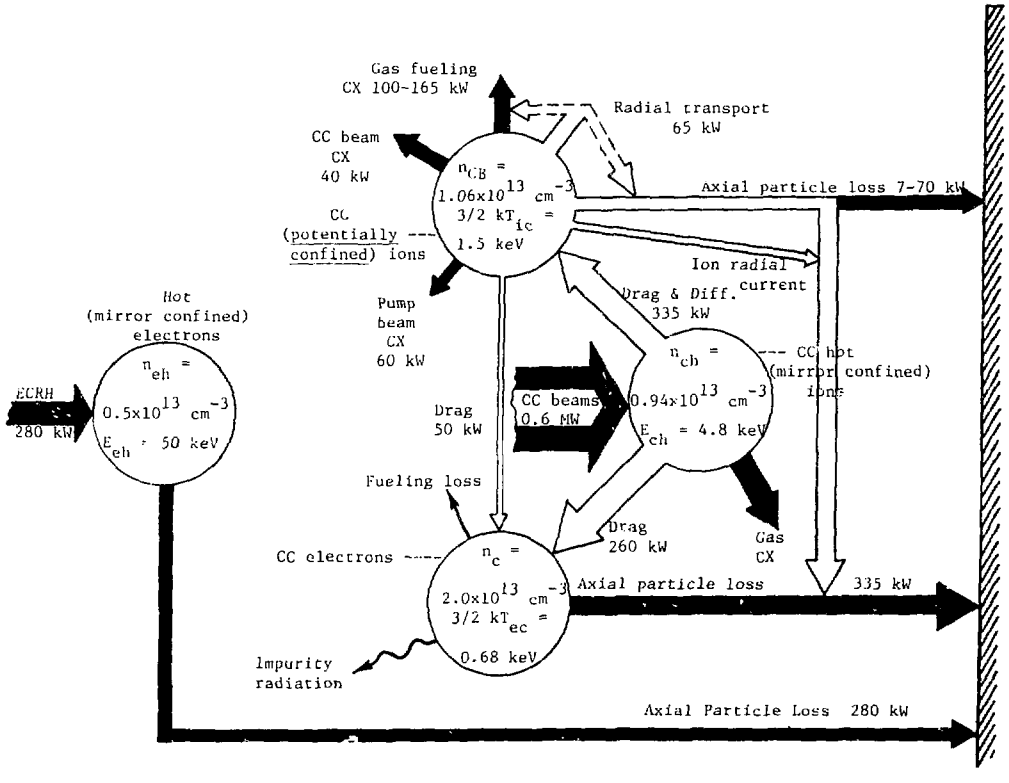

Fig. 4. The power flow in TMX-Upgrade operated in the negative mode (corresponds to Case A, Table I).

8. OPEN FORUM

MHD STABILITY OF TANDEM MIRRORS

P. Poulsen, A. Molvik, J. Shearer (LLNL)

The TMX Upgrade tandem mirror experiment at LLNL can test MHD stability boundaries. We are in the process of formulating the experiments. Of particular interest is the effect of the hot electron end plugs on the MHD stability of the plasma. The purpose of the discussion group was to acquaint MHD theorists (Antonsen, Berk, Spong, Van Dam) with the TMX-Upgrade experiment and its capabilities. The theorists would then be in a position to interact with TMX experimentalists and aid in defining experiments to test MHD stability boundaries and theories.

The TMX-Upgrade experiment was described, and the manner in which various plasma parameters could be affected was discussed. The initial analysis of the MHD stability of the tandem mirror was also discussed, with emphasis on the negative tandem configuration.

CAPABILITIES AND VARIABLES OF TMX-UPGRADE

The MHD stability regimes depend on the relative drift and precessional velocities and the β- ratios of the central cell (or core) plasma and the end plugs (location of the hot electron plasma). The TMX-Upgrade experimental facility appears capable of investigating the MHD stability boundaries since the β value, density, and temperature in the end plugs and the central cell can be varied independently to some extent. Fig. 1 shows a schematic of the experiment; the power and particle sources are: Central cell neutral beams, central cell ICRH (planned), central cell gas fueling, end cell ECRH (resonant at 1.0 T), and end cell sloshing ion and pumping beams. Significant plasma parameters and anticipated means of affecting the parameters are:

a. Minimum-B end cell vs. non-minimum-B end cell magnetic field: The magnetic geometry can be changed by changing the quadrupole magnetic field component. This is important for investigating the mechanism of hot electron ring vs. sphere formation.

b. The end cell and central cell β can be varied by changing the magnitude of the magnetic field strength without significantly changing the power input and plasma pressure.

c. The density and temperature of the hot electron population can be varied independently by altering the density at the $1\ \omega_{ce}$ resonance point; this can be achieved by means of altering the plug mirror ratio or the central cell density.

d. The hot electron pressure in the plug can be changed by altering the applied ECRH power.

e. The ion pressure in the plug can be changed by altering the current of sloshing ion beam neutrals injected.

f. The central cell plasma pressure can be affected by changes in neutral beam power input, in the ICRH power level, and the gas feed.

To summarize, the TMX Upgrade appears to be quite capable of varying the hot electron and thermal plasma parameters in such a way as to test theoretical MHD stability boundaries and hence the theory. Initial TMX Upgrade experiments will indicate over what range such variations are possible.

The initial analysis of the MHD stability of the TMX Upgrade negative tandem configuration was then discussed. The analysis consisted of three parts.

1. A frequency condition for the MHD stability contribution of the hot end cell electrons.

2. A condition on the β of the plug ions for the MHD stability contribution of the hot end cell electrons.

3. The stabilizing effect of increased radial Grad B due to the β of the hot electrons; this is the same effect that apparently stabilizes the EBT-type experiments.

The frequency condition employed for the analysis of the hot electron contribution to MHD stability of the negative TMX-Upgrade plasma was:

$$T_{eh} << T_{ic} \frac{R}{r_c} \sqrt{\frac{B_p}{B_c}} \quad \text{(for MHD stability contribution)}$$

It was suggested that a more correct relation would be:

$$\sqrt{\frac{V_i}{R_p R_c}} > \frac{V_{the}^2}{r R_c \, \omega_{ce}}$$

The condition on the β of the end plug ions used to analyze TMX negative was:

$$\beta_{ip} > 2 \frac{r_p}{R} \frac{(1 - \beta_H)}{(1 + \beta_H)} \quad \text{(for MHD stability contribution)}$$

This relation, together with a relation between the ion β in the plug and central cell, showed that the hot plug electrons would contribute to MHD stability for the nominal operating condition, but not necessarily during start-up. The question was raised whether hot ions would decouple from contributing to MHD stability as is predicted for hot electrons.

The stabilizing effect of increased radial Grad B due to the finite β of the hot electrons was discussed. This is the mechanism of stability for EBT-type plasma. The effect appears to be large and stabilizing for the hot electron plug β of 30% expected in TMX-Upgrade; detailed calculations are in progress at LLNL.

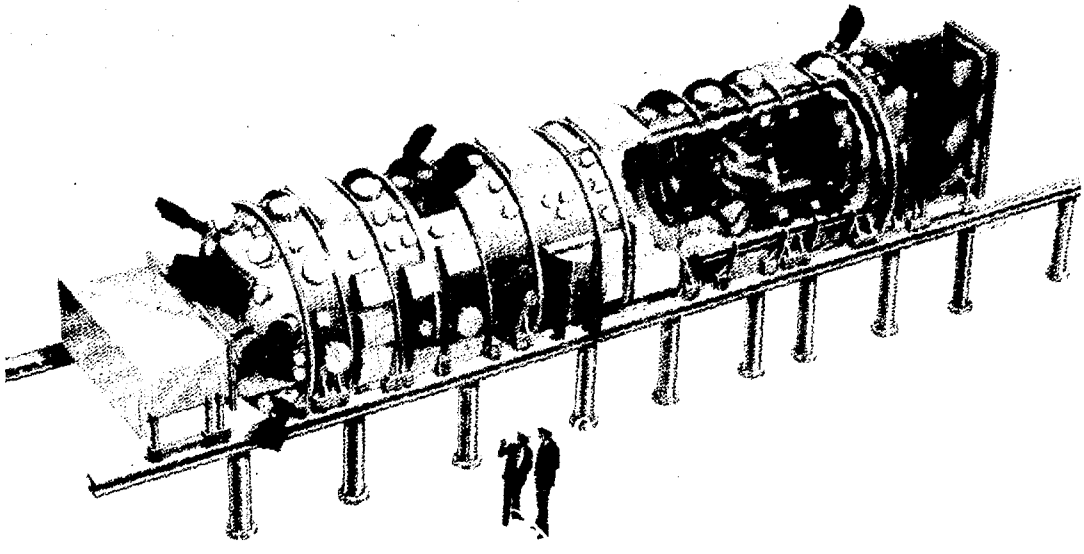

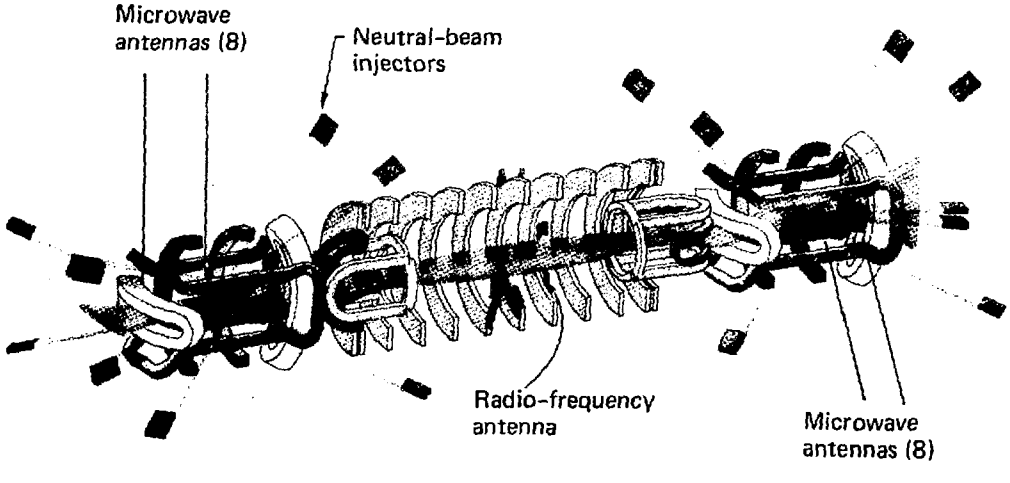

Fig. 1. A schematic of TMX-Upgrade showing the power and particle sources.

AUTHOR INDEX

H. Akiyama, 145
I. Alexeff, 181
W. B. Ard, 1
S. L. Allen, 815
T. M. Antonsen, 191
F. W. Baity, Jr., 597
J. Barter, 519
D. B. Batchelor, 1, 487
H. L. Berk, 1, 83, 93
L. A. Berry, 1, 167
F. M. Bieniosek, 609, 793
D. A. Boyd, 701
R. B. Campbell, 739
T. A. Casper, 815
P. J. Catto, 117
C. M. Celata, 717
Y-J. Chen, 279
C. Z. Cheng, 143
R. H. Cohen, 561
R. J. Colchin, 167
K. A. Connor, 793
R. A. Dandl, 393, 441, 463, 519
W. A. Davis, 609
J. M. Dawson, 213
L. E. Deleanu, 409
W. DiVergilio, 519
M. Fujiwara, 1, 339
N. T. Gladd, 1, 247
J. C. Glowienka, 167, 597, 609
R. C. Goldfinger, 487
M. R. Gordinier, 721
D. P. Grubb, 815
G. E. Guest, 393, 531
K. Hamamatsu, 761
S. Hamasaki, 373, 471
G. R. Haste, 1, 23, 167
B. I. Hauss, 531
C. L. Hedrick, 1, 409
D. L. Hillis, 167, 317, 597, 609
S. Hiroe, 145, 167
M. Hosokawa, 339
J. E. Howard, 561
H. Ikegami, 339
M. Inutake, 145
R. A. Jong, 815
R. E. Juhala, 425
T. Kammash, 289
R. J. Kashuba, 1, 289, 721
N. A. Krall, 1, 45, 373, 471
T. Kunibe, 145
L. L. Lao, 463
N. H. Lazar, 441, 463, 519
Y. C. Lee, 191
A. J. Lichtenberg, 561
M. A. Leiberman, 561
B. G. Logan, 739
Y. Matsuda, 505
J. B. McBride, 1
A. Molvig, 829
W. M. Nevins, 279, 505
W. E. Nexsen, 815
K. T. Nguyen, 289
K. Nishikawa, 761
Y. Ohsawa, 213
L. W. Owen, 409
T. L. Owens, 597

AUTHOR INDEX (Continued)

M. Porkolab, 237
G. D. Porter, 815
P. Poulsen, 815 829
M. A. Prelas, 425
B. H. Quon, 1, 441, 463, 519
T. D. Rognlien, 545
M. N. Rosenbluth, 83, 93
T. K. Samec, 531
J. W. Shearer, 583, 829
T. C. Simonen, 815
G. R. Smith, 279
L. Solensten, 609
J. L. Sperling, 1, 373, 471
D. A. Spong, 1, 83, 93
B. W. Stallard, 705
S. Tamor, 689
M. Tanaka, 339
G. D. Tsakiris, 701
K. T. Tsang, 1, 117
N. A. Uckan, 1, 361, 657
T. Uckan, 167, 609, 635, 657
J. W. Van Dam, 83, 93, 761
C. B. Wallace, 425
T. Watanabe, 1, 761
H. Weitzner, 487
J. Wilgen, 635
D. Winske, 701
R. F. Wuerker, 441, 519

ATTENDANCE LIST

2nd WORKSHOP ON HOT ELECTRON RING PHYSICS

December 1-3, 1981

San Diego, California

Thomas M. Antonsen
Laboratory for Plasma and Fusion Energy Studies
University of Maryland
College Park, MD 20742

W. B. Ard
McDonnell Douglas Astronautics Corp.
P. O. Box 516
St. Louis, MO 63166

D. Arnush
TRW, Incorporated
One Space Park
Redondo Beach, CA 90278

F. W. Baity
Oak Ridge National Laboratory
P. O. Box Y
Oak Ridge, TN 37830

D. B. Batchelor
Oak Ridge National Laboratory
P. O. Box Y
Oak Ridge, TN 37830

David Baxter
Science Applications, Inc.
P. O. Box 2351
La Jolla, CA 92038

H. L. Berk
Institute for Fusion Studies
University of Texas
Austin, TX 78712

L. A. Berry
Oak Ridge National Laboratory
P. O. Box Y
Oak Ridge, TN 37830

F. M. Bieniosek
McDonnell Douglas Astronautics Corp.
P. O. Box 516
St. Louis, MO 63166

Robert B. Campbell, L-644
TRW, Incorporated and
Lawrence Livermore National Lab.
P. O. Box 5511
Livermore, CA 94550

Maria Zales Caponi
TRW, Incorporated
One Space Park
Redondo Beach, CA 90278

Kenneth H. Carpenter
University of Missouri-Rolla
Department of Electrical Eng.
Rolla, MO 65401

Christine Celata
Dartmouth College
Physics Department
Hanover, NH 03755

Yu-Jiuan Chen
Lawrence Livermore National Lab.
P. O. Box 5511, L-630
Livermore, CA 94550

C. Z. Cheng
Institute for Fusion Studies
University of Texas
Austin, TX 78712

Melville Clark, Jr.
Combustion Engineering, Inc.
1000 Prospect Hill Road
Windsor, CT 06095

R. H. Cohen, L-644
Lawrence Livermore National Lab.
P. O. Box 5511
Livermore, CA 94550

Kenneth Connor
Rensselaer Polytechnic Institute
ECSE Department
Troy, NY 12181

R. A. Dandl
Applied Microwave Plasma Concepts
2210 Encinitas Blvd., Suite F
Encinitas, CA 92024

Burton Fried
UCLA, Physics Department
405 North Hilgord
Los Angeles, CA 90024

Masami Fujiwara
Institute of Plasma Physics
Nagoya University
Nagoya 464, Japan

N. T. Gladd
JAYCOR
P. O. Box 85154
San Diego, CA 92138

R. C. Goldfinger
Oak Ridge National Laboratory
P. O. Box Y
Oak Ridge, TN 37830

Gareth E. Guest
Applied Microwave Plasma Concepts
2210 Encinitas Blvd., Suite F
Encinitas, CA 92024

Seishi Hamasaki
JAYCOR
P. O. Box 85154
San Diego, CA 92138

G. R. Haste
Oak Ridge National Laboratory
P. O. Box Y
Oak Ridge, TN 37830

C. L. Hedrick
Oak Ridge National Laboratory
P. O. Box Y
Oak Ridge, TN 37830

D. L. Hillis
Oak Ridge National Laboratory
P. O. Box Y
Oak Ridge, TN 37830

Shinji Hiroe
Oak Ridge National Laboratory
P. O. Box Y
Oak Ridge, TN 37830

Jim Howard
University of California at Berkeley
Cory Hall
Berkeley, CA 94720

Mark Iskra
TRW/University of Michigan
One Space Park
Redondo Beach, CA 90278

R. Juhala, Dept. E230, Bldg. 107/2
McDonnell Douglas Astronautics Corp.
P. O. Box 516
St. Louis, MO 63166

Terry Kammash
University of Michigan
Dept. of Nuclear Engineering
Ann Arbor, MI 48109

R. J. Kashuba
McDonnell Douglas Astronautics Corp.
P. O. Box 516
St. Louis, MO 63166

H. H. Klein
JAYCOR
P. O. Box 85154
San Diego, CA 92138

Nicholas A. Krall
JAYCOR
P. O. Box 85154
San Diego, CA 92138

Lang Li Lao
TRW, Incorporated
One Space Park
Redondo Beach, CA 90278

Norman H. Lazar
TRW, Incorporated
One Space Park
Redondo Beach, CA 90278

Y. Matsuda
Lawrence Livermore National Lab.
P. O. Box 5511, L-630
Livermore, CA 94550

John B. McBride
Science Applications, Inc.
1200 Prospect Street
La Jolla, CA 92037

Arthur W. Molvik
Lawrence Livermore National Lab.
P. O. Box 5511, L-637
Livermore, CA 94550

Michael Mond
Courant Institute
New York University
251 Mercer Street
New York, NY 10012

Kenneth G. Moses
JAYCOR
P. O. Box 85154
San Diego, CA 92138

Yukiharu Ohsawa
University California Los Angeles
Department of Physics
405 Hilgard Avenue
Los Angeles, CA 90024

Miklos Porkolab
Massachusetts Institute of Tech.
Cambridge, MA 02139

Peter Poulsen
Lawrence Livermore National Lab.
P. O. Box 5511
Livermore, CA 94550

Bill H. Quon
TRW, Incorporated
One Space Park
Redondo Beach, CA 90278

A. C. Riviere
UKAEA
Culham Laboratory
Abingdon, Oxon, United Kingdom

T. D. Rognlien
Lawrence Livermore National Lab.
P. O. Box 5511, L-630
Livermore, CA 94550

Tom K. Samec
TRW, Incorporated
One Space Park
Redondo Beach, CA 90278

James W. Shearer
Lawrence Livermore National Lab.
P. O. Box 5511
Livermore, CA 94550

J. L. Sperling
JAYCOR
P. O. Box 85154
San Diego, CA 92138

D. A. Spong
Oak Ridge National Laboratory
P. O. Box Y
Oak Ridge, TN 37830

Barry Stallard
Lawrence Livermore National Lab.
P. O. Box 5511
Livermore, CA 94550

D. W. Swain
Oak Ridge National Laboratory
P. O. Box Y
Oak Ridge, TN 37830

Stephen Tamor
Science Applications, Inc.
1200 Prospect Street, Suite 480
La Jolla, CA 92037

Kang T. Tsang
Science Applications, Inc.
934 Pearl Street
Boulder, CO 80302

James Turner
U.S. Department of Energy
Office of Fusion Energy
Washington, DC 20745

Nermin A. Uckan
Oak Ridge National Laboratory
P. O. Box Y
Oak Ridge, TN 37830

Taner Uckan
Oak Ridge National Laboratory
P. O. Box Y
Oak Ridge, TN 37830

James W. Van Dam
Institute for Fusion Studies
University of Texas
Austin, TX 78712

Tsuguhiro Watanabe
Institute for Fusion Theory
Hiroshima University
Higashisenda-machi, Nakaku,
Hiroshima 730, Japan

J. B. Wilgen
Oak Ridge National Laboratory
P. O. Box Y
Oak Ridge, TN 37830

Dan Winske
Laboratory for Plasma and Fusion
Energy Studies
University of Maryland
College Park, MD 20742

J. T. Woo
Plasma Dynamics Laboratory
Rensselaer Polytechnic Institute
Troy, NY 12181

SECOND WORKSHOP ON HOT ELECTRON RING PHYSICS

December 1-3, 1981

Bahia Hotel
San Diego, California

Sponsored by

OAK RIDGE NATIONAL LABORATORY
Oak Ridge, Tennessee

and

JAYCOR
San Diego, California

AGENDA

Tuesday, December 1, 1981

8:30		N. A. Uckan and N. A. Krall: Opening Remarks
8:40		Session A: Overview N. A. Uckan, Chairman
	A.1	G. R. Haste, "Hot Electron Rings: Diagnostic Review and Summary of Measurements"
	A.2	N. A. Krall, "A Perspective on EBT Electron Ring Theory"
10:30		COFFEE BREAK
10:45		Session B: Stability I R. J. Kashuba and J. L. Sperling, Chairmen
	B.1	H. L. Berk, M. N. Rosenbluth, J. A. Van Dam, and D. A. Spong, "Curvature Driven Instabilities in a Hot Electron Plasma: Radial Analysis"
	B.2	D. A. Spong, H. L. Berk, J. A. Van Dam, and M. N. Rosenbluth, "Radial Structure of Instability Modes in the EBT Hot Electron Annulus"
	B.3	K. T. Tsang and P. J. Catto, "Stability of Low Frequency Modes in a Hot Electron Bumpy Torus"
	B.4	C. Z. Cheng, "Kinetic Theory of EBT Stability"
12:30		LUNCH
2:00		Session C: Stability II H. L. Berk and K. T. Tsang, Chairmen
	C.1	S. Hiroe, T. Kunibe, H. Akiyama, and M. Inutake "Stabilization of the High-Beta Plasma Instability with ECH Hot Electron Annulus in the Symmetric Mirror" S. Hiroe, L. A. Berry, R. J. Colchin, J. C. Glowienka, G. R. Haste, D. L. Hillis, and T. Uckan, "Experimental Hot-to-Warm Electron Density Ratio for Instability Thershold in the ELMO Bumpy Torus"

2:00 Session C: Stability II continued

C.2 I. Alexeff, Stabilization of the Flute Instability by a D.C. Electric Field in Toroidal Plasmas"

C.3 T. M. Antonsen, Jr. and Y. C. Lee, "Necessary and Sufficient Criteria for the Stability of a Hot Particle Ring - Plasma System"

C.4 Y. Ohsawa and J. M. Dawson, "Simulation Studies on Stability and β Limits of EBT"

3:30 COFFEE BREAK

3:45 C.5 M. Porkolab, "Parametric Decay Instabilities in ECR Heated Plasmas"

C.6 N. T. Gladd, "The Whistler Instability at Relativistic Energies"

C.7 Y-J. Chen, W. M. Nevins, and G. R. Smith, "High-Frequency Microinstabilities in Hot-Electron Plasmas"

C.8 K. T. Nguyen, T. Kammash, and R. J. Kashuba, "Stability of Anisotropic Relativistic Hot Electron Plasma in the Elmo Bumpy Torus"

6:00 RECEPTION, BAHIA BELLE, DOCKSIDE, BAHIA HOTEL (Complimentary Cocktails and Buffet Dinner)

Wednesday, December 2, 1981:

8:30 Session D: Ring Properties and Scaling
W. B. Ard and B. H. Quon, Chairmen

D.1 D. L. Hillis, "Hard X-ray Measurements of the Hot Electron Rings in EBT-S"

D.2 M. Tanaka, M. Hosokawa, M. Fujiwara, and H. Ikegami, "Experimental Studies on Hot Electron Rings in Nagoya Bumpy Torus (NBT-1)"

D.3 N. A. Uckan, "Ring Temperature Scaling"

D.4 S. Hamasaki, N. A. Krall, and J. L. Sperling, "Parametric Study of the Relativistic Electron Ring"

D.5 G. E. Guest and R. A. Dandl, "Prospects for Control of ELMO Rings"

10:30 COFFEE BREAK

10:45 D.6 L. W. Owen, L. E. Deleanu, and C. L. Hedrick, "Nonadiabaticity and High Energy Particle Orbits in EBT"

D.7 R. E. Juhala, M. A. Prelas, and C. B. Wallace, "The Nonadiabatic Motion of Hot Annulus Electrons in EBT-I and EBT-P"

D.8 B. H. Quon, R. A. Dandl, N. H. Lazar, and R. F. Wuerker, "Heating of Energetic Electrons and ELMO Ring Formation in Symmetric Mirror Facility"

D.9 L. L. Lao, B. H. Quon, R. A. Dandl, and N. H. Lazar, "Spatial Structure of the SM-1 Symmetric Mirror Hot Electron Ring Using Diamagnetic Measurements"

D.10 J. L. Sperling, S. Hamasaki, and N. A. Krall, "Bumpy Torus Annulus Startup"

Wednesday, December 2, 1981 continued

12:30 LUNCH

2:00 Session E: Ring Heating
B. G. Logan and C. L. Hedrick, Chairmen

E.1 D. B. Batchelor, R. C. Goldfinger, and H. Weitzner, "Ray Tracing Studies of Microwave Heating of the Annulus in EBT Devices"

E.2 B. W. Stallard, Y. Matsuda, and W. M. Nevins, "Fokker-Planck Calculations of Electron Cyclotron Resonant Heating (ECRH) in Mirror Geometry"

E.3 N. Lazar, J. Barter, R. Dandl, W. DiVergilio, B. Quon, and R. Wuerker, "Multiple Frequency ECH (MFECH) in SM-1 and STM-1"

E.4 T. K. Samec, B. I. Hauss, and G. Guest, "Simulation of Electron Cyclotron Resonance Heating with Multiple Frequencies

3:30 COFFEE BREAK

3:45 E.5 T. D. Rognlien, "Simulation of Multi-Frequency ECRH"

E.6 J. E. Howard, M. A. Lieberman, A. J. Lichtenberg, and R. H. Cohen, "Theory of Multifrequency ECRH"

E.7 J. W. Shearer, "Doppler-Shifted Resonance Absorption by Hot Electrons"

E.8 F. W. Baity, J. C. Glowienka, D. L. Hillis, and T. L. Owens, "Enhancement of EBT Ring Parameters During Ion Cyclotron Heating"

E.9 J. C. Glowienka, W. A. Davis, D. L. Hillis, T. Uckan, F. M. Bieniosek, and L. Solensten, "Nonstandard Heating Experiments in EBT"

Thursday, December 3, 1981

8:30 Session F: Synchrotron Emission
G. R. Haste, Chairman

F.1 J. Wilgen and T. Uckan, "Synchrotron Emission Measurements from the Hot Electron Rings in EBT"

F.2 T. Uckan and N. A. Uckan, "Synchrotron Emission from the Ring Electrons in EBT"

F.3 S. Tamor, "Electromagnetic Interactions of Anisotropic Electron Distributions"

F.4 D. Winski, D. A. Boyd, and G. D. Tsakiris, "Analytic Expressions for Synchrotron Radiation from EBT"

F.5 C. M. Celata, "Electron Synchrotron Emission from the EBT Ring Plasma"

10:30 COFFEE BREAK

10:45 Session G: Ions, Tandems, Equilibria, and Power Balance
L. A. Berry, Chairman

G.1 M. R. Gordinier and R. J. Kashuba, "Ion Ring Scaling Studies for an EBT Reactor"

Session G: Ions, Tandems, Equilibria, and Power Balance
Continued

G.2 R. B. Campbell and B. G. Logan, "Ring Power Balance Observing Plasma Stability Constraints"

G.3 T. Watanabe, K. Hamamatsu, J. W. Van Dam, and K. Nishikawa, "Numerical Study of Vlasov Equilibrium for Bumpy Cylinder Plasma with Hot Electron Rings"

G.4 F. M. Bieniosek and K. A. Connor, "Sensitivity of Heavy-Ion Beam Probe to Hot Electrons in EBT"

G.5 P. Poulsen, T. C. Simonen, G. D. Porter, S. L. Allen, R. A. Jong, D. P. Grubb, W. E. Nexsen, and T. A. Casper, "The 'Negative' Tandem Mirror"

12:30 LUNCH

2:00 Session O: Open Forum
N. A. Uckan and N. A. Krall, Chairmen

O.1 P. Poulsen, A. Molvig, and J. Shearer, "MHD Stability of Tandem Mirrors"

☆U.S. GOVERNMENT PRINTING OFFICE: 1982-546-067/42